Faculty
of Science

Palacký University
Olomouc

DOCTORAL THESIS

Mgr. Pavel Michal

Optimization of a Raman optical activity spectrometer for measurement in an extended spectral range

Olomouc 2024

Annotation

This thesis focuses on the development of experimental methodology and interpretation of Raman and Raman optical activity (ROA) spectra. Results concerning absolute configuration, structure and dynamic behavior of various chiral substances in the extended spectral range from 50 to 4000 cm^{-1} are presented. Studied samples were measured on a Raman optical activity spectrometer developed at the Department of Optics. The author of the thesis participated also in the instrumental development. In order to increase the potential of ROA spectroscopy in chemical practice, we suggested a new methodology for accurate determination of the enantiomeric excess of chiral samples. As another topic, a new approach to the conformational analysis of model biomolecules is discussed. We show that compared to the commonly analyzed range of 200–2400 cm^{-1}, the extended spectral region provides information about to date unexplored vibrational modes. The experimental data could be interpreted using quantum-chemical calculations and molecular dynamics. A crystal-like computational protocol to treat bulk liquid was developed, and a detailed analysis of low-frequency vibrational modes of small and medium-sized chiral molecules is performed. Some combination and overtone ROA bands were observed and successfully assigned for the first time.

Keywords: vibrational optical activity, Raman optical activity, quantum-chemical calculations, conformational analysis, molecular interactions, molecular dynamics, anharmonic corrections, enantiomeric excess

Title:	Optimization of a Raman optical activity spectrometer for measurement in an extended spectral range
Author:	Mgr. Pavel Michal
ORCID:	0000-0002-7648-6006
ResearcherID:	GPC-7467-2022
Supervisor:	RNDr. Josef Kapitán, Ph.D.
Consultant:	Prof. RNDr. Petr Bouř, DSc.
Ph.D. program:	Optics and Optoelectronics (full-time form)
Institution:	Department of Optics, Faculty of Science, Palacký University
Year:	2024
Pages:	192

Přírodovědecká
fakulta

Univerzita Palackého
v Olomouci

DISERTAČNÍ PRÁCE

Mgr. Pavel Michal

Optimalizace spektrometru pro měření Ramanovy optické aktivity v rozšířené spektrální oblasti

Olomouc 2024

Anotace

Tato disertační práce je zaměřena na rozvoj metodiky měření a interpretace spekter Ramanovy optické aktivity (ROA). V práci jsou uvedeny výsledky studia struktury a dynamického chování různých chirálních látek v rozšířeném spektrální rozsahu od 50 do 4000 cm^{-1}, které jsou měřeny pomocí ROA spektrometru vyvinutého na Katedře optiky. Autor se podílel i na vývoji přístroje. Abychom přispěli k užitečnosti ROA techniky v analytické chemii, vypracovali jsme metodiku přesnějšího určování enantiomerního přebytku u chirálních vzorků. Také je prezentován nový přístup ke konformační analýze studovaných molekul. Ukazujeme, že oproti běžně analyzovanému rozsahu 200–2400 cm^{-1} poskytuje rozšířená spektrální oblast navíc informaci o dosud neprobádaných vibračních pohybech molekul. Nedílnou součástí práce je také interpretace experimentálních dat s použitím kvantově-chemických a molekulárně dynamických metod. Je představen výpočetní protokol použitelný pro chirální kapaliny, založený na periodickém modelu kapaliny. S jeho pomocí je provedena podrobná analýza nízkofrekvenčních vibračních módů modelových chirálních molekul. Vůbec poprvé byl změřen ROA signál mnoha kombinačních a vyšších harmonických vibračních módů, a příslušné pásy byly přiřazeny ke konkrétním molekulovým vibracím.

Klíčová slova: vibrační optická aktivita, Ramanova optická aktivita, kvantově-chemické výpočty, konformační analýza, molekulární interakce, molekulární dynamika, anharmonické korekce, enantiomerní čistota/přebytek

Název: Optimalizace spektrometru pro měření Ramanovy optické aktivity v rozšířené spektrální oblasti
Autor: Mgr. Pavel Michal
ORCID: 0000-0002-7648-6006
ResearcherID: GPC-7467-2022
Školitel: RNDr. Josef Kapitán, Ph.D.
Konzultant: Prof. RNDr. Petr Bouř, DSc.
Studijní obor: Optika a optoelektronika (prezenční forma)
Instituce: Katedra optiky, Přírodovědecká fakulta, Univerzita Palackého
Rok: 2024
Počet stran: 192

Acknowledgements

I would like to thank to my supervisor Dr. Josef Kapitán for his guidance, patience, invaluable advices, endless effort, and all his hard work put into the development of the ROA spectrometer and leading his team through all these years. It was my pleasure to work with him and to be his friend since I began working in the field of Raman spectroscopy.

I am also thankful to my consultant Prof. Petr Bouř for his mentoring in the field of computational chemistry, providing me with his programs and computational resources, constant support during my studies, and motivation to finish my doctoral degree.

I am grateful to all my friends and colleagues in the Department of Optics, with special thanks to Dr. Jana Hudecová and Dr. Radek Čelechovský, for creating a friendly environment, being helpful, and always supportive. I also thank to members of Molecular Spectroscopy group at the Institute of Organic Chemistry and Biochemistry, Czech Academy of Sciences in Prague, for an inspirational environment and a series of discussions.

My great appreciation goes to Prof. Alison Rodger from the Macquarie University in Sydney (Australia) for the opportunity to work for three months in Australia and for introduction to other spectroscopic techniques.

The most important thanks belong to my parents to whom I owe more than I could say here. I would never have finished my studies without their support.

Declaration

This thesis is an original work of its author. All sources are cited under References. The thesis is based on scientific work that has been published in collaboration with other co-authors. The contribution of the author is outlined at the end of the thesis. This thesis may be freely distributed in an unchanged form. Palacký University Olomouc has the rights to archive, publish and distribute the thesis according to its internal regulations and Czech law.

In Olomouc 2nd January 2024

Contents

1. Introduction

The techniques of chiroptical spectroscopy are based on the different interactions of left- and right-handed circularly polarized radiation with chiral molecules. According to the optical phenomena reflecting this interaction, we recognize three main experimental branches of chiroptical spectroscopy: optical rotatory dispersion (ORD), circular dichroism (CD), and Raman optical activity (ROA). Exploring the unique equipment at the Department of Optics, this thesis focuses predominantly on ROA spectroscopy. Other spectroscopic techniques are briefly introduced in Subsection 2.1.3.

In recent years, ROA has become a quickly developing technique of vibrational spectroscopy. ROA has been established as a powerful and noninvasive tool to analyze molecular structures and interactions of chiral molecules in solution. One of the major advantages of ROA is the ease of measuring samples in aqueous solution. Second, a larger number of observable spectral bands compared to the complementary vibrational circular dichroism (VCD) spectroscopy provides a better basis for the analysis of observed spectra. A wide range of inorganic and organic molecules, including helicenes, peptides, proteins, fibrils, sugars, nucleic acids, or even viruses, have already been studied by this technique.

ROA provides extremely useful information about chiral molecules, however, the ROA signal is usually 4 to 5 orders of magnitude weaker than the already weak Raman scattering, so the spectra are sensitive to experimental artifacts. The signal can be affected by intensity fluctuations caused by the laser instability or by thermal fluctuations in the sample. Further, the baseline in the parent Raman spectrum can be plagued by the fluorescent background from impurities (e.g., dust) in the sample, which may change during the accumulation of the spectra. Last but not least, an experimental obstacle is also the need of relatively large sample volumes (~10 μL) and concentrations of at least 1 $\mathrm{mg \cdot mL^{-1}}$. In summary, ROA measurement is demanding and at least basic knowledge in optics is needed for conducting and understanding the experiment. So far, neither ROA nor VCD has been considered as a conventional tool for large-output structural and dynamical studies of chiral molecules or in such analyses of the optical purity – the relative amount of the opposite enantiomers contained in the sample. The goal of this work was to advance instrumentation and applications so that the advantage of ROA can be achieved.

The interpretation of experimental ROA spectra often relies on the comparison of the measured and calculated spectra looking for agreement of signs, relative intensities, and spectral shapes of the observed bands. Therefore, the development of simulation models is of particular importance. The simulations used in the thesis are based on a combined molecular dynamics and density functional theory approach. Simulations of large molecular complexes or solvent-solute systems are often computationally demanding, and a feasible computational protocol is required to overcome the computational limits.

The aim of our effort was to contribute to the development of experimental methodology and interpretation of Raman and ROA spectra of various chiral substances. The work is focused on unexplored spectral features within 50–4500 cm^{-1}, measured by a double-grating ROA spectrometer developed at the Department of Optics, Faculty of Science, Palacký University Olomouc. The thesis is based on four publications attached in the appendix, published in high impact journals.

The thesis has the following structure:

> Chapter 2 presents the methodology. Section 2.1 summarizes the necessary theoretical basics from optics and quantum chemistry. Section 2.2 describes modern computational approaches based on density functional theory in the harmonic approximation (Subsection 2.2.1) and including anharmonic corrections (Subsection 2.2.2). Subsection 2.2.3 is dedicated to potential energy surface (PES) scanning and procedures that incorporate more than one molecular conformation in the calculation. Approaches comprising implicit and explicit solvent models to mimic the environment are elaborated in Subsections 2.2.4 and 2.2.5. Tools useful for the optimization and spectra calculation of large molecular complexes are explained in Subsections 2.2.6 and 2.2.7, respectively. In Subsection 2.2.8, a new periodic crystal-like computational protocol to better treat chiral samples in a liquid phase is proposed. For the purpose of studying low-frequency vibrations, intermolecular coordinates are defined in Subsection 2.2.9. The experimental details of the ROA measurement are outlined in Section 2.3. Measured Raman spectra often exhibit an unstable baseline. In the upcoming Section 2.4, we delve into the techniques used to address and correct this baseline issue. This is followed by Section 2.5, which deals with the methods of comparison of experimental and predicted spectra. In Section 2.6 a new methodology to accurate enantiomeric excess determination using ROA is described.

A summary of the results discussed in Chapter 3 is arranged into three main topics that do not simply following publications, but the attached publications provide further details. The conformational analysis of flexible molecules is discussed in Subsection 3.1.1. This is followed by Subsection 3.1.2, where the original approach to the conformational analysis based on the similarity of the observed and calculated spectra is introduced and demonstrated. The next Section 3.2 shows the results achieved in the extended spectral range. In Subsection 3.2.1, the origin of the low-frequency ROA signal is discussed based on the interpretation of ROA spectra by the new periodic crystal-like model. Strong optical activity of several overtone and combination bands is measured for the first time and successfully assigned based on the perturbation and variational approaches described in Subsection 3.2.2. The last methodological project, introduced in Section 3.3, demonstrates a novel approach to accurate determination of the enantiomeric excess based on ROA measurement.

2. Methods

2.1. Theoretical basis

Chiroptical spectroscopy is based on the interaction of the electromagnetic radiation with chiral molecules. Its theoretical basis comprises properties of electromagnetic radiation, quantum molecular chemistry, chirality, and optical activity. In the beginning of this chapter, important terms from electromagnetic optics and stereochemistry are summarized. Later, the chapter is focused on the description of non-resonant Raman scattering and Raman optical activity.

2.1.1. Description of polarized light

The electromagnetic radiation is described by time-dependent electric and magnetic fields. For plane waves, the field vectors are synchronized and orthogonal to each other. Assuming a monochromatic plane wave which propagates through free space along the *z* direction, the electric (**E**) and magnetic (**H**) field vectors are

$$\mathbf{E}(z,t) = Re\left\{\mathbf{E_0} e^{i(\omega t - \mathbf{k}z)}\right\}, \tag{2.1}$$

$$\mathbf{H}(z,t) = Re\left\{\mathbf{H_0} e^{i(\omega t - \mathbf{k}z)}\right\}, \tag{2.2}$$

where $\omega = 2\pi\nu$ is the angular frequency, $\mathbf{k}$=$2\pi/\lambda\mathbf{n}$ is the wave vector, t is time, and **n** is unit vector in the direction of propagation. The wave vector **k** thus points to the propagation direction and its squared length is related to ω through the dispersion relation

$$\mathbf{k^2} = \frac{\omega^2}{c^2}, \tag{2.3}$$

where *c* is the velocity of light. Since the magnetic field can be calculated from the electric one, we just consider the complex envelope of the oscillating electric field $\mathbf{E_0}$, which lies in *x*-*y* plane as

$$\mathbf{E_0} = \mathbf{x} e_x e^{i\varphi_x} + \mathbf{y} e_y e^{i\varphi_y}, \tag{2.4}$$

where **x** and **y** are unit vectors along the coordinates, e_x and e_y are constants and φ_x and φ_y are phases. Substituting (2.4) into (2.1), we obtain

$$\mathbf{E}(z,t) = E_x\mathbf{x} + E_y\mathbf{y} = \\ = \mathbf{x}e_x \cos\left[2\pi\nu\left(t - \frac{z}{c}\right) + \varphi_x\right] + \mathbf{y}e_y \cos\left[2\pi\nu\left(t - \frac{z}{c}\right) + \varphi_y\right]. \tag{2.5}$$

The polarization of light is characterized by the particular field form and affects the interaction of light with matter, such as reflection, absorption, scattering, or propagation in anisotropic materials. The tip of the electric field vector of a general polarization state follows an ellipse in the *x*-*y* plane (**Figure 2.1**). The general equation of a polarization ellipse is

$$\frac{E_x^2}{e_x^2} + \frac{E_y^2}{e_y^2} - 2\frac{E_xE_y}{e_xe_y}\cos\varphi = \sin^2\varphi. \tag{2.6}$$

Its spatial orientation in *x*-*y* plane ψ is called the azimuth and is defined as

$$\tan 2\psi = \frac{2e_xe_y cos\varphi}{e_x^2 - e_y^2}, \tag{2.7}$$

where the $\varphi = \varphi_y - \varphi_x$ is the phase difference between the orthogonal components. $\sin\varphi$ in (2.6) describes the sense of electric field rotation. The ratio of the principal axes of the polarization ellipse

$$\sin 2\chi = \frac{2e_xe_y sin\varphi}{e_x^2 + e_y^2} \tag{2.8}$$

defines the ellipticity χ.

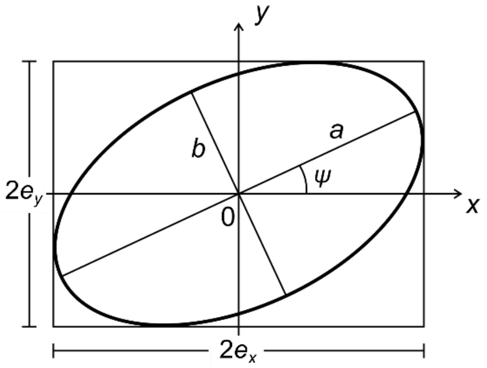

Figure 2.1: Polarization ellipse.

Particularly important in chiral spectroscopy are the linear and circular polarizations. The light is linearly polarized (LP) when one of the *x*-*y* components of the field is zero and circularly polarized when e_x and e_y are equal and the phase $\varphi = (2k-1)\pi/2$, $k = 0,1,2 \ldots$.

For right or left circular polarization (RCP/LCP), the electric field rotates clockwise or counterclockwise, respectively, if observed along the *z* axis facing the source (**Figure 2.2**) (Michal, 2015).

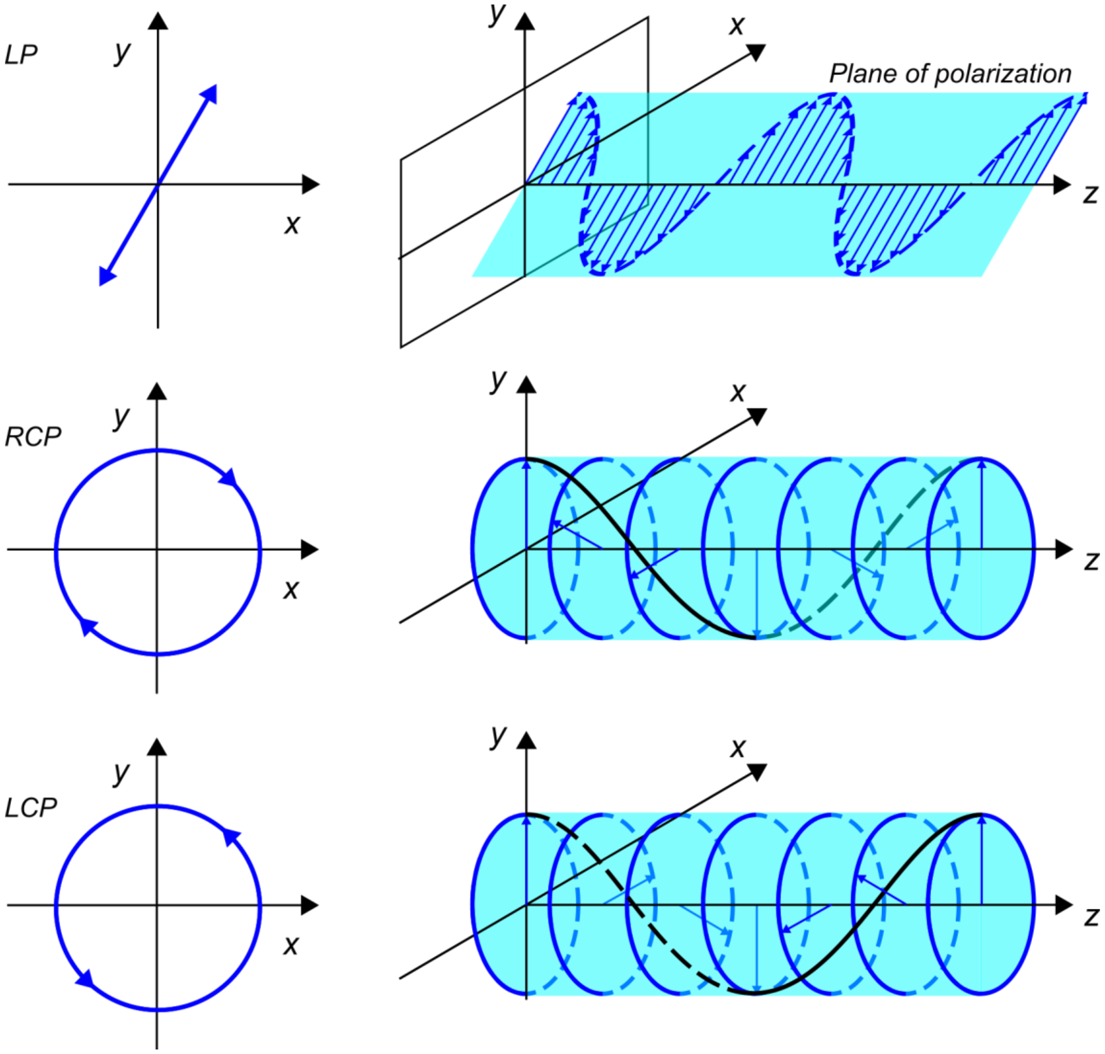

Figure 2.2: The path of the electric field vector in the *x-y* plane and in space, for the z-direction propagation, for linear, right circular and left circular polarization state.

2.1.2. Chirality

In chiroptical spectroscopy, three molecular symmetry operations are especially important – reflection, improper rotation, and inversion. Atoms in a molecule possessing the reflection symmetry are projected onto each other through a plane. If we obtain the same molecule after rotation and subsequent reflection through a plane perpendicular to the rotation axis, the molecule has improper rotation symmetry. Similarly, an inversion center defines the inversion symmetry. Details are described elsewhere (Harris & Bertolucci, 1989; Polavarapu, 2016).

Molecules that do not possess one of these three symmetries are chiral and may be optically active if they have spectroscopy to be probed. A chiral molecule and its mirror image are called enantiomers. The spatial arrangement (configuration) of the enantiomer affects some of its chemical and optical properties. In a presence of chiral center enantiomers may be labeled as "*R*" (from Latin word *rectus*, right) or "*S*" (*sinister*, left), the assignment is handled by Cahn-Ingold-Prelog (CIP) sequence rules (Cahn et al., 1966) followed by the viewing rule (**Figure 2.3**). First, the priority of each atom attached to the central one is determined according to their atomic numbers or mass in case of isotopes in descending order. If two atoms are same, the priority is assigned according to the atom attached to them. In case of identical secondary atoms, a triple bond is preferred over a double bond and a double bond over a single bond. After the priority assignment, the molecule is oriented so that the lowest priority atom points out from the observer. If the sense of rotation is a clockwise/counterclockwise by tracing the priority of remaining atoms in descending order, the molecule is labeled as "*R*"/"*S*" enantiomer.

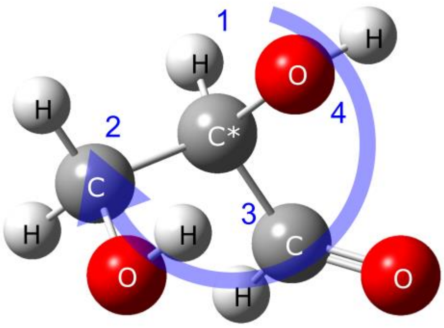

Figure 2.3: (*R*)-glyceraldehyde with assigned priorities according to the CIP sequence rules. Central carbon atom is marked by "C*". The priority of the attached atoms is labeled from the highest (4) to the lowest (1).

An older configurational notation is still in use, especially for carbohydrates and amino acids. This is referred to as the Fischer notation (Fischer, 1909). The molecule with a pyramidal (sp^3, carbon) chiral center is drawn in the plane according to the following rules. The main carbon chain is vertically oriented and relevant bonds point behind the plane with the chiral center, while other two bonds are plotted horizontally and point above the plane. The chiral center is located at the intersection of the vertical and horizontal line. The first carbon atom closest to the ketone group or its analogue is at the top (see **Figure 2.4**). Then if the OH group is located on the right, while the H group on the left, the carbohydrate is labeled as "D" enantiomer. The opposite orientation is labeled as "L" enantiomer. The "D"/"L" labels correspond to "*R*"/"*S*" labels in CIP notation. The notation is similar for amino acids, where COOH, *R*, and NH_2 groups are substituted for OH, CHO, and CH_2OH carbohydrate groups, in this order connected to the central atom.

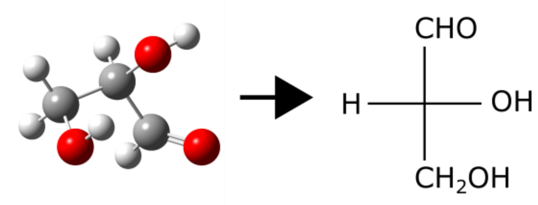

Figure 2.4: D-glyceraldehyde in the Fisher projection, H and OH point towards the observer, CHO and CH_2OH to the back.

In general, a molecule with N stereocenters may generate 2^N different absolute configurations. In addition, other types of the chirality, different from the central one described above, such as axial, helical, or planar chirality, are possible.

Within one enantiomer many conformations may exist, differing by the spatial orientation of ligands, by e.g. ring deformation (chair, boat, …) in case of cyclic molecules. This also affects measured chiroptical properties as they will be an average of the signals from the different conformations present. Peptides and proteins possess not only the central chirality, but also the structural chirality given by the secondary structure. Secondary structure is given by the protein backbone, the usual regular forms are α-helix, β-sheet, and polyproline-like helix.

2.1.3. Polarized light propagation in the optically active medium

The existence of optical activity was discovered by François Arago in quartz which rotated the plane of linear polarization of the light (Arago, 1812). Augustin-Jean Fresnel then suggested that the origin of the optical activity is in the circular double refraction, i.e. circular birefringence. Upon circular birefringence optical properties of such material are described by different refractive indices for RCP and LCP (Fresnel, 1824).

The dielectric tensor determining the optical activity in anisotropic medium can be defined as

$$\boldsymbol{\varepsilon}' = \boldsymbol{\varepsilon} + i\varepsilon_0\boldsymbol{\Gamma}, \tag{2.9}$$

where $\boldsymbol{\varepsilon}$ is isotropic part not contributing to optical activity, ε_0 is the vacuum permittivity and the matrix

$$\boldsymbol{\Gamma} = \begin{pmatrix} 0 & -G_z & G_y \\ G_z & 0 & -G_x \\ -G_y & G_x & 0 \end{pmatrix} \tag{2.10}$$

is the antisymmetric gyration tensor, where elements G_x, G_y, G_z are components of the gyration vector $\mathbf{G} = G\mathbf{s}$, and $\mathbf{s}$ is the unit vector in the propagation direction. Solving the wave equation using (2.9), we obtain a pair of orthogonal elliptically polarized waves with opposite sense of rotation. The ellipticity of them is then given as

$$\chi = \frac{-G}{\frac{1}{2}(n_2^2 - n_1^2) \pm \sqrt{\frac{1}{4}(n_2^2 - n_1^2)^2 + G^2}}, \tag{2.11}$$

where n_1 and n_2 are refractive indices in the absence of optical activity ($G = 0$). The Fresnel equation for the eigen indices of refraction is

$$(n^2 - n_1^2)(n^2 - n_2^2) = G^2. \tag{2.12}$$

In case of optically active isotropic medium ($n_1 = n_2 = \bar{n}$) we obtain RCP and LCP with refractive indices

$$n_{\substack{RCP \\ LCP}} = \bar{n} \pm \frac{G}{2\bar{n}}. \tag{2.13}$$

Therefore, the linear polarization of the incident beam is split into the superposition of two circularly polarized orthogonal modes that are propagating independently with different velocities through the optically active medium and the plane of the linear polarization of the wave emerging from the medium is then rotated by angle $\Delta\alpha$ per unit length z:

$$\frac{\Delta\alpha}{z} = \frac{\pi G}{\lambda\bar{n}} = \frac{\pi}{\lambda}(n_{LCP} - n_{RCP}) \tag{2.14}$$

with regard to the plane of incident polarization. If $n_{RCP} < n_{LCP}$ the sense of rotation is clockwise and the chiral sample is labeled as right-handed and vice versa (Yariv & Yeh, 1984). The spectroscopic method of measuring circular birefringence is referred to as optical rotation (OR).

Optically active medium affects not only the orientation of the linear polarization but also the ellipticity and total intensity of emerging wave, due to the difference in absorption of RCP and LCP light. For small angles, the ellipticity is

$$\chi \approx \frac{\pi z}{\lambda}(\beta_{LCP} - \beta_{RCP}), \tag{2.15}$$

where β_{LCP} and β_{RCP} are the absorption indices. This phenomenon is called circular dichroism (CD). In the presence of both OR and CD, a linearly polarized incident light along the *x* axis is transformed into an elliptically polarized light with its major ellipse axis rotated by angle (2.14) from the x axis on the exit. CD and wavelength-dependent OR, known as optical rotation dispersion (ORD), are related through the Kramers–Kronig dispersion relations. Hence, the ORD spectrum can be calculated based on the CD spectrum and vice versa.

OR and CD signals are usually formed by electronic transitions of chiral molecules, while the infrared form of CD, called vibrational circular dichroism (VCD), and ROA primarily target molecular vibrations, as explained in the following Subsection 2.1.4. VCD and ROA are complementary techniques and together they are referred to as vibrational optical activity (VOA). In general, VOA spectroscopy is more focused on local conformational changes and the analyzed signal is easier to interpret than in the case of electronic spectroscopic methods. Unlike OR, CD or VCD, ROA is two-photon processes and will be described in Subsection 2.1.5.

2.1.4. The nature of molecular vibrations

Fundamentals of vibrational spectroscopy comprise description of vibrational motions of molecules (Kapitán, 2006; Nafie, 2011; Polavarapu, 1998). As the nuclei are much heavier than electrons ($M_A \gg m_e$) the nuclear and electronic part of the molecular wavefunction $\Psi_{N,n}$ can be separated as

$$\Psi_{N,n}(\mathbf{r},\mathbf{R}) = \chi_N^{nuc}(\mathbf{R})\psi_n^{el}(\mathbf{r},\mathbf{R}). \tag{2.16}$$

In this Born-Oppenheimer approximation, the application of the nuclear kinetic energy operator to the electronic wavefunction is ignored and the nuclear and electronic part of the Schrödinger equation of the molecule are solved separately. The electronic Schrödinger equation is

$$\left[\hat{T}_{\mathbf{r}}^{el} + V(\mathbf{r},\mathbf{R})\right]\psi_n^{el} = \varepsilon_n(\mathbf{R})\psi_n^{el} \tag{2.17}$$

with the kinetic energy of the electrons

$$\hat{T}_{\mathbf{r}}^{el} = -\frac{\hbar^2}{2m_e}\sum_i \nabla_i^2, \tag{2.18}$$

and the potential including the nuclear-nuclear repulsion energy, the electron-nuclear attraction energy, and the electron-electron repulsion energy,

$$V(\mathbf{r},\mathbf{R}) = \frac{e^2}{4\pi\varepsilon_0}\sum_A\sum_{B>A}\frac{Z_A Z_B}{R_{AB}} - \frac{e^2}{4\pi\varepsilon_0}\sum_A\sum_i\frac{Z_A}{r_{Ai}} + \frac{e^2}{4\pi\varepsilon_0}\sum_j\sum_{i>j}\frac{1}{r_{ij}}, \tag{2.19}$$

where Z_A, Z_B are proton numbers, e is the electron charge, m_e is the mass of electrons located in position $\mathbf{r}$, M_A is the mass of nucleus A at position R_A, $\hbar$ is the reduced Planck constant, and ε_0 is the vacuum permittivity. Indices A, B denote the nuclei and i, j denote electrons. Once the solution of (2.17) for the electronic state n with the fixed nuclear position is determined, the corresponding electronic energy can be used in nuclear Hamiltonian operator as the potential energy:

$$\left[\hat{T}_{\mathbf{R}}^{nuc} + \varepsilon_n(\mathbf{R})\right]\chi_N^{nuc}(\mathbf{R}) = E_{n,N}\chi_N^{nuc}(\mathbf{R}), \tag{2.20}$$

where the nuclear kinetic energy

$$\hat{T}_{\mathbf{R}}^{nuc} = -\frac{\hbar^2}{2}\sum_A\frac{1}{M_A}\nabla_A^2. \tag{2.21}$$

The Taylor expansion of the potential energy in (2.20) for small deviations of nuclear coordinates from their equilibrium positions is

$$\begin{aligned}\varepsilon_n(\mathbf{R}_1,\dots,\mathbf{R}_N) = \varepsilon_n(\mathbf{R}_1^0,\dots,\mathbf{R}_N^0) + \sum_{J=1}^{N}\frac{\partial\varepsilon}{\partial R_{J,\alpha}}\left(R_{J,\alpha}-R_{J,\alpha}^0\right) + \\ +\frac{1}{2}\sum_{J,K=1}^{N}\frac{\partial^2\varepsilon}{\partial R_{J,\alpha}\partial R_{K,\beta}}\left(R_{J,\alpha}-R_{J,\alpha}^0\right)\left(R_{K,\beta}-R_{K,\beta}^0\right)+\cdots.\end{aligned} \tag{2.22}$$

The first term may be set to zero. The gradient of the potential energy at a minimum is equal to zero, since it is proportional to the force acting on the atoms and this force is zero in the equilibrium. When higher order energy derivatives are neglected (the harmonic approximation), the only non-zero term contains the matrix of the second derivatives known as the force field or Hessian matrix.

For *N* atoms, the molecule described by equation (2.20) possesses 3*N* degrees of freedom, of which 3 are translations and 3 for rotations of the whole molecule. Linear molecule possesses only 2 rotational motions. Remaining 3*N*-6(5) degrees are the vibrational motions. In the harmonic approximation the vibrational part of (2.20) becomes

$$\widehat{H}_{VIB}\phi_n(\mathbf{R}) = \left[-\frac{\hbar^2}{2}\sum_{i=1}^{3N-6}\frac{1}{M_i}\frac{\partial^2}{\partial X_i^2}+\frac{1}{2}\sum_{i,j=1}^{3N-6}f_{ij}^n\Delta X_i\Delta X_j\right]\phi_n(\mathbf{R}) = E_n\phi_n(\mathbf{R}), \tag{2.23}$$

where f_{ij}^n are elements of the force field matrix and $X_i = R_{J,\alpha}$ Cartesian coordinates. The equation (2.23) can be solved by diagonalization of the force filed matrix in the normal mode coordinates

$$\mathbf{\Lambda} = \mathbf{S}^{\mathrm{T}}\mathbf{F}\mathbf{S}, \tag{2.24}$$

which are defined by a transformation

$$Q_k = \sum_{j=1}^{3N} S_{kj}^{-1}\Delta X_j \tag{2.25}$$

for $k = 1,2,\dots,3N$. Elements of the matrix S_{kj} represent the contribution of each nucleus j to the normal mode Q_k. Once the force field matrix $\mathbf{\Lambda}$ is diagonalized, the transformation given by (2.25) is known. The eigenvalues (diagonal elements) of $\mathbf{\Lambda}$ are squares of *3N* normal mode frequencies ($\Lambda_{ij} = \delta_{ij}\omega_{ij}^2$). Normal coordinates for translations and rotations have zero frequency. Transformation (2.25) eliminates all cross-terms from the vibrational Hamiltonian

$$\hat{H}_{VIB} = \sum_{j=1}^{3N} \frac{1}{2}\left(\frac{\partial^2}{\partial Q_j^2} + \omega_j^2 Q_j^2\right) = \sum_{j=1}^{3N} \hat{H}_j, \tag{2.26}$$

which is now the sum of $3N$ harmonic oscillators. The vibrational wavefunction is a product of one-dimensional wavefunctions

$$\phi_n = \prod_{j=1}^{3N} \varphi_j(Q_j). \tag{2.27}$$

The Schrödinger equation for each normal mode j with the angular frequency ω_j and a quantum number n_j is then given as

$$\hat{H}_j \varphi_j = \left(\frac{1}{2} + n_j\right) \hbar\omega_j \varphi_j. \tag{2.28}$$

2.1.5. Raman optical activity

The scattering of light in a bulk with all its quantum-mechanical and relativistic aspects does not yet have a consistent theory. Fortunately, the semiclassical approach based on electromagnetic waves scattering by individual molecules appears to provide a reasonable description of experimental data. The aim of this section is to provide the reader with a basic theory of ROA. Details are already described in several good textbooks (Barron, 2004; Nafie, 2011; Polavarapu, 2016).

The light scattering is a two-photon process based on the interaction of incident electromagnetic waves with individual molecules of the sample. The oscillating electromagnetic field generates time-dependent electric dipole, magnetic dipole and electric quadrupole moments in each affected molecule, which are the sources of the scattered radiation. In case of Raman inelastic scattering, a quantum of a vibrational energy is gained (anti-Stokes) or lost (Stokes) in the molecular system. The scattered intensity (Nafie & Che, 1994) is defined as

$$I(\tilde{e}^{\mathrm{d}}, \tilde{e}^{\mathrm{i}}) = \mathrm{K}\langle \left| \tilde{e}_\alpha^{\mathrm{d}*} \tilde{a}_{\alpha\beta} \tilde{e}_\beta^{\mathrm{i}} \right|^2 \rangle \tag{2.29}$$

with the Raman scattering tensor $\tilde{a}_{\alpha\beta}$. For isotropic samples rotational average must be taken. The incident and scattered radiation are represented by the polarization vectors $\mathbf{e}^{\boldsymbol{i}}$ and $\mathbf{e}^{\boldsymbol{d}}$, respectively. Greek subscripts refer to the Cartesian components and the Einstein summation convention is applied here and further in the text. The tilde over the symbol indicates a complex quantity. The constant

$$K = \left(\frac{\omega^2 \mu_0 E^{(0)}}{4\pi R} \right)^2 \tag{2.30}$$

includes the incident electric field intensity $E^{(0)}$, the scattered angular frequency ω, magnetic permeability μ_0 for free space and the distance R travelled by scattered beam to the detector. The scattering tensor

$$\tilde{a}_{\alpha\beta} = \tilde{\alpha}_{\alpha\beta} + \frac{1}{c}\left[\varepsilon_{\gamma\delta\beta} n_\delta^i \tilde{G}_{\alpha\gamma} + \varepsilon_{\gamma\delta\alpha} n_\delta^d \tilde{\mathcal{G}}_{\gamma\beta} + \frac{i}{3}\left(\omega_0 n_\gamma^i \tilde{A}_{\alpha,\gamma\beta} - \omega n_\gamma^d \tilde{\mathcal{A}}_{\beta,\gamma\alpha} \right) \right] \tag{2.31}$$

consists of the electric dipole polarizability $\tilde{\alpha}_{\alpha\beta}$, that is sufficient to describe Raman (and Rayleigh) scattering, electric dipole-magnetic dipole ($\tilde{G}_{\alpha\gamma}, \tilde{\mathcal{G}}_{\gamma\beta}$) and electric dipole-electric quadrupole ($\tilde{A}_{\alpha,\gamma\beta}, \tilde{\mathcal{A}}_{\beta,\gamma\alpha}$) optical activity tensors. Higher order terms can be neglected because molecular dimensions are usually smaller than the wavelength. $\varepsilon_{\gamma\delta\beta}$ and $\varepsilon_{\gamma\delta\alpha}$ are components of the Levi-Civita tensors, c is the velocity of light, ω_0 is the incident light angular frequency and $\mathbf{n}^{\boldsymbol{i}}$ and $\mathbf{n}^{\boldsymbol{d}}$ are propagation vectors of incident and scattered light, respectively.

Assuming the experiment is far from resonance, when energy of the incident radiation is distinct from electronic transition energies, the far-from-resonance approximate tensors are

$$\alpha_{\alpha\beta} = \frac{2}{\hbar} \sum_{j \neq m,n} \frac{\omega_{jn}}{\omega_{jn}^2 - \omega_0^2} \mathrm{Re}\{\langle m|\hat{\mu}_\alpha|j\rangle\langle j|\hat{\mu}_\beta|n\rangle\}, \tag{2.32}$$

$$G'_{\alpha\beta} = -\frac{2}{\hbar} \sum_{j \neq m,n} \frac{\omega_0}{\omega_{jn}^2 - \omega_0^2} \mathrm{Im}\{\langle m|\hat{\mu}_\alpha|j\rangle\langle j|\hat{m}_\beta|n\rangle\}, \tag{2.33}$$

$$A_{\alpha,\beta\gamma} = \frac{2}{\hbar} \sum_{j \neq m,n} \frac{\omega_{jn}}{\omega_{jn}^2 - \omega_0^2} \mathrm{Re}\{\langle m|\hat{\mu}_\alpha|j\rangle\langle j|\hat{\theta}_{\beta\gamma}|n\rangle\}, \tag{2.34}$$

where $\omega_{jn} = \omega_j - \omega_n$ represents the angular frequency difference between the initial state n and excited state j, m is the final state. The electric dipole, magnetic dipole and electric quadrupole moment operators are given as

$$\hat{\mu}_\alpha = \sum_k e_k r_{k\alpha}, \tag{2.35}$$

$$\hat{m}_\alpha = \frac{1}{2} \sum_k \frac{e_k}{m_k} \varepsilon_{\alpha\beta\gamma} r_{k\beta} p_{k\gamma}, \tag{2.36}$$

$$\hat{\theta}_{\alpha\beta} = \frac{1}{2} \sum_k e_k \left(3 r_{k\alpha} r_{k\beta} - r_k^2 \delta_{\alpha\beta} \right), \tag{2.37}$$

where each particle k contributes with its mass m_k, charge e_k, position r_k and momentum p_k. $\varepsilon_{\alpha\beta\gamma}$ is Levi-Civita tensor and $\delta_{\alpha\beta}$ is Kronecker delta. Vibrational difference in energies of the initial or final state can be neglected in the far-from-resonance approximation. For Raman scattering and ROA, we can employ the Placzek's approximation (Placzek, 1934). For example, the polarizability tensors can be expressed as

$$\langle m_v | \alpha_{\alpha\beta}(Q) | n_v \rangle = \left(\alpha_{\alpha\beta}\right)_0 \delta_{m_v n_v} + \sum_P \left(\frac{\partial \alpha_{\alpha\beta}}{\partial Q_P}\right)_0 \langle m_v | Q_P | n_v \rangle, \tag{2.38}$$

i.e. using derivatives with respect to the normal mode coordinate Q_P. For isotropic samples measured in the back-scattering SCP ROA experiment, the unpolarized Raman and ROA intensities are

$$I_R + I_L = K\left[\left(\frac{\partial \alpha_{\alpha\alpha}}{\partial Q_P}\right)_0 \left(\frac{\partial \alpha_{\beta\beta}}{\partial Q_P}\right)_0 + 7\left(\frac{\partial \alpha_{\alpha\beta}}{\partial Q_P}\right)_0 \left(\frac{\partial \alpha_{\alpha\beta}}{\partial Q_P}\right)_0\right], \tag{2.39}$$

$$\begin{aligned} I_R - I_L = \frac{8K}{c}\Bigg[& 3\left(\frac{\partial \alpha_{\alpha\alpha}}{\partial Q_P}\right)_0 \left(\frac{\partial G'_{\alpha\beta}}{\partial Q_P}\right)_0 - \left(\frac{\partial \alpha_{\alpha\alpha}}{\partial Q_P}\right)_0 \left(\frac{\partial G'_{\beta\beta}}{\partial Q_P}\right)_0 \\ & + \frac{1}{3}\omega_0 \left(\frac{\partial \alpha_{\alpha\beta}}{\partial Q_P}\right)_0 \varepsilon_{\alpha\gamma\delta} \left(\frac{\partial A_{\gamma,\delta\beta}}{\partial Q_P}\right)_0\Bigg]. \end{aligned} \tag{2.40}$$

The subscript 0 means that the derivatives are considered in equilibrium nuclear positions. The mixed terms of the polarizability and the tensors of Raman optical activity in (2.40) thus generate different response of a chiral molecule to unpolarized light in the form of different Raman intensities for left and right circular polarizations.

2.2. Simulation methods of vibrational spectra

Quantum chemical calculations have become important parts of the interpretation of spectra. With increasing computing power, the range of calculation methods expands. One of the most popular modelling methods is the density functional theory (DFT). In this section are summarized computational approaches based on the DFT and the harmonic approximation or with the anharmonic corrections. Since vibrational optical activity is particularly sensitive to intermolecular interactions, simulations done in vacuum are often not realistic. Therefore, solvent models based on implicit (dielectric cavity based) or explicit (molecular dynamics) inclusion of solvent molecules into the calculation are also introduced.

2.2.1. Density functional theory

Kohn-Sham equations

The main principle of the DFT (Koch & Holthausen, 2001) is the substitution of the wave function Ψ of N electrons by the electron density defined as the multiple integral over the spin coordinates of all electrons and over all but one of the spatial variables

$$\rho(\mathbf{r}) = N \int \dots \int |\Psi(\mathbf{r_1}, \mathbf{r_2}, \dots, \mathbf{r_N})|^2 \mathrm{d}\, s_1 \mathrm{d}\mathbf{r_2} \dots \mathrm{d}\mathbf{r_N}. \tag{2.41}$$

The electron density is non-negative function obeying

$$\rho(\mathbf{r} \to \infty) = 0, \tag{2.42}$$

$$\int \rho(\mathbf{r}) \mathrm{d}\mathbf{r} = N. \tag{2.43}$$

The Hohenberg-Kohn (Hohenberg & Kohn, 1964) theorem justifies using the electron density as the fundamental quantity instead of the wave function to unambiguously determine all properties of the molecular system in the non-degenerated ground state. Levy generalized Hohenberg-Kohn theorem also to degenerated ground states (Parr, 1980). Thus, the electron density can be calculated by variation of the ground state energy

$$\frac{\delta E(\rho)}{\delta \rho} = 0. \tag{2.44}$$

The energy can be written as

$$E(\rho) = T(\rho) + \int \rho(\mathbf{r}) v(\mathbf{r}) \mathrm{d}\mathbf{r} + V_{ee}(\rho), \tag{2.45}$$

where T is the kinetic energy operator, the second term contains the "external" potential due to the nuclei and V_{ee} contains the electron-electron interactions. Today's DFT implementations are most often based on the idea of Kohn and Sham (Kohn & Sham, 1965), who introduced arbitrary orbitals (KS orbitals) and where the density is

$$\rho(\mathbf{r}) = \sum_{i=1}^{N} |\varphi_i(\mathbf{r})|^2. \tag{2.46}$$

Then, (2.45) can be written as

$$E(\rho) = T_S(\rho) + \int \rho(\mathbf{r}) v(\mathbf{r}) \mathrm{d}\mathbf{r} + \frac{1}{8\pi\varepsilon_0} \int \frac{\rho(\mathbf{r})\rho(\mathbf{r}')}{|\mathbf{r} - \mathbf{r}'|} \mathrm{d}\mathbf{r}\mathrm{d}\mathbf{r}' + E_{XC}\,(\rho), \tag{2.47}$$

where T_S is the kinetic energy of the non-interacting reference system, the third term is the Coulomb electron-electron repulsion and E_{XC} is the exchange-correlation energy. The exact E_{XC} form is unknown. By minimizing the energy in (2.47) as a function of the KS orbitals φ_i^{KS} the KS one-electron equations are obtained as

$$H_{KS}\varphi_i^{KS}(\mathbf{r}) = \left(-\frac{\hbar^2}{2m_e}\Delta_i + v(\mathbf{r}) + \frac{1}{4\pi\varepsilon_0}\int\frac{\rho(\mathbf{r}')}{|\mathbf{r}-\mathbf{r}'|}\mathrm{d}\mathbf{r}' + v_{XC}(\mathbf{r})\right)\varphi_i^{KS}(\mathbf{r}) = \varepsilon_i\varphi_i^{KS}, \quad (2.48)$$

where H_{KS} is KS Hamiltonian operator and the corresponding exchange-correlation potential is

$$v_{XC}(\mathbf{r}) = \frac{\partial E_{XC}(\rho)}{\partial\rho}. \quad (2.49)$$

Functionals

An important task of modern DFT is to develop better approximations to the exchange-correlation potential, with the aim of getting as close as possible to the solution of the Schrödinger equation. These efforts have resulted in several hundred different exchange-correlation potentials. Some of them are customized for a specific type of molecules. Therefore, it is important to make several benchmark tests to verify its appropriateness before drawing conclusions of a study. DFT potentials are usually classified as pure potentials (functionals), only dependent on the electron density or its derivatives, and hybrid functionals including the Hartree-Fock (HF) exchange energy (Koch & Holthausen, 2001)

$$E_X^{HF} = -\frac{1}{8\pi\varepsilon_0}\sum_i^N\sum_i^N\left\langle\varphi_j{}^{KS}(\mathbf{r}')\varphi_i^{KS}(\mathbf{r})\left|\frac{1}{|\mathbf{r}-\mathbf{r}'|}\right|\varphi_i{}^{KS}(\mathbf{r}')\varphi_j^{KS}(\mathbf{r})\right\rangle. \quad (2.50)$$

Modern DFT functionals provide results in a qualitative agreement with the second-order Møller–Plesset type perturbation theory (MP2) (Møller & Plesset, 1934), but are less computationally demanding (Bouř, 2000; Pai et al., 1996). Commonly used pure functional BPW91 combines Becke's exchange energy functional (Becke, 1988) with the correlation energy functional of Perdew and Wang (Burke et al., 1998; Perdew et al., 1996; Perdew et al., 1992, 1993; Perdew et al., 1991). The hybrid functionals combine HF exchange energy with empirically derived DFT exchange-correlation functionals. The most widespread hybrid functionals with a remarkable universality are the Becke three-parameter hybrid functionals B3LYP and B3PW91 (Becke, 1988, 1993; Lee et al., 1988).

However, the standard KS DFT approximations underestimate long-range dispersion (van der Waals) interactions. They provide satisfactory results only for short range interactions of not too large molecules. A correction was proposed by Grimme (Schwabe & Grimme, 2007), who added empirical dispersion term to the KS energy expression

$$E_{\text{disp}}^{\text{DFT-D}} = -\sum_{AB}\sum_{n=6,8,10,\ldots} s_n \frac{C_n^{AB}}{R_{AB}^n} f_{\text{damp}}(R_{AB}), \tag{2.51}$$

where s_n is the functional dependent scaling factor, C_n^{AB} is the dispersion coefficient for atom pair AB ($A \neq B$) with a mutual distance R_{AB} and f_{damp} is a damping function to avoid singularities for small R_{AB}. Hence, the damping function converges to zero for $R_{AB} \rightarrow 0$. Alternative E_{disp} can be given as

$$E_{disp} = -\sum_{AB} \frac{C_n}{R_{AB}^n + \text{const}}, \tag{2.52}$$

which is called Becke and Johnson (BJ)-damping (Becke & Johnson, 2005; Johnson & Becke, 2005, 2006) and may provide more accurate results by not including artificial repulsive forces at small and medium distances (Grimme et al., 2011). The last common version of Grimme's correction is called DFT-D3 and includes sixth-order and eighth-order coefficients (Grimme et al., 2010). Terms of the order $n > 6$ are found to be more suitable for short distances and also strongly interfere with DFT exchange-correlation contribution (Grimme, 2011).

Basis sets

In practice, the KS orbitals can be expanded to a set of L predefined basis functions

$$\varphi_i^{KS} = \sum_{\boldsymbol{\mu}=\mathbf{1}}^{\boldsymbol{L}} c_{\mu i}\eta_\mu, \tag{2.53}$$

which is referred to as linear combination of atomic orbitals (LCAO) (Roothaan, 1951). Over past decades, different sets of the basis functions were developed (Baerends et al., 1973; Baerends & Ros, 1978; Blöchl et al., 1996; Delley, 1990; Te Velde et al., 2001). Gaussian-type orbitals (GTO) are a linear combination of so-called primitive Gaussian functions (p):

$$\eta^{GTO} = \sum_{i=1}^{K} p^i, \tag{2.54}$$

$$p^i = P^i(x, y, z)\exp(-i\alpha r^2), \tag{2.55}$$

where P is a polynomial in the components x, y, and z of the position vector **r**, $r = \sqrt{x^2 + y^2 + z^2}$, $\alpha \in \mathbb{R}$. A simple GTO basis is STO-3G (Collins et al., 1976; Hehre et al., 1969), which combines only three Gaussian type functions and is default option in Gaussian16 software (Frisch et al., 2016), but it is practically useless for accurate simulations of vibrational spectra. It is necessary to choose sufficiently large basis sets so that the advantage of chosen DFT functional has not been wasted because of the errors caused by the small number of atomic orbitals included in the calculation. Routinely used split valence basis sets provide a compromise between accuracy and efficiency. For example, the basis set 6-31G (Ditchfield et al., 1971) combines six primitive Gaussian functions for each atomic orbital in the inner core electron shell and outer valence orbitals are split into two parts, described by three and one primitive Gaussian functions. The 6-311G is defined as 6-31G but with one more primitive Gaussian function for valence orbitals. This basis set can be augmented by polarization functions (indicated by stars, *) (Frisch et al., 1984), which possess higher sensitivity and better adaptation of the orbitals to the molecular environment. By adding the diffuse functions (indicated by plus, +) (Clark et al., 1983), the electrons further from the atomic core are better described.

Rarefied basis set

Incorporating larger basis sets, such as 6-311++G** or aug-cc-pVDZ for Raman and ROA intensity calculations is too cumbersome and computationally demanding, especially for large molecular clusters. Therefore, G. Zuber and W. Hug introduced the rDP and rDPS basis sets, which are the standard 3-21G and 3-21++G sets, respectively, augmented by diffuse p-type polarization functions ("DP") and a diffuse shell ("S") applied only on hydrogen atoms ("r" - reduced) (Thorvaldsen et al., 2012; Zuber & Hug, 2004). Performance of such basis sets in Raman and ROA scattering tensors calculations was comparable to more elaborate basis sets of Sadlej (Sadlej, 1988) and aug-cc-pVDZ (Kendall et al., 1992), but the calculations were 20 times faster. However, such rarefied basis sets are not convenient for molecular optimization and force field calculations.

2.2.2. Beyond the harmonic approximation

The harmonic approximation usually provides sufficient accuracy for vibrational spectra interpretation in the standard range of 200–2000 cm^{-1}. However, the calculated frequencies for high-frequency vibrations, such as CH, CN, or CO stretching, often deviate from the experimental spectra by tens of cm^{-1}. As we are interested in unusually high energy vibrations in this work, a treatment beyond the harmonic approximation is required.

The energy levels of the harmonic oscillator are evenly spaced by fixed energy difference $\hbar\omega$. Transitions when the quantum number changes by one are called fundamentals, others are overtones and combination transitions. For example, for two harmonic oscillators, the first overtone ($|00\rangle \rightarrow |02\rangle$) is a transition from the ground vibrational level to the second excited vibrational state of the second oscillator, while combination mode ($|00\rangle \rightarrow |11\rangle$) occurs when two or more fundamental transitions are excited simultaneously (**Figure 2.5**).

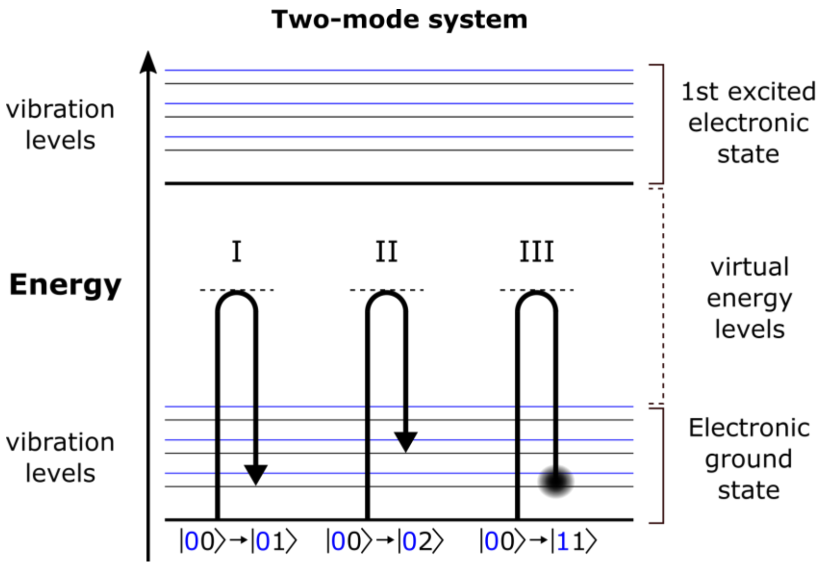

Figure 2.5: Energy level diagram of two-mode system with example of fundamental (I), overtone (II) and combination (III) vibrational transition as seen by Raman spectroscopy.

The vibrational potential energy can be expanded further than in (2.22) as

$$V(Q_1, \dots, Q_N) = \frac{1}{2}\sum_{i=1}^{N} v_i^2 Q_i^2 + \frac{1}{6}\sum_{i=1}^{N}\sum_{j=1}^{N}\sum_{k=1}^{N} c_{ijk} Q_i Q_j Q_k + \frac{1}{24}\sum_{i=1}^{N}\sum_{j=1}^{N}\sum_{k=1}^{N}\sum_{l=1}^{N} d_{ijkl} Q_i Q_j Q_k Q_l \tag{2.56}$$

for N normal mode coordinates Q, where f_{ij} is the Hessian matrix with harmonic frequencies v_i, c_{ijk} are cubic and d_{ijkl} are quartic force constants corresponding to the third and fourth potential energy derivatives, respectively. While second derivatives are calculated analytically, cubic and semidiagonal quartic force constants are usually computed by two-point numerical differentiation of the Hessian as

$$c_{ijk} = \frac{\partial^3 V}{\partial Q_i \partial Q_j \partial Q_k} = \frac{\partial \ f_{ij}}{\partial Q_k} = \frac{f_{ij}(Q_k + \Delta) - f_{ij}(Q_k - \Delta)}{2\Delta}, \tag{2.57}$$

$$d_{ijkk} = \frac{\partial^4 V}{\partial Q_i \partial Q_j \partial Q_k \partial Q_k} = \frac{\partial^2 f_{ij}}{\partial Q_k \partial Q_k} = \frac{f_{ij}(Q_k + \Delta) - f_{ij}(Q_k - \Delta) + 2f_{ij}(0)}{\Delta^2}, \tag{2.58}$$

where Δ is the differentiation step. Contrary to the fixed differentiation step used in Gaussian 16 (Frisch et al., 2016), the S4 program (Bouř, 2017) allows for differentiation with a variable normal mode step of $1000\sqrt{\nu}\Delta Q$, where ν is the frequency in cm^{-1} and $\Delta Q = 0.05$ Å. This frequency dependent differentiation step keeps the average displacement approximately constant for all normal modes. Off-diagonal quartic constants with all indices unique are omitted. Analytical calculation of the cubic and quartic force constants at the DFT level was introduced (Ringholm et al., 2014), but not yet been implemented into Gaussian16 (Frisch et al., 2016) or S4 (Bouř, 2017) that were used for spectral simulations in the thesis.

Not surprisingly, the anharmonic frequency calculation is much more time demanding than the harmonic calculation. Moreover, the separation of Schrödinger equation to a set of independent harmonic oscillators (eq. (2.28)) cannot be used for the anharmonic potential. Hence, perturbational or variational approaches are usually used, starting from the harmonic approximation.

Second-order perturbation theory

As the cubic and quartic terms in equation (2.56) often have only small effect, they can be treated as a perturbation. The vibrational second-order perturbation theory (VPT2) is very efficient approach with regards to the accuracy and computational cost for small to large molecules. Same as for the potential, intensity tensors at the VPT2 level are expanded up to the third order as

$$\begin{aligned} X(Q,P) = X(0) &+ \sum_{i=1}^{N} \frac{\partial X}{\partial Q_i} Q_i + \frac{1}{2} \sum_{i=1}^{N} \sum_{j=1}^{N} \frac{\partial^2 X}{\partial Q_i \partial Q_j} Q_i Q_j \\ &+ \frac{1}{6} \sum_{i=1}^{N} \sum_{j=1}^{N} \sum_{k=1}^{N} \frac{\partial^3 X}{\partial Q_i \partial Q_j \partial Q_k} Q_i Q_j \, Q_k, \end{aligned} \tag{2.59}$$

where X, for example, represents polarizability tensor α or optical activity tensors G' and A. $X(0)$ is the equilibrium value. Raman and ROA transition tensors are then given as

$$\langle X \rangle_{nm} = \frac{\langle n|X|m \rangle}{\sqrt{\langle n|n \rangle \langle m|m \rangle}}, \tag{2.60}$$

where the wavefunction norms are in the denominator because the perturbed wavefunctions for initial n and final m vibrational states are not normalized. Using (2.59), analytic formulas for intensities up to the three quanta transitions can be derived, as shown elsewhere (Barone, 2005; Bloino, 2015; Bloino & Barone, 2012).

Resonances

The VPT2 anharmonic approach can suffer from resonance effects, i.e., coupling of modes close in energy. Energies are mostly affected by the Fermi resonances (FR) of type I ($\nu_i \approx 2\nu_j$) and type II ($\nu_i \approx \nu_j + \nu_k$). Their occurrence increases with the size of the molecule. Fermi resonances are not the only source of errors in the perturbative calculus. Additional source of singularities, particularly critical for intensity calculations, are present and referred as Darling-Dennison resonances (DDR) (Darling & Dennison, 1940). DDR are categorized based on the number of interacting quanta in the wave mixing. Mostly, two types are being recognized, “$\nu_j \approx \nu_i$” and “$\nu_1 \approx \nu_i + \nu_j + \nu_k$”.

Several modified VPT2 versions were introduced to effectively treat specifically the Fermi and Darling−Dennison resonances. In the “deperturbed” VPT2 (DVPT2) case, the FR are identified by one or more criteria (e.g. “$\Delta\nu = \nu_i - (\nu_j + \nu_k)$” or Martin test (Martin et al., 1995)) and simply discarded from the calculation, whereas DDR are not corrected at all. This deficiency can be subsequently corrected by variational treatment of the excluded FR terms and reintroducing them back to the calculation. Only significant contribution of DDR, when applying similar criteria as for FR, can be introduced into the variational correction due to large computer memory cost of such procedure. This approach is referred to as the generalized VPT2 (GVPT2) and is based on diagonalization of the symmetry matrix, where diagonal elements correspond to the anharmonic energies and off-diagonal terms describe the resonant terms (Bloino et al., 2015).

Proposed tests for identification of resonance terms in the energy calculation can be somehow adapted in similar form to the intensity calculation. Sufficiently small tolerances and additional tests on the magnitude of the resonance terms must be applied because the intensity coupling terms are different. Robust strategies to the best treatment of DDR are still under investigation (Yang et al., 2021).

Limited vibrational configuration interaction

Alternatively, a limited vibrational configuration interaction (LVCI) (Daněček & Bouř, 2007; Hudecová et al., 2013) is based on solving Schrödinger equation by diagonalization of a large Hamiltonian matrix, where the vibrational wavefunction is expressed as a sum of many harmonic oscillator functions. As the Hamiltonian diagonalization is too computationally demanding, the number of harmonic states (matrix elements) must be restricted. Therefore, only up to five times excited harmonic states are usually considered in LVCI approach. For example, $|500\rangle$ or $|221\rangle$ excited states in a three-mode system, where $|000\rangle \rightarrow |001\rangle$ represents one fundamental transition, are included but not $|600\rangle$, $|224\rangle$, etc. Several restriction rules are applied for selection of the most relevant Hamiltonian elements, such as

$$|\langle n|V|m\rangle| > \eta|E_n - E_m|, \tag{2.61}$$

omitting states according to the parameter η for transition from the initial vibrational state n to the final state m.

Indirect iterative diagonalization methods such as Mitin's version (Mitin, 1994) of the Davidson procedure (Davidson, 1975) are based on iterative calculation of eigenvalues and eigenvectors. It is imperative that each new eigenvector be orthogonal to the previous ones. The Mitin's/Davidson procedure enables one to significantly increase Hamiltonian dimension ($\sim 10^6$), but quickly slows down when too many eigenstates are required.

2.2.3. Potential energy surface scan

The inhomogeneous spectral band broadening in solutions is usually caused by contributions from many molecular conformers and solvent-solute configurations. Such species differ in positions of the Raman bands or intensities and signs of ROA bands. The potential energy surface (PES) scan is a useful tool to understand the multi-dimensional conformational space of the studied molecule. The scanning procedure is usually based on increments of the analyzed coordinates, while the remaining coordinates are fully optimized at each step of the scan ("relaxed scan") (Kapitán et al., 2006).

In common practice, the contributions of conformers up to 2–3 $\text{kcal}\cdot\text{mol}^{-1}$ are considered significant, contributing to the simulated spectra according to their Boltzmann weights

$$p_i = \frac{\exp\left(-\frac{\Delta E_i}{kT}\right)}{\sum_j^N \exp\left(-\frac{\Delta E_j}{kT}\right)}, \tag{2.62}$$

where N is the number of conformers, k is the Boltzmann constant, and T is temperature.

2.2.4. Solvent modeling

Measured ROA signal reflects not only the molecular structure but may be also extraordinarily sensitive to the environmental effects and dynamics. Insufficient inclusion of intermolecular interactions into the *ab initio* calculations may lead to large errors in the interpretation of the experimental spectra, especially for strong intermolecular interactions, such as hydrogen bonding. Furthermore, it is difficult to distinguish between internal solute, solvent-solvent and solute-solvent spectral bands in the low-frequency region. Hence, the solvent models play an important role in correct Raman and ROA spectra interpretation. Incorporating solvent corrections can improve vibrational frequencies, provide the spectral band broadening, and more realistic intensities. The solvent can be included as a continuum or by explicitly incorporated solvent molecules into the calculations.

Simple and widely used continuum (“implicit”) solvent models are continuum solvation models (Mennucci & Cammi, 2008; Tomasi et al., 2005), namely the polarizable continuum models (PCM) (Caricato et al., 2005; Lipparini et al., 2010; Scalmani & Frisch, 2010), where the solute molecule is in a cavity surrounded by dielectric continuum. The Kohn-Sham equations are solved based on a self-consistent reaction field (SCRF) iterative procedure. The solute polarizes the continuum and the formed electrostatic field in turn affects the charge distribution in the solute. The cavity is formed by overlapping van der Waals spheres centered at the atomic positions. The sphere size depends on the atom type, connectivity, overall charge of the molecule, and the number of attached hydrogen atoms. The surface of the solvent cavity is divided into small shape segments (tesserae), in which the point charges of the reaction field are calculated (see **Figure 2.6b**). Similar conductor-like screening model (COSMO) originally treated the solvent as a perfect conductor ($\epsilon = \infty$), later a finite dielectric constant was included via an empirically determined scaling function (Klamt & Schuurmann, 1993). The Gaussian16 (Frisch et al., 2016) implementation of COSMO uses the PCM cavity and is called the conductor-like polarizable model (CPCM) (Barone & Cossi, 1998; Cossi et al., 2003). There are currently 184 pre-defined solvents in Gaussian16. The major parameter characterizing the solvent is the dielectric constant. In general, a custom solvent can be specified by its dielectric constant, but additional parameters, such as the refractive index or the surface tension at the liquid-air interface, are needed to specify the solvent properly. Despite the complications associated with these implicit models, the computational complexity (and computational time) is only slightly increased compared to vacuum.

More realistic models include solvent molecules around the solute. The positions are often based on the molecular dynamics (MD), introduced in the next Subsection 2.2.5 (see **Figure 2.6c**). This is especially important for polar molecules in polar environments (water, methanol) to accurately describe strongly directional interactions, such as the hydrogen bonding. As shown in several studies, such computations usually yield the most accurate results for simulations of spectroscopic properties of liquid systems (Hopmann et al., 2011; Cheeseman et al., 2011; Jungwirth et al., 2017). However, the necessary averaging over an ensemble of explicitly solvated geometries is more time-consuming than the implicit solvent corrections. The size of the studied molecular systems is limited by the available computational resources. Especially Raman and ROA intensity calculations require large basis sets to reliably predict experimental spectra. At the time of writing this thesis and with our computational resources, direct simulations of the vibrational spectra for molecular systems larger than about 200 with reasonable accuracy were too computationally demanding. However, additional approximations like ONIOM (short for 'Our own N-layered Integrated molecular Orbital and Molecular mechanics') (Dapprich et al., 1999; Chung et al., 2015) or Cartesian tensor transfer (CCT) (Bouř et al., 1997; Yamamoto et al., 2012) were developed. The latter approach is described in Subsection 2.2.7.

The ONIOM approach enables one to treat different parts of molecular systems at different computational levels. For instance, the solute can be treated quantum mechanically (QM) in combination with the molecular mechanics (MM) applied to the solvent molecules. Such calculations are referred to as QM/MM (Egidi et al., 2015).

The explicit and implicit solvent approaches can be combined (**Figure 2.6d**). In studied molecular systems we explicitly included solvent from the first solvation shell within 4-5 Å from the solute. Such clusters were partially optimized (see Subsection 2.2.6), and longer-range solvation effects taken into account using one of the dielectric continuum models.

To well represent the liquid, the clusters need to be in contact with the environment. As a part of the cluster-based approaches we used a crystal-based model, which is introduced in the Subsection 2.2.8.

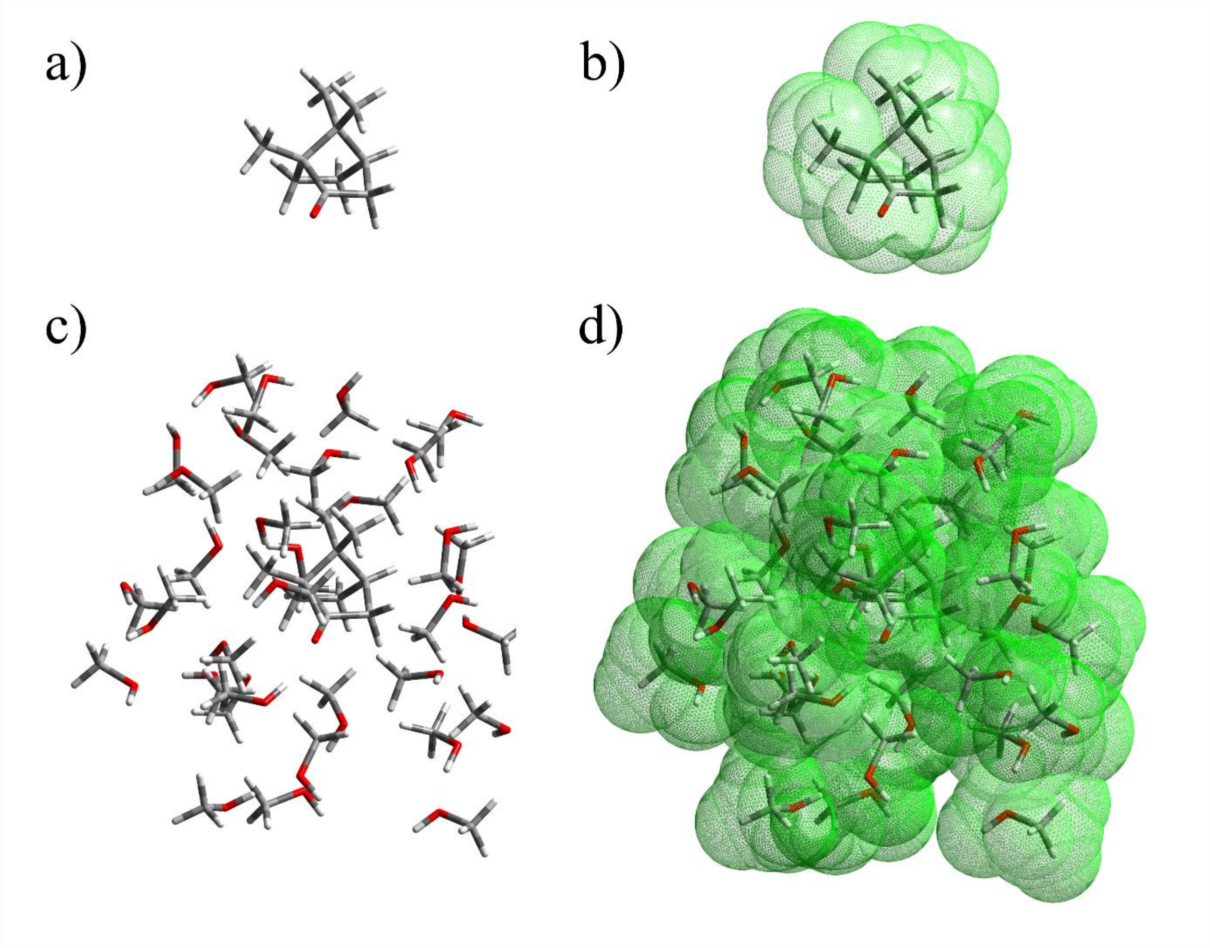

Figure 2.6: Example of the solvent models: molecule of camphor without solvent correction (in vacuum) (a), conductor-like screening model (COSMO, the solute cavity surface is displayed) (b), cluster of camphor and solvent molecules of the first solvation shell (33 methanol molecules on the picture) (c), and a combination of (b) and (c) = (d).

2.2.5. Molecular dynamics

Classical molecular dynamics is based on description of time evolution of the molecular system according to basic Newton's second law

$$\mathbf{F}_i' = m_i \frac{\partial^2 \boldsymbol{r}_i}{\partial t^2}, \tag{2.63}$$

where the force $\mathbf{F}_i'$ is applied to the i-th atom of mass m_i and causes the motion in time described by the second derivative of its position $\boldsymbol{r}_i$. The force $\mathbf{F}_i'$ can be calculated as the negative gradient of the potential energy, which in MD may look like this

$$V = \sum_{\substack{i,j=1\\ i<j}} 4\varepsilon_{ij}\left[\left(\frac{\sigma_{ij}}{r_{ij}}\right)^{12} - \left(\frac{\sigma_{ij}}{r_{ij}}\right)^{6}\right] + \sum_{\substack{i,j=1\\ i<j}} \frac{1}{4\pi\varepsilon_0}\frac{q_i q_j}{r_{ij}} + \sum_{bonds,i} k_i(d_i - d_{0i})^2$$
$$+ \sum_{angles,i} k_{\alpha i}(\alpha_i - \alpha_{0i})^2 + \sum_{torsions,i} [A_{1i}\cos(\tau_i) + A_{2i}\cos(2\tau_i) + A_{3i}\cos(3\tau_i)] \quad (2.64)$$
$$+ \sum_{oop,i} k_{oopi} s_i^2.$$

The first term in the equation (2.64) is the Lennard-Jones potential (Jones & Chapman, 1924), a simplified model of repulsive and attraction forces between two non-bonded atoms, where r_{ij} is the distance of the atoms, ε_{ij} defines the depth of the potential well referred to as dispersion energy and σ_{ij} describes equilibrium distance of the atoms. The repulsion is caused by the Pauli exclusion principle, while attraction is caused by the London dispersion interactions. The second non-bonding (intermolecular) term specifies the longer-distance Coulomb electrostatic interactions between two charges q_i and q_j, where ε_0 is the vacuum permittivity. Following bonding (intramolecular) terms correspond in order to the harmonic potential between two atoms with bond distance d_i from the equilibrium d_{0i} (**Figure 2.7a**), angle α_i deformation harmonic potential between two bonds from the equilibrium α_{0i} (**Figure 2.7b**), proper dihedral (torsion) angle τ_i deformation potential between two three-atom planes having two atoms in common (**Figure 2.7c**) and out-of-plane deformation harmonic potential of the central atom from the reference plane defined by three atoms (**Figure 2.7d**), where s_i is the distance from the plane. Parameters $(k_i, k_{\alpha i}, k_{oopi}, A_i, \varepsilon_{ij})$, equilibrium constants $(d_{0i}, \sigma_{ij}, \alpha_{0i})$ and partial charges q_i are empirically determined to simulate target properties. A set of these parameters is called force field (same name, but different meaning than the Hessian in equation (2.22)). To improve description of the modeled system, several force fields were developed for different kinds of molecules. The OPLSAA (Rizzo & Jorgensen, 1999) force field implemented into the Tinker molecular modeling package (Ponder, 2000) or the GAFF2 (J. Wang et al., 2004) force field used in the Amber 18 software (Case et al., 2018; Pearlman et al., 1995) are recommended sets of parameters for many general classes of organic molecules and were used in the results presented in Chapter 3. The TIP3P (Jorgensen et al., 1983) water model is simple and widely used force field for water molecules.

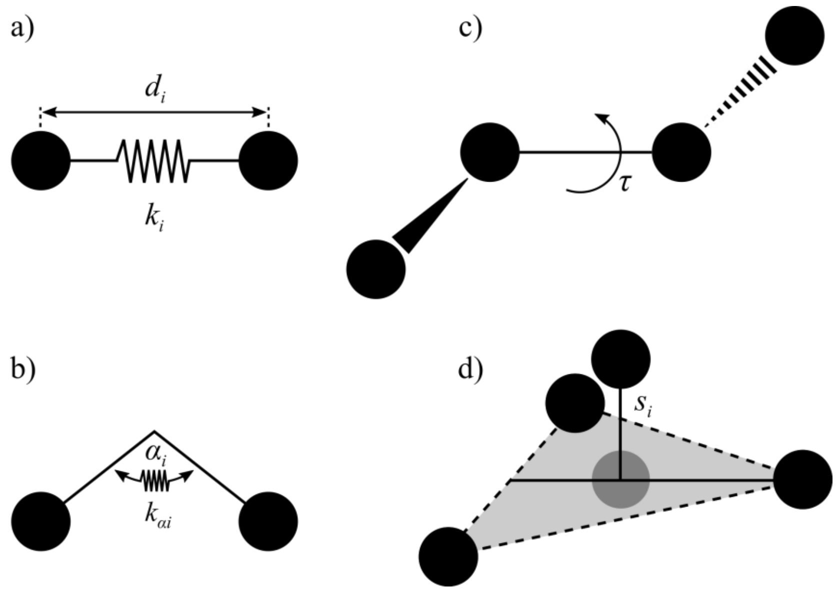

Figure 2.7: Illustration of the covalent bond length deformation (a), angle deformation (b), proper dihedral angle rotation (c) and out-of-plane deformation (d) used in equation (2.64).

To improve the potential (2.64) the bonding harmonic potential can be replaced by the Morse potential defined as

$$V_B = \sum_{bonds} D_{eq}\left[1 - e^{-a(r_{ij}-r_{eq})^2}\right], \tag{2.65}$$

where r_{eq} is the equilibrium distance between two atoms, D_{eq} is the dissociation energy (potential in $r_{ij} \to \infty$) and a is the bond strength. The Morse potential better represents the force as r_{ij} gets bigger (Harris & Bertolucci, 1989; Morse, 1929).

Before starting MD, energy minimization is recommended. The steepest descent and conjugate gradient are efficient minimization methods. The main idea of the steepest descent algorithm is to iteratively follow the opposite direction of the gradient of the potential energy up to a minimum using

$$\mathbf{r}_{i+1} = \mathbf{r}_i - \gamma \nabla E(\mathbf{r}_i), \tag{2.66}$$

where the parameter γ represents the displacement step and $\mathbf{r}_i$ is the position vector. The conjugate gradient method uses the previous iteration step in the following search to limit oscillations often present in the steepest descent algorithm. The conjugate gradient method is faster than the steepest descent, especially for geometries closer to the energy minimum. The convergence can be also improved by approximating the potential by a quadratic function, where the exact (Newton methods) or approximated (Quasi-Newton methods) inverse Hessians are included. In the latter case, the Hessian is updated in each optimization. One of the most popular Quasi-Newton method is the limited-memory Broyden-Fletcher-Goldfarb-Shanno (L-BFGS) algorithm (Nocedal & Wright, 1999). In the software used by us, the L-BFGS was the default method for Tinker, while the first-order optimization methods were chosen in Amber 18. Another molecular optimization method using the BFGS Hessian is based on the normal mode coordinates instead of Cartesian coordinates, which in certain cases may converge more smoothly and is described in the next Subsection 2.2.6.

Newton's equations of motion (2.63) can be solved numerically even for large molecular systems containing thousands of atoms. MD trajectories are propagated using the integration Verlet algorithm (Verlet, 1967). Molecular coordinates and trajectories can be saved during several nanoseconds long dynamical run of the molecular ensemble at the specific temperature and volume (NVT ensemble) or pressure (NpT ensemble).

In simulations of continuum (solutions, liquids, crystals, gases) molecular systems are usually confined to a small box, often rectangular, called the elementary cell, and the periodic boundary conditions are applied. The elementary cell geometry and interactions are propagated to all directions. For fluids, when molecule leaves of the cell on one side, it reappears on the opposite side with the same velocity.

2.2.6. Geometry optimization in normal coordinates

Geometries exported during MD run significantly deviate from the equilibrium. It was found that vibrational spectra generated from such raw cluster geometries possess unrealistic band broadening, mostly due to the anharmonic nature of the potential and vibrational mode coupling (Hudecová et al., 2012). Full optimization of the MD cluster geometries by the energy minimization discussed earlier is out of the question here, as all geometries may end in the same minimum and the structural information generated by MD would be lost. One solution to this problem is partial optimization in the normal-mode coordinates proposed by P. Bouř and T. Kiederling (Bouř, 2005, 2006; Bouř & Keiderling, 2002). This is particularly useful for the constrained optimization of weakly bonded molecular clusters.

The normal mode coordinates were already introduced in Subsection 2.1.4 in equation (2.25). The displacement in Cartesian coordinates ΔX is linked to the normal mode coordinates via “S-matrix” transformation

$$\Delta X_k = \sum_{j=1}^{3N} S_{kj} Q_j, \tag{2.67}$$

for $k = 1, 2, \dots, 3N$. The S-matrix is estimated from an initial calculation of Hessian. After that, the Hessian is continuously updated using iterative BFGS formula in the form

$$\mathbf{F}^{(i+1)} = \mathbf{F}^{(i)} - \left(\frac{{\Delta\mathbf{g}^{(i)}}^{t} \Delta\mathbf{g}^{(i)}}{\mathbf{dx}^{(i)} \cdot \Delta\mathbf{g}^{(i)}} + \frac{\left(\mathbf{F}^{(i)} \cdot \mathbf{dx}^{(i)}\right)^{t} \mathbf{dx}^{(i)} \cdot \mathbf{F}^{(i)}}{\mathbf{dx}^{(i)} \cdot \mathbf{F}^{(i)} \cdot \mathbf{dx}^{(i)}} \right), \tag{2.68}$$

where $\mathbf{dx}^{(i)} = \mathbf{x}^{(i)} - \mathbf{x}^{(i-1)}$ are Cartesian displacements and $\Delta\mathbf{g}^{(i)} = \mathbf{g}_c^{(i)} - \mathbf{g}_c^{(i-1)}$ are gradient differences in iteration step i and $i-1$. Next, the gradient is transformed to the normal mode coordinates as

$$\mathbf{g}^{(i)} = \mathbf{S}^{t} \cdot \mathbf{g}_c^{(i)}, \tag{2.69}$$

and if satisfies the convergence criterion, the procedure is terminated. Otherwise, a new Cartesian coordinates are produced as

$$\mathbf{x}^{(i+1)} = \mathbf{x}^{(i)} + \mathbf{S} \frac{2\mathbf{g}^{(i)}}{\Lambda_{ii} + \sqrt{\Lambda_{ii}^{2} + 4(\mathbf{g}^{(i)})^{2}}}, \tag{2.70}$$

where $\Lambda_{ij} = \omega_i^2 \delta_{ij}$ are diagonal elements of the transformed Hessian.

Usage of normal modes in the constrained optimization allows for a natural separation of the low-frequency modes, such as molecular translations, rotations, or intermolecular motions, from high-frequency intramolecular vibrational modes. In practice, such a separation is achieved by setting the maximum wavenumber parameter, typically $\omega_{\max} < 200\text{–}\,250$ cm^{-1} in order to keep the molecular backbone coordinates fixed, while the coordinates corresponding to the frequencies above the threshold are relaxed.

2.2.7. Cartesian coordinates transfer of molecular properties

Fairly accurate calculation of the vibrational spectra of large molecular complexes (e.g. proteins, nucleic acids) or solvated flexible molecular systems (e.g. sugars, terpenes), which exist in many stable conformations, are limited by the insufficient computational power. As a useful workaround, the fragment methodology based on breaking a large molecular system into a set of fragments was developed (Bouř et al., 1997; Yamamoto & Bouř, 2018), in which vibrational atomic properties (force field, Raman, and ROA intensity tensors) of each fragment are calculated independently with acceptable accuracy and then transferred back on large molecular system. This procedure results in a drastic reduction of computational demands, while the accuracy deteriorates only in a minor way.

The Cartesian transfer relies on finding the optimal topological overlap between part *f* of the fragment *xfx* and the segment *F* of the large molecular system *XXXFXXX*. Let's assume that each fragment *f* and the segment *F* contains atom pair $\lambda\mu$ and *m* attached atoms $\left(a^i\right)$ and $\left(a^i\right)'$ for *f* and *F*, respectively. The part *f* of the fragment *xfx* is then rotated to minimize difference between part *f* and *F* given as

$$\delta(\mathbf{U}) = \sum_{i=1,\ldots,m} \left(\mathbf{r}^i(F) - \mathbf{U}\cdot\mathbf{r}^i(f)\right)^2, \tag{2.71}$$

where $\mathbf{r}^i(F)$ and $\mathbf{r}^i(f)$ are the position vectors of atoms $\left(a^i\right)$ and $\left(a^i\right)'$ with origin at the geometric center T or T' of the atom pair $\lambda\mu$ corresponding to fraction f and segment *F* (see **Figure 2.8**).

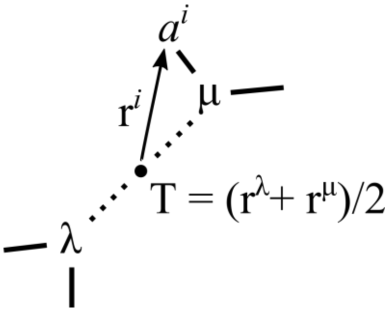

Figure 2.8: Illustration of the Cartesian coordinates transfer for a fragment *f* with atom pair $\lambda\mu$ (Bouř et al., 1997).

The unitary matrix **U** is defined in terms of the Euler angles. It transforms Cartesian force constants obtained for the atom pair λμ in fragment *f* to corresponding ones in the large segment *F* as

$$\frac{\partial^2 E}{\partial \mathbf{r}_\alpha^\lambda \partial \mathbf{r}_\beta^\mu}(F) = \sum_\gamma \sum_\delta \boldsymbol{U}_{\alpha\gamma} \boldsymbol{U}_{\beta\delta} \frac{\partial^2 E}{\partial \mathbf{r}_\gamma^\lambda \partial \mathbf{r}_\delta^\mu}(f), \tag{2.72}$$

for $\alpha, \beta, \gamma, \delta = 1 \ldots 3$. In order to estimate Raman and ROA intensities of the large system, the Cartesian transfer of the derivatives of transition tensors defined in equations (2.32) – (2.34) is required as well. Whereas the polarizability tensor is origin independent and can be easily transferred using the rotation only, derivatives of the origin dependent electric dipole-magnetic dipole and electric dipole-electric quadrupole tensors are firstly expressed in a reference frame (origin) on the moving atom λ as

$$\frac{\partial G'_{\alpha\beta}(\lambda)}{\partial R^{\lambda}_{\epsilon}} = \frac{\partial G'_{\alpha\beta}(0)}{\partial R^{\lambda}_{\epsilon}} + \frac{\omega}{2}\epsilon_{\beta\gamma\delta} \times R^{\lambda}_{\gamma}\frac{\partial \alpha_{\alpha\delta}(0)}{\partial R^{\lambda}_{\epsilon}}, \tag{2.73}$$

$$\frac{\partial A_{\alpha,\beta\gamma}(\lambda)}{\partial R^{\lambda}_{\epsilon}} = \frac{\partial A_{\alpha,\beta\gamma}(0)}{\partial R^{\lambda}_{\epsilon}} - \frac{3}{2}\left[R^{\lambda}_{\beta}\frac{\partial \alpha_{\alpha\gamma}(0)}{\partial R^{\lambda}_{\epsilon}} + R^{\lambda}_{\gamma}\frac{\partial \alpha_{\alpha\beta}(0)}{\partial R^{\lambda}_{\epsilon}}\right] + R^{\lambda}_{\delta}\frac{\partial \alpha_{\alpha\delta}(0)}{\partial R^{\lambda}_{\epsilon}}\delta_{\beta\gamma}, \tag{2.74}$$

i.e. using the distributed origin gauge (Barron, 2004). In these equations ϵ is the coordinate of moving atom λ, $\mathbf{R}^{\lambda}$ is its equilibrium position vector referred to the common origin (marked by “0”) and ω denotes the frequency of light. The unitary matrix **U** is used to rotate to the local tensors.

Each molecular fragment should be optimized before the force field and intensity calculations. In order to prevent large fragment changes during the optimization, which could subsequently cause problems with the fragment overlap, the partial optimization in normal mode coordinates (see Subsection 2.2.6) is used.

The accuracy of the tensor transfer can be improved by averaging contributions from multiple overlapping fragments a^i. Moreover, the method can be extended for the transfer of cubic and higher anharmonic constants, that are described in Subsection 2.2.2 (Parchaňský & Bouř, 2010).

2.2.8. Crystal-like computational protocol

In the attached publication (**Appendix B**), we introduced a new crystal-like computational protocol, where the MD cluster-based approach is adapted to better correspond to the liquid phase introducing a crystal-like periodicity in following steps. Based on the MD cluster of 10 molecules in the periodic elementary cell (cubic box, **Figure 2.9a**), smaller clusters were made by default containing two close molecules, presumably comprising the strongest intermolecular interaction within the periodic box and 26 neighboring boxes (**Figure 2.9b**).The geometries of the pairs were partially optimized in the normal mode coordinates. The modes within i100 – 225 cm^{-1} were fixed. The force field and polarizability derivatives obtained for the pairs (**Figure 2.9c**) were transferred back to the 3×3×3 supercube using the Cartesian coordinate transfer (CCT), see **Figure 2.9d**. Because of the periodicity, vibrational Hamiltonian can be described as a sum over the wave vectors **q** and atoms *i* within one cell only,

$$\hat{H} = \sum_{\mathbf{q}} \frac{1}{2} \left(\sum_i m_i \dot{x}_i^* \dot{x}_i + \sum_i \sum_j x_i^* D_{ij} x_j \right), \tag{2.75}$$

where m_i are atomic masses and x_i are atomic coordinates. The dynamic matrix for **q** = 0 is

$$D_{ij} = \sum_J f_{ij}, \tag{2.76}$$

where index *J* run over the elementary cells containing the *j*-coordinate and f_{ij} is the force field matrix. Since the Raman and ROA intensity tensors of symmetrical elementary cells (**q** ≠ 0) cancel out by the interference, only the basic elementary cell in the center (**q** = 0) produces non-zero Raman and ROA signal (**Figure 2.9e**).

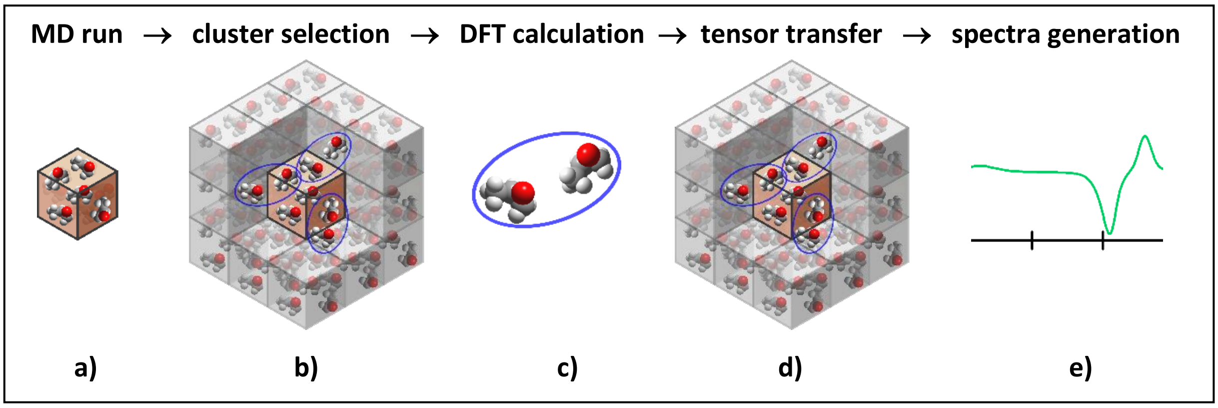

Figure 2.9: Simulations of the spectra by the default crystal-like model. Intermolecular interactions within the periodic elementary cell (brown/middle cube) and towards its environment were simulated for molecular pairs, in an arbitrary 27 cubes of the "supercube". The pair parameters (force field, intensity tensors) were transferred back to the supercube, and the spectra were simulated using periodic boundary conditions.

2.2.9. Intermolecular coordinates

Same as for groups within one molecule, six coordinates describing the vibrational motions of two molecules can be defined including distance of mass centers (*d*), angles between the axes defined by moments of inertia and the distance vector (α_1 and α_2), local rotation angles (β_1 and β_2) and the torsion angle (τ) , see **Figure 2.10**.

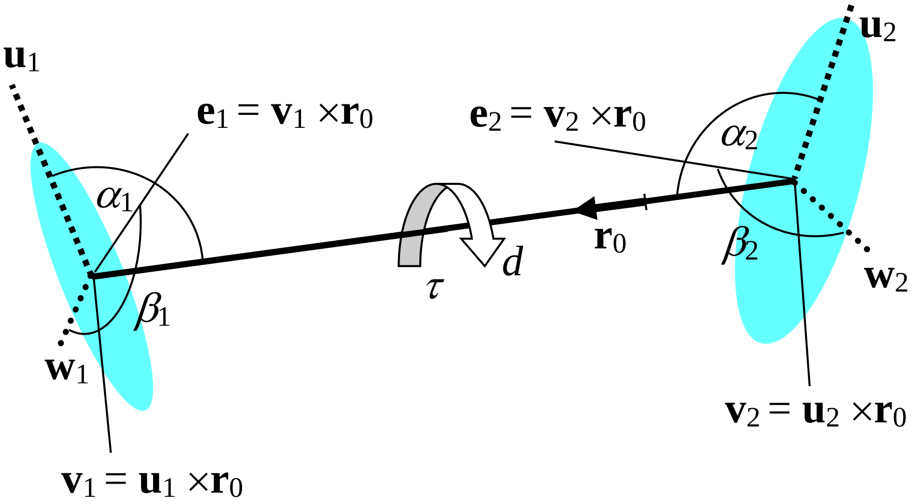

Figure 2.10: Definition of the six coordinates used for the characterization of intermolecular vibrational modes: (d) distance of the mass centers, (α_1 and α_2) angles between the largest moments of inertia and the distance vector, (β_1 and β_2) rotation angles, and (τ) the torsion angle. For the rotation angles, arbitrary vectors $\mathbf{e}_1$ and $\mathbf{e}_1$ were defined, using the largest (direction $\mathbf{u}_i$) and second largest ($\mathbf{w}_i$) moments of inertia. Lengths of all vectors $\mathbf{u}_i$, $\mathbf{w}_i$, $\mathbf{v}_i$, $\mathbf{e}_i$, $\mathbf{r}_i$, and $\mathbf{r}_0$ are equal to one.

2.3. Measurement of Raman optical activity

2.3.1. Introduction to the measurement of vibrational optical activity

Vibrational optical activity (VOA) consists of two complementary techniques, vibrational circular dichroism (VCD) and Raman optical activity (ROA). Both are based on detection of different response of a chiral sample to LCP and RCP radiation. While VCD represents small differences in IR absorption of the two polarization types, ROA is a difference in Raman scattering on chiral molecules. As the VCD to IR absorption ratio is typically 10^{-4}–10^{-5}, and ROA to Raman signal ratio is 10^{-3}–10^{-4}, many errors may arise from imperfect optical components and instrumental noise. In comparison to the electronic techniques such as CD and ORD, however, VOA provides more structural information. Also, Raman linear difference (RLD) (Kowalska et al., 2012) and vibrational linear dichroism (VLD) (Buffeteau & Pézolet, 2006) are techniques based on the polarization modulation and detection. In these cases, orthogonal linear polarizations are used instead of the circular polarization. Additional information about spatial orientation, bonding, or stacking of uniaxial molecular systems can be obtained from the LD measurements (Rodger et al., 2016).

2.3.2. Overview of experimental configurations

Since the ROA measurement is a two-photon process, it can be realized in four different ways regards to the polarization state of the exciting and scattered radiation, see **Figure 2.11**. Historically first instrument measured in the incident circular polarization ICP-ROA form and was based on the different Raman scattering response of the optically active sample to the modulation by RCP and LCP laser radiation (Barron et al., 1973b). The intensity was detected in fixed plane of linear polarization, defined by angle α, or unpolarized. Later, opposite to the ICP, the scattered circular polarization SCP-ROA was introduced, in which the sample is irradiated by effectively unpolarized or linearly polarized light and the RCP and LCP states of the scattered radiation are detected (Spencer et al., 1988). The last two ROA forms were realized by synchronous circular polarization modulation of the incident and scattered radiation. In in-phase dual circular polarization DCP_I-ROA, the incident and scattered polarization are both RCP or LCP, while in out-of-phase dual circular polarization DCP_{II}-ROA, the RCP and LCP states alternate in each step of the measurement. The parent Raman signal is defined as the sum, instead of difference, of the two orthogonal polarization measurements. The sum of DCP_I-ROA and DCP_{II}-ROA is equal to the unpolarized version of the ICP-ROA. According to the theory, DCP_{II}-ROA signal vanishes in far-from-resonance approximation. However, parent ICP and DCP_I Raman spectra are not the same, because only anisotropic part of total Raman scattering is measured in DCP_I case, as the result polarized vibrational bands are missing.

Another important experimental parameter is the detection angle referred to the direction of the incident radiation. This angle denotes the scattering geometry of the experimental setup, and the scattering plane is defined by the propagating vector of the incident and scattered radiation. The right-angle geometry was widely used until 1989, when the back-scattering geometry was introduced (Hecht et al., 1989) and quickly became the preferred experimental geometry, as it possess the best signal-to-noise ratio for ROA. The forward scattering geometry is also possible, where the magnetic dipole contributions dominate in Raman scattering and thus reveal further information about the vibrational structure (Barron et al., 1990).

In the right-angle ICP experimental setup, if the plane of the incident linear polarization is set perpendicular or parallel to the scattering plane, then any Raman scattering polarization state is parallel or perpendicular to the incident polarization and denoted as the polarized or depolarized Raman intensity, respectively.

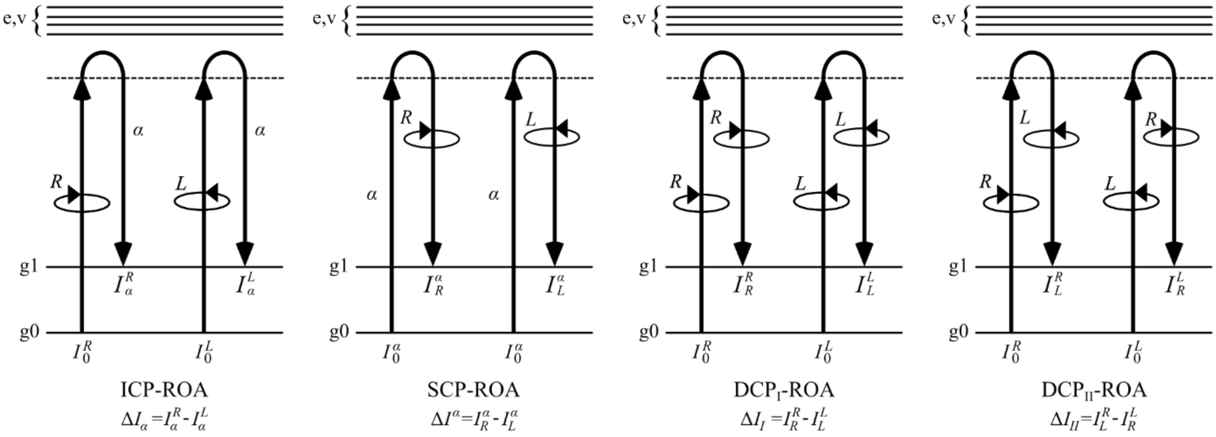

Figure 2.11: Energy level diagram of four ROA modulation forms of the fundamental vibrational transition, where the upper and lower indices denote the polarization state of the incident and scattered radiation, respectively. Greek index α represents the plane of linear polarization. Adapted from (Nafie, 2011).

2.3.3. Historical overview of ROA spectrometers

Early developments of the ROA instrumentation were performed by three research groups, L. Barron's group in Glasgow (UK) (Barron et al., 1973a; Barron et al., 1973b; Barron & Buckingham, 1971; Barron et al., 1989; Hecht et al., 1999; Hecht et al., 1992), W. Hug's group in Fribourg (Switzerland) (Hug, 1982; Hug & Surbeck, 1979) and L. Nafie's group in Syracuse (USA). The most modular ROA spectrometer was the one built in Syracuse, which allowed to measure all modulation forms in forward, backward and right-angle scattering (Hecht et al., 1991; Che et al., 1991; Vargek et al., 1997).

So far, the only commercially available ROA instrument was Chiral*RAMAN* spectrometer, that was introduced in 2003 by the company BioTools Inc. It is based on the SCP-ROA modulation in the back-scattering geometry. The excitation wavelength is 532 nm and the optical design originates from the W. Hug's work, which overcomes the main drawbacks of ROA measurement (Hug, 2003; Hug & Hangartner, 1999). At first, a flicker noise reduction can be achieved by simultaneous detection of RCP and LCP scattered radiation on the upper and lower halves of the CCD detector. Reduced noise has origin in random fluctuations in the measured optical power, flicker noise or thermal Schlieren fluctuation of the sample. Residual noise is statistical and can be suppressed by mild Savitzky-Golay smoothing procedure. Secondly, polarization artifacts and offset can be effectively reduced by measurement of both enantiomers, where the opposite enantiomer can be created by purely optical way (Hug, 2003).

In 2016 J. Kapitán developed a new back-scattering ROA instrument also based on the W. Hug's optical design, but with several novel features, such as additional use of the zero order of the diffraction grating to extend the measurement to the high-frequency spectral region. He also implemented a novel measurement algorithm of all ROA modulation forms simultaneously into the spectrometer (Li & Nafie, 2012). The instrument was built at Palacký University Olomouc and is commercially available since 2022 in collaboration with company ZEBR and Meopta (**Figure 2.12**). Description of the experimental setup are outlined further in this section.

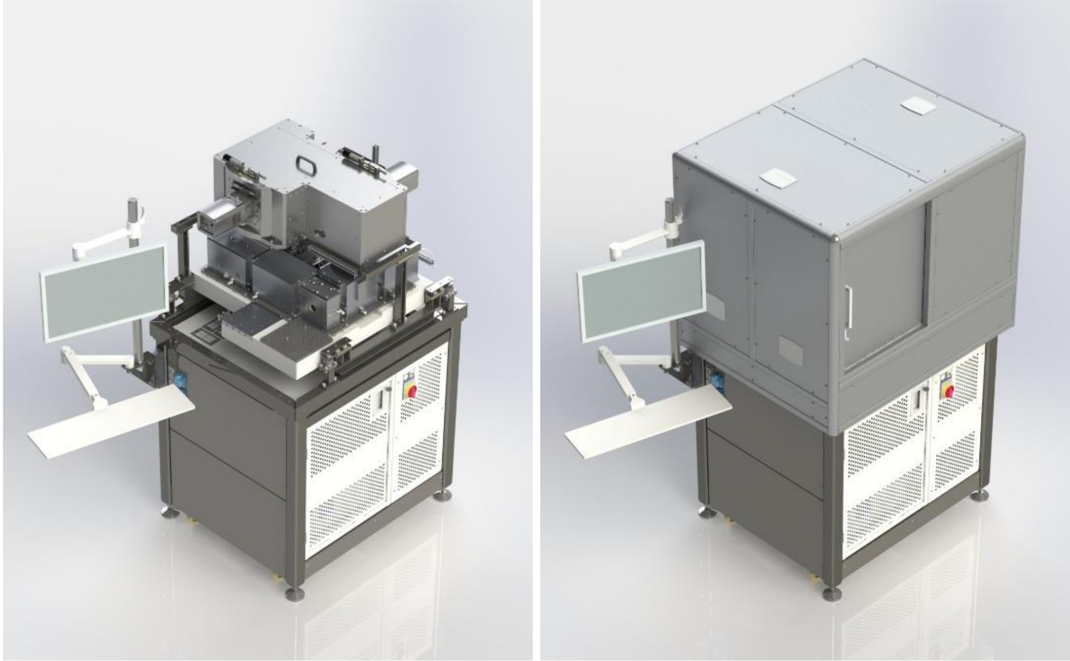

Figure 2.12: Illustration of the commercial version of double-grating ROA spectrometer.

2.3.4. Experimental setup of double-grating ROA spectrometer

The back-scattering ROA instrument, used in this thesis, in the most recent configuration is depicted in **Figure 2.13**.

The excitation part consists of Nd:YAG laser and set of high precision polarization optics to modulate the polarization state of the incident beam. The continuous laser beam (Laser Quantum opus, 532 nm, power 2 W, output beam diameter ~2 mm) is reduced to the beam with ~1 mm in diameter by two lenses with a common focal plane between them. The exposition of the sample is controlled by a shutter (Uniblitz-Vincent Associates). The degree of linear horizontal polarization is increased by the prism polarizer of Glan-Taylor type. A pair of counter-rotating linear rotators LR1 and LR2 consists of zero-order half-wave plates (Bernard Halle, HWP = λ/2 retardation plate) mounted in the hollow shaft servomotors (ZEBR, position accuracy ± 0.02°) and generates effectively depolarized light in time from the horizontal linear polarized light of the laser. The optimal rotating ratio 16:15 of the linear rotators was used in order to compensate the imprecisions in the retardance and mechanical irregularities. Moreover, the modulation rate of the linear polarization is two times higher (kilohertz range). The modulation converter consists of the quarter-wave plate (Bernard Halle, QWP = λ/4 retardation) mounted in the swinging module (ZEBR) with the fast axis aligned to 45° with respect to the orientation of the optical axis of prism polarizer in order to change the linear polarization of the laser beam to the circular polarization. Two circular converters CC0 and CC1 (Bernard Halle, HWP) after linear rotators reverse the sense of circular polarization rotation. Thus, with the CC in the beam path, the virtually opposite enantiomer with the corresponding ROA spectrum can be created by purely optical means (Hug, 2003).

After the desired polarization state is generated, the laser beam is focused by a lens (Meopta, *f*=150 mm) onto the rectangular cuvette (Starna, 3×4 mm, fused silica, antireflex coating) with approximately 70 mL of the liquid sample. The sample is placed in the temperature control cell developed in collaboration with the Institute of Scientific Instruments of the CAS in Brno, that allow to set temperature of the sample within 0–100°C with accuracy below 0.5°C. The transmitted laser power is measured by the integrating sphere (Thorlabs). In case of sample burning, detected laser power drops down and the measurement can be stopped immediately.

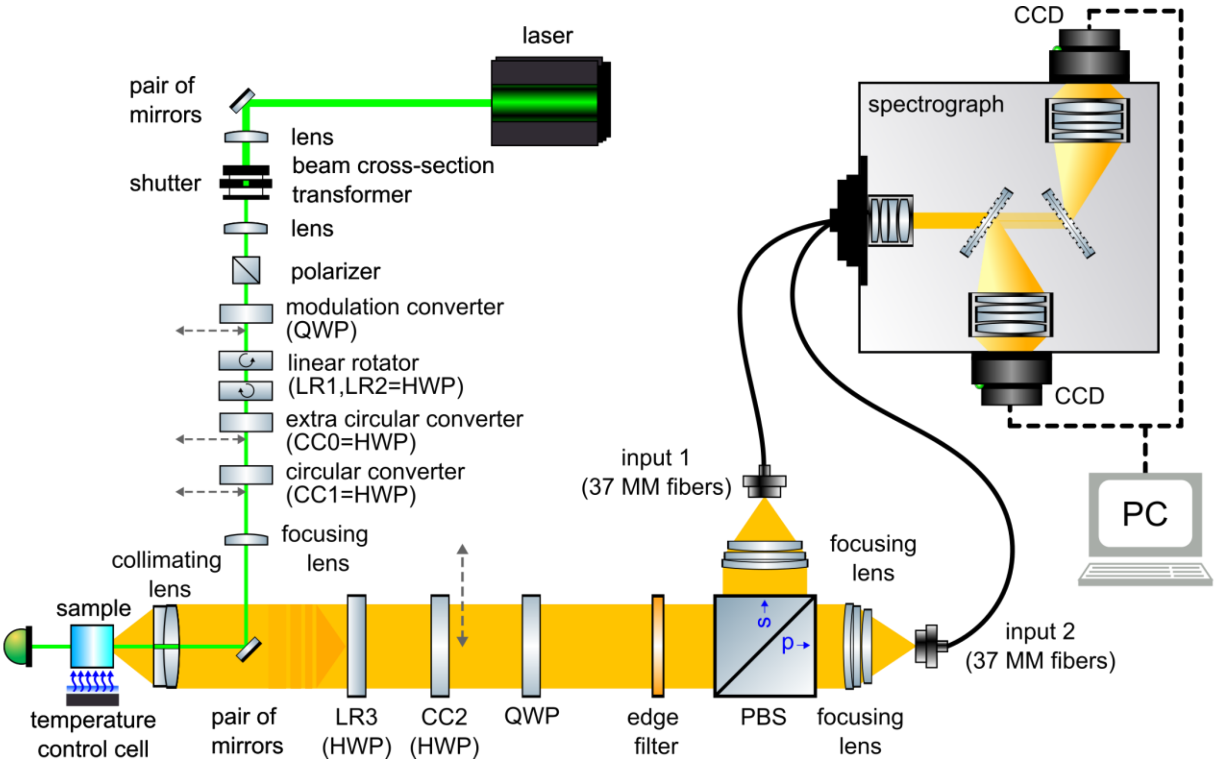

Figure 2.13: Optical layout of the back-scattering ROA spectrometer at Palacký University Olomouc.

Since the reflection efficiency of *s*- and *p*-polarized components is different and the purity of the incident polarization is crucial, the polarization neutral redirection of the laser beam by 90° is provided by the pair of same mirrors placed after the focusing lens. In two 45° reflections of the incident light in orthogonal planes the *s*- and *p*-polarized components are interchanged and the mutual difference in the intensity and phase shift is compensated (Hug & Hangartner, 1999).

Emitted Raman scattering is collimated by a doublet (Meopta, *f*=29 mm), in the backward direction. The drilled hole ensures free space transmission of the counterpropagating laser beam. The only task of the following linear rotator LR3 (HWP), mounted in the hollow shaft servomotor (ZEBR), is to eliminate the remaining linear polarization produced by the imprecision of the preceding optical components and the sample. Swinging circular converter CC2 (Bernard Halle, HWP) is part of the polarization artifact elimination procedure and creates the virtual enantiomer in the scattered radiation. The QWP (Bernard Halle) with the fast axis at a 45° clamped in the hollow shaft servomotor (ZEBR) converts the RCP and LCP of scattered radiation to the corresponding linear polarization. Precise rotation by 90° ensures interchanging the fast and slow axes of the QWP, thus the projections of the RCP and LCP to the orthogonal linear polarizations are exchanged. This ensures balanced exposition of the optical branches behind the polarizing beam splitter PBS (Meopta, extinction ratio in transition 1:1000, in reflection 1:100). Alternatively, the liquid crystal retarder (LCR) can be used. Its advantage is in the optical switching without moving mechanical parts is outweighed by the wavelength-dependent difference in the transmission efficiency (~2:1000) for the fast and slow axes. Rayleigh and anti-Stokes scattering are eliminated at the edge filter (Semrock, ~6 OD at 532 nm, see **Figure 2.14**), only Stokes scattering is analyzed. The PBS cube separates orthogonal linear polarizations. Linear polarization parallel to the plane of reflection of two optical prisms (*p*-polarized) is transmitted, while the perpendicular linear polarization (*s*-polarized) is reflected at the interface of two optical prisms. The light is then focused for each detection branch by focusing objective (Meopta, *f*=119 mm) on to the special fiber optics (SQS). Each branch contains of 37 multimode fibers, that are arranged into hexagonal pattern in the input cross-section and positioned to the one spectrograph slit-like shape at the exit cross-section. The *p*-branch is routed to the upper half of the detector and the *s*-branch to the lower part. The optical shutter (Uniblitz-Vincent Associates) in front of the entrance to each optical fiber controls the CCD exposition by the Raman scattering light. In addition, the pair of scattering shutters can be used during photobleaching to prevent long-time exposition of the CCDs. In the process of photobleaching, the sample is continuously irradiated by the intense laser beam in order to burn out the fluorescence background in the corresponding Raman spectrum. The standard measurement is controlled only by the incident shutter.

A specially designed spectrograph is based on two holographic transmission diffraction gratings (Kaiser Optical Systems, 2400 l/mm and 2200 l/mm), that allow to record Raman and ROA spectra in the wide spectral range from 50 to 4500 cm^{-1}. The light diffracted in zero-order of the first grating (direct transmission) is additionally diffracted by the second grating. Diffracted light is then projected by the focusing objective (Meopta, *f*=85 mm) to the CCD camera (Andor Newton). Due to relatively weak Raman scattering, the CCDs are cooled to −65°C to minimize thermal noise.

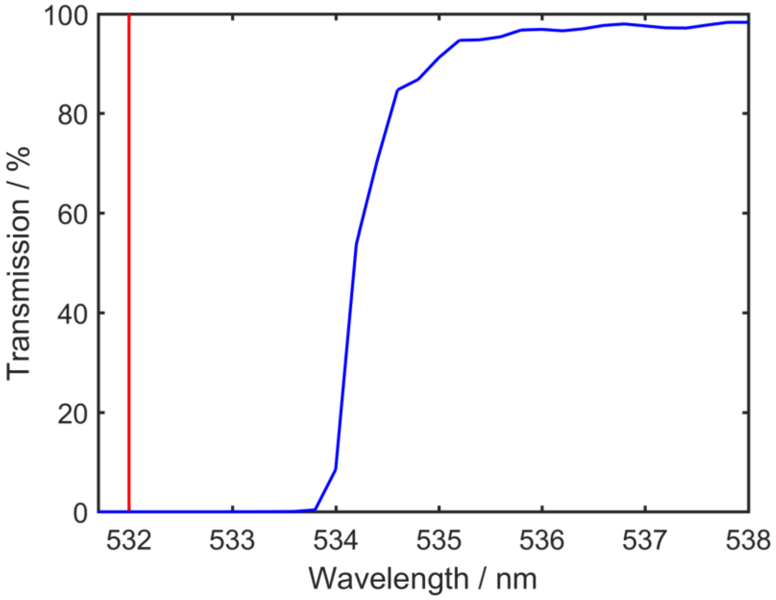

Figure 2.14: Absorption spectrum of the Semrock 532 nm razor edge filter (part. no. LP03-532RE-25, adapted from the Semrock catalogue).

2.3.5. Polarization artifacts

Polarization artifacts do not depend on the chiroptical properties of the sample but arise from the limited precision of the alignment and retardation of the polarizing optics. While typical mirror image of the ROA spectrum is achieved by the measurement of opposite enantiomers, the ROA signal of the polarization artifacts remains unchanged. In the ideal case, by subtracting their spectra, the artifact-free ROA spectrum can be achieved. However, it is conditioned by the availability of both physical enantiomers and their measurement under exactly the same conditions. W. Hug introduced a more generalized concept of the elimination of polarization artifacts based on generating the virtual enantiomer using the HWP as the circularity converter (Hug, 2003).

In the case of the SCP modulation, the remaining circular component in the linearly polarized excitation beam is the main source of systematic errors. On the other hand, the linearly polarized component is undesirable in the measurement of the circular intensity difference in Raman scattering. Incorporating linear rotators (LR1, LR2, LR3) into the experimental setup, the unwanted linear polarization is significantly reduced. Somewhat higher level of the polarization artifact correction can be achieved by adding two swinging circular convertors.

The CC1 and CC2 generates virtual enantiomer in the excitation and scattered path, respectively. In the four-phase correction scheme, it is recommended to move by the CC1 twice as often as the CC2. The CC2 operating in the scattering path must address the polychromatic and non-collimated radiation. Therefore, a zero-order or achromatic waveplates can be used.

Despite the high transmission efficiency of used waveplates, placing the CC1 into the excitation beam path causes the intensity differences between RCP and LCP measurement during the correction cycle. To avoid the intensity bias, the excitation path is equipped by additional HWP CC0. If the CC0 and CC1 are simultaneously placed into the beam path the same circular polarization is produced as with both converters out of the beam path. Contrary, when only one circular converter is on the place the reversed circular polarization is generated. This leads to the balanced intensity for both circular polarizations and same acquisition times for the circular polarization modulation with and without HWPs in the incident beam path (Li & Nafie, 2012).

2.3.6. Data acquisition cycle

The data acquisition cycle of the instrument is synchronized to the motion of the rotators by choosing the length of the exposure window (Hug, 2003). The standard cycle consists of 32 scans (expositions) divided into four repetitions of eight CC0, CC1, CC2 and rotating QWP combinations. Each repetition has slightly different orientations of the LR1, LR2, LR3 rotators. The purpose of the acquisition cycle is to suppress the polarization artifacts due to imperfections in the optical system, as described above.

In the past, all four modulation forms (ICP, SCP, DCPI and DCPII) have been measured independently using different experimental setups. By simple introducing the QWP as the modulation converter into the excitation beam path all four modulation ROA forms can be simultaneously measured within one acquisition cycle. Moreover, as a product of the same measurement, the unpolarized, polarized and depolarized Raman spectra together with the degree of circularity (DOC) (Hug & Hangartner, 1999) can be also obtained. Basically, only four Raman intensity measurements are needed to extract all polarization information (Li & Nafie, 2012).

2.3.7. Wavenumber calibration

Spectral lines of neon are used as a calibration standard for converting pixel number to wavenumbers. The neon lamp is placed on the side of the PBS. The laser is turned off during the calibration procedure, and the incident shutter is opened. The recorded neon lamp spectrum provides enough well-resolved narrow bands that can be fitted by a polynomial function of the third order.

2.3.8. Intensity calibration

Raman signal is recorded in electrons by the CCD chip. The intensities are calibrated using a tungsten-halogen calibration source (HL-3-CAL, Ocean Optics). The halogen spectra (**Figure 2.15a**) were recorded in several positions shifting the halogen source out of the focus ±1.5 mm with increment 0.25 mm. The halogen calibration spectrum was then multiplied by the spectral width of the spectrograph (**Figure 2.15b**) in order to obtain the multiplication factor in reciprocal centimeters. Raman signal in electrons was then divided by the spectral width in the minima of the calibration spectrum. Additionally, the experimental spectra are automatically normalized to the excitation energy, which is the product of the accumulation time and the laser power at the sample. Thus, the experimental spectra are in ($e^{-}\cdot cm\cdot J^{-1}$) unit that allow to compare the spectra recorded under different experimental conditions.

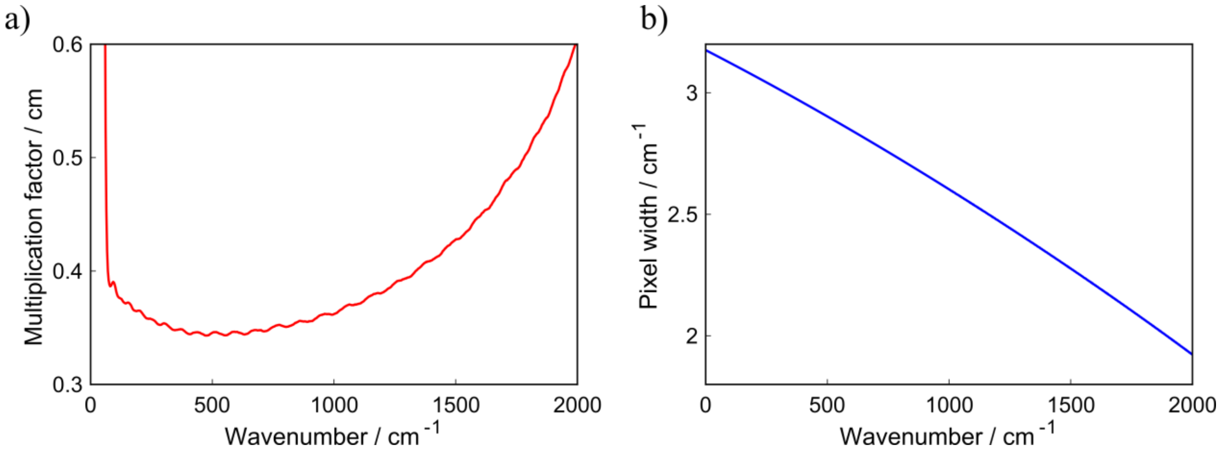

Figure 2.15: (a) Halogen calibration source HL-3-CAL by Ocean Optics. (b) Spectral width of used spectrograph.

2.4. Raman baseline correction

Measured Raman spectra often exhibit an unstable baseline. The acquired spectrum contains both the intended signal and unwanted elements, including background noise stemming from various sources such as the sample holder, instrumentation, and the samples themselves (e.g. impurities, chromophores, …). The baseline may cause detection issues if the CCD reaches its detection limits or prevent further data processing of useful signal. Therefore, the baseline correction methods are routinely used.

Several methods have been suggested with regards to the baseline correction. Methods can be considered more (interactive peak fitting, polynomial fitting) or less (rolling ball algorithm, piece wise linear correction) manual in dependence on the level of human intervention. A more detailed comparison of some of these methods can be found in the literature (Schulze et al., 2005). In this work we used two different semi-manual methods of the baseline estimation.

2.4.1. Asymmetric least squares smoothing

Asymmetric least squares smoothing (ALSS) (Eilers & Boelens, 2005) is based on Whittaker smoother (Eilers, 2003), where ordinary least squares are penalized. Positive deviations with respect to the baseline are weighted less than negative deviations. The baseline correction can be controlled by two parameters, making ALSS completely reproducible.

The ALSS is defined by the following system of equations:

$$(W + \lambda D'D)z = Wy, \tag{2.77}$$

where y is measured signal of length m and z is smoothed signal faithful to y, $W = \mathrm{diag}(w)$ is diagonal matrix of weights w_i, $Dz = \Delta^2 z$ is a difference matrix and $\Delta^2 z_i = (z_i - z_{i-1})$. The first term in (2.77) measures the fit to the data, while the second term is a penalty on non-smooth behavior of z. The level of smoothing is controlled by a parameter known as the smoothing parameter or lambda (λ). The ALSS weights are controlled by asymmetry parameter p defined as follows:

$$\begin{gathered} w_i = p \text{ if } y_i > z_i, \\ w_i = 1 - p \text{ if } y_i \le z_i. \end{gathered} \tag{2.78}$$

The iterative form of ALSS baseline estimation can be implemented in MATLAB, as the following code fragment shows (adapted from (Eilers & Boelens, 2005)). In practice 5 to 10 iterations are sufficient for convergence. Parameters p and λ need to be tuned by the analyst according to the specific data being analyzed. In general, it is recommended to set $10^{-4} \le p \le 10^{-2}$ and $10^2 \le \lambda \le 10^9$, but exceptions may occur. Parameters

$(p = 1.0 \times 10^{-4}, \lambda = 8.5 \times 10^{4})$ in the attached publication **Appendix B**, $(p = 1.3 \times 10^{-4}$, $\lambda = 3.2 \times 10^{5})$ in publication **Appendix D**, were used.

```
function z = alss(y, lambda, p)
% Estimate baseline with asymmetric least squares
m = length(y);
D = diff(speye(m), 2);
w = ones(m, 1);
   for it = 1:10
           W = spdiags(w, 0, m, m);
           C = chol(W + lambda * D' * D);
           z = C \ (C' \ (w .* y));
           w = p * (y > z) + (1 - p) * (y < z);
   end
end
```

2.4.2. Iterative polynomial smoothing

The iterative polynomial smoothing algorithm (IPSA) (T. Wang & Dai, 2017) combines the advantages of polynomial filter and iteration method. Hence, IPSA effectively addresses certain limitations of conventional polynomial fitting algorithms, particularly their dependence on spectral range selection and the fixed polynomial order throughout the process, that can make the algorithm less robust when dealing with changes in the background in continuous measurements.

In the IPSA three crucial parameters are introduced – the filter window width ω_f (odd, bigger than the filter order), the iteration accuracy β and the termination range Θ, that includes all necessary signal for background estimation. In the first step the input spectrum $R_{orig}(\tilde{\nu})$ is smoothed by a 2nd order Savitzky-Golay filter of window width ω_f (odd, bigger than the filter order) in order to get broad background. The output is assigned to $R_{bg}(\tilde{\nu})$ and the residual spectrum is calculated as follows:

$$R_{res}(\tilde{\nu}) = R_{orig}(\tilde{\nu}) - R_{bg}(\tilde{\nu}). \tag{2.79}$$

A crucial factor

$$eRatio = \frac{|\min\left(R_{res}(\tilde{\nu}_\Theta)\right)|}{|\max\left(R_{res}(\tilde{\nu}_\Theta)\right)|} \tag{2.80}$$

is then calculated, where $\tilde{\nu}_\Theta$ are wavenumbers from the termination range Θ. If $eRatio > \beta$, the next iteration is initiated. The new input spectrum is formed as follows:

$$R_{inp}(\tilde{\nu}) = \min\left(R_{orig}(\tilde{\nu}), R_{bg}(\tilde{\nu})\right) \tag{2.81}$$

and inserted to the equation (2.79). When iteration is over, the last $R_{bg}(\tilde{\nu})$ is the final background spectrum. According to the reference the iteration process reasonably converges when the filter window width ω_f is set between 100 and 200, the iteration accuracy $\beta < 10^{-5}$ and Θ is set as the minimum wavenumber range that includes all available signal for backgrounds. If more accuracy is needed, the smaller filter window width must be set. However, this can significantly increase the iteration number and computing time. When the IPSA was tested in the data set of attached publication **Appendix D**, it led to similar results as for ALSS but with a longer computing time. The IPSA can be implemented in MATLAB, as the following fragment shows.

```
function Rbg_final = ipsa(xdata,Rorig,beta,omega_f,Theta,iterN)

% Original spectrum
    Rinp = Rorig;
% Initial smoothing
    Rbg = sgolayfilt(Rinp,2,omega_f);
    Rres = Rorig - Rbg;
% Calculate eRatio
    Rres_theta = Rres(Theta(1)<xdata & Theta(end)>xdata);
    eRatio = abs(min(Rres_theta))./abs(max(Rres_theta));
% Iteration part
    for j = 1:iterN
        if eRatio > beta && j ~= iterN
            Rinp = transpose(min(vertcat(Rorig',Rbg')));
            Rbg = sgolayfilt(Rinp,2,omega_f);
            Rres = Rinp - Rbg;
            Rres_theta = Rres(Theta(1)<xdata & Theta(end)>xdata);
            eRatio = abs(min(Rres_theta))./abs(max(Rres_theta));
            j = j+1;
        elseif eRatio < beta
            Rbg_final = Rbg;
            disp('OK')
            break
        elseif j == iterN
            Rout = NaN*ones(length(Rorig),1);
            error('IPSA algorithm not converge! Try to increase
                   iterN or change parameters.')
        end
    end
end
```

2.5. Comparison of experimental and calculated spectra

The efficiency of the molecular structural analysis from chiroptical spectra lies in the comparison of experimental and predicted spectra. If the spectral pattern of the specific predicted conformation meets the observed spectral pattern in the same wavenumber range, then the conformation can be assigned to the measured sample. Analyzed spectra are usually compared first qualitatively and then quantitatively.

2.5.1. Qualitative comparison

The aim of the qualitative analysis is the assignment of the most characteristic spectral patterns in the experimental spectrum by visual comparison of band intensities and a sign pattern to the reference. However, this procedure should be taken with caution due to its subjective nature.

2.5.2. Quantitative comparison

In recent years, several diverse metrics of similarity have been introduced to address comparison of experimental and calculated spectra (Polavarapu, 2016).

Similarity factors

The similarity of the experimental and simulated experimental spectra can be quantitively compared using similarity overlap integral (Kuppens et al., 2003)

$$S_1 = \frac{\int f(\tilde{v})g(\tilde{v})d\tilde{v}}{\sqrt{\int f(\tilde{v})^2\, d\tilde{v} \int g(\tilde{v})^2\, d\tilde{v}}} = \int \hat{f}(\tilde{v})\hat{g}(\tilde{v})d\tilde{v}, \tag{2.82}$$

where $f(\tilde{v})$ and $g(\tilde{v})$ represents calculated and experimental spectrum, respectively, and the denominator implies normalization

$$\hat{f}(\tilde{v}) = \frac{f(\tilde{v})}{\sqrt{\int f(\tilde{v})^2\, d\tilde{v}}}, \tag{2.83}$$

$$\hat{g}(\tilde{v}) = \frac{g(\tilde{v})}{\sqrt{\int g(\tilde{v})^2\, d\tilde{v}}}. \tag{2.84}$$

In case of compared spectra possess zero intensity in analyzed region the denominator in (2.82) would be also zero, which causes numerical problems. Therefore, an alternative definition of similarity can be used as follows (Shen et al., 2010):

$$S_2 = \frac{I_{fg}}{I_{ff} + I_{gg} - |I_{fg}|}, \tag{2.85}$$

where the overlap integrals are given as:

$$I_{ff} = \int f(\tilde{v}) f(\tilde{v}) d\tilde{v}, \tag{2.86}$$

$$I_{gg} = \int g(\tilde{v}) g(\tilde{v}) d\tilde{v}, \tag{2.87}$$

$$I_{fg} = \int f(\tilde{v}) g(\tilde{v}) d\tilde{v}, \tag{2.88}$$

and $f(\tilde{v})$ and $g(\tilde{v})$ are not normalized. For $\hat{f}(\tilde{v})$ and $\hat{g}(\tilde{v})$, the overlap integrals are

$$I_{\hat{f}\hat{f}} = \int \hat{f}(\tilde{v}) \hat{f}(\tilde{v}) d\tilde{v} = 1, \tag{2.89}$$

$$I_{\hat{g}\hat{g}} = \int \hat{g}(\tilde{v}) \hat{g}(\tilde{v}) d\tilde{v} = 1, \tag{2.90}$$

$$I_{\hat{f}\hat{g}} = S_1, \tag{2.91}$$

and the similarity factor (2.85) is reduced to

$$S_2 = \frac{S_1}{2 - |S_1|}, \tag{2.92}$$

In the comparison of experimental and predicted Raman or ROA spectra, their magnitudes may not be on the same scale. Therefore, spectral normalization or multiplication by a constant is necessary. The similarity values in (2.82) and (2.92) vary in a range from 0 to 1 for the Raman spectra and within −1 and 1 for chiroptical spectra (ROA and CID – ratio of the ROA and Raman spectra). Calculated frequencies can be corrected introducing frequency (wavenumber) scaling factor or function in order to match corresponding experimental frequencies. By frequency scaling of the predicted spectra and calculating the similarity factor, the maximum similarity can be determined. In present results we used and compared similarity factors (2.82) and (2.92). Alternative criteria of the similarity factor exist and can be used as long as it is consistent in all spectral comparisons.

Methods of conformational analysis based on the spectral comparison

As was recently confirmed, the conformational analysis based on calculated energies suffers from large uncertainties (Bootsma & Wheeler, 2019; Koenis et al., 2019). The relative conformational contribution may vary more than 2 kcal·mol^{-1} based on the molecular structure, the chosen DFT approximation and the size of used integration grid. The uncertainty in energy affects the predicted spectra and prevents reliable assignment of the absolute configuration. As an alternative, methods that fit a set of calculated spectra in order to minimize the difference with the experimental spectra were suggested.

Very first conformational analysis based on the linear fitting of calculated and experimental dipole and rotational strengths of the methylcyclohexanone fundamental bands was introduced by F. J. Devlin and P. J. Stephens (Devlin & Stephens, 1999). In the fitting procedure experimental dipole or rotational strengths were plotted against the calculated values of each available conformer. The ratio of two slopes of the fitted linear function for each conformer determined the ratio of their populations.

Another approach is based on the genetic algorithms that continuously modify the calculated conformational (Gibbs) energies according to the predefined mutation rules and optimize Boltzmann weights to obtained the best possible similarity overlap of the predicted spectrum and the experiment (2.85) (Koenis et al., 2019; Polavarapu et al., 2020). In one of published approaches (Koenis et al., 2019), the starting energy set is based on the calculated DFT energies for each conformer. Another energy sets are modification of the starting set by randomized energy variation in specified energy range. For each energy set, the similarity factor is calculated. If the similarity does not improve over 2000 generations, the convergence criterium is achieved. Otherwise, the three best energy sets are used to generate the sets of conformational energies for the next iteration. In order to explore the conformational space, next iterations of the energies are forced to significantly differ, and many random new sets are produced. Once the genetic algorithm starts to converge towards a specific similarity maximum, the optimization conditions are changed to find the best similarity close to the specific maxima. The substantial energy sets are allowed to change with much smaller energy mutations and only few random population sets are employed. The algorithm is able to find the optimized weights for less than 200 conformations in the set with significant differences in the compared spectral range.

Conformational analysis based on the spectral decomposition of the observed spectrum $g(\tilde{v})$ to the calculated N conformer subspectra $f_i(\tilde{v})$ was also proposed by P. Bouř. The algorithm is based on the minimization of the function

$$\Delta = \left(g(\tilde{v}) - \sum_{i}^{N} c_i f_i(\tilde{v})\right)^2 + \alpha \sum_{i}^{N} \left(c_i - \frac{1}{N}\right)^2, \qquad (2.93)$$

where α is the bias factor and $c_i > 0$ are coefficients of the decomposition with a normalization condition

$$\sum_{i}^{N} c_i = 1. \tag{2.94}$$

The algorithm is implemented in the *Specomp* program (Bouř, 2023).

The original approach is introduced in the attached publication (**Appendix C**). Conformational analysis is based on maximizing the similarity overlap of the weighted conformer spectra with the experiment by employing a global minimization algorithm to optimize the conformer populations and wavenumber scaling factor. The experimental and simulated vibrational spectra were compared using introduced similarity factor (2.92). The real chiral sample is considered to be a mixture of all possible conformers with a different abundance. This can be specified by the normalized linear combination of all stable conformers in the predicted spectrum

$$f(\tilde{v}) = \sum_{i}^{N} c_i f_i(\tilde{v}), \tag{2.95}$$

where each linear combination coefficient c_i represents the relative abundance of conformer *i* and *N* is the number of conformers. For a molecule with *N* conformations, *N*–1 conformer populations c_i in relation (2.95) and the scaling factor for predicted wavenumbers is allowed to change towards maximizing similarity overlap. The remaining conformer population is calculated as

$$c_N = 1 - \sum_{i}^{N-1} c_i. \tag{2.96}$$

The MATLAB implementation of the algorithm for estimating conformational populations is exemplified in the following fragment, demonstrating reduced calculation for three conformers for clarity purposes.

```
% Spectral interval
IX = 300:1750;

% Linear combination of predicted spectra
f = @(P) (P(1).*interp1(P(3)*data1(:,1),data1(:,2),IX,'linear') +
P(2).*interp1(P(3).*data2(:,1),data2(:,2),IX,'linear')+ (1-P(1)-
P(2)).*interp1(P(3).*data3(:,1),data3(:,2),IX,'linear'));

% Experiment
g = interp1(dataexp(:,1),dataexp(:,2),IX,'linear');

% Overlap integrals
I_fg = @(P) trapz(f(P).*g)./sqrt(trapz(f(P).*f(P)).*trapz(g.*g));
I_ff = @(P) trapz(f(P).*f(P))./sqrt(trapz(f(P).*f(P)).*trapz(f(P).*f(P)));
I_gg = trapz(g.*g)./sqrt(trapz(g.*g).*trapz(g.*g));

S2 = @(P) -I_fg(P)./(2 - abs(I_fg(P))).*((1-P(1)-P(2))>=0 && P(1)>0 &&
P(2)>0) + 1.*((1-P(1)-P(2))<0);

% Starting points
P0 = [0.3;0.3;0.98]; % for P1, P2 and wavenumber factor

% Minimization
opts = optimset('MaxIter',1e8,'TolX',1e-8,'TolFun',1e-8,'MaxFunEvals',1e5);
P = fminsearch(S2,P0,opts);
P3 = 1-P(1)-P(2);   % P3

% Output
out = [P(3) P(1) P(2) P3 -S2([P(1) P(2) P(3)])]; % = [SCF P1 P2 P3 SIM];
```

As the complexity of conformational space increases with the flexibility of the studied molecular system, careful selection of the starting points in the optimization procedure is needed due to the tendency to slide down to the nearest local minimum. Therefore, a more general two-step global optimization procedure can be applied. In the first step M sets of $N{-}1$ randomly distributed coefficients are generated as the starting points (Monte-Carlo method), each satisfying condition

$$0 \leq \sum_{i}^{N-1} c_i \leq 1, \tag{2.97}$$

and the wavenumber scaling factor is left fixed in order to map the $N{-}1$ conformational space and localize a global maximum of equation (2.92). In the second stage, the process of local optimization is repeated, using the previously optimized $N{-}1$ set of coefficients as the new starting points and the wavenumber scaling factor is allowed to be modified in order to achieve the best possible similarity within the global maxima region.

2.6. Procedure for determining the enantiomeric excess

One of the main applications of ROA is the measurement of optical purity of chiral samples. In this work, we have demonstrated a new methodology of enantiomeric excess determination by ROA (see **Appendix D**) as it is presented below. It is based on an effective algorithm that includes Raman baseline correction, ROA intensity normalization, and systematic errors elimination procedure applied to experimental ROA data.

2.6.1. Sample preparation

It is common practice to suppose the ideal purity ($e_A = -e_B = 1$) of the mixed chiral substances *A* and *B*. Then the enantiomeric excess (EE) of the mixture is defined as

$$e_i^0 = \frac{m_{Ai} - m_{Bi}}{m_{Ai} + m_{Bi}}, \tag{2.98}$$

according to mass ratios m_A and m_B. However, for real samples, it is not possible to achieve exactly unit enantiomeric excess. Additionally, the EE is always specified by the manufacturer with a limited precision, and therefore it can be assumed not to be the same. Thus, the EE can be expressed as

$$e_i^1 = \frac{m_{Ai} - c_{B1} m_{Bi}}{m_{Ai} + m_{Bi}}, \tag{2.99}$$

where the optical purity of the chiral substance *A* is assumed to be $e_A = 1$ and the constant c_{B1} needs to be determined.

2.6.2. Sample measurement and ROA spectra normalization

At first, Raman and ROA spectra for *N* EE samples, containing *M* spectral points, are measured and usually normalized to the used excitation energy. The dataset is a matrix of size *N*×*M*. Secondly, the background in all Raman spectra must be subtracted according to the procedure described in Section 2.4 in order to obtain the spectra S_{iv}^{bas}. Because of the intensity fluctuations caused by the laser instability or thermal fluctuations in the sample, the ROA spectra D_{iv}^{raw} were then normalized according to the parent baseline corrected Raman spectra as

$$D_{iv} = D_{iv}^{raw} \frac{\sum_v S_{Av}^{bas}}{S_{iv}^{bas}} = D_{iv}^{raw} n_{norm}, \tag{2.100}$$

where the sum is performed over the selected spectral region, and index *A* denotes the Raman spectrum of the reference. For diluted stock samples, a variation in the molar concentration of analyzed mixtures must be taken into account.

2.6.3. Enantiomeric excess determination

The most straightforward approach to calculate the enantiomeric excess involves solving a system of overdetermined linear equations.

$$D_{i\nu} = \hat{e}_i^D D_{A\nu}, \tag{2.101}$$

by the least squares method, where $D_{i\nu}$ is one element of the matrix N×M, $\hat{e}_i$ is one element of the column vector N×1 representing unknown enantiomeric excess and $D_{A\nu}$ is one element of the row vector 1×M of ROA spectra of the reference A. The fundamental assumption of this approach is that the enantiomeric excess of reference A is set to the unity (100%). Subsequently, all spectra for which the enantiomeric excess is to be determined are compared to this reference A. Since, the minimum of used spectra is $N = 2$, the equation (2.101) represents overdetermined set of linear equations and can be solved by the least square method as follows:

$$\min_{\hat{e}_i} \sum_{\nu=1}^{M} (D_{i\nu} - \hat{e}_i D_{A\nu})^2. \tag{2.102}$$

2.6.4. Performance of enantiomeric excess determination

The correctness of the EE determination can be defined as the standard deviation of the errors

$$\sigma(\Delta) = \sqrt{\frac{\sum_{i=1}^{N} \Delta_i^2}{N}}, \tag{2.103}$$

where

$$\Delta_i = e_i - \hat{e}_i \tag{2.104}$$

is a difference of the EE determined from spectra $\hat{e}_i$ and from the sample preparation e_i according to the equation (2.98). Alternatively considering the EE definition (2.99), the constant c_{B1} is determined assuming that the sum of all errors is zero as follows:

$$\Delta_i^1(c_{B1}) = e_i^1(c_{B1}) - \hat{e}_i, \sum_{i=1}^{N} \Delta_i^1(c_{B1}) = 0. \tag{2.105}$$

2.6.5. Correction of residual artifacts in ROA spectra

Despite the fact that polarization artifacts can be significantly reduced by W. Hug's proposed concept of virtual enantiomers (Hug, 2003) generated during the measurement (see Subsection 2.3.5), residual artifacts that occur in ROA spectra are still proportional to the degree of circularity. Thus, all ROA spectra of the enantiomeric mixtures of same compounds will be affected by the same amount of artifacts. The accuracy of the EE determination can be further improved reducing the artifacts in the post-processing procedure.

The simplest method for determining artifacts is to sum the ROA spectra of the two optically pure opposite enantiomers:

$$a_\nu^{AB} = \frac{D_{A\nu} + D_{B\nu}}{2}. \tag{2.106}$$

On the contrary, by subtraction one can receive the artifact-free ROA spectrum:

$$D_\nu^{trueAB} = \frac{D_{A\nu} - D_{B\nu}}{2}. \tag{2.107}$$

If both pure enantiomeric forms are not available, an alternative and more universal approach is proposed in the publication **Appendix D**, based on solving an overdetermined set of linear equations for $N > 2$:

$$D_{i\nu} = D_\nu^{trueN} e_i + a_\nu^N, \tag{2.108}$$

for different enantiomeric measurements i by the least squares method, where e_i is the known enantiomeric excess from the sample preparation and variables are the ROA artifact-free spectrum D_ν^{trueN} and artifact spectrum a_ν^N. The artifact spectrum determined by (2.108) possess better signal-to-noise ratio then using only the sum of opposite enantiomers.

3. Results

3.1. Conformational analysis

3.1.1. Conformational analysis based on the potential energy scan

The molecular flexibility of (*R*)-2-chloropropionitrile (nitrile) and three ethylbenzene derivatives ((*R*)-(+)-1-phenylethanol, (*R*)-(+)-*α*-methylbenzylamine, (*S*)-(+)-*α*-(trifluoromethyl)benzyl alcohol) was analyzed using potential energy surface scans (see Subsection 2.2.3). The results are published in **Appendix A** for nitrile and **Appendix B** for ethylbenzene derivatives, respectively.

Nitrile was selected as a small yet relatively inflexible molecule ideal for representing a model liquid. The methyl group (CH_3) rotates freely within a limited range of 35° ($\Delta E < 2$ kcal·mol^{-1}). The nitrile's C−C≡N group is particularly well-suited for studying two-dimensional conformational changes. The energy dependence of the selected nitrile angles (Φ, ω) is displayed in **Figure 3.1** and overlayed by the distribution of 200 geometries of the MD clusters partially optimized in normal modes (see Subsection 2.2.6) with fixed frequencies of i100–225 cm^{-1} ($i = \sqrt{-1}$ for imaginary frequencies). Various values of the normal mode frequency limit were tested. Reducing the upper frequency limit further would cause collapse of the MD geometries toward the equilibrium geometry in the center ($\Delta E = 0$ kcal·mol^{-1}). Surprisingly flexible C−C≡N bending angle (ω) was observed based on DFT calculation (see Subsection 2.2.1), requiring to overcome energy barrier of 2 kcal·mol^{-1} for deviation of 16° from the equilibrium angle ω ∼ 179°.

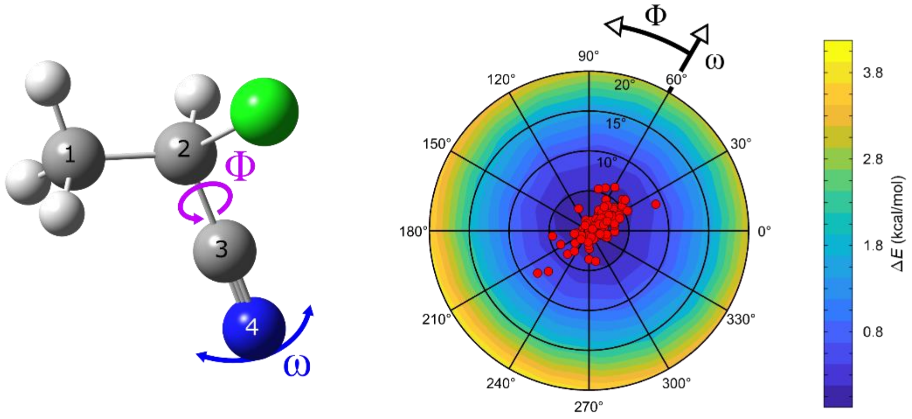

Figure 3.1: Dependence of (*R*)-2-chloropropionitrile (nitrile) electronic energy on selected angles Φ and 180° − ω calculated at the B3PW91/6-311++G**/COSMO(ACN) level (contour map) and coordinates of 200 MD clusters partially optimized with normal modes in range i100 – 225 cm^{-1} (red dots). Nitrile angular coordinates are defined as Φ = C1-C2-C3-N4 and ω = C2-C3-N4. The energy scan was controlled by 49 combinations of Φ and 155° < ω < 180°, selected, so that the resultant nitrogen positions were evenly distributed on a sphere around C3 atom.

Spectral parameters, such as the relative ROA intensity or the frequency of normal modes, are to a large extent dependent on the selected angular coordinates, as can be seen for example, for the nitrile C−C−C≡N bending mode 561 cm^{-1}, C≡N stretching mode 2356 cm^{-1} or the intensity ratio of the 672 and 1003 cm^{-1} in **Figure 3.2**. Modes 561 cm^{-1} and 2356 cm^{-1} shifts in frequencies within ~ 10 cm^{-1}, while modes 672 and 1003 cm^{-1} are less frequency dependent. The corresponding C≡N stretching mode possesses positive sign for Φ ~ 90°, while it is negative for other selected conformers in **Figure 3.2d**. The frequency shift of the C≡N stretching mode is consistent with its harmonic nature (cf. **Figure 3.1** and **Figure 3.2b**).

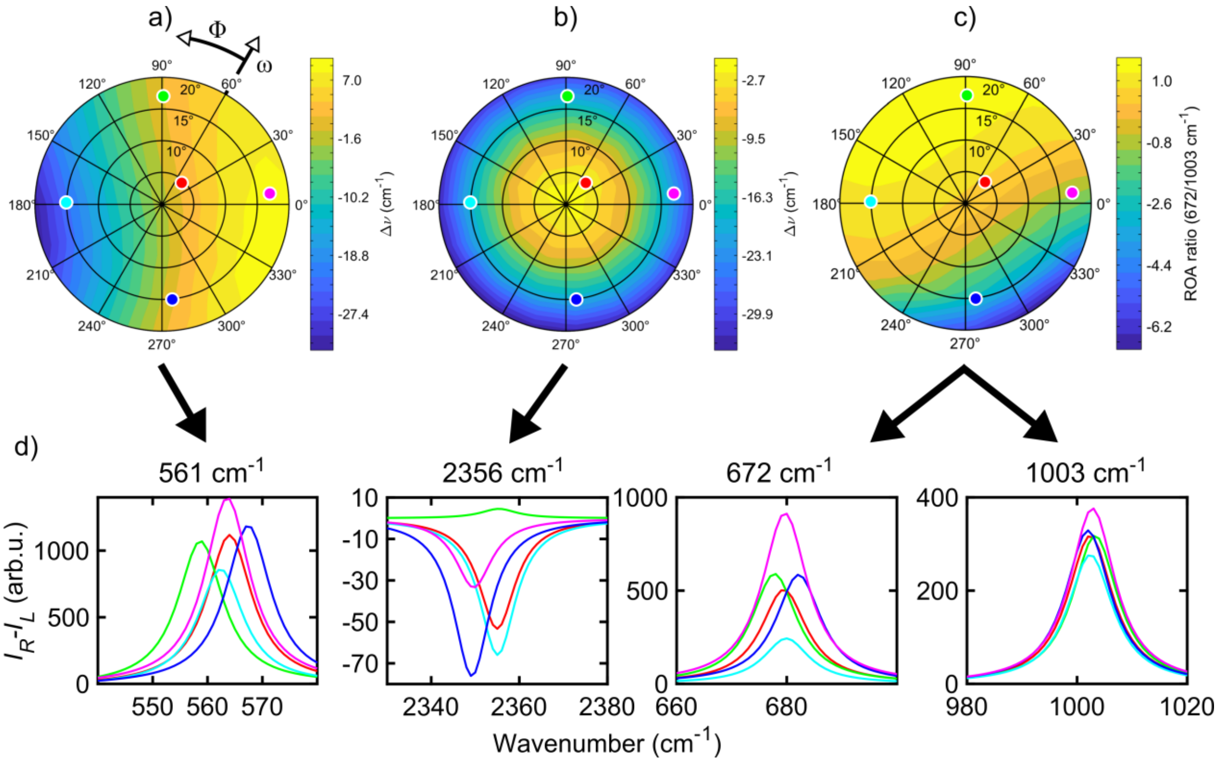

Figure 3.2: Frequency shift ($\Delta\nu$ / cm^{-1}) of selected nitrile normal modes 561 cm^{-1} **(a)** and 2356 cm^{-1} **(b)**, from values for the equilibrium geometry, and **(c)** ROA intensity ratio of the 672 and 1003 cm^{-1}, plotted as a function of the Φ and 180° − ω angles. Five ROA spectra of analyzed bands **(d)** for selected conformers **(a**, color points**)** are depicted.

The conformational analysis of (*R*)-(+)-1-phenylethanol, (*R*)-(+)-α-methylbenzylamine and (*S*)-(+)-α-(trifluoromethyl)benzyl alcohol is described by the rotation of the three functional groups (methyl, phenyl an hydroxyl/amine). The methyl group employs similar energetical barrier as for nitrile (~ 4 kcal·mol^{-1}). Rotation of the methyl group isolated from rotation of other groups has minor effect to resulting simulated spectra. Therefore, the conformational analysis of the ethylbenzene derivatives could be limited to the 2D PES scan only (Kapitán et al., 2009). The 2D PES scan as a function of the phenyl (φ), hydroxyl (ψ) and amine (χ) groups is shown in **Figure 3.3** and Boltzmann-averaged Raman and ROA spectra are plotted in **Figure 3.4**. The orientation of the polar OH or NH groups out of the phenyl plane (φ ~ 100°) is preferred by each of the three molecules. The freely rotating NH and OH groups give arise to three local minima (ψ = −60°, 60° and 180°) with small energy barrier up to ~ 2 kcal·mol^{-1} (3 kcal·mol^{-1} for methylbenzylamine). Revised PES calculations at the B3PW91/6-311++G**/COSMO(benzylalcohol) are consistent with the previous study of phenylethanol and methylbenzylamine at the B3LYP/6-311++G**/vacuum level (Kapitán et al., 2009). 2D PES scans are overlayed by the conformer distribution from the MD models (see **Appendix B**). The MD distributions differ from the PES scan because of hydrogen bonding to the explicit solvent molecules in the cluster-based model (see Subsection 2.2.4). The effect of the different computational models on the conformational preference is discussed further in Subsection 3.1.2.

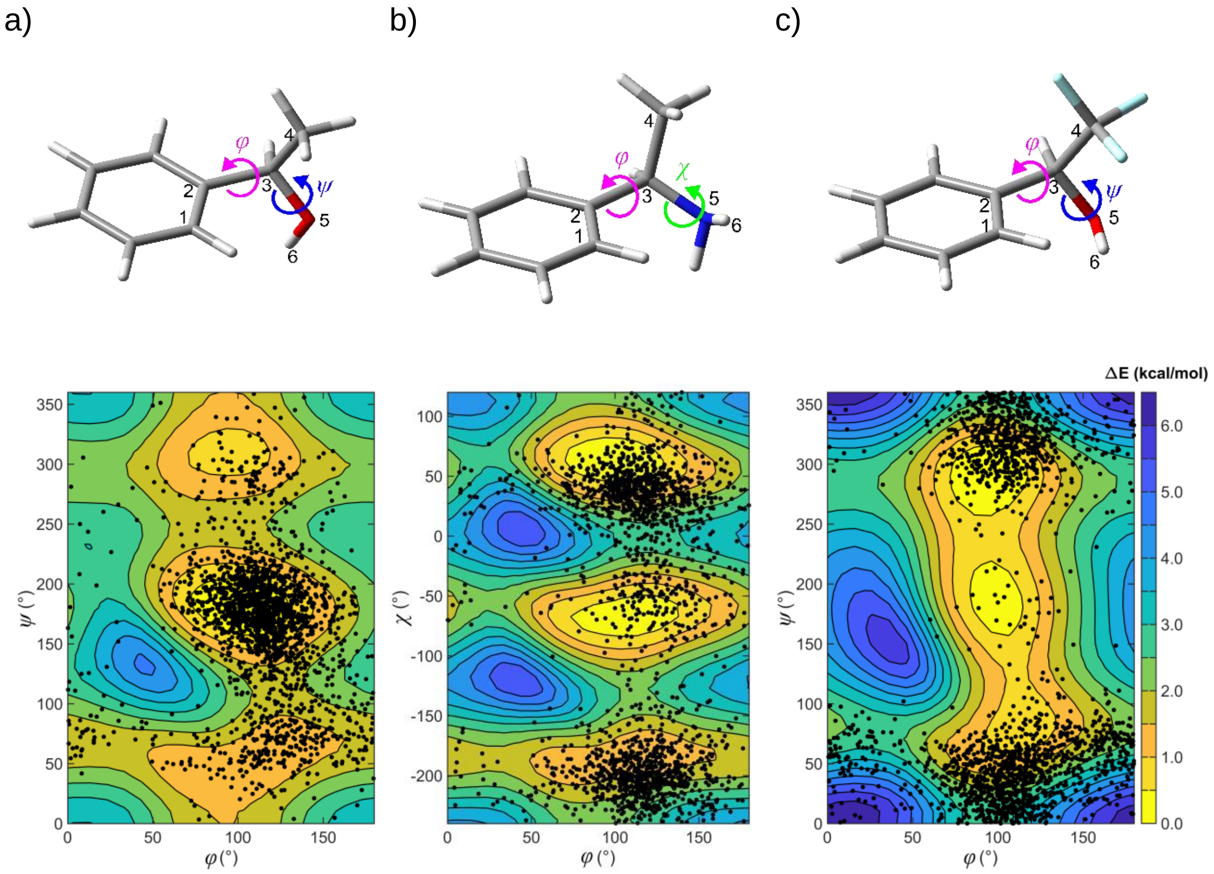

Figure 3.3: Dependencies of the (*R*)-(+)-1-phenylethanol, (*R*)-(+)-*α*-methylbenzylamine, (*S*)-(+)-*α*-(trifluoromethyl)benzyl alcohol electronic energy on selected torsion angles calculated at the B3PW91/6-311++G**/COSMO(benzylalcohol) level (contour map) and coordinates from 200 MD snapshots (2000 black dots in total). The describe phenyl rotation, φ = C1-C2-C3-C4, hydroxyl rotation, ψ = C4-C3-O5-H6, and amine rotation, χ = C2-C3-N5-H6.

The Boltzmann averaging for conformers below 2 kcal·mol^{-1} clearly reflects the flexibility of studied molecules and improves single molecule Raman and ROA spectra (**Figure 3.4**). Conformer averaging is especially important for interpretation of low-frequency modes (< 400 cm^{-1}) but the experimental spectra are reproduced only partially as the intermolecular interactions are not included in the 2D PES scan.

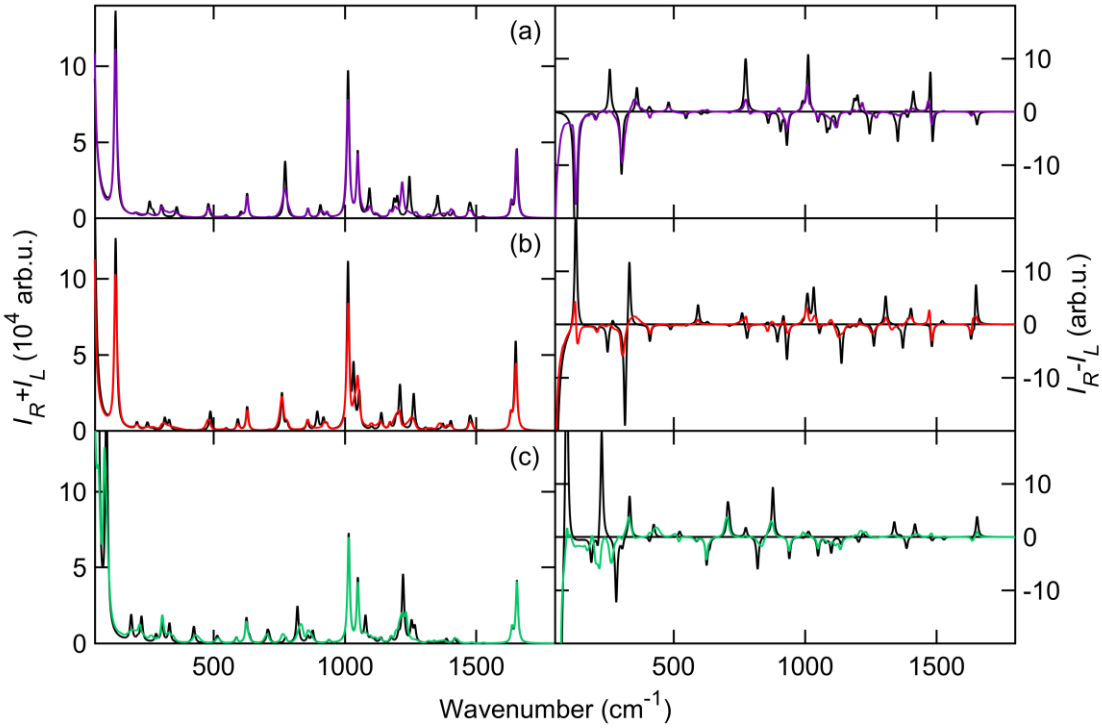

Figure 3.4: Boltzmann-averaged Raman (left) and ROA (right) spectra of (*R*)-(+)-1-phenylethanol (a), (*R*)-(+)-*α*-methylbenzylamine (b) and (*S*)-(+)-*α*-(trifluoromethyl)benzyl alcohol (c) for conformers below 2 kcal·mol^{-1} according to 2D PES scan. Black spectra represent single molecule DFT (B3PW91/6-311++G**/COSMO) calculation.

3.1.2. Conformational analysis based on the spectral similarity

One of the main applications of ROA is the structural analysis of chiral molecules in a solution. Therefore, a reliable methodology is required for the quantitative comparison of experimental and calculated spectra and subsequent determination of conformer populations. The original approach was applied to IR, Raman, VCD, and ROA spectra of amphetamine and methamphetamine hydrochloride in an aqueous solution supplemented by corresponding dimensionless quantities, dissymmetry factor (DF=VCD/IR) and normalized circular intensity difference (CID=ROA/Raman). The findings have been published in the attached publication (**Appendix C**). Conducting the PES-based conformational analysis is not within the scope of this study; however, given the flexibility of amphetamine derivatives, it presents a multidimensional challenge.

The conformational analysis of amphetamine and its derivatives is complex because of the flexibility of the alkyl chain and interactions with surrounding water molecules. Thus, different computational models, namely, conformers derived from the single molecule (SM) DFT calculations (see Subsection 2.2.1) using only the implicit solvent model (COSMO, ref. Subsection 2.2.4), MD geometries with fixed selected torsion angles and excluded solvent molecules, and partially optimized MD solute-solvent clusters (see Subsection 2.2.5) with varying numbers of water molecules, were discussed.

The results of the conformational analysis for amphetamine hydrochloride are summarized in **Table 3.1** and the corresponding VCD and ROA spectra are depicted in **Figure 3.5** for all computational models and the experiment. Determined conformational ratios are same for similarity factor defined by equation (2.82) and (2.92). Corresponding similarity values are depicted in **Table 3.1**. The accuracy of the reliable conformer determination by the similarity overlap mainly depends on the spectral range selection, the number of compared vibrational bands, the band integral intensity, and the number of conformations taking into account. Therefore, it is desirable to compare the experimental and calculated spectra in the widest possible spectral range. The IR and VCD spectra were compared in the spectral range from 1250 to 1700 cm^{-1}, while the Raman, ROA and CID spectra made it possible to compare them in a wider spectral range of 300–1750 cm^{-1}. The VCD spectral region was limited by the D_2O absorption bands. Additionally, due to uncertain and large values caused by dividing VCD signal by IR numbers close to zero, the dimensionless DF spectra were the most limited in the compared spectral range of 1300–1550 cm^{-1}, therefore the conformer populations based on the DF similarity factor cannot be trusted. However, this is not the case for ROA and CID spectra, where recording of the data in a wider spectral range is clearly beneficial (**Figure 3.6**). Although the Raman and ROA measurements were conducted within the range of 50–4500 cm^{-1}, the spectral region utilized for analysis was limited to 300–1800 cm^{-1}. The CH stretching vibrations are highly anharmonic with a relatively low ROA to Raman ratio, and a different scaling factor is needed. The region below 300 cm^{-1} is usually plagued by intermolecular vibrations (described in Subsection 3.2.1) that can bias the conformer population determination.

Table 3.1: Optimized conformer populations for (*S*)-amphetamine hydrochloride obtained from the comparison of experimental spectra and different calculation models. The population derived from the NMR study (Neville et al., 1971) is shown for reference.

Type	Spectral Range	Scaling Factor	c_1	c_2	c_3	S_1^*	$S_2^\dagger$
NMR	-	-	0.45	0.50	0.05	-	-
Single molecule geometry B3PW91/6-311++G**/COSMO							
IR	1250–1700	0.98	0.70	0.09	0.20	0.85	0.75
VCD	1250–1700	0.98	0.36	0.60	0.04	0.67	0.50
DF	1300–1550	0.98	0.24	0.55	0.22	0.87	0.77
Raman	300–1750	0.99	0.35	0.41	0.24	0.80	0.68
ROA	300–1750	0.98	0.60	0.13	0.26	0.51	0.34
CID	300–1750	0.98	0.59	0.25	0.16	0.50	0.34
Geometries from MD, water molecules excluded, B3PW91/6-311++G**/COSMO level with rDPS for Raman, ROA and CID							
IR	1250–1700	0.98	0.96	0.00	0.04	0.88	0.79
VCD	1250–1700	0.98	0.52	0.32	0.15	0.70	0.54
DF	1300–1550	0.98	0.25	0.36	0.40	0.85	0.74
Raman	300–1750	0.99	0.25	0.61	0.14	0.80	0.67
ROA	300–1750	0.98	0.58	0.25	0.17	0.49	0.33
CID	300–1750	0.99	0.42	0.33	0.25	0.59	0.42
Geometries from MD with explicit 1st solvation shell, B3PW91/6-31G**/GD3BJ/COSMO level with rDPS for Raman, ROA and CID							
IR	1250–1700	0.97	0.80	0.00	0.20	0.90	0.82
VCD	1250–1700	0.97	0.40	0.47	0.13	0.90	0.82
DF	1300–1550	0.97	0.28	0.54	0.19	0.94	0.88
Raman	300–1750	0.98	0.70	0.09	0.21	0.80	0.66
ROA	300–1750	0.97	0.43	0.41	0.16	0.78	0.64
CID	300–1750	0.97	0.42	0.46	0.12	0.69	0.52

* According to equation (2.82).

† According to equation (2.92).

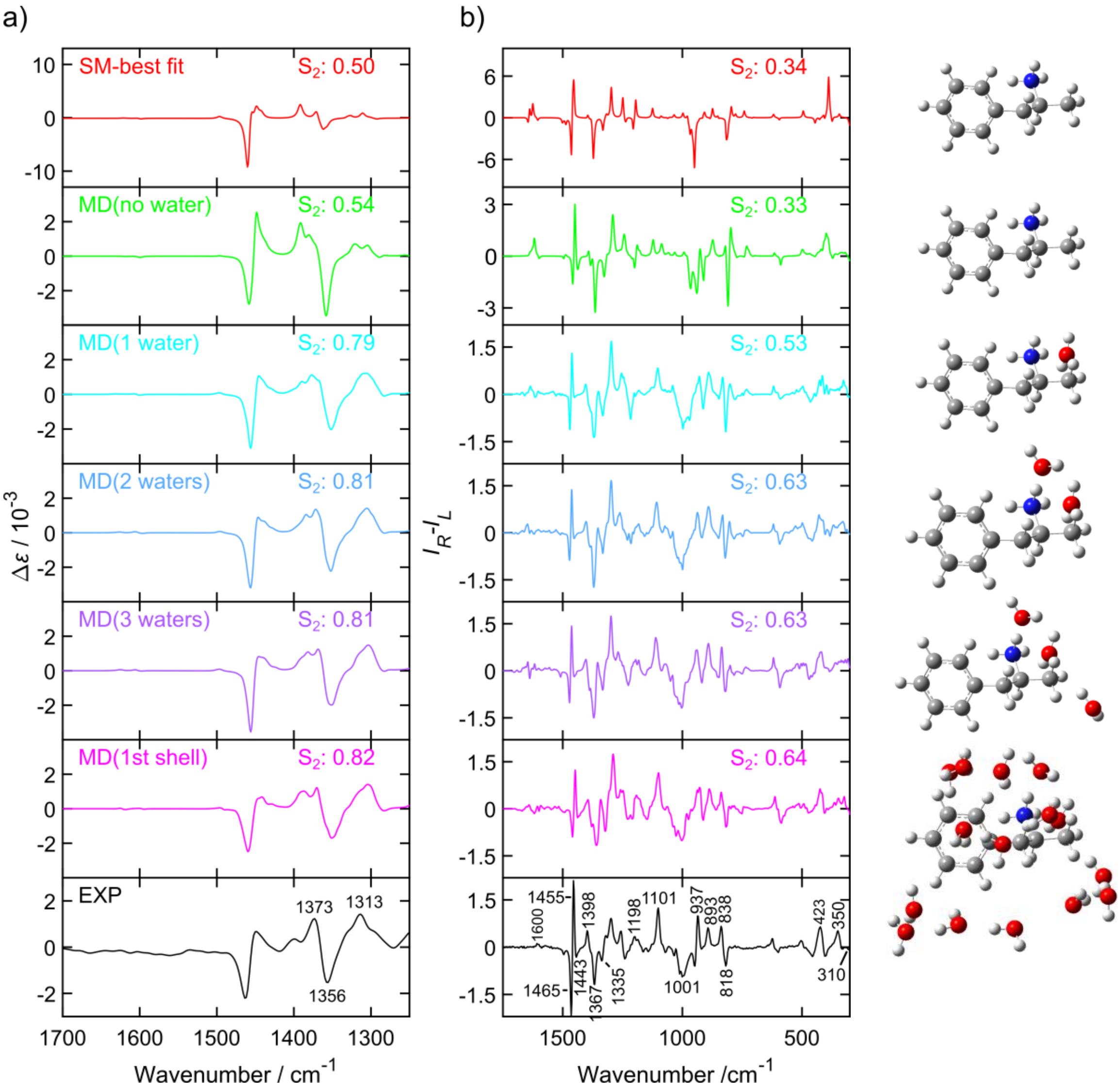

Figure 3.5: VCD (a) and ROA (b) spectra of (*S*)-amphetamine hydrochloride. Experimental spectra (black, bottom) were compared to the single molecule geometry (red), MD cluster-based models including only one (cyan), two (blue), or three (purple) closest water molecules, the cluster of the first water shell (magenta) and without explicit water molecules (green). For all MD cluster-based models 100 snapshots per conformer were averaged. The similarity factors (S_2) are given for individual spectra. Conformer populations and wavenumber scaling factors for selected models (SM, MD no water and MD 1st shell) are listed in **Table 1**. The VCD intensities are in epsilon units ($L \cdot mol^{-1} \cdot cm^{-1}$), the ROA experiment in ($e^{-} \cdot cm \cdot J^{-1} \cdot g^{-1} \cdot L$) and the ROA calculations are in arbitrary units.

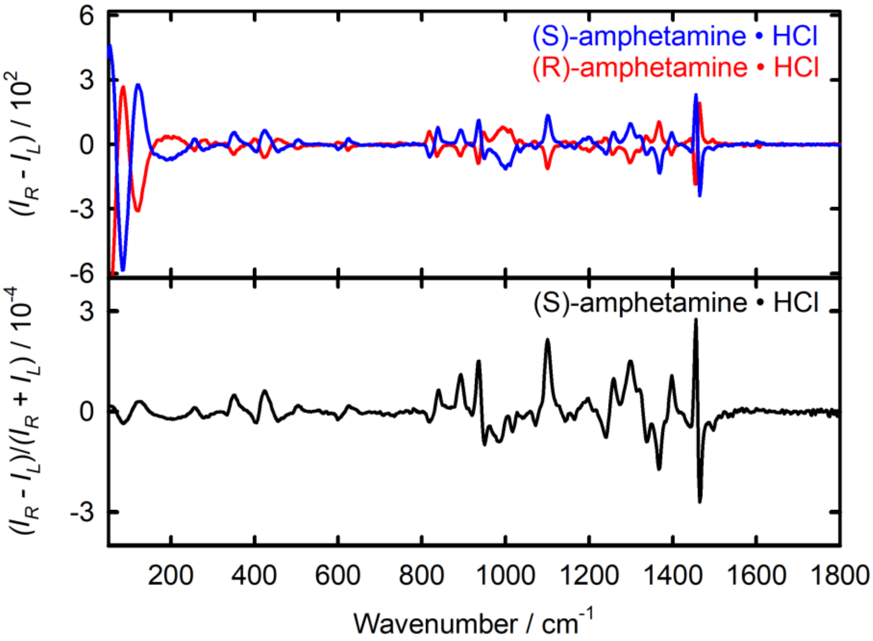

Figure 3.6: Experimental ROA (I_R–I_L) spectra of both amphetamine hydrochloride enantiomers (top), and CID ((I_R–I_L)/(I_R+I_L)) spectrum of (S)-amphetamine hydrochloride enantiomer (bottom); the intensity is in (e^- cm J^{-1}).

Overall, the similarity of IR and Raman spectra obtained with optimized populations for all different computational approaches are larger than for the corresponding chiroptical spectra (except for the DF case). However, the determined conformer populations are burdened with a large error, since the Raman and IR spectra reflect the conformations of chiral molecules only partially and the optimization algorithm tends to favor one conformer if the conformers' spectra are nearly identical.

The comparison between VCD and ROA methods is intriguing. The achieved results showed that both VCD and ROA give a significantly smaller similarity index for simpler models, and with a more advanced model of the molecular system including more realistic solvent and conformational effects, the similarity index increases substantially, and the determination of the population of states thus better converges to reliable values (the NMR values 0.45/0.50/0.05 from the previous study were taken as the reference (Neville et al., 1971)).

The simplified MD cluster models with different numbers of water molecules show that ROA is even able to distinguish the influence of different numbers of solvent molecules. The closest water molecules are mainly bound to charged NH_3^+ groups of amphetamines, see **Figure 3.7**. The most significant improvement in similarity overlap with the experiment is already achieved for the average spectra of the clusters with a single water molecule. Subsequent improvement with increasing number of water molecules in the cluster is rather minor but systematical, which can be demonstrated by the monotonously increasing similarity factor and noticeable improvements for the ROA bands around 300–500, 800, 1000, 1200 and 1600 cm^{-1} in **Figure 3.5**. On the opposite, VCD spectra of clusters with an increasing number of water molecules are almost identical.

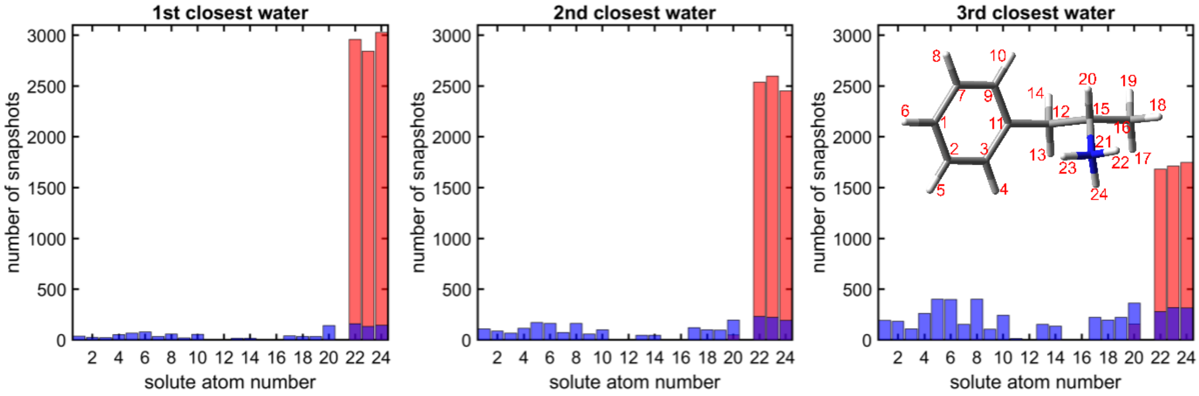

Figure 3.7: MD distribution of three water molecules to the amphetamine (100 ns MD, 10000 snapshots). The blue bars mark the interaction with H-atom, while the red bars with O-atom of H_2O molecule.

With its broad spectral range and numerous compared bands, ROA proved to be the most sensitive technique of vibrational optical activity for identifying the spatial arrangement and dominant conformation of the amphetamine and its derivatives. The amphetamine conformational ratio for the most advanced computational model determined from ROA spectra (0.43/0.41/0.16), CID spectra (0.42/0.46/0.12) and also VCD spectra (0.40/0.47/0.13) in **Table 3.1** are in good agreement with the conformational ratio 0.45/0.50/0.05 determined by NMR (Neville et al., 1971). According to the results, conformational averaging and the need for explicit solvent models are essential for the interpretation of the amphetamine vibrational spectra.

The conformational analysis of methamphetamine hydrochloride is more complex as the number of stable conformers increases due to a longer alkyl chain. Similarity overlaps for different spectroscopic methods confirm the findings discussed for amphetamine hydrochloride. Similarity overlaps with corresponding conformer populations are listed in **Table 3.2**. The methamphetamine results are discussed in the attached publication (**Appendix C**).

Table 3.2: Optimized conformer populations for (*S*)-methamphetamine hydrochloride obtained from the comparison of experimental spectra and different calculation models.

Type	Spectral Range	Scaling Factor	c_1	c_2	c_3	c_4	c_5	c_6	S_1^*	$S_2^\dagger$
Single molecule geometry B3PW91/6-311++G**/COSMO										
IR	1250–1700	0.98	0.00	0.08	0.04	0.52	0.37	0.00	0.91	0.84
VCD	1250–1700	0.98	0.00	0.33	0.00	0.39	0.04	0.23	0.50	0.34
DF	1300–1700	0.98	0.83	0.00	0.00	0.08	0.00	0.08	0.60	0.43
Raman	300–1750	0.99	0.17	0.44	0.20	0.00	0.00	0.18	0.83	0.71
ROA	300–1750	0.98	0.21	0.16	0.07	0.11	0.36	0.08	0.58	0.41
CID	300–1750	0.99	0.32	0.40	0.08	0.06	0.10	0.05	0.57	0.40
Geometries from MD, water molecules excluded, B3PW91/6-311++G**/COSMO level with rDPS for Raman, ROA and CID										
IR	1250–1700	0.98	0.07	0.36	0.00	0.58	0.00	0.00	0.90	0.82
VCD	1250–1700	0.98	0.00	0.00	0.00	0.50	0.14	0.36	0.54	0.37
DF	1300–1700	0.98	0.00	0.39	0.00	0.61	0.00	0.00	0.63	0.46
Raman	300–1750	0.99	0.00	0.76	0.18	0.00	0.00	0.07	0.84	0.72
ROA	300–1750	0.99	0.43	0.00	0.00	0.00	0.49	0.08	0.62	0.45
CID	300–1750	0.99	0.40	0.26	0.00	0.00	0.21	0.13	0.60	0.43
Geometries from MD with explicit 1st solvation shell, B3PW91/6-31G**/GD3BJ/COSMO level with rDPS for Raman, ROA and CID										
IR	1250–1700	0.97	0.06	0.38	0.00	0.00	0.00	0.56	0.97	0.95
VCD	1250–1700	0.97	0.10	0.08	0.14	0.34	0.33	0.00	0.81	0.68
DF	1300–1700	0.97	0.00	0.00	0.15	0.51	0.34	0.00	0.67	0.50
Raman	300–1750	0.98	0.11	0.49	0.00	0.00	0.00	0.40	0.80	0.66
ROA	300–1750	0.98	0.37	0.29	0.05	0.00	0.26	0.03	0.77	0.63
CID	300–1750	0.98	0.40	0.27	0.00	0.00	0.27	0.07	0.68	0.52

* According to equation (2.82).

† According to equation (2.92).

3.2. ROA in the extended spectral range

3.2.1. Low-frequency ROA

Vibrational frequencies of intermolecular modes in liquids are close to the excitation frequency. The corresponding Raman signal is rather unstructured, unresolved, and quickly increases towards the excitation line. On the other hand, ROA low-frequency spectra are more structured and better reflect the conformational changes and intermolecular interactions in the studied system. In publication **Appendix A**, an unexpectedly strong ROA signal of (*R*)-2-chloropropionitrile (nitrile) has been observed (see **Figure 3.8**) within the low-frequency region (50−150 cm^{-1}), carrying information about intermolecular interactions. On the basis of the combined MD cluster model (see Subsection 2.2.5) and DFT theory (Subsection 2.2.1), the signal was assigned to intermolecular vibrations. However, it remained unclear whether this signal had a direct connection to particular intermolecular interactions, like a molecule's capability to engage in hydrogen bonding.

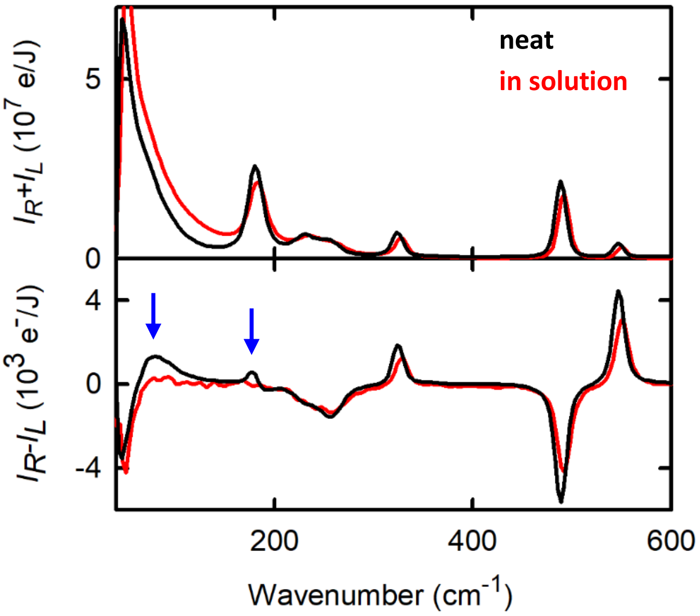

Figure 3.8: Raman and ROA spectra of (*R*)-2-chloropropionitrile in the low-frequency region for pure liquid (black) and its about 10 % solution in methanol (red). Clearly vanishing ROA bands are marked by blue arrows.

Ad hoc MD calculations of large clusters have been computationally demanding, and the simulation of the first solvation shell did not correspond to the real situation. Hence, ROA spectra of six chiral neat liquids[†] were recorded and a crystal-like computational protocol (see Subsection 2.2.8) that allowed us to analyze in detail the origin of the low-frequency modes was developed. The results are more deeply explained in the publication (**Appendix B**).

Various computational strategies used for modeling nitrile spectra are demonstrated and compared to the experiment in **Figure 3.9**. The low-frequency intermolecular signal is obviously missing in the single molecule spectra. The periodic crystal-like model is technically the most advanced one and avoids the surface cluster effects, but it comprises pair molecular interactions only. Some experimental features, such as the relatively monotonic increase in ROA intensity between 250 and 90 cm^{-1}, are therefore better reproduced with smaller clusters containing more intermolecular interactions. The large cluster model seems to give the worst results. Increasing the number of molecules in one elementary cell (i.e., size of the MD box) or including more than pairs interactions did not seem to bring improvement and is computationally demanding. A serious problem limiting the precision of the all MD computations is the large number of MD snapshots that need to be averaged for low-frequency ROA. Even 10 molecules in the box were too many for the direct calculation of a large number of snapshots needed for convergence, especially for larger molecules, such as phenylethanol or α-pinene, in the cluster. The convergence problem makes the computation expensive. Thus, the crystal-like approach is a useful alternative, providing satisfactory agreement with the experiment.

[†] (*R*)-2-chloropropionitrile (nitrile), (*R*)-(+)-propylene oxide (methyloxirane), (*R*)-(+)-1-phenylethanol (phenylethanol), (*R*)-(+)-α-methylbenzylamine (MBA), (*S*)-(+)-α-(trifluoromethyl)benzyl alcohol (TFB), and (+)(1*R*,5*R*)-α-pinene (α-pinene)

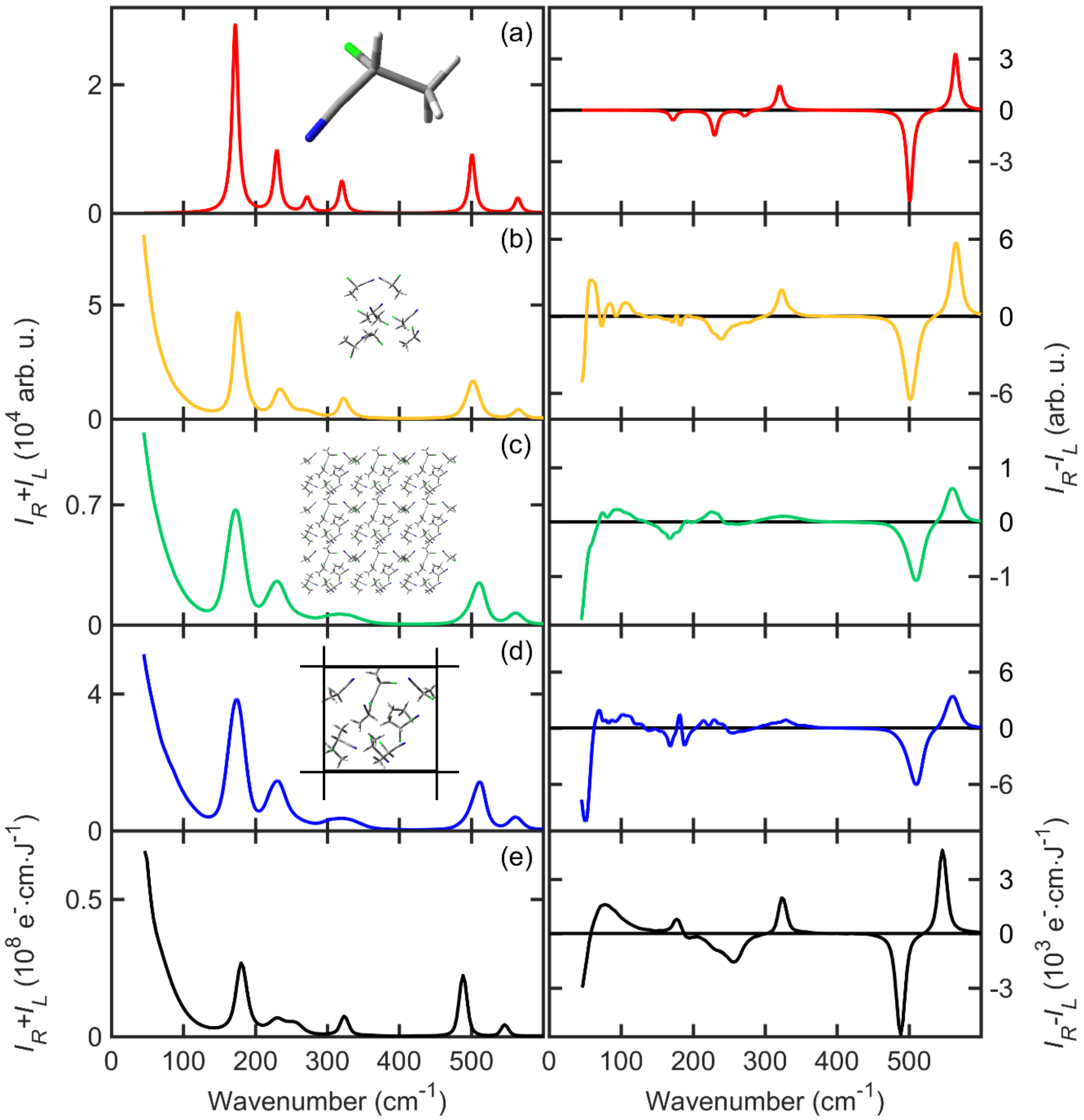

Figure 3.9: Raman and ROA nitrile spectra calculated with different models: (a) single molecule, (b) small cluster of ~ 15 nitrile molecules/all interactions, (c) large cluster/pair interactions (supercube), (d) periodic crystal/pair interactions, and (e) experimental spectrum. For b – d 200 MD snapshots were averaged.

Interestingly, neat methyloxirane gave nearly the same low-frequency ROA signal as its water solution (**Figure 3.10**). This observation was successfully reproduced by the crystal-like model and provided a phenomenological insight into the low-frequency chirality.

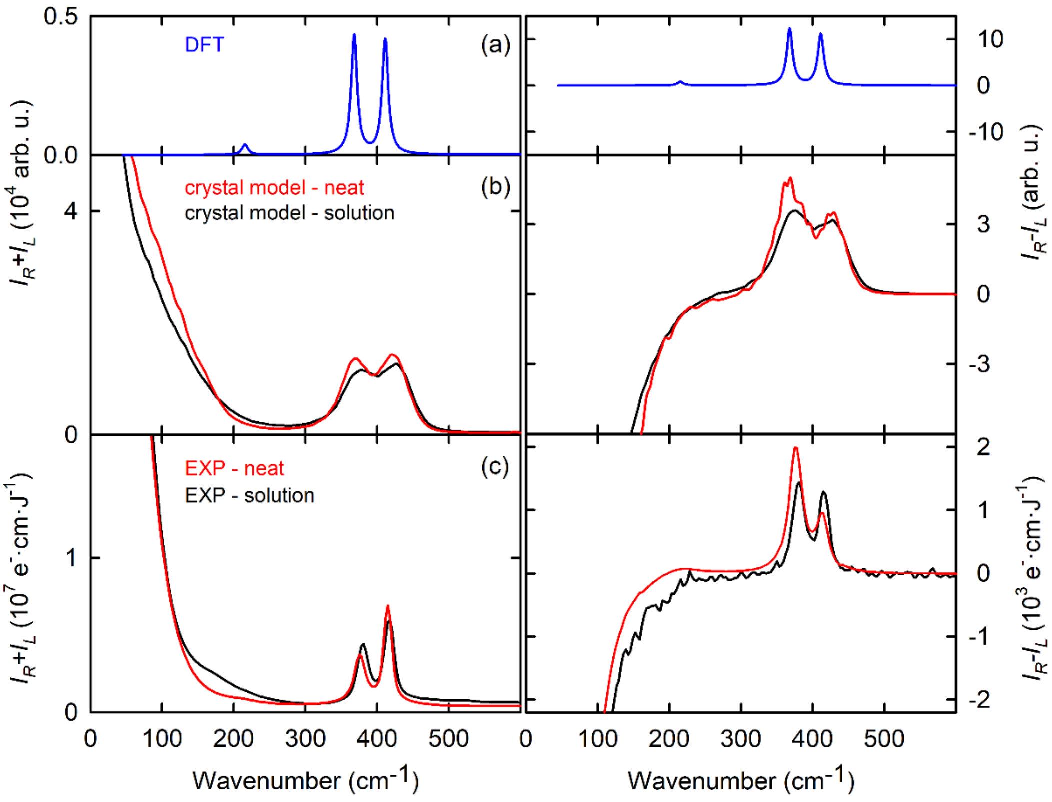

Figure 3.10: Raman and ROA spectra of neat methyloxirane and its water solution (1:22 methyloxirane:H_2O molar ratio): (a) single molecule computation, (b) crystal model, and (c) experiment.

To understand the low-frequency vibrations introducing intermolecular coordinates, or translations and rotations of one molecule, the potential energy distribution (PED) has been used. Same as for groups within one molecule, six coordinates describing the molecular positions were defined, see Subsection 2.2.9.

The low-frequency modes are not too specific; nevertheless, the PED analysis suggests that for small rigid molecules (e.g. nitrile and methyloxirane) the low-frequency signal comes primarily from translations and rotations of individual chiral molecules (**Figure 3.11d, e**). For instance, the PED analysis of the methyloxirane (**Figure 3.11a-c**) reveals that intermolecular motions formally contribute differently to the vibrational energy in methyloxirane, water, and the mixture. Obviously, a pure water band ~ 220 cm^{-1} can be predominantly assigned to the intermolecular stretching. The stretching modes of the neat methyloxirane start to contribute in the lowest frequencies only, and the contribution is smoothed out in the mixture. The contribution of bending and torsion modes is more structured, reflecting the more complicated shape of the molecule.

methyloxirane **water** **methyloxirane in water**

- intermolecular coordinates

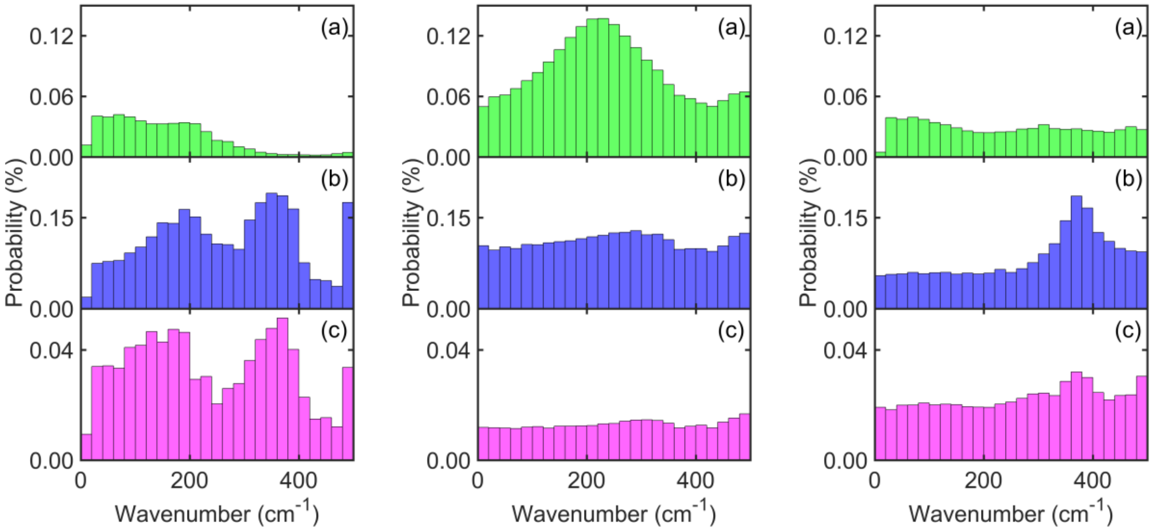

- monomolecular motions

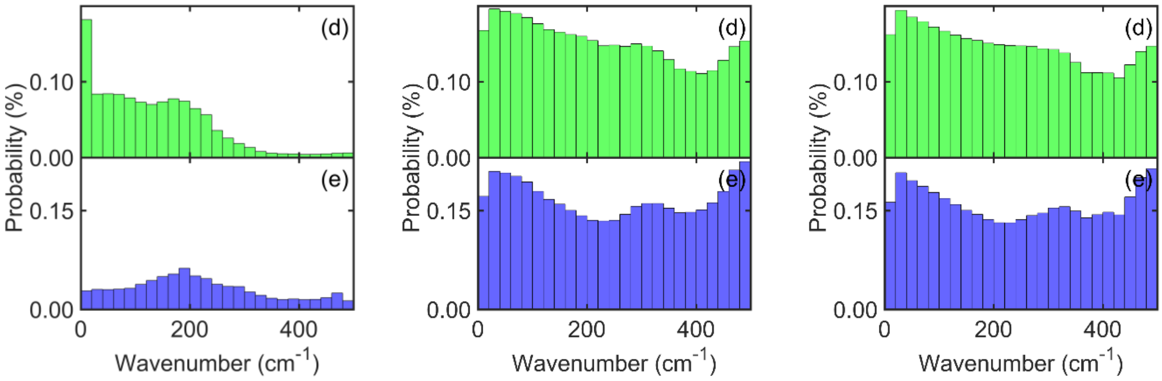

Figure 3.11: Relative vibrational potential energies of intermolecular motions related to two (stretching (a), bending (b), torsion (c)) and one (translations (d), rotations (e)) molecule, for neat methyloxirane, water and a mixture. Displayed PED values are averaged over the snapshots and normal modes in a wavenumber interval.

For more flexible molecules (phenylethanol, MBA, TFB) the intermolecular low-frequency modes are mixed with intramolecular motions, such as rotations of the phenyl, methyl, hydroxyl, trifluoromethyl and amine groups. The interpretation of the phenylethanol spectra is shown in **Figure 3.12**. Although the single molecule calculation reproduces some main features of the low-frequency region reasonably well, the crystal-like model performs better. Although the precision of used simulations is limited due to available computer power, they provide a sound theoretical basis to interpret the observed spectra and can be systematically improved in the future.

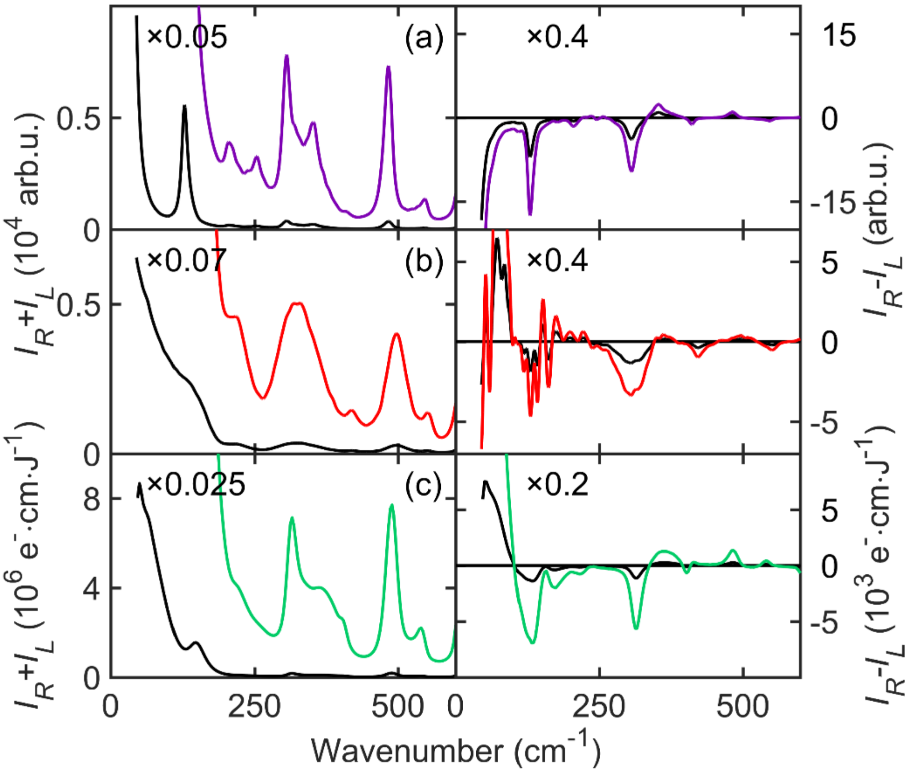

Figure 3.12: Raman and ROA spectra of (*R*)-(+)-1-phenylethanol; (a) simulation of one molecule (weighted average of 386 conformers < 2 kcal·mol^{-1}), (b) the crystal-like model, and (c) the experiment.

3.2.2. Anharmonic overtone and combination bands

The new double-grating ROA spectrometer exhibits a large signal-to-noise ratio and a flat baseline. On the other edge of the spectrum, using this instrument we thus were able to measure not only high-energy CH stretching fundamental transitions (2700–3300 cm^{-1}) but also a set of almost two orders weaker overtone and combination bands, largely ignored in previous studies. For the first time, many combination and overtone ROA bands have been observed for 2-chloropropionitrile and α-pinene, mostly within 1490–3800 cm^{-1}. Simulations of high-frequency molecular vibrational properties in general require treatment beyond the harmonic approximation (see Subsection 2.2.2). Using the 2nd order vibrational perturbation approach (VPT2), its modification (GVPT2), better treating the Fermi and Darling−Dennison resonances, and limited vibrational configuration interaction (LVCI), the most intense bands were unambiguously assigned to double-excited overtone or combination transitions. The obtained results are summarized in **Appendix A**.

For nitrile, the experimental and simulated Raman and ROA spectra within 1490−3800 cm^{-1} are displayed in **Figure 3.13**. Only the fundamental modes comprising C≡N stretching and CH stretching are plotted scaled in the gray areas. The spectral shape of the fundamentals was already reproduced by the harmonic level (B3PW91/6-311++G**/COSMO(ACN)). However, both the VPT2 and LVCI anharmonic methods significantly reduced the frequency error and provided nearly the experimental CH stretching frequencies. For the C≡N band, the error about 73 cm^{-1} remains most probably due to an inherent inaccuracy of the B3PW91 and similar functionals for molecular systems with triple bonds.

Below 3100 cm^{-1}, the VPT2 and LVCI methods provide similar Raman shapes, whereas for ROA, the VPT2 simulation looks more realistic when compared with experiment. The GVPT2 introduced only minor corrections in this case, however, for larger molecules (α-pinene, see **Appendix A**) provides a very good agreement with the experimental spectra, whereas the VPT2 failed in the entire spectral region. The VPT2 results diverge due to the higher number of resonances in the molecule. Only LVCI includes up to five times excited modes. Based on the similarity between LVCI and VPT2 simulations, we can conclude that double-excited overtones and combination transitions dominate, while the contribution of higher excitations is minor.

Based on VPT2, many combination and overtone bands can be unambiguously assigned to the experiment (see Table S2 and S3 in **Appendix A**). Moreover, the main contributions to the overtone and combination bands can be classified, see the color legend at the top of **Figure 3.13**. For example, within 1500–2220 cm^{-1}, CH_3 rocking and CC stretching seem to generate most of the spectral intensities. In wavenumber regions closer to the fundamental CH stretching bands (2600–2900 cm^{-1}), the CH bending modes, such as the CH_3 umbrella or CH_3 scissoring, dominate. Above 3000 cm^{-1}, higher-energy fundamental modes, such as C≡N stretching, contribute more. In addition, the lower-frequency fundamental motions can combine with the CH stretching modes.

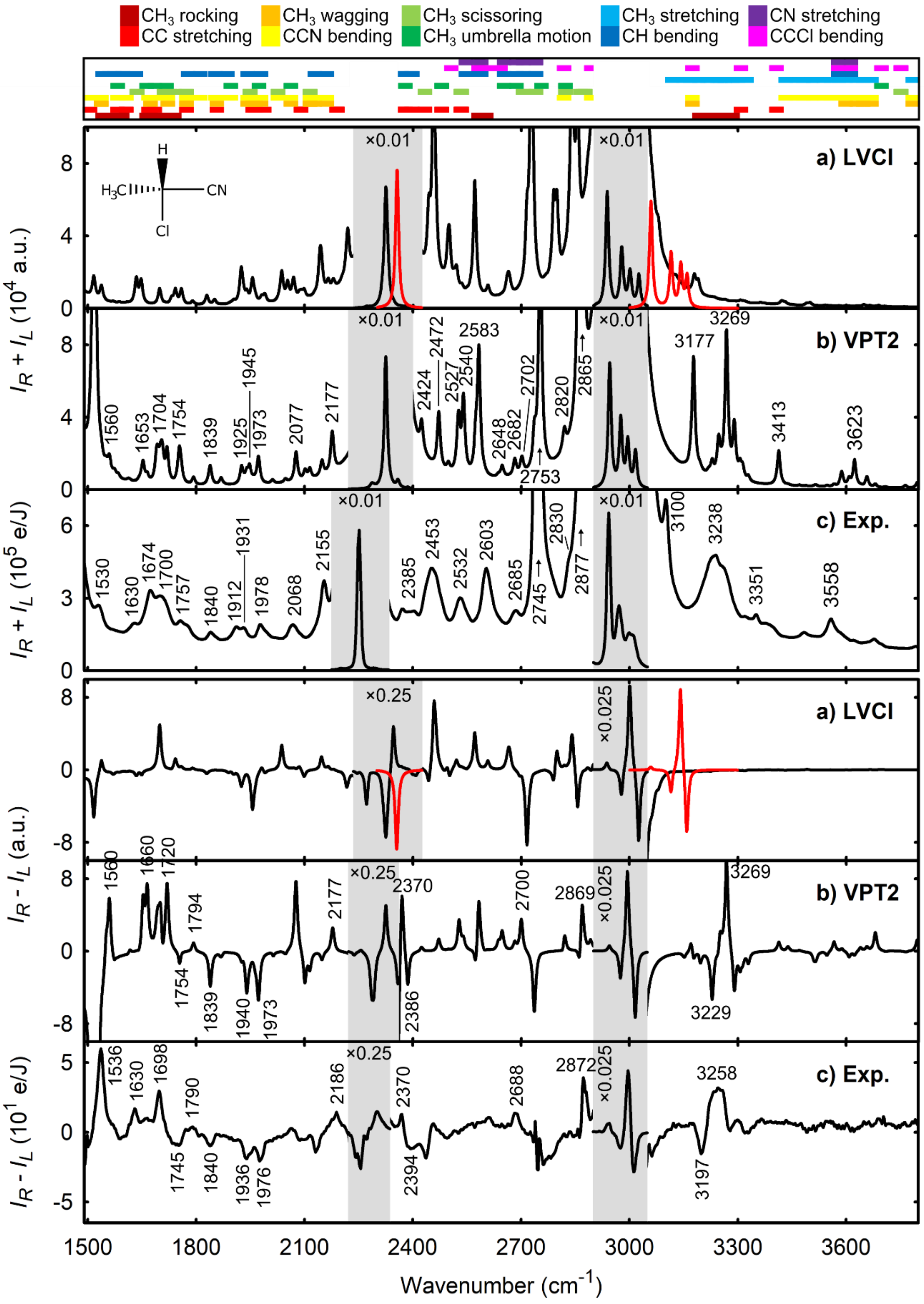

Figure 3.13: Raman and ROA spectra of (*R*)-2-chloropropionitrile, plotted within 1490–3800 cm^{-1}, as calculated using the limited vibrational configuration interaction (LVCI; a), vibrational second-order perturbation calculus (VPT2; b), and the experiment (c). The fundamental bands (scaled gray area) are compared to the harmonic approximation (red line). At the top, main coordinate contributions to the overtone and combination bands are indicated.

3.3. Enantiomeric excess determination

Another principal application of ROA spectroscopy is the measurement of optical purity of chiral samples. To date, the most commonly employed approach for determining enantiomeric excess involves chiral chromatography. However, this method is demanding from an experimental perspective and necessitates the use of specialized columns designed for different chiral substances. VOA spectroscopy in general, being a noninvasive technique, allows for the observation of a significant number of vibrational bands. This feature proves valuable in assessing enantiomeric excess (EE) while enhancing the ability to detect experimental artifacts or impurities within the sample, thereby improving the reliability of EE. The EE determination of a chiral sample is of particular importance, especially to the analytical chemistry and pharmaceutical industries. With the aim of augmenting the utility of ROA spectroscopy in the realm of chemical practice, we have proposed a new methodology for the precise assessment of EE in chiral samples.

Conventional methods of EE determination from the VOA spectra were based on band-to-band comparison or the partial least squares analysis (PLS) (Guo et al., 2004; Hecht et al., 1995). However, published methods reported a relatively limited accuracy in the range of about 1–2 %, mostly caused by a limited statistical ensemble of the experimental data, spectral range or insufficient data post-processing. Therefore, we have demonstrated a new methodology of enantiomeric excess determination described in Section 2.6. It is based on an effective algorithm that includes Raman baseline correction (see Section 2.4), ROA intensity normalization (Subsection 2.6.2), and systematic errors elimination procedure (Subsection 2.6.5) applied to experimental ROA data.

In the attached publication (**Appendix D**) the new methodology is demonstrated on nine approximately equally distributed enantiomeric mixtures of neat α-pinene and alanine in an aqueous solution. Neat α-pinene is often used as a chiroptical calibration standard. Alanine was chosen as representative of chiral sample in aqueous solution, which is difficult or nearly impossible to measure by complementary VCD technique. For both α-pinene enantiomers the manufacturer states that the optical purity exceeding 97 % and for alanine the optical purity is not declared. Analytical weights (Adam Equipment) with a 0.01 mg resolution were used for the sample preparation. In order to reduce systematic errors in the EE determination caused by weighing, a relatively large stock volumes of 0.75 mL and 0.50 mL had to be prepared for α-pinene and alanine solution, respectively. The maximal error caused by weighing was estimated approximately to 0.02 % of the EE. Only volumes of 70 μL per sample were used for the ROA measurement. Set of nine approximately equally distributed mixtures were prepared and measured for both analyzed samples.

The Raman and ROA raw data within 100–2000 cm^{-1} used for the further analysis of α-pinene and alanine EE are presented in **Figure 3.14** and **Figure 3.15**, respectively. **Figure 3.14c** and **Figure 3.15c** show the Raman spectrum after the ALSS baseline correction (see Subsection 2.4.1). The aim of this procedure was not to make the baseline as flat as possible but to unify Raman spectra in the data set before the ROA normalization. Even a relatively minor baseline corrections as were applied for α-pinene have a crucial effect on the performance of the EE determination. Clearly, the baseline correction procedure was essential for alanine measurements, as the background exhibits substantial variability across each EE mixture. **Figure 3.14d** and **Figure 3.15d** show the artifact ROA spectrum of α-pinene and alanine, respectively, determined by equations (2.106) and (2.108) in Subsection 2.6.5. Strongly polarized and also the most intense Raman bands, such as α-pinene breathing vibration 667 cm^{-1} are the most artifact prone. Their contribution to the relatively weak ROA signal is approximately 10%.

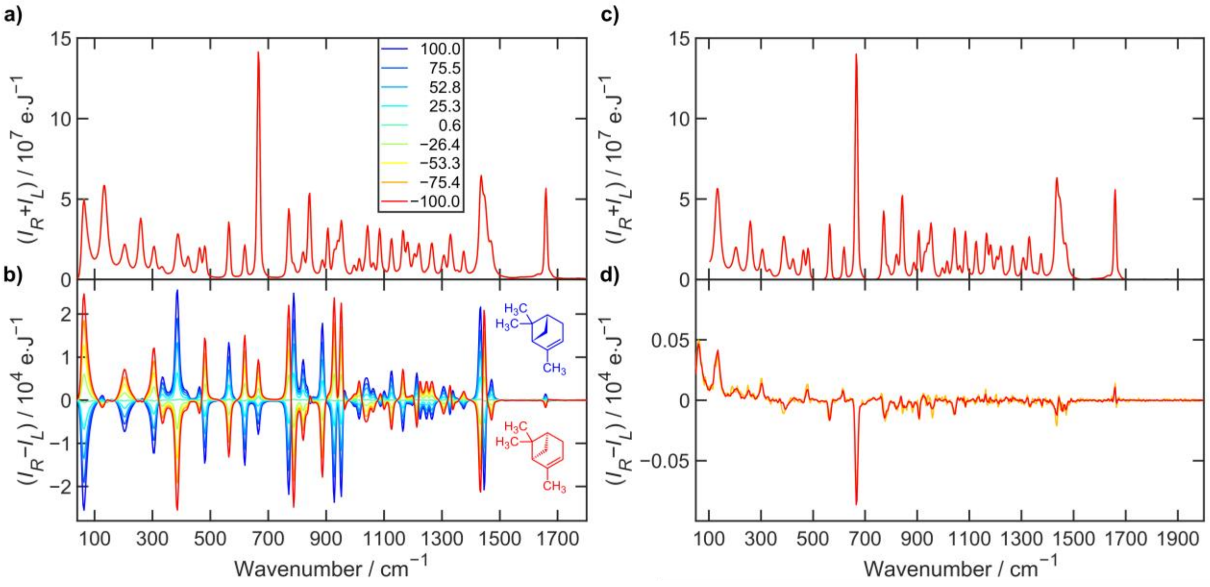

Figure 3.14: a) Raman and b) ROA spectra of neat liquid α-pinene enantiomeric mixtures after 5.5 hours of exposition time each. The legend shows EE determined from sample preparation. c) Raman spectra after baseline correction. d) ROA artifact spectrum calculated according to Eq. (2.106) is depicted in orange and according to eq. (2.108) is red. All spectra were subjected to third-order five-point Savitzky–Golay smoothing.

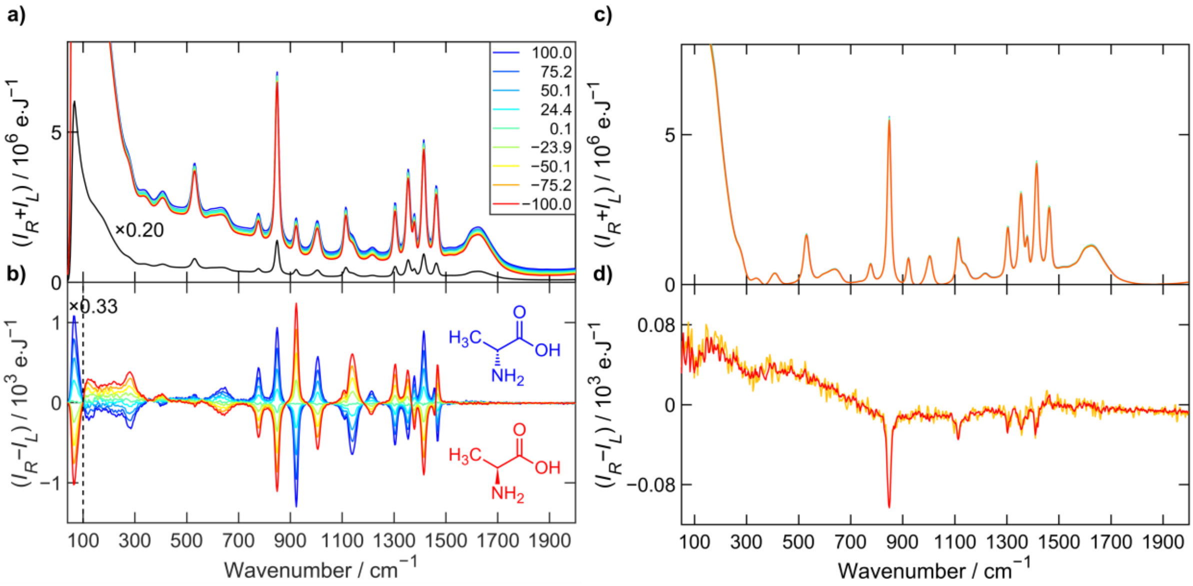

Figure 3.15: a) Raman and b) ROA spectra of alanine enantiomeric mixtures in water solution at a molar concentration ~1.2 M after 5.7 hours of exposition time each. The legend shows EE determined from sample preparation. The Raman spectrum of the reference (black) was multiplied by a factor of 0.2 in order to show strong low-wavenumber Raman scattering. c) Raman spectra after baseline correction. d) ROA artifact spectrum calculated according to Eq. (2.106) is depicted in orange and according to eq. (2.108) is red. All spectra were subjected to third-order five-point Savitzky–Golay smoothing.

The results of the EE analysis for α-pinene and alanine are summarized in **Table 3.3** and **Table 3.4**, respectively. The columns in these tables represent the spectral range selection for different steps of the EE determination routine (Raman baseline correction, ROA intensity normalization, artifact correction and EE determination). For the evaluation, last two columns show the standard deviation of the EE errors ($\sigma(\Delta_i)$) and determined EE of enantiomer B according to the reference enantiomer A ($\hat{e}_B$), calculated by equations (2.103) and (2.104). Individual EE determination errors for options in the tables are depicted in **Figure 3.16**.

The importance of introduced post-processing procedure is supported by comparison of the first and second row in the tables. The results show that, unless the baseline correction, Raman normalization and the artifacts spectra subtraction is performed, it is not possible to reduce the standard deviation of the EE errors below 0.26 % for α-pinene and approximately 1.72 % for alanine. The significant improvement in accuracy of the EE determination is mainly caused by the subtraction of calculated artifacts. Alanine in **Table 3.4** shows large deviations from −100 % of EE of reference B. Note that absolute values of EE determination for enantiomer *B* above 100 % are possible, since it is a relative value to the reference enantiomer *A*.

The spectral range selection for Raman baseline correction, ROA normalization, artifact correction and EE determination was also tested. These results confirmed that the appropriate choice of spectral range especially for baseline correction and ROA normalization can lead to a substantial reduction in EE determination errors. This is illustrated by examining option 2 and 3 in **Table 3.3** and **Table 3.4** in contrast to option 1, where a fixed spectral range was used in the whole post-processing procedure. For example, if the spectral range used for ROA normalization of α-pinene is limited around the relatively isolated C=C stretching band of 1660 cm^{-1}, the most accurate results can be achieved. However, two caveats must be noted. Due to the oxidation of the α-pinene the relative Raman band intensities change, especially the sideband 1622 cm^{-1} appears in the presence of the oxidation products in the measured sample. Despite that the region 1700 cm^{-1} and above is free of fundamental vibrations, there are numerous low-intensity anharmonic combination and overtone modes (see **Appendix A**), that make proper baseline correction not an easy task. Not overly surprisingly, the exclusion of the bands carrying the largest polarization artifacts (667 cm^{-1} for α-pinene and 848 cm^{-1} for alanine) leads to an increase in the accuracy of the EE determination. For example, limiting the EE determination of α-pinene to the 700–940 cm^{-1} range, the outstanding accuracy of 0.05 % was achieved. This can be explained by a large ROA to Raman ratio and minimal occurrence of artifacts in the selected region.

Table 3.3: Enantiomeric excess analysis results of α-pinene for different spectral ranges in each step of EE determination.

Option	**Baseline correction**		**Raman normalization**		**Artifact correction**		**EE determination**		$\sigma(\Delta_i)$ / %	$\hat{e}_B$ / %
0	-	-	-	-	-	-	100	2000	0.26	-99.95
1	100	2000	100	2000	100	2000	100	2000	0.18	-99.65
2	100	2000	1500	1800	100	2000	100	2000	0.08	-99.92
3	100	2000	1500	1800	100	2000	700	940	0.05	-100.00

Table 3.4: Enantiomeric excess analysis results of alanine for different spectral ranges in each step of EE determination.

Option	Baseline correction		Raman normalization		Artifact correction		EE determination		$\sigma(\Delta_i)$ / %	$\hat{e}_B$ / %
0	-	-	-	-	-	-	100	2000	1.72	-101.49
1	100	2000	100	2000	100	2000	100	2000	0.26	-99.87
2	100	2000	100	1500	100	2000	100	2000	0.25	-99.88
3	100	2000	100	1500	100	2000	900	1500	0.24	-99.77

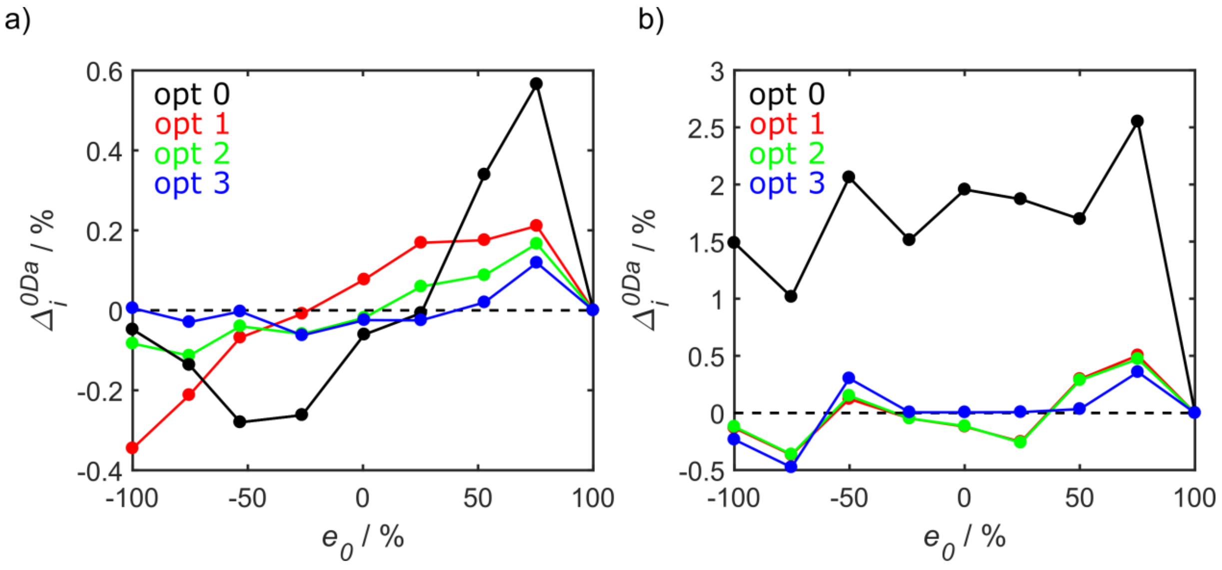

Figure 3.16: Errors of EE determination $\boldsymbol{\Delta_i}$ for a) α-pinene and b) alanine for various options in spectral range selection described in **Table 3.3** and **Table 3.4**, respectively.

We also investigated dependence of accuracy of the EE determination on the measurement time of the ROA spectra. Raman and ROA spectra were exported periodically during the experiment and the time dependence is calculated for every cumulative step. The results for different spectral range options from **Table 3.3** and **Table 3.4** are summarized in **Figure 3.17**. Since the signal-to-noise ratio increases with a square root of the exposition time, it is reasonable to fit datapoints of the standard deviation of EE determination errors by the equation

$$\sigma(t) = \sigma_\infty + \frac{\sigma_1}{\sqrt{t}}, \tag{3.1}$$

where σ_1 is the standard deviation expected for the unit exposition time t and σ_∞ is the limit of standard deviation for infinite time measurement, which can be interpreted as a residual systematic error. For α-pinene, the EE accuracy of 0.1 % was already achieved after 100 minutes of exposition time and accuracy of 0.05 % after 330 minutes of exposition time for the best choice of parameters. Alanine in an aqueous solution exhibited a comparable convergence pattern, albeit with lower precision, reaching approximately 0.22 % after 345 minutes. The diminished accuracy of alanine can be attributed to its ROA signal being ten times weaker than that of α-pinene.

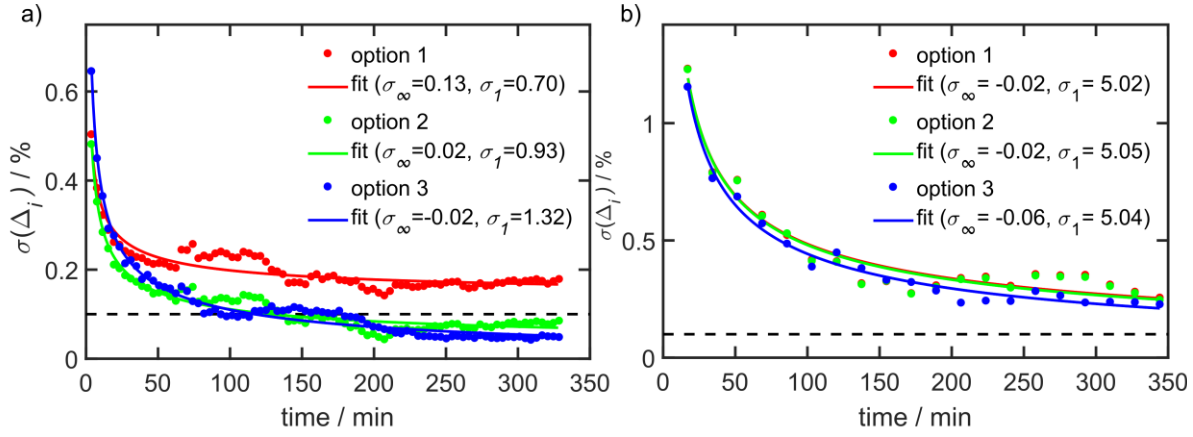

Figure 3.17: Dependence of standard deviation of the errors of EE determination $\sigma(\Delta_i)$ on the total exposition time of one mixture of α-pinene (a; 3.91 min per step) and alanine in aqueous solution (b; 17.22 min per step). Selected options point to the parameters listed in **Table 3.3** and **Table 3.4**, respectively. Data were fitted by the function in eq. (3.1).

4. Conclusions

In our work we focused on the developing of experimental methodology for Raman and Raman optical activity spectra (ROA). We also explored spectral interpretation and simulation procedures, and the information we can get from measured spectra of various chiral substances. An extended spectral range 50–4500 cm^{-1} was reached by the unique double-grating ROA spectrometer developed at the Department of Optics.

We explored the sensitivity of ROA to the geometry, absolute configuration, structure and dynamic behavior on various chiral substances. Compounds, such as 2-chloropropionitrile, methyloxirane and ethylbenzene derivatives were studied. The spectral range from 50 to 4000 cm^{-1} was measured, although not all bands could be simulated with sufficient accuracy. For 2-chloropropionitrile, a detailed dependence of the spectral parameters and potential energy on selected coordinates was discussed. Rather surprising flexibility of the C−C≡N group was observed. The distribution of conformers obtained from molecular dynamics differed from that obtained from DFT; the former one was more consistent with the spectroscopic data.

In other conformational analysis, we developed an approach maximizing the similarity overlap of weighted conformer spectra with the experiment. Then IR, Raman, VCD, and ROA spectra of amphetamine and methamphetamine hydrochlorides in aqueous solution were interpreted, using DFT and molecular dynamics simulations. Relative populations of three and six stable conformers of amphetamine and methamphetamine, respectively, were determined and found consistent with a previous NMR study. Cluster-based simulations with different number of water molecules also allowed us to track the solvation effects in ROA spectra, not much seen in VCD.

The measurement in the broader vibrational range significantly extended the information that could be obtained by optical spectroscopy from the spectra. For example, we found that intermolecular interactions contribute to ROA in the wavenumber range lower than 150 cm^{-1}. To understand origin of this low-frequency ROA signal, we developed a crystal-like computational protocol to model bulk liquids. For molecules like methyloxirane or α-pinene the signal originates predominantly in molecular translations and rotations. For more flexible and polar molecules, intramolecular motions, specific intramolecular interactions, such as hydrogen bond stretching, also contribute.

Within 1490−3800 cm^{-1} we observed for the first time a large set of overtone and combination ROA bands in the spectra of 2-chloropropionitrile and α-pinene. Using various perturbation and variational approaches, the most intense bands were assigned, mostly to double-excited overtone and combination transitions. The results were verified by comparison of Raman, IR absorption and VCD measurements. The perturbational approach as implemented in Gaussian 16 software appeared as more practical than the limited vibrational configuration method.

We proposed accurate methodology for determining the enantiomeric excess (EE) of chiral samples. The algorithm consists of the Raman baseline correction, ROA intensity normalization and systematic error elimination procedures. It was applied to nine enantiomeric mixtures of neat α-pinene and alanine in aqueous solutions. The enantiomeric excess was determined by solving an overdetermined set of linear equations. The accuracy of the EE determination was discussed with respect to the spectral range analyzed, purity of the reference, and the accumulation time of the ROA spectra. After exclusion of the strongly polarized Raman bands and with spectral range optimal for ROA normalization, accuracy of about 0.05 % and 0.22 % was achieved within reasonable accumulation times for α-pinene and alanine, respectively. ROA spectroscopy can thus serve as a non-destructive and very accurate technique for the enantiomeric excess determination. This may find applications in organic chemistry as well as in the pharmaceutical industry, where the chiral purity is often a critical factor for reactivity and biological activity.

Overall, the results indicate that the synergy of the experimental and computational Raman and ROA methodologies may be useful to understand fundamental molecular properties, with applications including analytical chemistry, biology, or medicine.

List of abbreviations

ALSS	asymmetric least squares
BFGS	Broyden-Fletcher-Goldfarb-Shanno
BJ	Becke-Johnson
CC	circular convertor
CCD	charge-coupled device
CCT	Cartesian coordinate transfer
CD	circular dichroism
CID	circular intensity difference
CIP	Cahn-Ingold-Prelog
COSMO	conductor-like screening model
CPCM	conductor-like polarizable continuum model
$\mathrm{DCP}_{\mathrm{I}}$	in-phase dual circular polarization
$\mathrm{DCP}_{\mathrm{II}}$	out-of-phase dual circular polarization
DDR	Darling−Dennison resonances
DF	dissymmetry factor
DFT	density functional theory
DOC	degree of circularity
DVPT2	deperturbed VPT2
EE	enantiomeric excess
FR	Fermi resonances
GTO	Gaussian type orbitals
GVPT2	generalized VPT2
HWP	half-wave plate
ICP	incident circular polarization
IPSA	iterative polynomial smoothing algorithm
L-BFGS	limited-memory Broyden-Fletcher-Goldfarb-Shanno
LCAO	linear combination of atomic orbitals
LCP	left circular polarization
LCR	liquid crystal retarder
LD	linear dichroism

LP	linear polarization
LR	linear rotator
LVCI	limited vibrational configuration interaction
KS	Kohn-Sham
MM	molecular mechanics
MD	molecular dynamics
OD	optical density
ONIOM	Our own N-layered Integrated molecular Orbital and molecular Mechanics
OR	optical rotation
ORD	optical rotation dispersion
PBS	polarizing beam splitter
PCM	polarizable continuum model
PES	potential energy surface
PED	potential energy distribution
QM	quantum mechanics
QWP	quarter-wave plate
ROA	Raman optical activity
RCP	right circular polarization
RLD	Raman linear dichroism
SCP	scattered circular polarization
SCRF	self-consistent reaction field
Sim	similarity factor
SM	single molecule
VCD	vibrational circular dichroism
VLD	vibrational linear dichroism
VOA	vibrational optical activity
VPT2	vibrational second-order perturbation theory

List of figures

List of tables

References

Arago, F. (1812). *Mémoire sur une modification remarquable qu'éprouvent les rayons lumineux dans leur passage à travers certains corps diaphanes et sur quelques autres nouveaux phénomènes d'optique*.

Baerends, E. J., Ellis, D. E., and Ros, P. (1973). Self-consistent molecular Hartree—Fock—Slater calculations I. The computational procedure. *Chemical Physics, 2*(1), 41-51.

Baerends, E. J., and Ros, P. (1978). Evaluation of the LCAO Hartree—Fock—Slater method: Applications to transition-metal complexes. *International Journal of Quantum Chemistry, 14*(S12), 169-190.

Barone, V. (2005). Anharmonic vibrational properties by a fully automated second-order perturbative approach. *The Journal of chemical physics, 122*(1), 014108.

Barone, V., and Cossi, M. (1998). Quantum Calculation of Molecular Energies and Energy Gradients in Solution by a Conductor Solvent Model. *The Journal of Physical Chemistry A, 102*(11), 1995-2001.

Barron, L. D. (2004). *Molecular Light Scattering and Optical Activity*. Cambridge, UK: Cambridge University Press.

Barron, L. D., Bogaard, M. P., and Buckingham, A. D. (1973a). Differential Raman scattering of right and left circularly polarized light by asymmetric molecules. *Nature, 241*(5385), 113-114.

Barron, L. D., Bogaard, M. P., and Buckingham, A. D. (1973b). Raman Scattering of Circularly Polarized Light by Optically Active Molecules. *J. Am. Chem. Soc., 95*, 603-605.

Barron, L. D., and Buckingham, A. D. (1971). Rayleigh and Raman scattering from optically active molecules. *Molecular Physics, 20*(6), 1111-1119.

Barron, L. D., Hecht, L., Gargaro, A. R., and Hug, W. (1990). Vibrational Raman optical activity in forward scattering: Trans-pinane and β-pinene. *Journal of Raman Spectroscopy, 21*(6), 375-379.

Barron, L. D., Hecht, L., Hug, W., and MacIntosh, M. J. (1989). Backscattered Raman optical activity with a CCD detector. *Journal of the American Chemical Society, 111*(23), 8731-8732.

Becke, A. D. (1988). Density-functional exchange-energy approximation with correct asymptotic behavior. *Physical review A, 38*(6), 3098.

Becke, A. D. (1993). Density-functional thermochemistry. III. The role of exact exchange. *The Journal of Chemical Physics, 98*(7), 5648–5652.

Becke, A. D., and Johnson, E. R. (2005). A density-functional model of the dispersion interaction. *The Journal of chemical physics, 123*(15), 154101.

Blöchl, P. E., Margl, P., and Schwarz, K. (1996). Ab initio molecular dynamics with the projector augmented wave method. In *Chemical Applications of Density-Functional Theory* (pp. 54-69): ACS Publications.

Bloino, J. (2015). A VPT2 Route to Near-Infrared Spectroscopy: The Role of Mechanical and Electrical Anharmonicity. *The Journal of Physical Chemistry A, 119*(21), 5269-5287.

Bloino, J., and Barone, V. (2012). A second-order perturbation theory route to vibrational averages and transition properties of molecules: General formulation and application to infrared and vibrational circular dichroism spectroscopies. *The Journal of chemical physics, 136*(12), 124108.

Bloino, J., Biczysko, M., and Barone, V. (2015). Anharmonic effects on vibrational spectra intensities: infrared, Raman, vibrational circular dichroism, and Raman optical activity. *The Journal of Physical Chemistry A, 119*(49), 11862-11874.

Bootsma, A. N., and Wheeler, S. (2019). Popular integration grids can result in large errors in DFT-computed free energies. *ChemRxiv*.

Bouř, P. (2000). Comparison of Hartree–Fock and Kohn–Sham determinants as wave functions. *Journal of Computational Chemistry, 21*(1), 8-16.

Bouř, P. (2005). Convergence Properties of the Normal Mode Optimization and its Combination with Molecular Geometry Constraints. *Collect. Czech. Chem. Commun., 70*, 1315-1340.

Bouř, P. (2006). Qgrad. Prague, Czech Republic: IOCB, Academy of Sciences.

Bouř, P. (2017). S4: Program for calculation of anharmonic molecular vibrational properties. Prague, Czech Republic: IOCB, Academy of Sciences.

Bouř, P. (2023). Specomp. Prague, Czech Republic: IOCB, Academy of Sciences.

Bouř, P., and Keiderling, T. A. (2002). Partial optimization of molecular geometry in normal coordinates and use as a tool for simulation of vibrational spectra. *J. Chem. Phys., 117*, 4126-4132.

Bouř, P., Sopková, J., Bednárová, L., Maloň, P., and Keiderling, T. A. (1997). Transfer of molecular property tensors in Cartesian coordinates: A new algorithm for simulation of vibrational spectra. *J. Comput. Chem., 18*, 646-659.

Buffeteau, T., and Pézolet, M. (2006). Linear dichroism in infrared spectroscopy. *Handbook of Vibrational Spectroscopy*.

Burke, K., Perdew, J. P., and Wang, Y. (1998). Derivation of a generalized gradient approximation: The PW91 density functional. In *Electronic density functional theory* (pp. 81-111): Springer.

Cahn, R. S., Ingold, C., and Prelog, V. (1966). Specification of molecular chirality. *Angewandte Chemie International Edition in English, 5*(4), 385-415.

Caricato, M., Ingrosso, F., Mennucci, B., and Tomasi, J. (2005). A time-dependent polarizable continuum model: Theory and application. *The Journal of chemical physics, 122*(15), 154501.

Case, D. A., Ben-Shalom, I. Y., Brozell, S. R., Cerutti, D. S., Cheatham, T. E., Cruzeiro, V. W. D., Darden, T. A., Duke, R. E., Ghoreishi, D., Gilson, M. K., Gohlke, H., Goetz, A. W., Greene, D., Harris, R., Homeyer, N., Huang, Y., Izadi, S., Kovalenko, A., Kurtzman, T., Lee, T. S., LeGrand, S., Li, P., Lin, C., Liu, J., Luchko, T., Luo, R., Mermelstein, D. J., Merz, K. M., Miao, Y., Monard, G., Nguyen, C., Nguyen, H., Omelyan, I., Onufriev, A., Pan, F., Qi, R., Roe, D. R., Roitberg, A., Sagui, C., Schott-Verdugo, S., Shen, J., Simmerling, C. L., Smith, J., SalomonFerrer, R., Swails, J., Walker, R. C., Wang, J., Wei, H., Wolf, R. M., Wu, X., Xiao, L., York, D. M., and Kollman, P. A. (2018). AMBER 18. San Francisco: University of California.

Che, D., Hecht, L., and Nafie, L. A. (1991). Dual and incident circular polarization Raman optical activity backscattering of (—)-trans-pinane. *Chemical physics letters, 180*(3), 182-190.

Cheeseman, J. R., Shaik, M. S., Popelier, P. L. A., and Blanch, E. W. (2011). Calculation of Raman optical activity spectra of methyl-β-D-glucose incorporating a full molecular dynamics simulation of hydration effects. *Journal of the American Chemical Society, 133*(13), 4991-4997.

Chung, L. W., Sameera, W. M. C., Ramozzi, R., Page, A. J., Hatanaka, M., Petrova, G. P., Harris, T. V., Li, X., Ke, Z., and Liu, F. (2015). The ONIOM method and its applications. *Chemical Reviews, 115*(12), 5678-5796.

Clark, T., Chandrasekhar, J., Spitznagel, G. W., and Schleyer, P. V. R. (1983). Efficient diffuse function-augmented basis sets for anion calculations. III. The 3-21+G basis set for first-row elements, Li–F. *Journal of Computational Chemistry, 4*(3), 294-301.

Collins, J. B., von R. Schleyer, P., Binkley, J. S., and Pople, J. A. (1976). Self-consistent molecular orbital methods. XVII. Geometries and binding energies of second-row molecules. A comparison of three basis sets. *The Journal of chemical physics, 64*(12), 5142-5151.

Cossi, M., Rega, N., Scalmani, G., and Barone, V. (2003). Energies, structures, and electronic properties of molecules in solution with the C-PCM solvation model. *Journal of Computational Chemistry, 24*(6), 669-681.

Daněček, P., and Bouř, P. (2007). Comparison of the numerical stability of methods for anharmonic calculations of vibrational molecular energies. *Journal of Computational Chemistry, 28*(10), 1617-1624.

Dapprich, S., Komáromi, I., Byun, K. S., Morokuma, K., and Frisch, M. J. (1999). A new ONIOM implementation in Gaussian98. Part I. The calculation of energies, gradients, vibrational frequencies and electric field derivatives. *Journal of Molecular Structure: THEOCHEM, 461*, 1-21.

Darling, B. T., and Dennison, D. M. (1940). The water vapor molecule. *Physical Review, 57*(2), 128.

Davidson, E. R. (1975). The iterative calculation of a few of the lowest eigenvalues and corresponding eigenvectors of large real-symmetric matrices. *Journal of Computational Physics, 17*(1), 87-94.

Delley, B. (1990). An all-electron numerical method for solving the local density functional for polyatomic molecules. *The Journal of chemical physics, 92*(1), 508-517.

Devlin, F. J., and Stephens, P. J. (1999). Conformational Analysis Using ab Initio Vibrational Spectroscopy: 3-Methylcyclohexanone. *Journal of the American Chemical Society, 121*(32), 7413-7414.

Ditchfield, R., Hehre, W. J., and Pople, J. A. (1971). Self-Consistent Molecular-Orbital Methods. IX. An Extended Gaussian-Type Basis for Molecular-Orbital Studies of Organic Molecules. *The Journal of chemical physics, 54*(2), 724-728.

Egidi, F., Carnimeo, I., and Cappelli, C. (2015). Optical rotatory dispersion of methyloxirane in aqueous solution: assessing the performance of density functional theory in combination with a fully polarizable QM/MM/PCM approach. *Optical Materials Express, 5*(1), 196-209.

Eilers, P. H. C. (2003). A perfect smoother. *Analytical chemistry, 75*(14), 3631-3636.

Eilers, P. H. C., and Boelens, H. F. M. (2005). *Baseline Correction with Asymmetric Least Squares Smoothing*. Leiden University Medical Centre report.

Fischer, E. (1909). Synthese des traubenzuckers. In *Untersuchungen Über Kohlenhydrate und Fermente (1884–1908)* (pp. 355-361): Springer.

Fresnel, A. (1824). Considérations théoriques sur la polarisation de la lumière. *Bull. Sci. Soc. Philomath., 23*, 147-158.

Frisch, M. J., Pople, J. A., and Binkley, J. S. (1984). Self‐consistent molecular orbital methods 25. Supplementary functions for Gaussian basis sets. *The Journal of chemical physics, 80*(7), 3265-3269.

Frisch, M. J., Trucks, G. W., Schlegel, H. B., Scuseria, G. E., Robb, M. A., Cheeseman, J. R., Scalmani, G., Barone, V., Petersson, G. A., Nakatsuji, H., Li, X., Caricato, M., Marenich, A. V., Bloino, J., Janesko, B. G., Gomperts, R., Mennucci, B., Hratchian, H. P., Ortiz, J. V., Izmaylov, A. F., Sonnenberg, J. L., Williams, Ding, F., Lipparini, F., Egidi, F., Goings, J., Peng, B., Petrone, A., Henderson, T., Ranasinghe, D., Zakrzewski, V. G., Gao, J., Rega, N., Zheng, G., Liang, W., Hada, M., Ehara, M., Toyota, K., Fukuda, R., Hasegawa, J., Ishida, M., Nakajima, T., Honda, Y., Kitao, O., Nakai, H., Vreven, T., Throssell, K., Montgomery Jr., J. A., Peralta, J. E., Ogliaro, F., Bearpark, M. J., Heyd, J. J., Brothers, E. N., Kudin, K. N., Staroverov, V. N., Keith, T. A., Kobayashi, R., Normand, J., Raghavachari, K., Rendell, A. P., Burant, J. C., Iyengar, S. S., Tomasi, J., Cossi, M., Millam, J. M., Klene, M., Adamo, C., Cammi, R., Ochterski, J. W., Martin, R. L., Morokuma, K., Farkas, O., Foresman, J. B., and Fox, D. J. (2016). Gaussian 16 Rev. A.03. Wallingford, CT.

Grimme, S. (2011). Density functional theory with London dispersion corrections. *Wiley Interdisciplinary Reviews: Computational Molecular Science, 1*(2), 211-228.

Grimme, S., Antony, J., Ehrlich, S., and Krieg, H. (2010). A consistent and accurate ab initio parametrization of density functional dispersion correction (DFT-D) for the 94 elements H-Pu. *J. Chem. Phys., 132*(15), 154104.

Grimme, S., Ehrlich, S., and Goerigk, L. (2011). Effect of the damping function in dispersion corrected density functional theory. *Journal of Computational Chemistry, 32*(7), 1456-1465.

Guo, C., Shah, R. D., Dukor, R. K., Cao, X., Freedman, T. B., and Nafie, L. A. (2004). Determination of Enantiomeric Excess in Samples of Chiral Molecules Using Fourier Transform Vibrational Circular Dichroism Spectroscopy: Simulation of Real-Time Reaction Monitoring. *Analytical chemistry, 76*(23), 6956-6966.

Harris, D. C., and Bertolucci, M. D. (1989). *Symmetry and spectroscopy: an introduction to vibrational and electronic spectroscopy*: Courier Corporation.

Hehre, W. J., Stewart, R. F., and Pople, J. A. (1969). self‐consistent molecular‐orbital methods. i. use of gaussian expansions of Slater‐type atomic orbitals. *The Journal of chemical physics, 51*(6), 2657-2664.

Hecht, L., Barron, L. D., Blanch, E. W., Bell, A. F., and Day, L. A. (1999). Raman optical activity instrument for studies of biopolymer structure and dynamics. *Journal of Raman spectroscopy, 30*(9), 815-825.

Hecht, L., Barron, L. D., Gargaro, A. R., Wen, Z. Q., and Hug, W. (1992). Raman optical activity instrument for biochemical studies. *Journal of Raman Spectroscopy, 23*(7), 401-411.

Hecht, L., Barron, L. D., and Hug, W. (1989). Vibrational Raman optical activity in backscattering. *Chemical physics letters, 158*(5), 341-344.

Hecht, L., Che, D., and Nafie, L. A. (1991). A new scattered circular polarization Raman optical activity instrument equipped with a charge-coupled-device detector. *Applied spectroscopy, 45*(1), 18-25.

Hecht, L., Phillips, A. L., and Barron, L. D. (1995). Determination of enantiomeric excess using Raman optical activity. *Journal of Raman spectroscopy, 26*(8-9), 727-732.

Hohenberg, P., and Kohn, W. (1964). Inhomogeneous Electron Gas. *Physical Review, 136*(3B), B864-B871.

Hopmann, K. H., Ruud, K., Pecul, M., Kudelski, A., Dracinsky, M., and Bour, P. (2011). Explicit versus implicit solvent modeling of Raman optical activity spectra. *The Journal of Physical Chemistry B, 115*(14), 4128-4137.

Hudecová, J., Hopmann, K. H., and Bouř, P. (2012). Correction of vibrational broadening in molecular dynamics clusters with the normal mode optimization method. *J. Phys. Chem. B, 116,* 336-342.

Hudecová, J., Profant, V., Novotná, P., Baumruk, V., Urbanová, M., and Bouř, P. (2013). CH Stretching Region: Computational Modeling of Vibrational Optical Activity. *J. Chem. Theory Comput., 9*, 3096−3108.

Hug, W. (1982). Instrumental and theoretical advances in Raman optical activity. *Raman Spectroscopy,* 3-12.

Hug, W. (2003). Virtual Enantiomers as the Solution of Optical Activity's Deterministic Offset Problem. *Applied spectroscopy, 57*(1), 1-13.

Hug, W., and Hangartner, G. (1999). A novel high-throughput Raman spectrometer for polarization difference measurements. *Journal of Raman spectroscopy, 30*(9), 841-852.

Hug, W., and Surbeck, H. (1979). Vibrational raman optical activity spectra recorded in perpendicular polarization. *Chemical physics letters, 60*(2), 186-192.

Johnson, E. R., and Becke, A. D. (2005). A post-Hartree–Fock model of intermolecular interactions. *The Journal of chemical physics, 123*(2), 024101.

Johnson, E. R., and Becke, A. D. (2006). A post-Hartree-Fock model of intermolecular interactions: Inclusion of higher-order corrections. *The Journal of chemical physics, 124*(17), 174104.

Jones, J. E., and Chapman, S. (1924). On the determination of molecular fields. —II. From the equation of state of a gas. *Proceedings of the Royal Society of London. Series A, Containing Papers of a Mathematical and Physical Character, 106*(738), 463-477.

Jorgensen, W. L., Chandrasekhar, J., Madura, J. D., Impey, R. W., and Klein, M. L. (1983). Comparison of simple potential functions for simulating liquid water. *The Journal of chemical physics, 79*(2), 926-935.

Jungwirth, J., Šebestík, J., Šafařík, M., Kapitán, J., and Bouř, P. (2017). Quantitative determination of Ala-Ala conformer ratios in solution by decomposition of Raman optical activity spectra. *The Journal of Physical Chemistry B, 121*(38), 8956-8964.

Kapitán, J. (2006). *Theoretical and Experimental Development of Raman Optical Activity as a Stereochemical Probe for Aqueous Environment.* (PhD. Thesis (CZ)), Charles University in Prague.

Kapitán, J., Baumruk, V., Kopecký, V., and Bouř, P. (2006). Conformational flexibility of L-alanine zwitterion determines shapes of Raman and Raman optical activity spectral bands. *The Journal of Physical Chemistry A, 110*(14), 4689-4696.

Kapitán, J., Johannessen, C., Bouř, P., Hecht, L., and Barron, L. D. (2009). Vibrational Raman Optical Activity of 1-Phenylethanol and 1-Phenylethylamine: Revisiting Old Friends. *Chirality, 21,* E4-E12.

Kendall, R. A., Dunning Jr, T. H., and Harrison, R. J. (1992). Electron affinities of the first-row atoms revisited. Systematic basis sets and wave functions. *The Journal of chemical physics, 96*(9), 6796-6806.

Klamt, A., and Schuurmann, G. (1993). COSMO: A New Approach to Dielectric Screening in Solvent with Explicit Expression for the Screening Energy and its Gradient. *J. Chem. Soc. Perkin Trans., 2,* 799-805.

Koenis, M. A. J., Xia, Y., Domingos, S. R., Visscher, L., Buma, W. J., and Nicu, V. P. (2019). Taming conformational heterogeneity in and with vibrational circular dichroism spectroscopy. *Chemical Science, 10*(33), 7680-7689.

Kohn, W., and Sham, L. J. (1965). Self-Consistent Equations Including Exchange and Correlation Effects. *Physical Review, 140*(4A), A1133-A1138.

Koch, W., and Holthausen, M. C. (2001). *A chemist's guide to density functional theory* (2 ed.). Weinheim, Germany: Wiley-VCH Verlag.

Kowalska, P., Cheeseman, J. R., Razmkhah, K., Green, B., Nafie, L. A., and Rodger, A. (2012). Experimental and theoretical polarized Raman linear difference spectroscopy of small molecules with a new alignment method using stretched polyethylene film. *Analytical chemistry, 84*(3), 1394-1401.

Kuppens, T., Langenaeker, W., Tollenaere, J. P., and Bultinck, P. (2003). Determination of the Stereochemistry of 3-Hydroxymethyl-2,3-dihydro-[1,4]dioxino[2,3-b]- pyridine by Vibrational Circular Dichroism and the Effect of DFT Integration Grids. *The Journal of Physical Chemistry A, 107*(4), 542-553.

Lee, C., Yang, W., and Parr, R. G. (1988). Development of the Colle-Salvetti correlation-energy formula into a functional of the electron density. *Physical Review B, 37*(2), 785.

Li, H., and Nafie, L. A. (2012). Simultaneous acquisition of all four forms of circular polarization Raman optical activity: results for α-pinene and lysozyme. *Journal of Raman spectroscopy, 43*(1), 89-94.

Lipparini, F., Scalmani, G., Mennucci, B., Cancès, E., Caricato, M., and Frisch, M. J. (2010). A variational formulation of the polarizable continuum model. *The Journal of chemical physics, 133*(1), 014106.

Martin, J. M. L., Lee, T. J., Taylor, P. R., and François, J. P. (1995). The anharmonic force field of ethylene, C2H4, by means of accurate ab initio calculations. *The Journal of Chemical Physics, 103*(7), 2589-2602.

Mennucci, B., and Cammi, R. (2008). *Continuum solvation models in chemical physics: from theory to applications*: John Wiley & Sons.

Michal, P. (2015). *Mueller matrix polarimetry of interface of two isotropic materials.* (Bachelor Thesis (CZ)), Palacký University Olomouc.

Mitin, A. V. (1994). Iterative methods for the calculation of a few of the lowest eigenvalues and corresponding eigenvectors of the AX= λBX equation with real symmetric matrices of large dimension. *Journal of Computational Chemistry, 15*(7), 747-751.

Møller, C., and Plesset, M. S. (1934). Note on an Approximation Treatment for Many-Electron Systems. *Physical Review, 46*(7), 618-622.

Morse, P. M. (1929). Diatomic molecules according to the wave mechanics. II. Vibrational levels. *Physical Review, 34*(1), 57.

Nafie, L. A. (2011). *Vibrational optical activity: Principles and applications* Chichester: Wiley.

Nafie, L. A., and Che, D. (1994). Theory and measurement of Raman optical activity. *Advances in Chemical Physics, Part 3: Modern Nonlinear Optics, 85*, 105-149.

Neville, G. A., Deslauriers, R., Blackburn, B. J., and Smith, I. C. (1971). Conformational studies of amphetamine and medicinally important derivatives by nuclear magnetic resonance spectroscopy. *J Med Chem, 14*(8), 717-721.

Nocedal, J., and Wright, S. J. (1999). *Numerical optimization*: Springer.

Pai, S. V., Chabalowski, C. F., and Rice, B. M. (1996). Comparative Study of Nonlocal Density Functional Theory and ab Initio Methods: The Potential Energy Surface of sym-Triazine Reactions. *The Journal of Physical Chemistry, 100*(38), 15368-15382.

Parchaňský, V., and Bouř, P. (2010). Transferability of anharmonic force fields in simulations of molecular vibrations. *The Journal of chemical physics, 133*(4), 044117.

Parr, R. G. (1980). Density functional theory of atoms and molecules. In *Horizons of quantum chemistry* (pp. 5-15): Springer.

Pearlman, D. A., Case, D. A., Caldwell, J. W., Ross, W. S., Cheatham, T. E., Debolt, S., Ferguson, D. M., Seibel, G., and Kollman, P. A. (1995). AMBER, a package of computer programs for applying molecular mechanics, normal mode analysis, molecular dynamics and free energy calculations to simulate the structural and energetic properties of molecules. *Comp. Phys. Commun., 91*, 1-41.

Perdew, J. P., Burke, K., and Wang, Y. (1996). Generalized gradient approximation for the exchange-correlation hole of a many-electron system. *Physical Review B, 54*(23), 16533-16539.

Perdew, J. P., Chevary, J. A., Vosko, S. H., Jackson, K. A., Pederson, M. R., Singh, D. J., and Fiolhais, C. (1992). Atoms, molecules, solids, and surfaces: Applications of the generalized gradient approximation for exchange and correlation. *Physical Review B, 46*(11), 6671-6687.

Perdew, J. P., Chevary, J. A., Vosko, S. H., Jackson, K. A., Pederson, M. R., Singh, D. J., and Fiolhais, C. (1993). Erratum: Atoms, molecules, solids, and surfaces: Applications of the generalized gradient approximation for exchange and correlation. *Physical Review B, 48*(7), 4978-4978.

Perdew, J. P., Ziesche, P., and Eschrig, H. (1991). Electronic structure of solids' 91. In: Akademie Verlag, Berlin.

Placzek, G. (1934). *Rayleigh-streuung und Raman-effekt* (Vol. 2): Akademische Verlagsgesellschaft.

Polavarapu, P. L. (1998). *Vibrational spectra: principles and applications with emphasis on optical activity*: Elsevier.

Polavarapu, P. L. (2016). *Chiroptical Spectroscopy: Fundamentals and Applications* (1 ed.). Boca Raton: CRC Press.

Polavarapu, P. L., Santoro, E., Covington, C. L., and Raghavan, V. (2020). Enhancement of the chiroptical response of α-amino acids via N-substitution for molecular structure determination using vibrational circular dichroism. *Chirality, 32*(5), 564-578.

Ponder, J. W. (2000). Tinker, Software Tools for Molecular Design (Version 3.8). Saint Louis: Washington University School of Medicine.

Ringholm, M., Jonsson, D., Bast, R., Gao, B., Thorvaldsen, A. J., Ekström, U., Helgaker, T., and Ruud, K. (2014). Analytic cubic and quartic force fields using density-functional theory. *The Journal of chemical physics, 140*(3), 034103.

Rizzo, R. C., and Jorgensen, W. L. (1999). OPLS All-Atom Model for Amines: Resolution of the Amine Hydration Problem. *J. Am. Chem. Soc., 121*(20), 4827-4836.

Rodger, A., Dorrington, G., and Ang, D. L. (2016). Linear dichroism as a probe of molecular structure and interactions. *Analyst, 141*(24), 6490-6498.

Roothaan, C. C. J. (1951). New developments in molecular orbital theory. *Reviews of modern physics, 23*(2), 69.

Sadlej, A. J. (1988). Medium-size polarized basis sets for high-level correlated calculations of molecular electric properties. *Collection of Czechoslovak Chemical Communications, 53*(9), 1995-2016.

Scalmani, G., and Frisch, M. J. (2010). Continuous surface charge polarizable continuum models of solvation. I. General formalism. *The Journal of chemical physics, 132*(11), 114110.

Shen, J., Zhu, C., Reiling, S., and Vaz, R. (2010). A novel computational method for comparing vibrational circular dichroism spectra. *Spectrochimica Acta Part A: Molecular and Biomolecular Spectroscopy, 76*(3), 418-422.

Schulze, G., Jirasek, A., Marcia, M., Lim, A., Turner, R. F., and Blades, M. W. (2005). Investigation of selected baseline removal techniques as candidates for automated implementation. *Applied spectroscopy, 59*(5), 545-574.

Schwabe, T., and Grimme, S. (2007). Double-hybrid density functionals with long-range dispersion corrections: higher accuracy and extended applicability. *Physical Chemistry Chemical Physics, 9*(26), 3397-3406.

Spencer, K. M., Freedman, T. B., and Nafie, L. A. (1988). Scattered circular polarization Raman optical activity. *Chemical physics letters, 149*(4), 367-374.

Te Velde, G., Bickelhaupt, F. M., Baerends, E. J., Fonseca Guerra, C., van Gisbergen, S. J. A., Snijders, J. G., and Ziegler, T. (2001). Chemistry with ADF. *Journal of Computational Chemistry, 22*(9), 931-967.

Thorvaldsen, A. J., Gao, B., Ruud, K., Fedorovsky, M., Zuber, G., and Hug, W. (2012). Efficient Calculation of ROA Tensors with Analytical Gradients and Fragmentation. *Chirality, 24*(12), 1018-1030.

Tomasi, J., Mennucci, B., and Cammi, R. (2005). Quantum mechanical continuum solvation models. *Chemical reviews, 105*(8), 2999-3094.

Vargek, M., Freedman, T. B., and Nafie, L. A. (1997). Improved backscattering dual circular polarization Raman optical activity spectrometer with enhanced performance for biomolecular applications. *Journal of Raman spectroscopy, 28*(8), 627-633.

Verlet, L. (1967). Computer "experiments" on classical fluids. I. Thermodynamical properties of Lennard-Jones molecules. *PHYSICAL REVIEW, 159*(1), 98.

Wang, J., Wolf, R. M., Caldwell, J. W., Kollman, P. A., and Case, D. A. (2004). Development and testing of a general amber force field. *Journal of Computational Chemistry, 25*(9), 1157-1174.

Wang, T., and Dai, L. (2017). Background subtraction of Raman spectra based on iterative polynomial smoothing. *Applied spectroscopy, 71*(6), 1169-1179.

Yamamoto, S., and Bouř, P. (2018). Calculation of Vibrational Spectra of Large Molecules from Their Fragments. In *Frontiers of Quantum Chemistry* (pp. 181-197): Springer.

Yamamoto, S., Li, X., Ruud, K., and Bouř, P. (2012). Transferability of various molecular property tensors in vibrational spectroscopy. *J. Chem. Theory Comput., 8*(3), 977-985.

Yang, Q., Mendolicchio, M., Barone, V., and Bloino, J. (2021). Accuracy and Reliability in the Simulation of Vibrational Spectra: A Comprehensive Benchmark of Energies and Intensities Issuing From Generalized Vibrational Perturbation Theory to Second Order (GVPT2). *Frontiers in Astronomy and Space Sciences, 8*.

Yariv, A., and Yeh, P. (1984). *Optical waves in crystals: propagation and control of laser radiation*. New York: Wiley.

Zuber, G., and Hug, W. (2004). Rarefied basis sets for the calculation of optical tensors. 1. The importance of gradients on hydrogen atoms for the Raman scattering tensor. *J. Phys. Chem. A, 108*(11), 2108-2118.

List of Author's Publications

Publications covering the presented results:

[1] Michal, P., Čelechovský, R., Dudka, M., Kapitán, J., Vůjtek, M., Berešová, M., Šebestík, J., Thangavel, K., and Bouř, P. (**2019**). Vibrational Optical Activity of Intermolecular, Overtone, and Combination Bands: 2-Chloropropionitrile and α-Pinene. *The Journal of Physical Chemistry B*, *123*(9), 2147-2156.
DOI: 10.1021/acs.jpcb.9b00403

Contribution: DFT and MD and anharmonic computations (perturbational and variational methods), conducted VCD experiments, analysis and discussion of the results, preparation of the manuscript

[2] Michal, P., Kapitán, J., Kessler, J., and Bouř, P. (**2022**). Low-frequency Raman optical activity provides insight into the structure of chiral liquids. *Physical Chemistry Chemical Physics*, *24*(33), 19722-19733.
DOI: 10.1039/d2cp02290g

Contribution: DFT and MD calculations, analysis and discussion of the results, preparation of the manuscript

[3] Michal, P., Hudecová, J., Čelechovský, R., Vůjtek, M., Dudka, M., and Kapitán, J. (**2022**). Accurate Determination of Enantiomeric Excess Using Raman Optical Activity. *Symmetry*, *14*(5), 990.
DOI: 10.3390/sym14050990

Contribution: work on the methodology, conducted ROA experiments, wrote software for the spectra processing, preparation of the manuscript

[4] Dobšíková, K., Michal, P., Spálovská, D., Kuchař, M., Paškanová, N., Jurok, R., Kapitán, J., and Setnička, V. (**2023**). Conformational analysis of amphetamine and methamphetamine: a comprehensive approach by vibrational and chiroptical spectroscopy. *Analyst*, *148*(6), 1337-1348.
DOI: 10.1039/d2an02014a

Contribution: DFT and MD calculations, work on the methodology, conducted ROA experiments, wrote software for the analysis, analysis and discussion of the results, preparation of the manuscript. K.D. and P. M. are equal contributors to this work and designated as co-first authors.

Other publications:

[5] Palivec, V., Michal, P., Kapitán, J., Martinez-Seara, H., and Bouř, P. (**2020**). Raman Optical Activity of Glucose and Sorbose in Extended Wavenumber Range. *ChemPhysChem*, *21*(12), 1272-1279.
DOI: 10.1002/cphc.202000261

Contribution: conducted ROA experiments and processed experimental data

[6] Das, M., Gangopadhyay, D., Šebestík, J., Habartová, L., Michal, P., Kapitán, J., and Bouř, P. (**2021**). Chiral detection by induced surface-enhanced Raman optical activity. *Chemical Communications*, *57*(52), 6388-6391.
DOI: 10.1039/d1cc01504d

Contribution: reproduced ROA experiments and processed experimental data

[7] Hudecová, J., Kapitán, J., Dračínský, M., Michal, P., Profant, V., and Bouř, P. (**2022**). Structure of Zinc and Nickel Histidine Complexes in Solution Revealed by Molecular Dynamics and Raman Optical Activity. *Chemistry – A European Journal*, *28*(59), e202202045.
DOI: 10.1002/chem.202202045

Contribution: utilized software for the baseline correction previously used in [3], wrote software for spectral decomposition

[8] Corujo, M. P., Michal, P., Wesson, R., Amarasinghe, D. P., Rodger, A., and Chmel, N. P. (**2022**). Reduction of Background Fluorescence from Impurities in Protein Samples for Raman Spectroscopy. *Journal of Spectroscopy*, *2022*, 1928091.
DOI: 10.1155/2022/1928091

Contribution: conducted 532 nm Raman measurements, preparation of the manuscript

[9] Wormell, P., Michal, P., Scott, A., Venkatesan, K., Mylvaganam, K., von Arx, T., Kitamura, J., Koshoubu, J., and Rodger, A. (**2023**). New Approaches to Stretched Film Sample Alignment and Data Collection for Vibrational Linear Dichroism. *ACS Omega*, *8*(40), 37490-37500.
DOI: 10.1021/acsomega.3c05774

Contribution: conducted the first measurements, preparation of the manuscript

Publications covering the presented results

Appendix A – J. Phys. Chem. B, 123 (9), 2147-2156 (2019).

THE JOURNAL OF
PHYSICAL CHEMISTRY B

Article

Cite This: J. Phys. Chem. B 2019, 123, 2147−2156

pubs.acs.org/JPCB

Vibrational Optical Activity of Intermolecular, Overtone, and Combination Bands: 2-Chloropropionitrile and α-Pinene

Pavel Michal,[*,†] Radek Čelechovský,[†] Michal Dudka,[†] Josef Kapitán,[†] Milan Vůjtek,[†]
Marie Berešová,[‡,§] Jaroslav Šebestík,[§] Karthick Thangavel,[§] and Petr Bouř[*,‡,§]

[†]Department of Optics, Palacký University Olomouc, 17. listopadu 12, 77146 Olomouc, Czech Republic
[‡]Department of Analytical Chemistry, University of Chemistry and Technology, Technická 5, 16628 Prague, Czech Republic
[§]Institute of Organic Chemistry and Biochemistry, Academy of Sciences, Flemingovo náměstí 2, 16610 Prague, Czech Republic

Supporting Information

ABSTRACT: Spectroscopy of vibrational optical activity has been established as a powerful tool to study molecular structures and interactions. In most cases, only fundamental molecular transitions are analyzed. In the present study, we analyze a broader range of vibrational frequencies (40−4000 cm^{-1}), which could be measured on a new Raman optical activity (ROA) instrument. An unexpectedly strong vibrational Raman optical activity of 2-chloropropionitrile has been observed within the low-frequency region (40−150 cm^{-1}). On the basis of combined molecular dynamics and density functional theory simulations, it could be assigned to intermolecular vibrations. A detailed analysis also revealed connection between spectral shapes and molecular structure and flexibility, such as bending of the CCN group. At the other edge of the scale, within ~1500−4000 cm^{-1}, for the first time, many combination and overtone ROA bands have been observed for 2-chloropropionitrile and α-pinene. These were also partially assigned, using quantum-chemical computations. The band assignment was confirmed by a comparison with Raman, absorption, and vibrational circular dichroism spectra. The measurement in the broader vibrational range thus significantly extends the information that can be obtained by optical spectroscopy, including intermolecular interactions of chiral molecules and liquids.

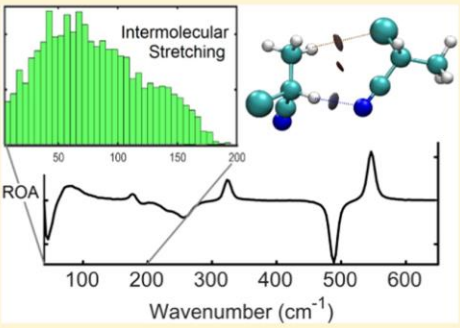

■ INTRODUCTION

Raman optical activity (ROA) is a quickly developing optical spectroscopic technique that explores differential scattering of left and right circularly polarized light by chiral molecules.[1,2] Similar to vibrational circular dichroism (VCD),[3] it can not only distinguish absolute configuration[4] but also provide higher structural sensitivity than that from techniques using unpolarized light. ROA bands carry information about conformational states[5] and system dynamics,[6] too. As one of rather few methods, ROA spectroscopy is applicable for molecules in solutions. It has been applied to a broad range of inorganic, organic, and biomolecules, including helicenes,[7,8] peptides,[9−11] proteins,[12,13] fibrils,[14,15] sugars,[16,17] nucleic acids,[18] and even to whole viruses.[19,20]

In the past, ROA spectra have been almost exclusively analyzed with a limited spectral range. For example, the commercial ROA spectrometer of Biotools operates within 200−2450 cm^{-1}. The range is broader than for common VCD spectrometers,[21] for example, but important parts of the spectra including hot, combination, and overtone bands are missing.

Further restrictions are imposed by difficult interpretation of the "nonstandard" spectral regions. For example, high-energy CH stretching modes (~3000 cm^{-1}) often exhibit resonance and other effects not included in the usual harmonic approximation.[2,22−25]

In the present study, we show that some of these obstacles can be overcome. We focus on new physical insight into properties of two model molecules, which can be obtained by measurement of the low- and high-frequency bands. Raman and ROA data were recorded on a custom-built two-grid spectrometer operating within 40−3800 cm^{-1}. The instrument exhibits a large signal-to-noise ratio and a flat baseline. This makes possible the measurement of even weak overtone and combination bands, largely ignored in previous studies. ROA spectra in the high-frequency region have been reported, but they comprised fundamental transitions (CH stretching) only.[23,24]

The first molecule, 2-chloropropionitrile, is selected as a model liquid. As noticed already before,[25] it is sufficiently small to allow for precise molecular mechanics and quantum mechanics (MM/QM) computations. Surprisingly, we observed a very large ROA signal within 40−150 cm^{-1}, carrying information about intermolecular interactions. At the high-

Received: January 14, 2019
Revised: February 12, 2019
Published: February 13, 2019

DOI: 10.1021/acs.jpcb.9b00403
J. Phys. Chem. B 2019, 123, 2147−2156

frequency part of the spectrum, ROAs of overtone and combination transitions were detected. These were also obtained for α-pinene, for which the first report indicating their presence in infrared and Raman spectra appeared already in 1976,[26] followed by a series of other works.[27,28] Both molecules serve as convenient systems for testing the accuracy of contemporary computational procedures, allowing to simulate the "anharmonic" spectral features. To verify our Raman and ROA results, VCD and IR intensities are measured and compared with the simulated ones, too.

Analysis of the spectra provides interesting insight into molecular behavior. Although there is no universal way to treat the low-frequency vibrational transitions theoretically, experience shows that the conformer distribution can be obtained using methods of classical molecular mechanics (MM) and spectral properties can be calculated quantum-mechanically (QM), which is sometimes referred to as the instantaneous normal mode[29] or frozen field[30] approximation. The "multiscale" MM/QM methodology for vibrational optical activity (VOA) has been elaborated by us and other authors in the past.[31−36] Averaging of spectra from partially optimized molecular dynamics (MD) clusters takes into consideration both molecular flexibility and solvent−solute (or solvent−solvent in our case) interactions. Dielectric solvent models, such as the polarizable continuum model (PCM)[37,38] and conductor-like screening model (COSMO),[39] are used to account for longer-range solvent effects. For 2-chloropropionitrile, this procedure provided a satisfactory basis to understand the intermolecular vibrations of the liquid.

Simulations of high-frequency molecular vibrational properties in general require treatment beyond the harmonic approximation. This is a very difficult problem, accurately solvable only for simple molecules.[40−45] Fortunately, for semirigid molecules, perturbation approaches have been developed in recent years that can be applied for larger systems as well. They quite often fairly well explain the main spectral features observed experimentally below about 4000 cm^{-1}, that is, in the range of most fundamental transitions.[46,47] Obviously, they do not always provide a band-to-band correspondence to the experiment and are not usable for higher excitations. However, for the molecules studied here, a second-order perturbation approach reproduced the most prominent anharmonic features and made it possible to link observed spectral shapes to the structure.

We find these observations also useful for future developments of vibrational optical activity (VOA) spectroscopy, in particular Raman optical activity. The wavenumber extension allows for better exploitations of the information available in the vibrational spectra. In particular, the extreme chirality observed for the lowest-frequency intermolecular modes of 2-chloropropionitrile suggests that the ROA methodology may become a useful tool to study solvent−solute and other weak interactions of chiral molecules, similar to, for example, the terahertz spectroscopy.[48]

■ METHODS

Chemicals. Both enantiomers of α-pinene were purchased from Sigma-Aldrich; (*R*)- and (*S*)-2-chloropropionitrile (Figure 1) were prepared by a modified four-step synthesis described elsewhere.[25] Briefly, L and D-alanine were converted to (*S*)- and (*R*)-2-chloropropanoic acids, respectively.[49] Then, the acids were converted to (*S*)- and (*R*)-ethyl-2-chloropropionate by azeotropic esterification, using a mixture of benzene/ethanol and a small amount of sulfuric acid. The following reaction of the ester with cooled aqueous ammonia solution led to (*S*)- or (*R*)-2-chloropropionamide.[50] Final dehydration of the amide with P_4O_{10} provided the desired (*R*/*S*)-2-chloropropionitriles. This reaction was carried out as a bulb-to-bulb distillation using a Kugelrohr apparatus at 220 °C (8 Torr), and the product was rapidly cooled down. (*S*)-2-Chloropropionitrile: overall yield 13%. ^{1}H NMR (400 MHz, DMSO-d_6) δ 5.27 (q, J = 7.0 Hz, 1H, CHCl), 1.77 (d, J = 7.0 Hz, 3H, CH_3). ^{13}C NMR (100 MHz, DMSO) δ 118.84 (CN), 38.70 (CHCl), 22.81 (CH_3). EI-HRMS (m/z): For M^+ C_3H_4NCl calcd 89.0032, found 89.0028 (−4.5 ppm). (*R*)-2-Chloropropionitrile: overall yield 13%. ^{1}H NMR (400 MHz, DMSO-d_6) δ 5.27 (q, J = 7.0 Hz, 1H, CHCl), 1.77 (d, J = 7.0 Hz, 3H, CH_3). ^{13}C NMR (100 MHz, DMSO) δ 118.83 (CN), 38.69 (CHCl), 22.81 (CH_3). EI-HRMS (m/z): for M^+ C_3H_4NCl calcd 89.0032, found 89.0031 (−1.1 ppm).

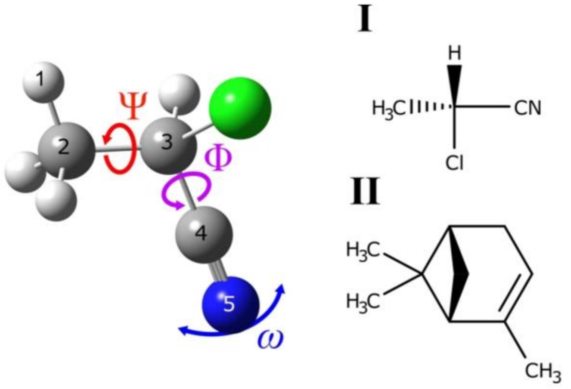

Figure 1. Studied molecules: (*R*)-2-chloropropionitrile ("nitrile", **I**) and (+)(1*R*,5*R*)-α-pinene ("α-pinene", **II**). On the left, characteristic coordinates in **I** are defined $\Psi = \angle(1,2,3,4)$, $\Phi = \angle(2,3,4,5)$, and $\omega = \angle(3,4,5)$.

Spectra Measurement. Raman and ROA spectra were acquired on an ROA instrument constructed at Palacký University, Olomouc, largely based on the design of Hug.[51,52] Neat-liquid chiral samples were measured in a rectangular fused silica cell of 70 μL volume at room temperature (298 K), using the back-scattering geometry, scattered circular polarization (SCP) modulation scheme, and Nd:YAG laser with 532 nm excitation wavelength. Laser powers and accumulation times are listed in Table S1. *R*-Enantiomer ROA spectra are presented as averages of both enantiomers, "$(R - S)/2$"; unprocessed spectra can be found in the Supporting Information (Figures S1 and S2). IR and VCD nitrile spectra were measured on a BioTools ChiralIR-2X spectrometer for neat liquid, using a BaF_2 cell, 15 μm spacer, and 4 cm^{-1} resolution. For α-pinene, the CH stretching and the rest of the anharmonic region were measured using CaF_2 cells with 6 and 50 μm spacers, respectively. Experimental Raman and ROA spectra are given as number of detected electrons per excitation energy, $e \cdot J^{-1}$, and IR and VCD are expressed in $L \cdot mol^{-1} \cdot cm^{-1}$.

Computations. Optimized geometries; harmonic frequencies; and IR, VCD, Raman, and ROA intensities were calculated at the B3PW91[53,54]/6-311++G** level, using the Gaussian 16[55] program. The environment was mimicked by the conductor-like screening model (COSMO) with parameters for acetonitrile (ACN, mimicking compound **I**) and cyclohexane (in the case of **II**).[39,56,57] Alternatively, the default Gaussian polarizable continuum model (PCM)[37] was used, which gave, however, very similar results, and is not discussed further. Presented spectra are Boltzmann-corrected to account for hot transitions in the lowest wavenumber region[58] and are given in arbitrary units (see also below, eq 5).

To understand the low-frequency vibrations of the nitrile, we calculated the dependence of its energy on the Ψ, Φ, and ω angles (see Figure 1 for their definition). The methyl group (Ψ) was rotated by 2.5° increments, within 0−120°, and 49 Φ and ω combinations were created so that the resultant nitrogen positions were evenly distributed on a sphere around C4 (ref 59, $155° < \omega < 180°$).

For liquid nitrile, molecular dynamics (MD) simulations were performed within Tinker software,[60] using the OPLSAA force field,[61] periodic boundary conditions, cubic box (16.9 Å per side), production run of 1 ns, 1 fs integration time, NVT ensemble, and temperature of 298 K. From the snapshots saved each 5 ps, 200 clusters were created, consisting of 12−19 nitrile molecules closer than 5 Å to a central one. The cluster geometries were partially optimized by the normal mode optimization procedure[62,63] as implemented in the Qgrad[64] program. In the optimization algorithm, apart from using a constant value,[36] the frequency cutoff limit was also distributed within 50−700 cm^{-1} (using a product of random and exponential functions, cf. Figure S3), which provided somewhat more realistic bandshapes. The B3PW91/6-31G*/COSMO(ACN) computational level with Grimme's dispersion correction with Becke−Johnson damping (GD3BJ)[65,66] was used for the quantum chemistry.

Modes with a significant amount of the intermolecular interactions were identified using the potential energy distribution (PED).[67] Same as for groups within one molecule,[68] six coordinates defining the molecular positions were defined (Figure 2), and PED was calculated by our Fortran programs.

Intermolecular interactions in nitrile were also inspected using the quantum topological atom-in-molecule (AIM) analysis. For 14 randomly selected dimers, noncovalent interactions were recognized as saddle points of electron density in space.[69−72]

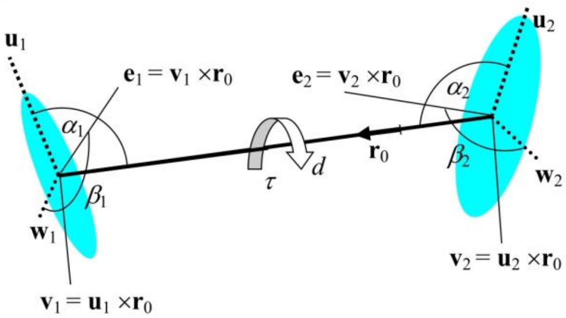

Figure 2. Definition of the six coordinates used for characterization of intermolecular vibrational modes: d, distance of the mass centers; α_1 and α_2, angles between the largest moments of inertia and the distance vector; β_1 and β_2, rotation angles; and τ, the torsion angle. For the rotation angles, arbitrary vectors $\mathbf{e}_1$ and $\mathbf{e}_1$ were defined, using the largest (direction $\mathbf{u}_i$) and second largest ($\mathbf{w}_i$) moments of inertia. Lengths of all vectors $\mathbf{u}_i$, $\mathbf{w}_i$, $\mathbf{v}_i$, $\mathbf{e}_i$, $\mathbf{r}_i$, and $\mathbf{r}_0$ are equal to 1.

Anharmonic constants (third and fourth energy derivatives, second dipole moment, and polarizability derivatives) were obtained using the Gaussian 16 and S4[73] programs at the same approximation level as for the harmonic ones. For Gaussian, two-point numerical differentiation with a step of 0.01 Å was used (steps 0.001−0.08 Å led to similar results, Figure S4). For the S4 program, a variable normal mode step was used, $q \cdot 1000 \cdot \nu^{1/2}$, where ν is the frequency in cm^{-1} and $q = 0.05$ Å.

The usual Taylor-expanded nuclear vibrational potential V was used as[46,74]

$$V(Q_1, \dots, Q_N) = \frac{1}{2}\sum_{i=1}^{N} \nu_i^2 Q_i^2 + \frac{1}{6}\sum_{i=1}^{N}\sum_{j=1}^{N}\sum_{k=1}^{N} c_{ijk} Q_i Q_j Q_k + \frac{1}{24}\sum_{i=1}^{N}\sum_{j=1}^{N}\sum_{k=1}^{N}\sum_{l=1}^{N} d_{ijkl} Q_i Q_j Q_k Q_l \tag{1}$$

where Q_i's are the normal mode coordinates, ν_i's are the harmonic frequencies, N is the number of normal modes, c_{ijk}'s are the cubic constants, and d_{ijkl}'s are the quartic constants. Quartic constants where all indices are unique were neglected.

Using the potential (eq 1), anharmonic vibrational energies and spectral intensities were calculated using the second-order vibrational perturbation approach (VPT2)[46,74] and its modification (GVPT2) better treating the Fermi and Darling−Dennison resonances[75] as implemented in Gaussian. Alternatively, limited vibrational configuration interaction (LVCI) was applied as described in refs 46 and 23 using our S4 software.

Same as for the potential, Raman and ROA polarizabilities (α, G', and A)[74] and electric dipole moment (μ) were considered as Taylor expansions

$$X(Q, P) = X(0) + \sum_{i=1}^{N} \frac{\partial X}{\partial Q_i} Q_i + \frac{1}{2}\sum_{j=1}^{N}\sum_{i=1}^{N} \frac{\partial^2 X}{\partial Q_i \partial Q_j} Q_i Q_j + \frac{1}{6}\sum_{i=1}^{N}\sum_{j=1}^{N}\sum_{k=1}^{N} \frac{\partial^3 X}{\partial Q_i \partial Q_j \partial Q_k} Q_i Q_j Q_k \tag{2}$$

where $X(0)$ is the equilibrium value of each electromagnetic tensor. For the magnetic moment m, the expansion is slightly different[47,76,77]

$$m(Q, P) = \hbar \sum_{i=1}^{N} \frac{\partial m}{\partial P_i} P_i + \hbar \sum_{j=1}^{N}\sum_{i=1}^{N} \frac{\partial^2 m}{\partial P_i \partial Q_j} P_i Q_j + \frac{\hbar}{2}\sum_{i=1}^{N}\sum_{j=1}^{N}\sum_{k=1}^{N} \frac{\partial^3 m}{\partial P_i \partial Q_j \partial Q_k} P_i Q_j Q_k \tag{3}$$

where $\hbar$ is the reduced Planck constant and P_i is the normal mode momentum associated with Q_i.

From the polarizabilities, Raman and SCP ROA intensities for each transition i were calculated as[1]

$$I_{i,\mathrm{Raman}} = 6 \sum_{\beta=1}^{3}\sum_{\alpha=1}^{3} (\alpha_{i,\alpha\alpha}\alpha_{i,\beta\beta} + 7\alpha_{i,\alpha\beta}\alpha_{i,\alpha\beta}) \tag{4a}$$

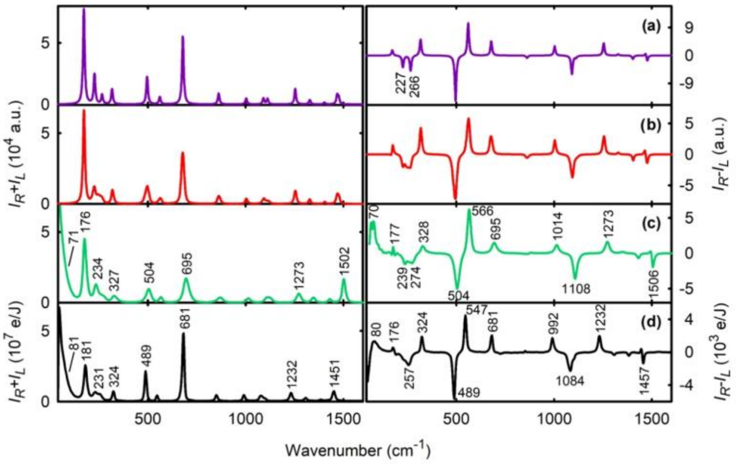

Figure 3. Raman and ROA (*R*)-2-chloropropionitrile spectra calculated for the lowest-energy conformer (a), Boltzmann average of selected density functional theory (DFT) conformers (b), and average of clusters obtained from molecular dynamics (c) and experiment (d, pure liquid).

$$I_{i,\mathrm{ROA}} = 48\sum_{\beta=1}^{3}\sum_{\alpha=1}^{3}(3\alpha_{i,\alpha\beta}G'_{i,\beta\alpha} - \alpha_{i,\alpha\alpha}G'_{i,\beta\beta} + \sum_{\varepsilon=1}^{3}\sum_{\gamma=1}^{3}\varepsilon_{\alpha\beta\gamma}\alpha_{i,\alpha\varepsilon}A_{i,\beta\gamma\varepsilon}) \tag{4b}$$

where $\alpha_i = \langle 0|\alpha|i\rangle$ (similarly for G' and A) and $|0\rangle$ and $|i\rangle$ are the ground and excited vibrational states, respectively. From these line intensities (in atomic units), theoretical spectra $S(\nu)$ dependent continuously on the frequency ν were generated using convolution with a Lorentzian function and multiplication by a Boltzmann factor

$$S(\nu) = \sum_i I_i\left[1 - \exp\left(-\frac{\nu_i}{kT}\right)\right]^{-1}\left[4\left(\frac{\nu - \nu_i}{\Delta}\right)^2 + 1\right]^{-1} \tag{5}$$

where ν_i is the transition frequency, k is the Boltzmann constant, T is the temperature, and the full width at half-maximum $\Delta = 10$ cm^{-1}. Note that the Boltzmann factor is exactly valid for the harmonic approximation only.[58] Also, if polarizability derivatives are used instead of the transition polarizabilities, as is the case of Gaussian output, a prefactor ($\frac{1}{\nu_i}$ in the harmonic limit) must be added to eq 5.

Absorption and VCD intensities were obtained from the dipole D_i and rotational strength R_i,[1] respectively

$$D_i = \sum_{\alpha=1}^{3}\langle 0|\mu_\alpha|i\rangle\langle i|\mu_\alpha|0\rangle \tag{6a}$$

$$R_i = \mathrm{Im}(\sum_{\alpha=1}^{3}\langle 0|\mu_\alpha|i\rangle\langle i|m_\alpha|0\rangle) \tag{6b}$$

as

$$\varepsilon(\nu) = \frac{435}{4\pi}\frac{2\nu}{\Delta}\sum_i D_i\left[4\left(\frac{\nu - \nu_i}{\Delta}\right)^2 + 1\right]^{-1} \tag{7a}$$

$$\Delta\varepsilon(\nu) = \frac{435}{\pi}\frac{2\nu}{\Delta}\sum_i R_i\left[4\left(\frac{\nu - \nu_i}{\Delta}\right)^2 + 1\right]^{-1} \tag{7b}$$

where $\varepsilon/\Delta\varepsilon$ are in L·mol^{-1}·cm^{-1} and D_i/R_i are in debye^2.[78]

Minor variation of computational parameters (basis sets, functionals, omission of low-energy vibrations; see Figure S5) did not lead to significantly different results.

■ RESULTS AND DISCUSSION

Low-Frequency Vibrations of (*R*)-2-Chloropropionitrile Liquid. The calculated and experimental Raman and ROA spectra are presented in Figure 3. The single-conformer computation (Figure 3a) reasonably well approximates the experimental Raman and ROA intensities within ∼175−1600 cm^{-1}. Nevertheless, within 176−324 cm^{-1}, we can see a significant improvement when the Boltzmann-averaged spectra are used (for one molecule, Figure 3b), using the scans over the Ψ, Φ, and ω angles. Detailed dependence of energy, geometry, and spectral parameters on these coordinates can also be seen in Figures S6−S10. Indeed, as follows from the mode assignment in Table S2 (fundamental) and Table S3 (combinations and overtones), these three coordinates to a large extent participate in the six lowest-frequency vibrations, calculated within ∼170−570 cm^{-1}. Thus, for example, the two negative ROA peaks calculated for the equilibrium structure at 227 and 266 cm^{-1} become broader and merge into a broad negative signal, i.e., closer to the experimental shape (Figure 3d).

The monomolecular models a−b in Figure 3, however, cannot explain the measured signal below 176 cm^{-1}. The experimental Raman intensity rises sharply as the frequency goes to zero, almost monotonically, with a shoulder at 81 cm^{-1}. The ROA intensity is even more interesting, with a maximum at 80 cm^{-1}, and at about 62 cm^{-1}, changing its sign and becoming negative up to the optical filter limit (∼40 cm^{-1}). This is to a large extent reproduced by the spectrum obtained as an average from the MD clusters (Figure 3c). This most advanced model also provides a broader and ROA-less intense "monomolecular" band at 695 cm^{-1} and minor changes in other parts of the spectra, suggesting a coupling of intermolecular and higher-frequency intramolecular vibrations.

The normal mode assignment is in agreement with the detailed analysis reported previously.[25] However, we would like to mention a rather unexpected flexibility of the C−C≡N

DOI: 10.1021/acs.jpcb.9b00403
J. Phys. Chem. B 2019, 123, 2147−2156

bond system, seen, for example, during visualization of the normal mode motion. Vibrational modes connected to the C−C≡N bending have relatively low harmonic frequencies (e.g., modes 173−561 cm^{-1}, Table S2). The equilibrium angle is calculated as $\omega \sim 179°$, but it can easily change. For example, a deviation of 16° requires energy of about 2 $\mathrm{kcal{\cdot}mol}^{-1}$. Taking into account other degrees of freedom, the most probable value at room temperature is thus predicted as 177.4° (Figure S10).

According to AIM analysis,[69−72] the nitrile−nitrile intermolecular interactions are rather nonspecific and weak, including van der Waals dispersion and weak (aliphatic) hydrogen bonds with participation of the electronegative chlorine and nitrogen atoms (Table S4, Figure S11). Still, these forces generate intermolecular vibrational modes containing different contributions of the geometrical coordinates. The assignment to intermolecular modes is also confirmed with the ROA spectra obtained for a nitrile solution in methanol, where some low-frequency bands nearly vanish (Figure S12).

According to the potential energy distribution, the intermolecular stretching vibration (d, cf. Figure 2) is the most probable for modes around 70 cm^{-1} and the bending (α_i, β_i) and torsional (τ) intermolecular motions are dominant for even lower vibrational frequencies (Figure 4). Above about 180 cm^{-1}, the intermolecular modes vanish. Interestingly, the resultant spectra can, to a large extent, be thought of as products of dimer−dimer interactions. At least in trial computations, the ensemble of dimers obtained from the MD snapshots provided Raman and ROA shapes very similar to those obtained using the complete clusters.

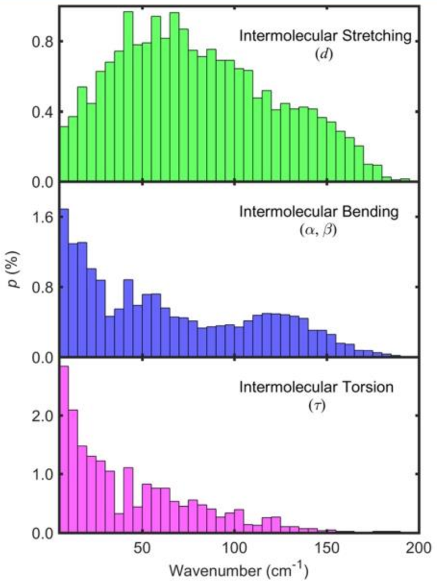

Figure 4. Relative probabilities of intermolecular coordinates (nitrile−nitrile) to the potential energy distribution, for the low-frequency modes as obtained from 200 MD clusters (a B3PW91/GD3BJ/6-31G*/COSMO(ACN) calculation).

To conclude this section, we could measure a strong nitrile Raman optical activity in the low-frequency region and showed that it is related to intermolecular interactions. These results suggest that the ROA spectroscopy may find new applications in studies of solvent−solute and other weak interactions including chiral discrimination. For α-pinene, a large monosign ROA (positive for the + enantiomer) close to 40 cm^{-1} is apparent as well. However, the intermolecular interactions are weaker and most of the relevant transitions probably lie under the instrumental limit.

Raman Optical Activity of Overtone and Combination Vibrations. On the other edge of the spectrum, the new ROA instrument makes it possible to record the CH stretching fundamental transitions, but also the weak overtone and combination bands. The ROA measurement of the fundamental CH vibrations has been achieved previously by a dedicated spectrometer[24] or a combination of three different interchangeable spectral gratings and intensity calibration using a fluorescence standard.[23,79] The ROA bands, however, were hampered by the strong underlying Raman scattering and were prone to instrumental artifacts. As far as we know, the overtones and combination bands have not been measured yet. In our spectrometer, the possibility to measure the extended range simultaneously is ensured by analysis of the zero-order diffraction beam by an additional spectrograph and detector. This arrangement also provides a good baseline stability and detection sensitivity.

For nitrile, the experimental and simulated Raman and ROA spectra within 1490−3800 cm^{-1} are plotted in Figure 5. As expected, the largest intensities are exhibited by the fundamental modes comprising C≡N stretching (experimentally at 2252 cm^{-1}) and CH stretching (about 3000 cm^{-1}). They are plotted within the gray areas in Figure 5. For this molecule, relative Raman and ROA intensities of the fundamental transitions seem to be fairly well modeled already at the harmonic level (the red curve), although with a huge frequency error of about 104 and 136 cm^{-1} for CN and CH stretching, respectively. Both the VPT2 and LVCI anharmonic methods correct it and provide nearly the experimental CH stretching frequencies. For the C≡N band, however, a significant energy error of 73 cm^{-1} remains even after the anharmonic corrections (cf. also Table S2). On the basis of benchmark computations (CCSD(T), MP4) on smaller model systems containing the triple bond, we can relate the remaining deviation to an inherent inaccuracy of the B3PW91 and similar functionals.

As discussed previously, the approximate anharmonic approaches comprise many simplifications and may themselves introduce errors comparable with the actual corrections.[46,75] For example, because the four lowest-frequency modes had to be omitted from the LVCI computation, resultant intensities above 3100 cm^{-1} are significantly underestimated. Below 3100 cm^{-1}, the VPT2 and LVCI methods provide similar Raman shapes, whereas for ROA, the VPT2 simulation looks more realistic when compared with experiment. Overall, the VPT2 procedure appears more practical than LVCI in this case. Based on VPT2, many combination and overtone bands can be unambiguously assigned (Figure 5 and Table S3). It is interesting that the technically more advanced generalized VPT2 variant (GVPT2), which includes corrections to Fermi and Darling−Dennison resonances, does not perform so well, although the differences are mostly minor (Figure S5). From the similarity of LVCI and VPT2 simulations, we can deduce that double-excited overtone and combination transitions involved in VTP2 are dominating, whereas contributions of higher excitations are much smaller. Higher excitations are

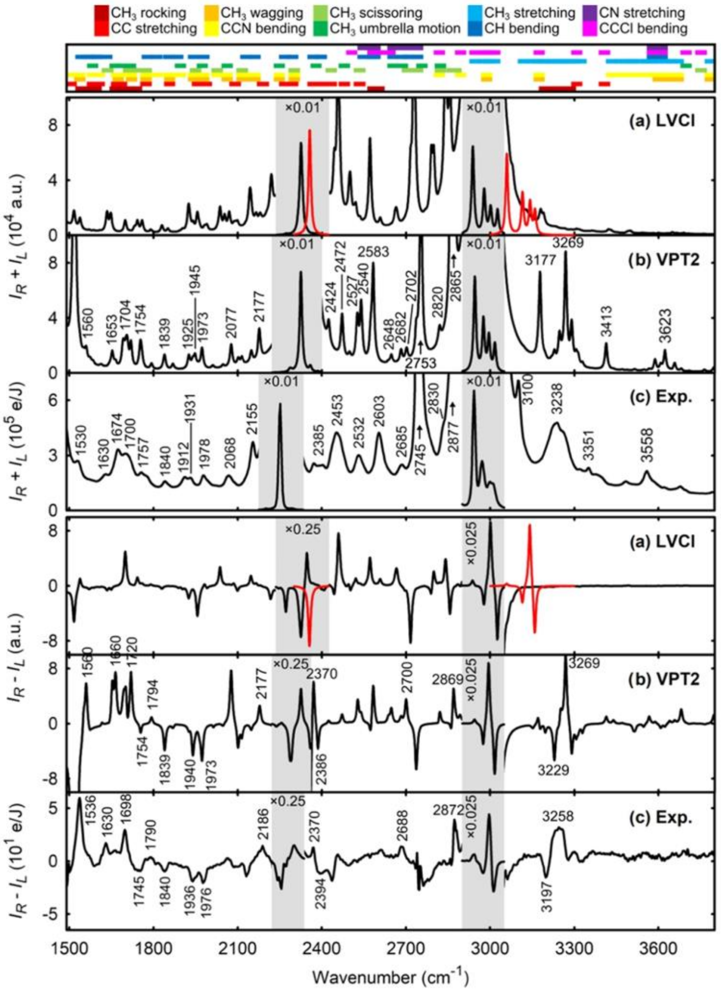

Figure 5. Raman and ROA spectra of the nitrile, plotted within 1490−3800 cm^{-1}, as calculated using the limited vibrational configuration interaction (a), vibrational second-order perturbation calculus (b), and the experiment (c). For the fundamental C≡N and CH stretching signals, spectral shapes calculated at the harmonic level are plotted by the red line. Spectral parts in the gray areas are plotted in a different scale. At the top, main coordinate contributions to the overtone and combination bands are indicated (see also Tables S2−S3).

included in the LVCI approach only, up to five times excited modes.

Same as for the fundamental modes, overtone and combination bands can also be vaguely related to chemical groups, as indicated at the very top of Figure 5. For example, within 1500−2220 cm^{-1}, CH_3 rocking and CC stretching seem to generate most of the spectral intensities. In wavenumber regions closer to the fundamental CH stretching bands (2600−2900 cm^{-1}), the CH bending modes, such as the CH_3 umbrella or CH_3 scissoring, contribute more. Below 1950 cm^{-1}, more diverse patterns take place, including CC stretching, CH_3 wagging, CCN bending, CH_3 scissoring, and CH bending. Above 3000 cm^{-1}, higher-energy fundamental modes, such as C≡N stretching, contribute more. Also, the lower-frequency fundamental motions can combine with the CH stretch.

The assignment based on the Raman and ROA bands can be confirmed by a comparison of computed and experimental IR and VCD spectra (Figure S13). The experimental VCD is somewhat hampered by the noise, in particular, above 3000 cm^{-1}. It is interesting that, contrary to the Raman and ROA bands, the C≡N stretching IR and VCD intensities (exp. 2252 cm^{-1}) are significantly overestimated by the simulations.

Analogously as for the nitrile in Figure 5, Raman and ROA spectra of α-pinene with the emphasis on the overtone and combination bands are plotted in Figure 6. Compared with the nitrile, we see several differences. As discussed previously,[23] the harmonic calculus is not adequate to reproduce the fundamental CH stretching intensity of α-pinene (~2750−3050 cm^{-1}). In addition, the bare VPT2 theory (Figure 6a) failed for the entire spectral region. This can be explained by the greater number of resonances in the molecule, which causes a divergence of the VPT2 results. Also, the LVCI method (Figure S14) did not reproduce the anharmonic region well, in spite of the extensive computational time required. Fortunately, the general GVPT2 approach (Figure 6b) gives a very good agreement with the experimental Raman and ROA spectra. Within 1800−2800 cm^{-1}, for example, the GVPT2 simulation sometimes almost amazingly faithfully reproduces the complicated ROA experimental pattern. The VOA spectroscopy combined with the theory can thus well

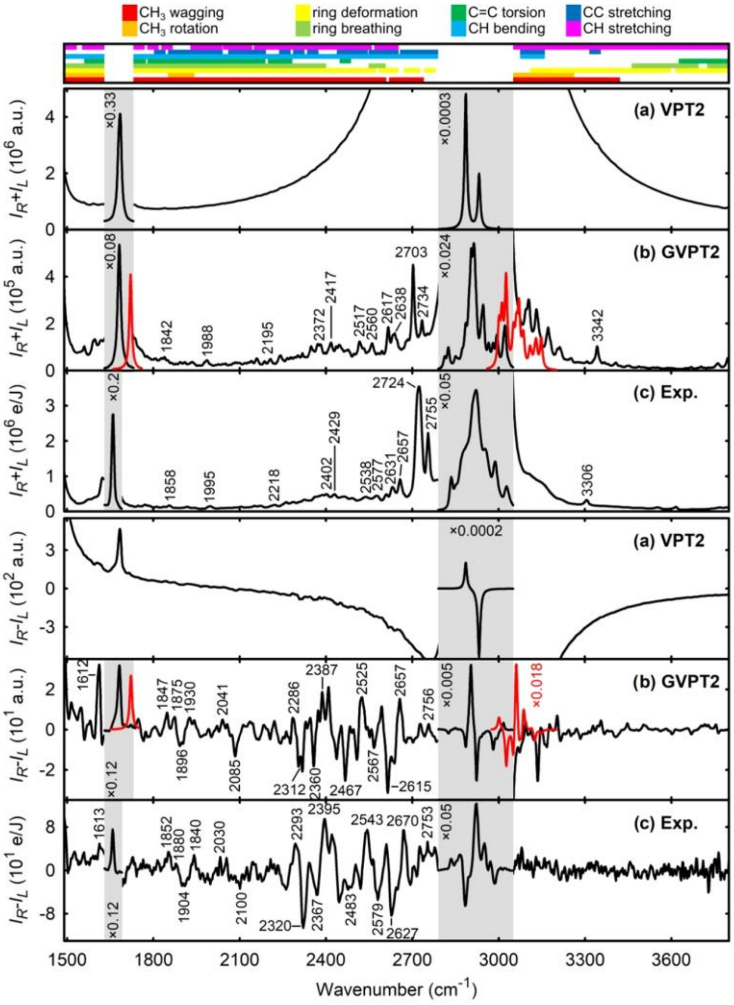

Figure 6. (+)-α-Pinene Raman and ROA spectra within 1490−3800 cm^{-1} calculated using vibrational second-order perturbation without (a) and with (b) the degeneracy correction and experiment (c). The signal of the fundamental C═C and CH stretching bands calculated at the harmonic level is plotted by the red line. At the top, main coordinate contributions to the overtone and combination bands are indicated (for vibrational normal mode assignment, see also refs 26 and 82).

complement, for example, the overtone and combination vibrational band assignments based on the isotope editing[27] or vibrational sum frequency generation studies.[80,81]

Still, inconsistencies between the simulation and experiment are apparent even for GVPT2. Relative ROA intensities of fundamental CH stretching bands are not much improved when compared with the harmonic approximation, while they grew about 3 times (cf. the multiplication factors in Figure 6). Such intensity over-estimation was not observed for LVCI (Figure S14) and can be attributed to the arbitrary wave function normalization utilized in GVPT2. The theoretical and experimental IR and VCD spectra (Figure S15) confirm that the assignment and performance of the theoretical methods are same as for the Raman and ROA data.

■ CONCLUSIONS

On the two model molecules, we analyzed Raman and ROA spectra obtained within the extended wavenumber range of 40−3800 cm^{-1}. The measurement was made possible by using a new spectrometer based on two detection channels. For the low-frequency region (40−150 cm^{-1}), we observed a strong optical activity of 2-chloropropionitrile that could be assigned to intermolecular vibrations. This rather surprising result suggests that the ROA spectroscopy can provide valuable information on interactions of chiral molecules and documents the convenience of chiral spectroscopy against unpolarized techniques. The underlying Raman signal was much less structured. To decipher the signal, relatively complex molecular mechanics/quantum mechanics computations were necessary, which, however, are possible with contemporary computational techniques and programs.

For the first time, we could also observe a large set of overtone and combination ROA bands in the nitrile and α-pinene spectra, mostly within 1490−3800 cm^{-1}. The experimental Raman and ROA intensities could be compared with experimental IR and VCD intensities. On the basis of the simulated spectra obtained by various perturbation and variational approaches, most intense bands could be

DOI: 10.1021/acs.jpcb.9b00403
J. Phys. Chem. B 2019, 123, 2147−2156

unambiguously assigned to double-excited overtone or double-excited combination transitions.

We thus hope that the presented results will stimulate further development of the ROA and VCD spectroscopies as incisive probes of molecular structure and behavior.

■ ASSOCIATED CONTENT

Supporting Information

The Supporting Information is available free of charge on the ACS Publications website at DOI: 10.1021/acs.jpcb.9b00403.

> Computational details and tests and complementary experimental data including unprocessed nitrile and α-pinene vibrational spectra; dependence of the anharmonic force constants on differentiation step; nitrile Raman and ROA spectra calculated with various harmonic methods; energy and frequency shifts as a function of Ψ and ω; IR and VCD spectra of nitrile and α-pinene, LVCI Raman and ROA spectra of α-pinene, and AIM topological parameters of interacting atoms (PDF)

■ AUTHOR INFORMATION

Corresponding Authors

*E-mail: michal@optics.upol.cz (P.M.).

*E-mail: bour@uochb.cas.cz (P.B.).

ORCID

Pavel Michal: 0000-0002-7648-6006

Josef Kapitán: 0000-0002-1916-9186

Jaroslav Šebestík: 0000-0002-0614-2064

Petr Bouř: 0000-0001-8469-1686

Notes

The authors declare no competing financial interest.

■ ACKNOWLEDGMENTS

The work was supported by the Czech Grant Agency (17-00121S, 18-05770S), Ministry of Education (LTC17012), and computational grants of CESNET (LM2015042) and the CERIT-SC (LM2015085).

■ REFERENCES

(1) Nafie, L. A. *Vibrational Optical Activity: Principles and Applications*; Wiley, 2011.

(2) Polavarapu, P. L. *Chiroptical Spectroscopy: Fundamentals and Applications*; Taylor & Francis, 2016.

(3) Barron, L. D. *Molecular Light Scattering and Optical Activity*, 2nd ed.; Cambridge University Press: Cambridge, 2004.

(4) Haesler, J.; Schindelholz, I.; Riguet, E.; Bochet, C. G.; Hug, W. Absolute Configuration of Chirally Deuterated Neopentane. *Nature* **2007**, *446*, 526−529.

(5) Kessler, J.; Andrushchenko, V.; Kapitán, J.; Bouř, P. Insight into Vibrational Circular Dichroism of Proteins by Density Functional Modeling. *Phys. Chem. Chem. Phys.* **2018**, *20*, 4926−4935.

(6) Kapitán, J.; Baumruk, V.; Kopecký, V., Jr.; Bouř, P. Conformational Flexibility of L-Alanine Zwitterion Determines Shapes of Raman and Raman Optical Activity Spectral Bands. *J. Phys. Chem. A* **2006**, *110*, 4689−4696.

(7) Johannessen, C.; Blanch, E. W.; Villani, C.; Abbate, S.; Longhi, G.; Agarwal, N. R.; Tommasini, M.; Lightner, D. A. Raman and ROA Spectra of (−)- and (+)-2-Br-Hexahelicene: Experimental and DFT Studies of a π-Conjugated Chiral System. *J. Phys. Chem. B* **2013**, *117*, 2221−2230.

(8) Shen, C.; Srebro-Hooper, M.; Weymuth, T.; Krausbeck, F.; Navarrete, J. T. L.; Ramírez, F. J.; Nieto-Ortega, B.; Casado, J.; Reiher, M.; Autschbach, J.; et al. Redox-Active Chiroptical Switching in Mono- and Bis-Iron Ethynylcarbo[6]Helicenes Studied by Electronic and Vibrational Circular Dichroism and Resonance Raman Optical Activity. *Chem. - Eur. J.* **2018**, *24*, 15067−15079.

(9) Zhu, F.; Isaacs, N. W.; Hecht, L.; Barron, L. D. Polypeptide and Carbohydrate Structure of an Intact Glycoprotein from Raman Optical Activity. *J. Am. Chem. Soc.* **2005**, *127*, 6142−6143.

(10) Kapitán, J.; Baumruk, V.; Bouř, P. Demonstration of the Ring Conformation in Polyproline by the Raman Optical Activity. *J. Am. Chem. Soc.* **2006**, *128*, 2438−2443.

(11) Mensch, C.; Barron, L. D.; Johannessen, C. Ramachandran Mapping of Peptide Conformation Using a Large Database of Computed Raman and Raman Optical Activity Spectra. *Phys. Chem. Chem. Phys.* **2016**, *18*, 31757−31768.

(12) Barron, L. D.; Blanch, E. W.; Hecht, L. Unfolded Proteins Studied by Raman Optical Activity. In *Advances in Protein Chemistry*; Academic Press, 2002; Vol. *62*, pp 51−90.

(13) Syme, C. D.; Blanch Ewan, W.; Holt, C.; Jakes, R.; Goedert, M.; Hecht, L.; Barron Laurence, D. A Raman Optical Activity Study of Rheomorphism in Caseins, Synucleins and Tau. *Eur. J. Biochem.* **2002**, *269*, 148−156.

(14) Kessler, J.; Keiderling, T. A.; Bouř, P. Arrangement of Fibril Side Chains Studied by Molecular Dynamics and Simulated Infrared and Vibrational Circular Dichroism Spectra. *J. Phys. Chem. B* **2014**, *118*, 6937−6945.

(15) Kessler, J.; Yamamoto, S.; Bouř, P. Establishing the Link between Fibril Formation and Raman Optical Activity Spectra of Insulin. *Phys. Chem. Chem. Phys.* **2017**, *19*, 13614−13621.

(16) Šugar, J.; Bouř, P. Quantitative Analysis of Sugar Composition in Honey Using 532-nm Excitation Raman and Raman Optical Activity Spectra. *J. Raman Spectrosc.* **2016**, *47*, 1298−1303.

(17) Wu, T.; Průša, J.; Kessler, J.; Dračínský, M.; Valenta, J.; Bouř, P. Detection of Sugars Via Chirality Induced in Europium(III) Compounds. *Anal. Chem.* **2016**, *88*, 8878−8885.

(18) Barron, L. D.; Hecht, L.; Blanch, E. W.; Bell, A. F. Solution Structure and Dynamics of Biomolecules from Raman Optical Activity. *Prog. Biophys. Mol. Biol.* **2000**, *73*, 1−49.

(19) Blanch, E. W.; McColl, I. H.; Hecht, L.; Nielsen, K.; Barron, L. D. Structural Characterization of Proteins and Viruses Using Raman Optical Activity. *Vib. Spectrosc.* **2004**, *35*, 87−92.

(20) Hobro, A. J.; Rouhi, M.; Conn, G. L.; Blanch, E. W. Raman and Raman Optical Activity (ROA) Analysis of RNA Structural Motifs. *Vib. Spectrosc.* **2008**, *48*, 37−43.

(21) Keiderling, T. A. Vibrational Circular Dichroism. Comparison of Technique and Practical Considerations. In *Practical Fourier Transform Infrared Spectroscopy*; Krishnan, K., Ferraro, J. R., Eds.; Academic Press: San Diego, 1990; pp 203−284.

(22) Paterlini, M. G.; Freedman, T. B.; Nafie, L. A. Ring Current Enhanced Vibrational Circular Dichroism in the CH-Stretching Motion of Sugars. *J. Am. Chem. Soc.* **1986**, *108*, 1389−1397.

(23) Hudecová, J.; Profant, V.; Novotná, P.; Baumruk, V.; Urbanová, M.; Bouř, P. CH Stretching Region: Computational Modeling of Vibrational Optical Activity. *J. Chem. Theory Comput.* **2013**, *9*, 3096−3108.

(24) Hug, W.; Kint, S.; Bailey, G. F.; Schere, J. R. Raman Circular Intensity Differential Spectroscopy. The Spectra of (−)-α-Pinene and (+)-α-Phenylethylamine. *J. Am. Chem. Soc.* **1975**, *97*, 5589−5590.

(25) Wiberg, K. B.; Wang, Y.-g.; Wilson, S. M.; Vaccaro, P. H.; Cheeseman, J. R. Chiroptical Properties of 2-Chloropropionitrile. *J. Phys. Chem. A* **2005**, *109*, 3448−3453.

(26) Wilson, H. W. The Infrared and Raman Spectra of α- and β-Pinenes. *Appl. Spectrosc.* **1976**, *30*, 209−212.

(27) Upshur, M. A.; Chase, H. M.; Strick, B. F.; Ebben, C. J.; Fu, L.; Wang, H.; Thomson, R. J.; Geiger, F. M. Vibrational Mode Assignment of α-Pinene by Isotope Editing: One Down, Seventy-One to Go. *J. Phys. Chem. A* **2016**, *120*, 2684−2690.

(28) Stokes, G. Y.; Chen, E. H.; Buchbinder, A. M.; Paxton, W. F.; Keeley, A.; Geiger, F. M. Atmospheric Heterogeneous Stereochemistry. *J. Am. Chem. Soc.* **2009**, *131*, 13733−13737.

(29) Keyes, T. Instantaneous Normal Mode Approach to Liquid State Dynamics. *J. Phys. Chem. A* **1997**, *101*, 2921−2930.

(30) Ojamäe, L.; Tegenfeldt, J.; Lindgren, J.; Hermansson, K. Simulation of Band Widths in Liquid Water Spectra. The Breakdown of the Frozen-Field Approximation. *Chem. Phys. Lett.* **1992**, *195*, 97−103.

(31) Kapitán, J.; Baumruk, V.; Kopecký, V.; Pohl, R.; Bouř, P. Proline Zwitterion Dynamics in Solution, Glass, and Crystalline State. *J. Am. Chem. Soc.* **2006**, *128*, 13451−13462.

(32) Kapitán, J.; Johannessen, C.; Bouř, P.; Hecht, L.; Barron, L. D. Vibrational Raman Optical Activity of 1-Phenylethanol and 1-Phenylethylamine: Revisiting Old Friends. *Chirality* **2009**, *21*, E4−12.

(33) Hopmann, K. H.; Ruud, K.; Pecul, M.; Kudelski, A.; Dračínský, M.; Bouř, P. Explicit Versus Implicit Solvent Modeling of Raman Optical Activity Spectra. *J. Phys. Chem. B* **2011**, *115*, 4128−4137.

(34) Zielinski, F.; Mutter, S. T.; Johannessen, C.; Blanch, E. W.; Popelier, P. L. A. The Raman Optical Activity of β-D-Xylose: Where Experiment and Computation Meet. *Phys. Chem. Chem. Phys.* **2015**, *17*, 21799−21809.

(35) Cheeseman, J. R.; Shaik, M. S.; Popelier, P. L. A.; Blanch, E. W. Calculation of Raman Optical Activity Spectra of Methyl-β-D-Glucose. Incorporating a Full Molecular Dynamics Simulation of Hydration Effects. *J. Am. Chem. Soc.* **2011**, *133*, 4991−4997.

(36) Hudecová, J.; Hopmann, K. H.; Bouř, P. Correction of Vibrational Broadening in Molecular Dynamics Clusters with the Normal Mode Optimization Method. *J. Phys. Chem. B* **2012**, *116*, 336−342.

(37) Tomasi, J.; Mennucci, B.; Cammi, R. Quantum Mechanical Continuum Solvation Models. *Chem. Rev.* **2005**, *105*, 2999−3094.

(38) Cossi, M.; Scalmani, G.; Rega, N.; Barone, V. New Developments in the Polarizable Continuum Model for Quantum Mechanical and Classical Calculations on Molecules in Solution. *J. Chem. Phys.* **2002**, *117*, 43−54.

(39) Klamt, A.; Schuurmann, G. Cosmo: A New Approach to Dielectric Screening in Solvents with Explicit Expressions for the Screening Energy and Its Gradient. *J. Chem. Soc., Perkin Trans. 2* **1993**, 799−805.

(40) Cappelli, C.; Monti, S.; Scalmani, G.; Barone, V. On the Calculation of Vibrational Frequencies for Molecules in Solution Beyond the Harmonic Approximation. *J. Chem. Theory Comput.* **2010**, *6*, 1660−1669.

(41) Cappelli, C.; Bloino, J.; Lipparini, F.; Barone, V. Toward Ab Initio Anharmonic Vibrational Circular Dichroism Spectra in the Condensed Phase. *J. Phys. Chem. Lett.* **2012**, *3*, 1766−1773.

(42) Carnimeo, I.; Puzzarini, C.; Tasinato, N.; Stoppa, P.; Charmet, A. P.; Biczysko, M.; Cappelli, C.; Barone, V. Anharmonic Theoretical Simulations of Infrared Spectra of Halogenated Organic Compounds. *J. Chem. Phys.* **2013**, *139*, No. 074310.

(43) Merten, C.; Bloino, J.; Barone, V.; Xu, Y. Anharmonicity Effects in the Vibrational CD Spectra of Propylene Oxide. *J. Phys. Chem. Lett.* **2013**, *4*, 3424−3428.

(44) Barone, V.; Biczysko, M.; Bloino, J. Fully Anharmonic IR and Raman Spectra of Medium-Size Molecular Systems: Accuracy and Interpretation. *Phys. Chem. Chem. Phys.* **2014**, *16*, 1759−1787.

(45) Barone, V.; Biczysko, M.; Bloino, J.; Puzzarini, C. Accurate Molecular Structures and Infrared Spectra of Trans-2,3-Dideuterooxirane, Methyloxirane, and Trans-2,3-Dimethyloxirane. *J. Chem. Phys.* **2014**, *141*, No. 034107.

(46) Daněček, P.; Bouř, P. Comparison of the Numerical Stability of Methods for Anharmonic Calculations of Vibrational Molecular Energies. *J. Comput. Chem.* **2007**, *28*, 1617−1624.

(47) Bloino, J.; Biczysko, M.; Barone, V. Anharmonic Effects on Vibrational Spectra Intensities: Infrared, Raman, Vibrational Circular Dichroism and Raman Optical Activity. *J. Phys. Chem. A* **2015**, *119*, 11862−11874.

(48) Mihrin, D.; Wugt Larsen, R. THz Spectroscopy of Weakly Bound Cluster Molecules in Solid Para-Hydrogen: A Sensitive Probe of van Der Waals Interactions. *Phys. Chem. Chem. Phys.* **2019**, 349−358.

(49) Koppenhoefer, B.; Schurig, V. (S)-2-Chloroalkanoic Acids of High Enantiomeric Purity from (S)-2-Amino Acids: (S)-2-Chloropropanoic Acid. *Org. Synth.* **1988**, *66*, 151.

(50) Stork, G.; Worrall, W. S.; Pappas, J. J. Synthesis and Reactions of Glycidonitriles. Transformation into α-Haloacyl Compounds and Aminoalcohols. *J. Am. Chem. Soc.* **1960**, *82*, 4315−4323.

(51) Hug, W.; Hangartner, G. A Novel High-Throughput Raman Spectrometer for Polarization Difference Measurements. *J. Raman Spectrosc.* **1999**, *30*, 841−852.

(52) Hug, W. Virtual Enantiomers as the Solutuion of Optical Activity's Deterministic Offset Problem. *Appl. Spectrosc.* **2003**, *57*, 1−13.

(53) Kohn, W.; Sham, L. J. Self-Consistent Equations Including Exchange and Correlation Effects. *Phys. Rev.* **1965**, *140*, A1133−A1138.

(54) Becke, A. D. Density Functional Thermochemistry. III. The Role of Exact Exchange. *J. Chem. Phys.* **1993**, *98*, 5648−5652.

(55) Frisch, M. J.; Trucks, G. W.; Schlegel, H. B.; Scuseria, G. E.; Robb, M. A.; Cheeseman, J. R.; Scalmani, G.; Barone, V.; Petersson, G. A.; Nakatsuji, H.;et al.et al.*Gaussian 16*, revsion A.03; Wallingford, CT, 2016.

(56) Barone, V.; Cossi, M. Quantum Calculation of Molecular Energies and Energy Gradients in Solution by a Conductor Solvent Model. *J. Phys. Chem. A* **1998**, *102*, 1995−2001.

(57) Cossi, M.; Rega, N.; Scalmani, G.; Barone, V. Energies, Structures, and Electronic Properties of Molecules in Solution with the C-PCM Solvation Model. *J. Comput. Chem.* **2003**, *24*, 669−681.

(58) Polavarapu, P. L. *Vibrational Spectra: Principles and Applications with Emphasis on Optical Activity*; Elsevier: Amsterdam, 1998; Vol. 85.

(59) Deserno, M. *How to Generate Equidistributed Points on the Surface of a Sphere*; Max-Planck-Institut für Polymerforschung: Germany, 2004.

(60) Ponder, J. W. *Tinker, Software Tools for Molecular Design*, 7.2.1st ed.; Washington University: St. Louis, Missouri, 2000.

(61) Rizzo, R. C.; Jorgensen, W. L. OPLS All-Atom Model for Amines: Resolution of the Amine Hydration Problem. *J. Am. Chem. Soc.* **1999**, *121*, 4827−4836.

(62) Bouř, P.; Keiderling, T. A. Partial Optimization of Molecular Geometry in Normal Coordinates and Use as a Tool for Simulation of Vibrational Spectra. *J. Chem. Phys.* **2002**, *117*, 4126−4132.

(63) Bouř, P. Convergence Properties of the Normal Mode Optimization and Its Combination with Molecular Geometry Constraints. *Collect. Czech. Chem. Commun.* **2005**, *70*, 1315−1340.

(64) Bouř, P. *Qgrad*; Institute of Organic Chemistry and Biochemistry, Academy of Sciences: Prague, Czech Republic, 2006.

(65) Grimme, S.; Antony, J.; Ehrlich, S.; Krieg, H. A Consistent and Accurate Ab Initio Parametrization of Density Functional Dispersion Correction (DFT-D) for the 94 Elements H-Pu. *J. Chem. Phys.* **2010**, *132*, No. 154104.

(66) Grimme, S.; Ehrlich, S.; Goerigk, L. Effect of the Damping Function in Dispersion Corrected Density Functional Theory. *J. Comput. Chem.* **2011**, *32*, 1456−1465.

(67) Wilson, E. B. A Method of Obtaining the Expanded Secular Equation for the Vibration Frequencies of a Molecule. *J. Chem. Phys.* **1939**, *7*, 1047−1052.

(68) Hug, W.; Fedorovsky, M. Characterizing Vibrational Motion Beyond Internal Coordinates. *Theor. Chem. Acc.* **2008**, *119*, 113−131.

(69) Kumar, P. S. V.; Raghavendra, V.; Subramanian, V. Bader's Theory of Atoms in Molecules (AIM) and Its Applications to Chemical Bonding. *J. Chem. Sci.* **2016**, *128*, 1527−1536.

(70) Bader, R. F. W. A Quantum Theory of Molecular Structure and Its Applications. *Chem. Rev.* **1991**, *91*, 893−928.

(71) Johnson, E. R.; Keinan, S.; Mori-Sánchez, P.; Contreras-García, J.; Cohen, A. J.; Yang, W. Revealing Noncovalent Interactions. *J. Am. Chem. Soc.* **2010**, *132*, 6498−6506.

(72) Lu, T.; Chen, F. Multiwfn: A Multifunctional Wavefunction Analyzer. *J. Comput. Chem.* **2012**, *33*, 580−592.

(73) Bouř, P. *S4: Program for Calculation of Anharmonic Molecular Vibrational Properties*; Institute of Organic Chemistry and Biochemistry, Academy of Sciences: Prague, Czech Republic, 2017.

(74) Barone, V. Anharmonic Vibrational Properties by a Fully Automated Second-Order Perturbative Approach. *J. Chem. Phys.* **2004**, *122*, No. 014108.

(75) Bloino, J. A VPT2 Route to Near-Infrared Spectroscopy: The Role of Mechanical and Electrical Anharmonicity. *J. Phys. Chem. A* **2015**, *119*, 5269−5287.

(76) Stephens, P. J. Theory of Vibrational Circular Dichroism. *J. Phys. Chem.* **1985**, *89*, 748−752.

(77) Keiderling, T. A.; Bouř, P. Theory of Molecular Vibrational Zeeman Effects as Measured with Circular Dichroism. *Phys. Rev. Lett.* **2018**, *121*, No. 073201.

(78) Bouř, P.; McCann, J.; Wieser, H. Measurement and Calculation of Absolute Rotational Strengths for Camphor, Alpha-Pinene, and Borneol. *J. Phys. Chem. A* **1998**, *102*, 102−110.

(79) Profant, V.; Pazderková, M.; Pazderka, T.; Maloň, P.; Baumruk, V. Relative Intensity Correction of Raman Optical Activity Spectra Facilitates Extending the Spectral Region. *J. Raman Spectrosc.* **2014**, *45*, 603−609.

(80) Ho, J.; Psciuk, B. T.; Chase, H. M.; Rudshteyn, B.; Upshur, M. A.; Fu, L.; Thomson, R. J.; Wang, H.; Geiger, F. M.; Batista, V. S. Sum Frequency Generation Spectroscopy and Molecular Dynamics Simulations Reveal a Rotationally Fluid Adsorption State of α-Pinene on Silica. *J. Phys. Chem. C* **2016**, *120*, 12578−12589.

(81) Buchbinder, A. M.; Gibbs-Davis, J. M.; Stokes, G. Y.; Peterson, M. D.; Weitz, E.; Geiger, F. M. Method for Evaluating Vibrational Mode Assignments in Surface-Bound Cyclic Hydrocarbons Using Sum-Frequency Generation. *J. Phys. Chem. C* **2011**, *115*, 18284−18294.

(82) Bouř, P.; Baumruk, V.; Hanzlíková, J. Measurement and Calculation of the Raman Optical Activity of Alpha-Pinene and Trans-Pinane. *Collect. Czech. Chem. Commun.* **1997**, *62*, 1384−1395.

Supplementary Information

Vibrational Optical Activity of Inter-Molecular, Overtone and Combination Bands: 2-Chloropropionitrile and α-Pinene

Pavel Michal,[†*] Radek Čelechovský,[†] Michal Dudka,[†] Josef Kapitán,[†] Milan Vůjtek,[†] Marie Berešová,[#‡] Jaroslav Šebestík,[‡] Karthick Thangavel,[‡] and Petr Bouř[#‡*]

[†]*Department of Optics, Palacký University Olomouc, 17. listopadu 12,*
77146, Olomouc, Czech Republic
[#]*Department of Analytical Chemistry, University of Chemistry and Technology, Technická 5,*
16628, Prague, Czech Republic
[‡]*Institute of Organic Chemistry and Biochemistry, Academy of Sciences, Flemingovo náměstí 2,*
16610, Prague, Czech Republic

Content

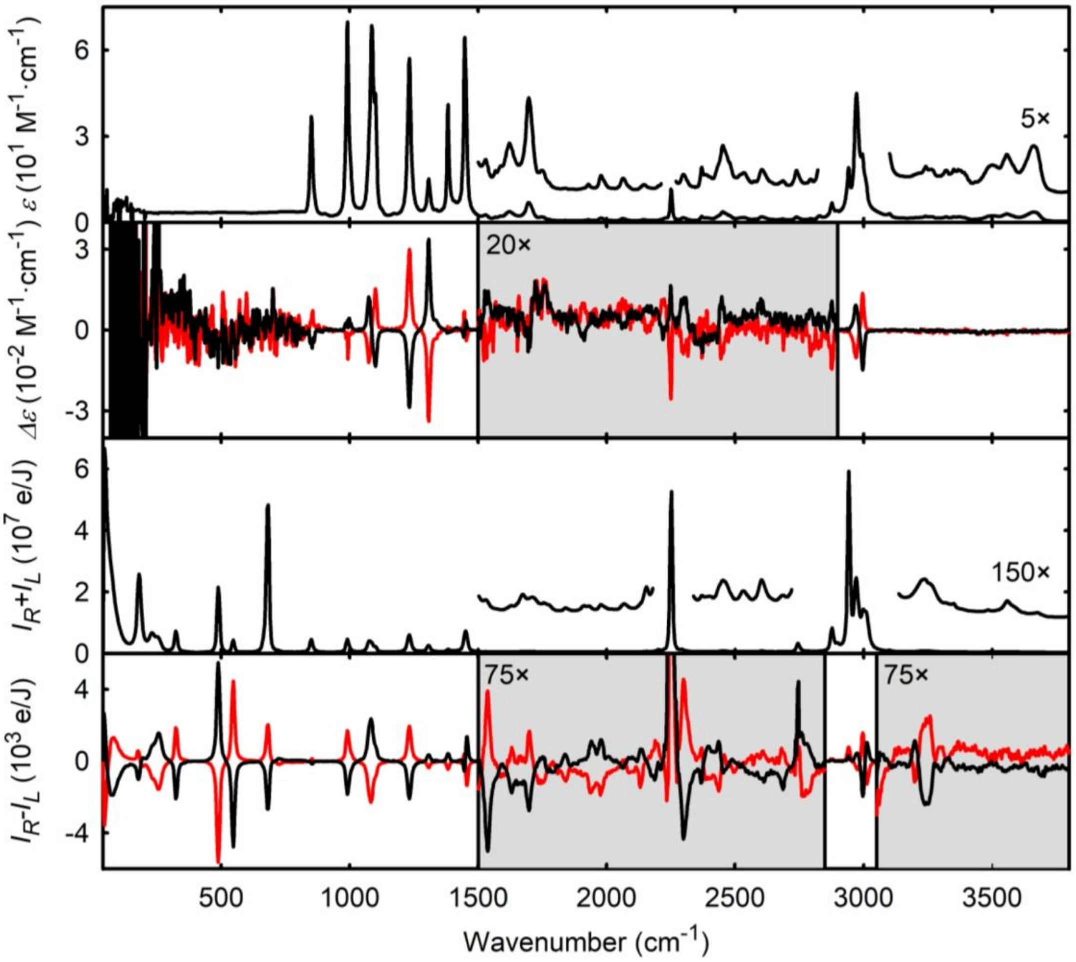

Figure S1. Experimental IR, VCD, Raman and ROA raw spectra of (R-red, S-black) 2-chloropropionitrile; regions of overtone and combination modes are enlarged.

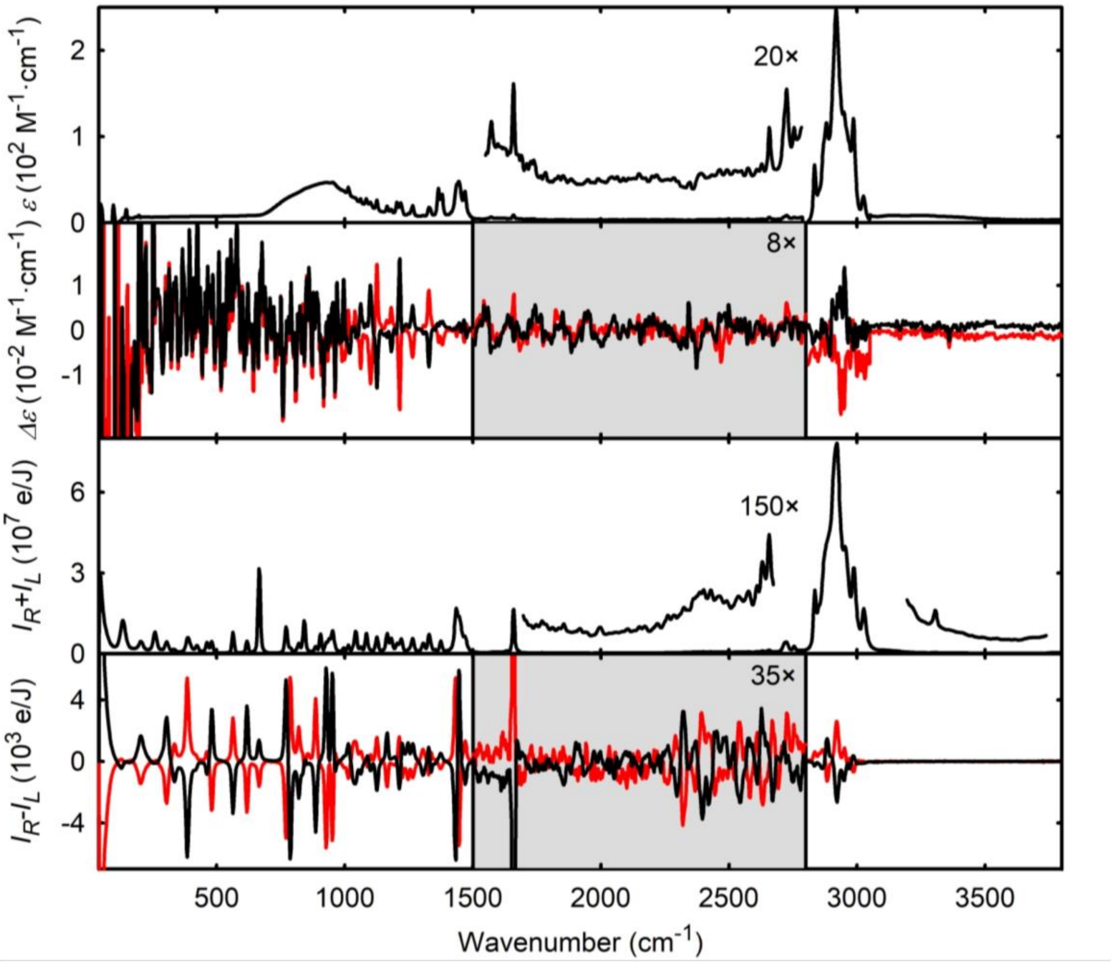

Figure S2. Experimental IR, VCD, Raman and ROA raw spectra of ((+)-red, (-)-black))-α-pinene; regions of overtone and combination modes are enlarged.

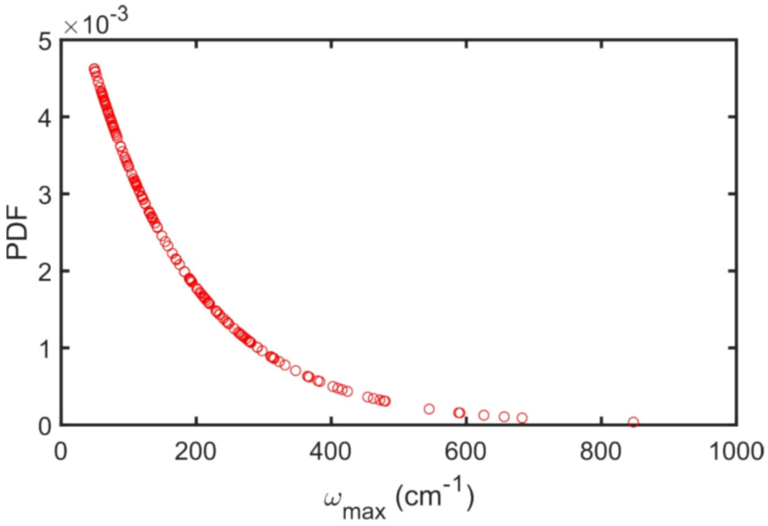

Figure S3. Random exponential function used for the optimization frequency limit for 200 nitrile clusters.

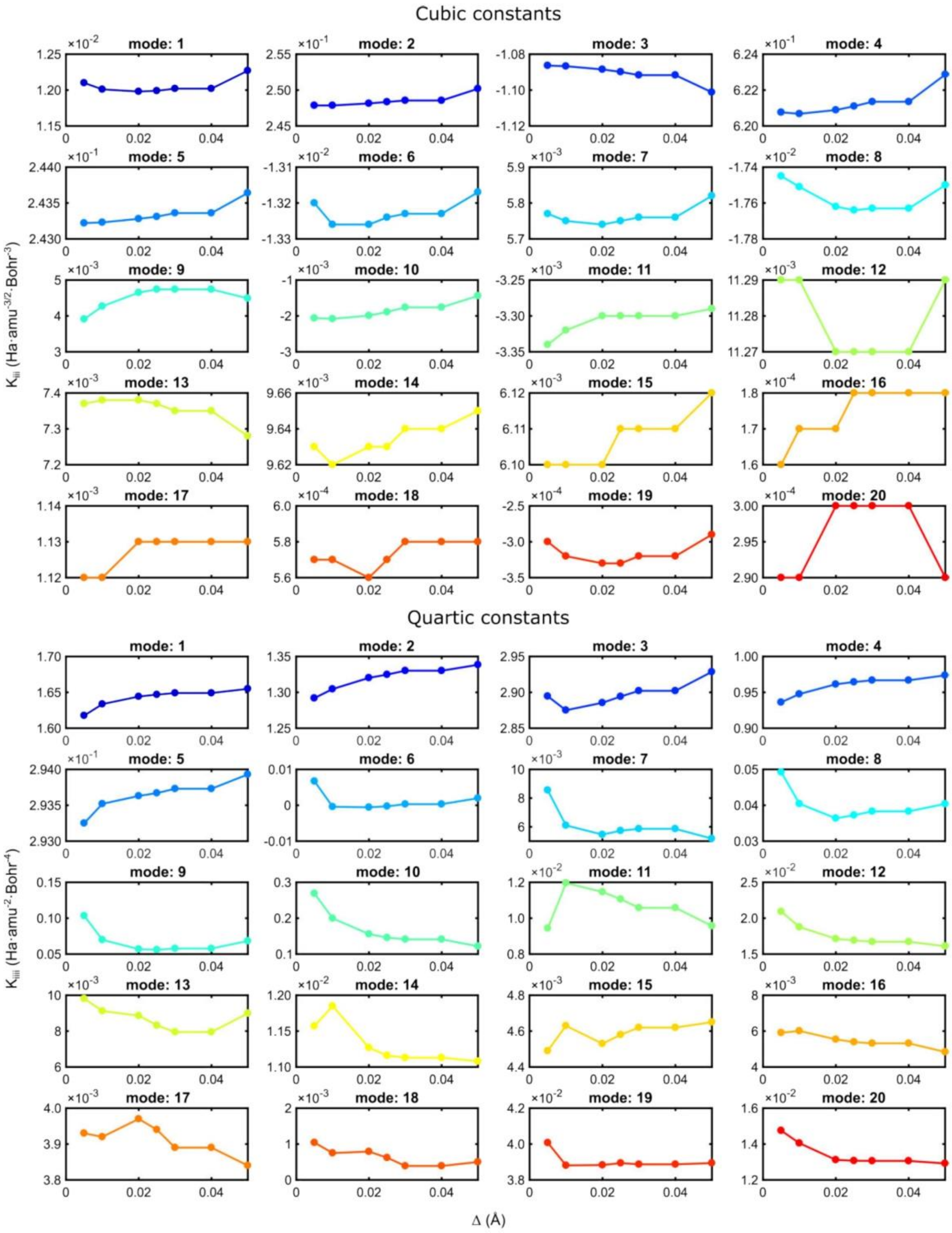

Figure S4. Dependence of calculated cubic and quartic diagonal normal mode nitrile force constants on the size of the numerical differentiation step.

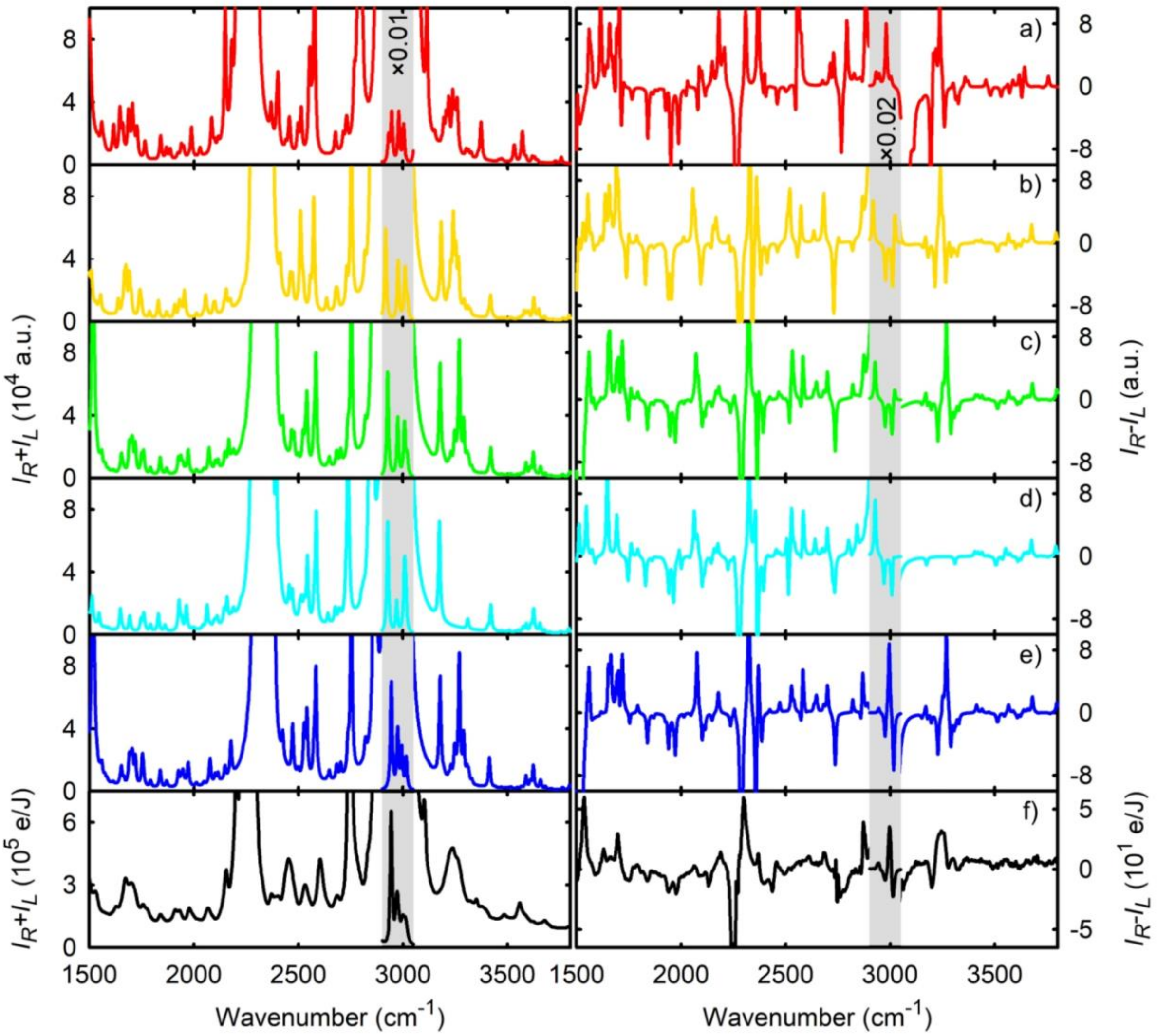

Figure S5. Nitrile Raman and ROA spectra within 1490-3800 cm^{-1} calculated using different methods: 6311G basis set (a), 6-311G** basis set (b), 6-311++G** basis set (c-e), all mode calculations (a-c, e) and with modes 1-4 frozen (d), and the GVPT2 (a-d) and VPT2 (e) approaches, (f) is the experiment.

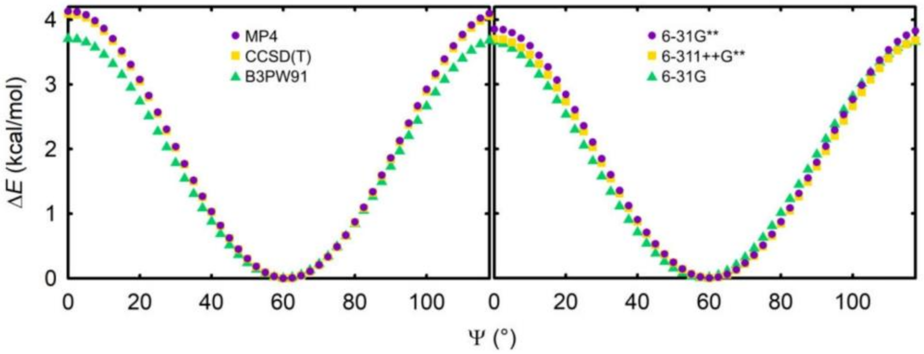

Figure S6. Calculated nitrile energy dependence on the Ψ angle (cf. **Figure 1**), calculated at different levels, left: MP4, CCSD(T) and B3PW91 with 6-311++G**/ (ACN), right: B3PW91 calculation in three basis sets.

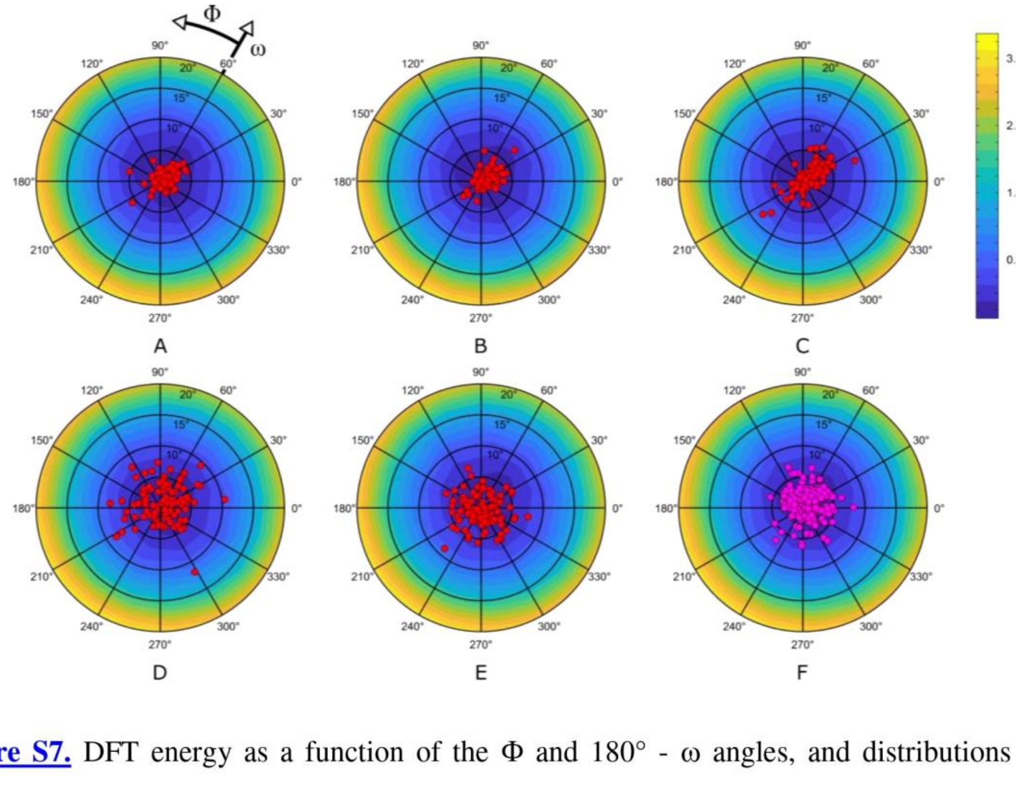

Figure S7. DFT energy as a function of the Φ and 180° - ω angles, and distributions of nitrile geometries in 200 clusters obtained from MD partially optimized with various values of the normal mode frequency limit (A: 40 cm^{-1}, B: 150 cm^{-1}, C: 225 cm^{-1}, D: 390 cm^{-1}, E: no optimization, F: exponential distribution within 50-900 cm^{-1}, see **Figure S2**).

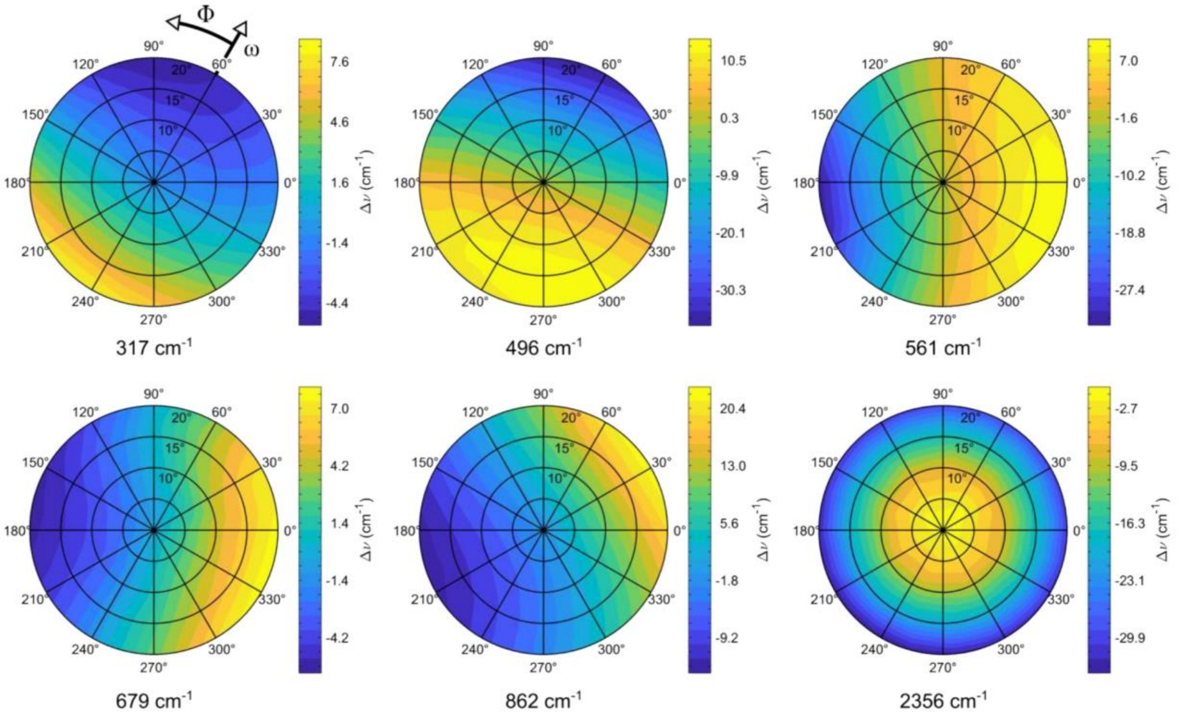

Figure S8. Frequency shift (Δ/cm^{-1}) of selected nitrile normal modes, from values for the equilibrium geometry, plotted as a function of the Φ and 180° - ω angles.

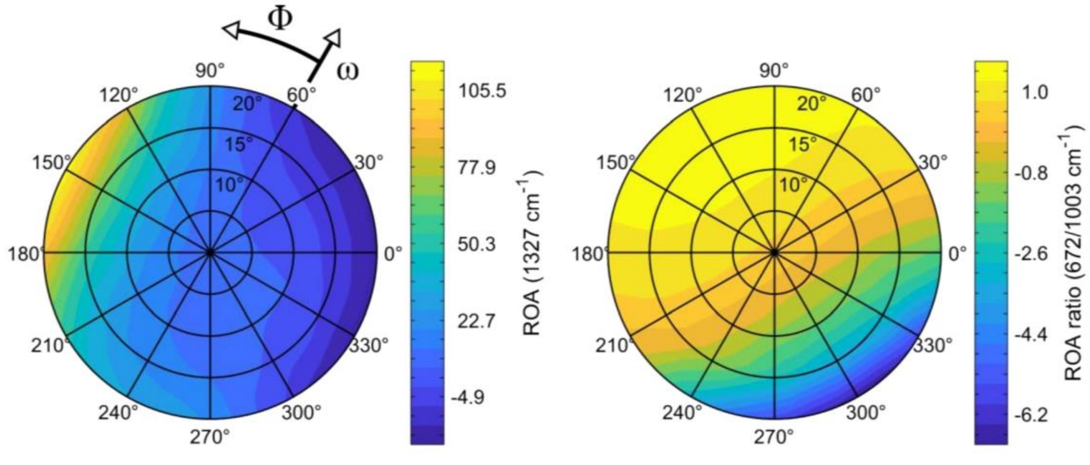

Figure S9. ROA intensity of the 1327 cm^{-1} nitrile mode (left), and intensity ratio of the 672 and 1003 cm^{-1} modes as dependent on the Φ and 180° - ω angles.

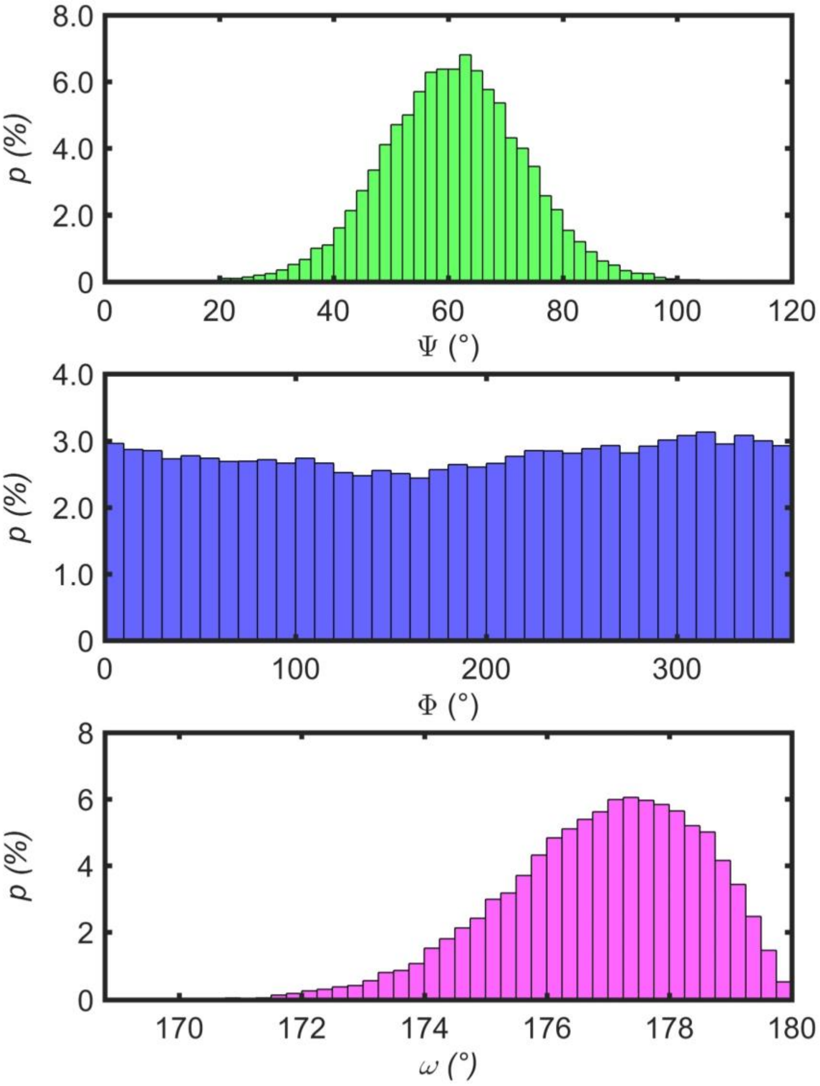

Figure S10. Angle distributions of the nitrile characteristic angles obtained during the free molecular dynamics run (1 ns).

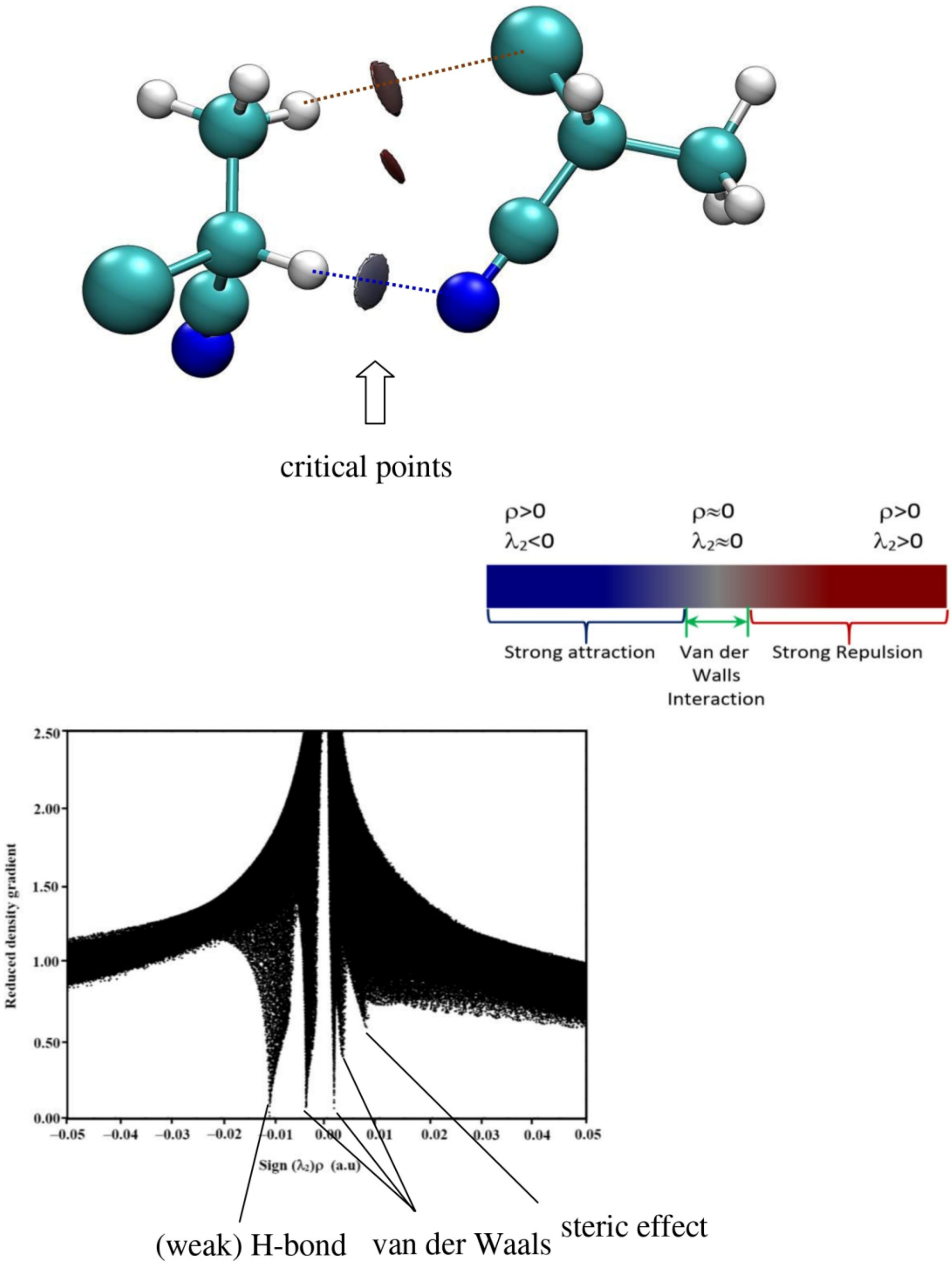

Figure S11. Example of the AIM analysis of nitrile-nitrile interactions (dimer number 9 in **Table S4**). Top – reduced density gradient (RDG) in critical points, bottom – RDG vs. signed density AIM graph.

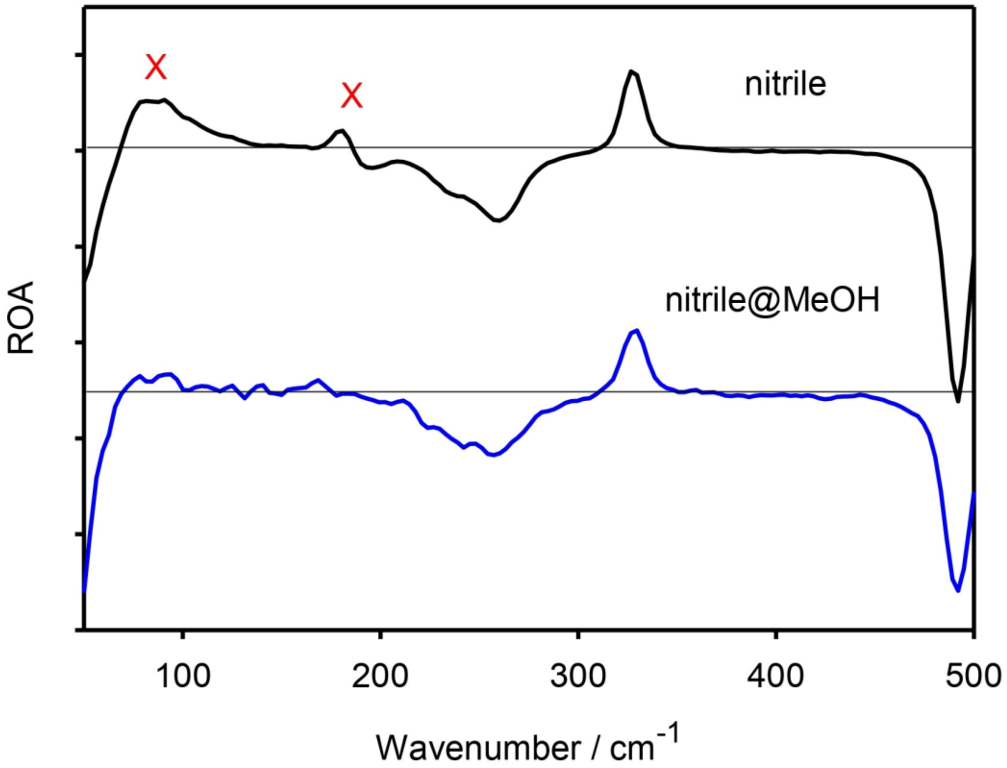

Figure S12. Nitrile ROA spectra in the low-frequency region, for pure liquid (top) and its about 10 % solution in methanol (bottom). Clearly vanishing bands are marked by the red crosses.

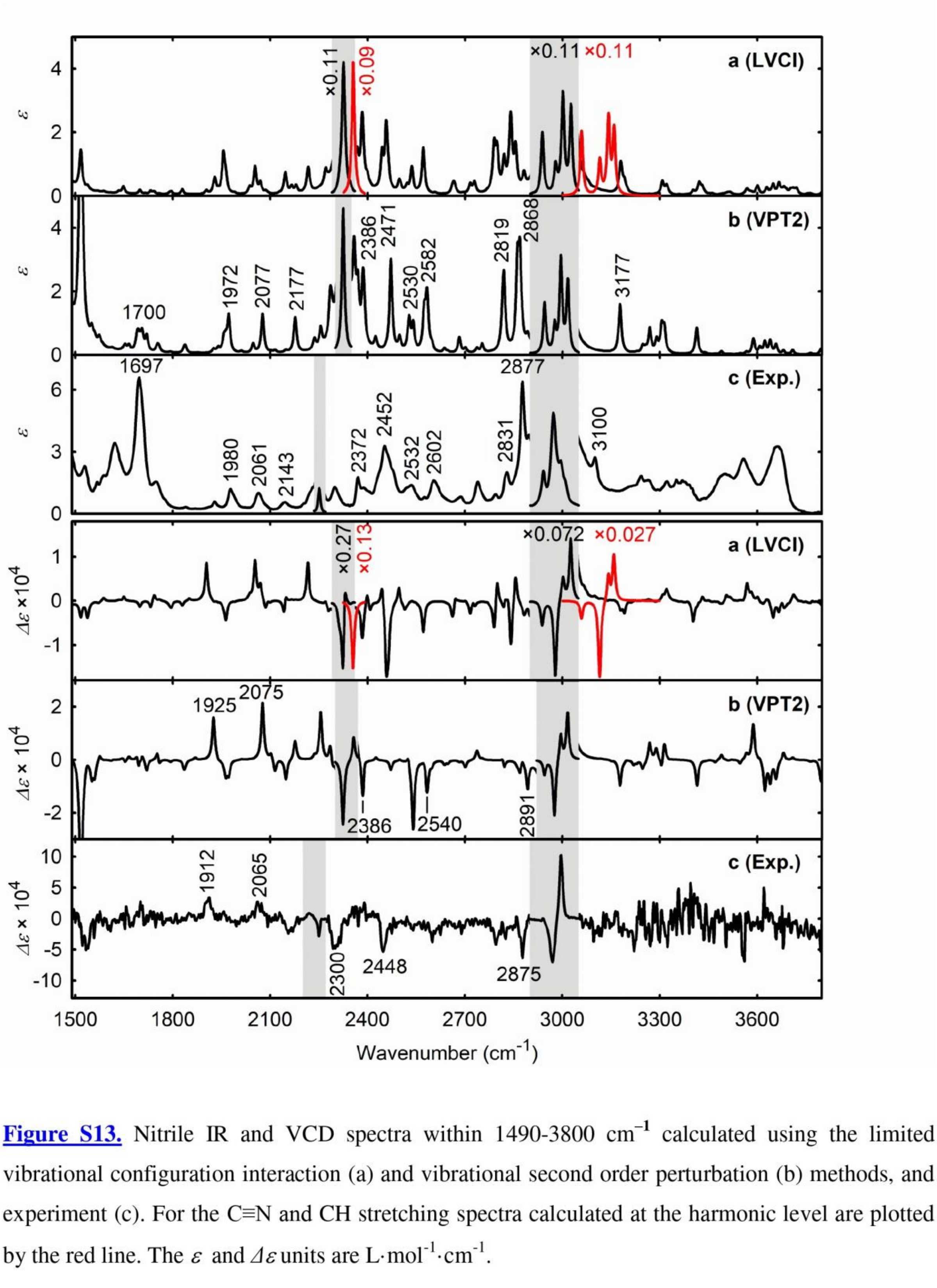

Figure S13. Nitrile IR and VCD spectra within 1490-3800 cm^{-1} calculated using the limited vibrational configuration interaction (a) and vibrational second order perturbation (b) methods, and experiment (c). For the C≡N and CH stretching spectra calculated at the harmonic level are plotted by the red line. The ε and $\Delta\varepsilon$ units are L·mol^{-1}·cm^{-1}.

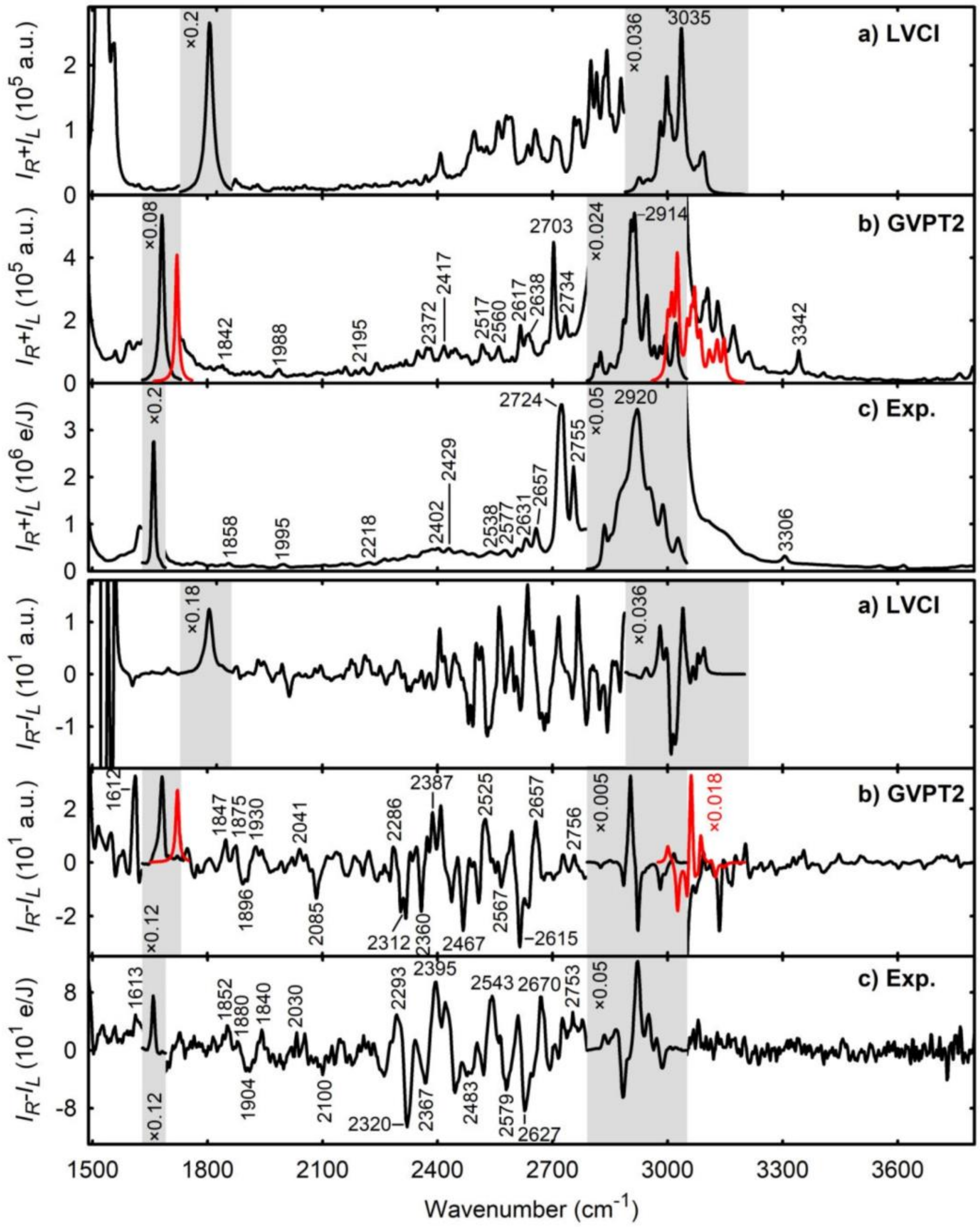

Figure S14. Raman and ROA spectra of α-pinene, plotted within 1490−3800 cm^{-1}, as calculated using the limited vibrational configuration interaction (a), generalized vibrational second order perturbation calculus (b), and the experiment (c). For the fundamental C≡N and CH stretching signal, spectral shapes calculated at the harmonic level are plotted by the red line. These signals in the gray areas are plotted in a different scale. LVCI spectra above 3100 cm^{-1} were not calculated.

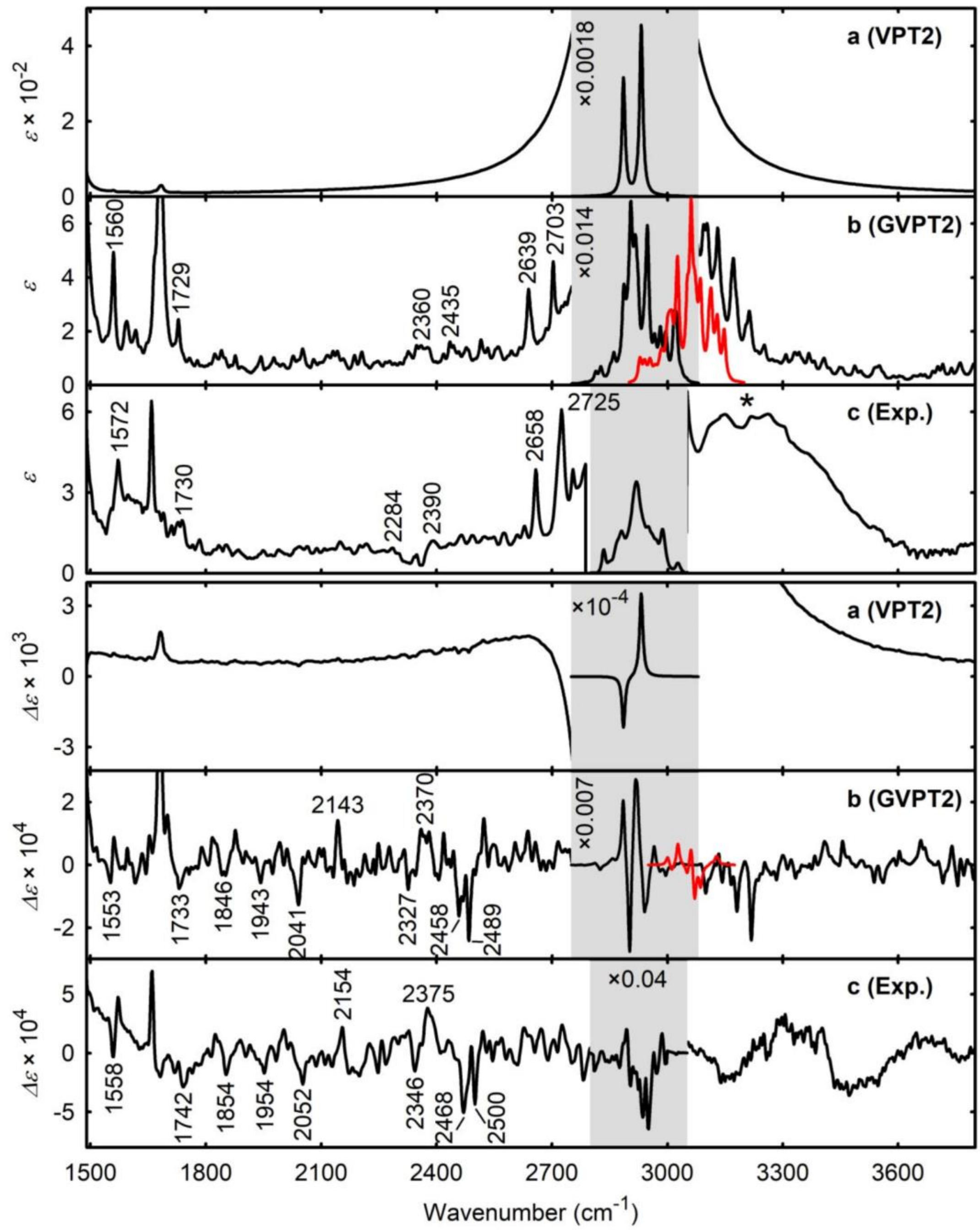

Figure S15. (+)-α-pinene IR and VCD spectra within 1490-3800 cm^{-1} calculated using vibrational second order perturbation before (a) and after including corrections to resonances (b), and experiment (c). For the CH stretching spectra calculated at the harmonic level are plotted by the red line. The ε and $\Delta\varepsilon$ units are L·mol^{-1}·cm^{-1}. Above 3100 cm^{-1} the experimental spectrum is hampered by BaF_2 absorption (marked by the asterisk, *), impossible to subtract.

Table S1. Laser power on the sample (*P*) and total accumulation time (*t*) used for ROA measurement. Weak combination and overtone bands of the nitrile were measured using different conditions (P^*, t^*). Reported spectra are normalized to unit excitation energy obtained as a product of the power and acquisition time.

solvent	enantiomer	*P* / mW	*t* / h	*P** / mW	t^* / h
2-chloropropionitrile	*R*	83	9.7	340	29.7
	S	83	13.2	340	55.2
α-pinene	*R*	102	4.1	-	-
	S	68	9.8	-	-

Table S2. Nitrile, assignment of fundamental modes, frequencies in cm^{-1}.

Mode	Harmonic	Anharmonic (VPT2)	EXP	Type
1	3159	3016	3013	asymmetric CH_3 stretching
2	3142	2995	2997	asymmetric CH_3 stretching
3	3115	2971	2976	αCH stretching
4	3059	2945	2943	symmetric CH_3 stretching
5	2356	2325	2252	CN stretching
6	1476	1438	1456	CH_3 scissoring
7	1469	1439	1445	CH_3 scissoring
8	1403	1384	1383	CH_3 umbrella motion
9	1329	1300	1307	CH bending
10	1254	1264	1232	CH bending
11	1112	1104	1100	CC stretching
12	1091	1090	1077	CC stretching
13	1003	989	991	CC stretching
14	862	853	851	CH_3 wagging, CCN bending
15	679	664	681	CH_3 wagging, CCN bending, CCl stretching
16	561	571	547	CCN bending to CH_3
17	496	494	489	CCN bending perpendicular to CH_3
18	317	313	324	CCCl bending, CCCN torsional twisting
19	266	273	250	CH_3 rotation
20	227	252	231	CH_3 rotation and, CCCN torsional twisting
21	173	176	181	CCN bending to CH_3, CH_3 rocking

Table S3. Nitrile, frequencies (cm^{-1}) of combination modes and overtones.

Modes	Calculated (VPT2)	Experimental (Raman)
21+8; 20+9; 16+13	1560	1530
16+11; 15+13; 16+12	1653	1630
20+6; 20+7; 18+8; 2x14; 19+6; 19+7	1704	1674; 1700
18+6; 18+7; 15+11; 15+12; 17+10	1754	1757
16+10; 14+13	1839	1840
15+10; 17+6; 17+7; 14+11; 14+12; 16+8; 15+9	1925; 1945	1912; 1931
2x13	1973	1978
13+11; 13+12	2077	2068
2x11; 2x12; 11+12	2177	2155
13+6;13+7	2424	2385
11+8; 12+8	2472	2453
12+6; 11+6; 11+7; 12+7; 2x10	2527; 2540	2532
10+9; 20+5; 19+5; 2x9	2583	2603
10+8; 9+8; 10+6; 10+7	2648; 2682; 2702	2685
2x8	2753	2745
8+6; 8+7	2820	2830
2x7; 2x6	2865	2877
21+2; 14+5; 21+1; 20+4	3177	3100
19+4; 19+3; 19+2; 19+1; 20+3; 20+2; 20+1; 18+4; 18+3; 18+2; 18+1; 13+5	3269	3238
11+5; 12+5	3413	3351
9+5	3623	3358

Table S4. AIM topological parameters of interacting atoms in 14 nitrile dimers. The intermolecular threshold was 0.01 kcal/mol, electron density (ρ) and Laplacian ($\Delta\rho$) are in atomic units.

Dimer number	Critical points ($\nabla\rho = 0$)			
	Atoms	Distance (Å)	ρ	$\Delta\rho$
1	C-Cl	1.8324	0.1653	-0.185
	C-N	1.1526	0.4792	0.301
	C-C	1.4908	0.2559	-0.648
	C-H	1.0900	0.4792	-1.000
1	C5···H17	4.7417	1.76×10^{-4}	7.57×10^{-4}
	Cl9···H18	4.8686	1.67×10^{-4}	6.54×10^{-4}
	Cl9···H11	4.6185	1.91×10^{-4}	7.01×10^{-4}
2	Cl14···H2	2.8821	6.00×10^{-3}	2.10×10^{-2}
	H16···N4	3.3554	1.72×10^{-3}	5.76×10^{-3}
3	H8···Cl14	2.9977	5.21×10^{-3}	1.77×10^{-2}
	H7···H16	2.7502	2.30×10^{-3}	7.87×10^{-3}
	H18···Cl9	3.3750	2.14×10^{-3}	7.67×10^{-3}
4	Cl14···Cl9	4.1806	2.26×10^{-3}	6.29×10^{-3}
5	Cl9···Cl14	4.1894	1.83×10^{-3}	5.39×10^{-3}
6	N15···N4	4.8218	2.42×10^{-4}	9.67×10^{-4}
7	C5···Cl14	4.0798	2.06×10^{-3}	6.25×10^{-3}
	H2···Cl14	3.5624	1.74×10^{-3}	5.66×10^{-3}
8	N4···C12	3.2145	5.79×10^{-3}	1.88×10^{-2}
9	H11···N4	2.3913	1.08×10^{-2}	3.40×10^{-2}
	H16···Cl9	3.1998	3.90×10^{-3}	1.29×10^{-2}
	H18···N4	3.7215	7.83×10^{-4}	2.77×10^{-3}
10	N4···Cl14	4.6051	6.82×10^{-4}	2.31×10^{-3}
11	Cl9···N15	4.4090	8.43×10^{-4}	2.87×10^{-3}
12	Cl9···N15	4.9235	3.43×10^{-4}	1.24×10^{-3}
13	H6···H16	3.0306	1.32×10^{-3}	4.43×10^{-3}
	H7···Cl14	3.0265	4.95×10^{-3}	1.65×10^{-2}
	N4···N15	3.5535	4.14×10^{-3}	1.27×10^{-2}
14	N15···Cl9	3.5070	5.25×10^{-3}	1.61×10^{-2}
	H6···Cl14	2.6718	1.02×10^{-2}	3.54×10^{-2}
	Cl9···Cl14	4.0496	3.05×10^{-3}	8.88×10^{-3}

Appendix B – Phys. Chem. Chem. Phys., 24 (33), 19722-19733 (2022).

PCCP

PAPER

Cite this: *Phys. Chem. Chem. Phys.*, 2022, **24**, 19722

Low-frequency Raman optical activity provides insight into the structure of chiral liquids†

Pavel Michal, *[a] Josef Kapitán, [a] Jiří Kessler [b] and Petr Bouř *[bc]

Received 20th May 2022, Accepted 28th July 2022

DOI: 10.1039/d2cp02290g

rsc.li/pccp

Vibrational frequencies of modes involving intermolecular motions in liquids are relatively small, in the Raman scattering close to the excitation frequency, and the bands may merge into a diverging uninterpretable signal. Raman optical activity (ROA) spectral shapes in this region, however, are structured more and may better reflect the nature of the studied systems. To understand the origin of the signal and its relation to the molecules, ROA spectra of six chiral neat liquids are recorded and analyzed on the basis of molecular dynamics and density functional theory computations. The theory of Raman scattering of liquids is discussed and adapted for modeling based on clusters and periodic boundary conditions. A plain cluster approach is compared to a crystal-like model. The results show that the low-frequency optical activity can be reliably modeled and related to the structure. However, momentary arrangement of molecules leads to large variations of optical activity, and a relatively large number of geometries need to be averaged for accurate simulations. The intermolecular modes are intertwined with intramolecular ones and start to dominate as the frequency goes down. The low-frequency ROA signal thus reflects the chemical composition and coupled with the modeling it provides a welcome means to study the structure and interactions of chiral liquids.

1. Introduction

Low-frequency Raman spectroscopy has been possible due to the availability of narrow wavelength optical filters and stable diode lasers, and is gaining popularity in chemical and pharmaceutical analyses.[1] It is also referred to as terahertz (THz) or low-wavenumber Raman spectroscopy. In crystals and crystalline-like polymers, it can reveal their structure, polymorphism and phonon dynamics.[2,3] Both intra and intermolecular vibrational modes provide strong Raman signal.[4] On the other hand, it is very difficult to obtain useful information from the low-frequency Raman spectrum of a liquid, because the signal is rather unstructured, unresolved, and quickly increases when the frequencies approach the excitation line.[5] Better results are obtained by optical Kerr spectroscopy exploring time dependence of the liquid polarization induced by laser pulses. In this case, low-frequency Raman spectra can be obtained by Fourier transformation techniques.[6–8]

If we look at the differential scattering of the right and left circularly polarized light, chiral liquids and solutions may provide more diverse signals than for unpolarized Raman. The bands can be both positive and negative, and are more sensitive to chemical composition and conformation.[9] Usually, only the higher-frequency region (above ~400 cm^{-1}) is interpreted in terms of band assignment to the molecular structure. For a polyalanine solution in dichloroacetic acid, however, we observed a Raman optical activity (ROA) signal at 128 cm^{-1} that was about 10× stronger than the one typical for this spectroscopy.[10] Monosaccharide solutions gave rather weak low-frequency ROA,[11] whereas for several globular proteins dissolved in water the relative signal strength compared well to the big signal of polyalanine.[12] For a cryptophane molecule the intensity of the ROA band at 150 cm^{-1} significantly decreased in the presence of xenon.[13] These observations suggest that the low-frequency ROA well reacts to the structure and intermolecular interactions in the studied systems.

Also for a chiral neat liquid, 2-chloropropionitrile, we identified a strong low-frequency ROA outside the region of monomolecular fundamental modes.[14] On the basis of a cluster model the signal was assigned to intermolecular motions involving changing a distance (stretching) and mutual orientation between molecules. However, it was not clear if such a signal is related to specific intermolecular interactions, such as the ability of a molecule to make hydrogen bonds. *Ad hoc* computations based on large clusters have been quite costly in terms of computer time and memory. In the clusters most

---

[a] *Department of Optics, Palacký University Olomouc, 17. listopadu 12, 77146, Olomouc, Czech Republic. E-mail: michal@optics.upol.cz*

[b] *Department of Analytical Chemistry, University of Chemistry and Technology, Technická 5, 16628 Prague, Czech Republic*

[c] *Institute of Organic Chemistry and Biochemistry, Academy of Sciences, Flemingovo náměstí 2, 16610, Prague, Czech Republic. E-mail: bour@uochb.cas.cz*

† Electronic supplementary information (ESI) available: Further computational details and tests, measurement conditions, and complementary experimental data. See DOI: **https://doi.org/10.1039/d2cp02290g**

molecules remained at the surface, which did not correspond to the real situation. *Ab initio* molecular dynamics suggested for ROA relatively recently[15,16] is probably technically the most advanced way to simulate bulk phase spectra. However, it currently appears too computationally demanding.

In the present study we therefore use the cluster approach adapted to better correspond to the liquid phase, introducing a crystal-like periodicity. This enables us to investigate the low-frequency region more systematically. We also briefly review the theory of Raman scattering on liquids, which we believe has not been previously clearly linked to the cluster computational modeling. High-quality Raman and ROA experimental spectra were recorded for six chiral liquids of variable chemical structures, down to ∼50 cm^{-1}. One of them, methyloxirane, was also investigated as an aqueous solution. Molecular dynamics is used to understand the structure of model liquids, and density functional theory is utilized for the spectroscopic properties. This computational approach seems to be fit to explain the main spectral features including low-frequency ROA signs and intensities, and thus to couple the chiral signals with the liquid structure.

2. Methods

2.1 Theory of Raman scattering in liquids

While the Rayleigh scattering[17] of gasses and liquids reflects long-range inhomogeneities in the structure, such as the radial distribution function,[18] opalescence and density fluctuations,[19,20] Raman scattering samples the structure more locally. This is because non-interacting molecules scatter Raman light in an incoherent way.[21,22]

As far as we know, there is no consistent theory comprising all quantum-mechanical and relativistic aspects of light scattering in bulk. Fortunately, the semiclassical approach based on the scattering of electromagnetic waves on individual molecules seems to provide a reasonable description of the experimental data.[9,21] To illustrate the physical basis of scattering and to justify our cluster approach, let us summarize some important relationships for the backscattering intensities. The light passing through the liquid induces time-dependent electric (**μ**) and magnetic (**m**) dipoles and electric quadrupoles (**Θ**) in individual molecules, which then radiate part of the energy away. Higher moments can be neglected, because molecular dimensions are usually much smaller than the wavelength. The moments are related to the electric intensity of light through molecular polarizabilities. For example, *x*-polarized light of the electric field traveling along the *z*-direction induces a dipole moment in each molecule m[16]

$$\mu_{m\alpha} = \left(\alpha_{m\alpha x} - i\frac{k}{3}A_{m\alpha,xz} + i\frac{k}{\omega}G'_{m\alpha y}\right)E_x \tag{1}$$

where k is the wave vector, ω is the angular frequency, t is time, and α, A and G' are the electric dipole–dipole, electric dipole–quadrupole and electric dipole–magnetic dipole polarizabilities.

The induced moments are sources of scattered radiation. For Raman scattering the incident and scattered frequencies and wave vectors are close ($\omega \sim \omega'$, $k \sim k'$), so that $\Delta k = k - k' \sim 2k$ for backscattering. The electric field of light scattered from N molecules is[21]

$$\begin{aligned} E'_\alpha &= \frac{\omega^2\mu_0\mu_\mathrm{r}}{4\pi r}E_0\sum_{m=1}^{N}\mathrm{e}^{\mathrm{i}(\Delta k z_m - \omega t)}\Big[\alpha_{m\alpha x} - \frac{ik}{3}(A_{m\alpha,xz} + A_{mx,\alpha z}) \\ &\quad + \frac{i}{c}\Big(G'_{m\alpha y} - \varepsilon_{\alpha z\gamma}G'_{mx\gamma}\Big)\Big] \end{aligned} \tag{2}$$

where μ_0 and μ_r are the vacuum and relative permeabilities, and r is the distance. Unpolarized (total) Raman intensity can be associated with the S_0 Stokes parameter,

$$\begin{aligned} I_\mathrm{R} + I_\mathrm{L} = S_0 = E'^2_x + E'^2_y &= 30\,K\sum_{m,n}\mathrm{e}^{\mathrm{i}\Delta k z_{mn}}\left(\alpha_{mxx}\alpha_{nxx} + \alpha_{myx}\alpha_{nyx}\right) \\ &= 30\,K\sum_{m}\left(\alpha_{mxx}\alpha_{mxx} + \alpha_{myx}\alpha_{myx}\right) \end{aligned} \tag{3}$$

where $K = \frac{1}{30}\left(\frac{\omega^2\mu_0\mu_\mathrm{r}}{4\pi r}E_0\right)^2$, $z_{mn} = z_m - z_n$ is the difference of positions of molecules m and n, and $I_\mathrm{R/L}$ is intensity of the right/left circularly polarized light. The double sum in (3) disappears because of different phase factors of transition vibrational polarizabilities of different molecules.[20,21] For isotropic samples we can further average over molecular orientations, and express S_0 with polarizabilities related to one molecule as follows:

$$S_0 = \frac{KN}{2}\left(7\alpha_{\alpha\beta}\alpha_{\alpha\beta} + \alpha_{\alpha\alpha}\alpha_{\beta\beta}\right). \tag{4}$$

In (4) the Greek indices are related to a molecule-fixed coordinate system and the Einstein summation convention is applied here and further in the text. Adding the magnetic dipolar and electric quadrupolar parts, we similarly get the ROA intensity related to the S_3 Stokes parameter as[21]

$$\begin{aligned} I_\mathrm{R} - I_\mathrm{L} = S_3 &= \frac{8KN}{c}\Big(3\alpha_{\alpha\beta}G'_{\alpha\beta} - \alpha_{\alpha\alpha}G'_{\beta\beta} \\ &\quad + \frac{1}{3}\,\omega\alpha_{\alpha\beta}\boldsymbol{\varepsilon}_{\alpha\gamma\delta}A_{\gamma,\delta\beta}\Big) \end{aligned} \tag{5}$$

where c is the velocity of light and $\boldsymbol{\varepsilon}$ is the antisymmetric tensor.

The single-molecule theory can be formally extended for simulations based on molecular clusters if we consider the liquid also as a sum of clusters. Any liquid volume V of N molecules can be divided into a sum of one molecule volumes v_i, volumes of molecular pairs $v_{ij} = v_i + v_j$, *etc.* (We do not consider the case when the size of the volume approaches the wavelength of the light.) For example, we can treat 3 molecules ($N = 3$) as monomers ($m = 1$) with $V = v_1 + v_2 + v_3$, dimers ($m = 2$) with $V = \frac{1}{2}(v_{12} + v_{13} + v_{23})$, where $v_{12} = v_1 + v_2$, *etc.* In general, for clusters of m molecules,

$$V = \frac{(m-1)!(N-m)!}{(N-1)!}\sum_{i_1 < i_2 < \ldots < i_m} v_{i_1 i_2 \ldots i_m}. \tag{6}$$

The total polarizability is then

$$\alpha = \frac{(m-1)!(N-m)!}{(N-1)!}\sum_{i_1 < i_2 < \ldots < i_m} \alpha_{i_1 i_2 \ldots i_m}, \tag{7}$$

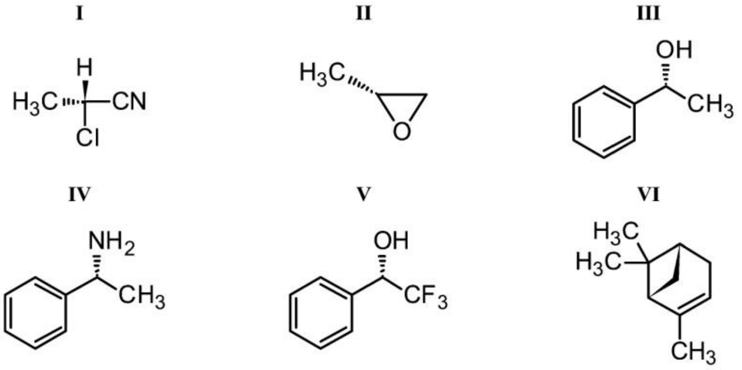

Fig. 1 Studied molecules: **I** (*R*)-2-chloropropionitrile (nitrile), **II** (*R*)-(+)-propylene oxide (methyloxirane,), **III** (*R*)-(+)-1-phenylethanol, **IV** (*R*)-(+)-α-methylbenzylamine, **V** (*S*)-(+)-α-(trifluoromethyl)benzyl alcohol, and **VI** (+)(1*R*,5*R*)-α-pinene.

where $\alpha_{i_1 i_2 \ldots i_m}$ is the polarizability of a cluster containing molecules $i_1 \ldots i_m$. The exact result is obtained for $m \rightarrow N$, when all important intermolecular interactions are included. Note that although eqn (6) and (7) may justify both the cluster and crystal-cell approaches they were not directly used in any calculation.

2.2 The periodic model

To well-represent the liquid, the clusters need to be in contact with the environment. This can be achieved using a periodic crystal-like model. Because of the periodicity, vibrational Hamiltonian *H* can be written as a sum over the phonon (wave) vectors **q** and atoms *i* within one cell only,[23]

$$H=\sum_{\mathbf{q}}\frac{1}{2}\left(\sum_i m_i\dot{x}_i^*\dot{x}_i+\sum_i\sum_j x_i^* D_{ij}x_j\right), \qquad (8)$$

where m_i and x_i are atomic masses and coordinates, and $\mathbf{D}(\mathbf{q})$ is the dynamic matrix. Only for $\mathbf{q} = 0$ we get non-zero Raman and ROA intensities. For other values signals of different elementary cells cancel out by interference. For zero wave vector,

$$D_{ij}=\sum_J f_{ij}, \qquad (9)$$

where J runs over the elementary cells containing the j-coordinate, f_{ij} are the harmonic force constants (force field). The Cartesian-normal mode transformation matrix **S** is obtained by the force field diagonalization, and the transition polarizabilities in (3) and (5) are obtained from the polarizability derivatives.[9] For example, for a fundamental transition involving the normal mode Q_J, the transition polarizability needed in eqn (4) and (5) for Raman scattering is[9]

$$\alpha(\omega,\omega')=\langle 0|\hat{\alpha}|1\rangle=\sqrt{\frac{\hbar}{2\omega_J}}S_{iJ}\alpha_i, \qquad (10)$$

where ω_J is the normal mode frequency, $\hat{\alpha}$ is the polarizability dependent on atomic coordinates, α_i is a derivative with respect to coordinate i.

2.3 Spectral measurement

The six molecules studied are summarized in Fig. 1. Experimental spectra of nitrile **I** were already published.[14] Its small size, availability of both enantiomers, and relative rigidity make it a convenient testing compound. Also methyloxirane **II** is used as a convenient benchmark model for the theory.[15,24–26] A series of the ethylbenzene derivatives **III**, **IV** and **V** allows one to evaluate the spectroscopic properties of similar molecules with a mixture of inter and intramolecular low-frequency vibrational modes. (For **III** and **IV**, the very first ROA spectra were observed in 1973.[27,28]) Finally, α-pinene **VI** is an example of a non-polar molecule with weak intermolecular interactions.

Raman and ROA spectra were acquired on a custom-made ROA instrument made at Palacký University Olomouc.[14] The samples were measured in a rectangular fused silica cell of 70 μl volume, the temperature was stabilized at (20.0 ± 0.1) °C, and the back-scattering scattered circular polarization (SCP) modulation scheme was used, with a 532 nm excitation wavelength. All compounds were measured as neat liquids, and methyloxirane was additionally measured in aqueous solution at a 1 : 22 methyloxirane : H_2O molar ratio. Lower temperature (6.0 ± 0.1) °C was used for the neat and dissolved methyloxirane (boiling point at 34 °C), to prevent its evaporation. Laser powers at the sample and accumulation times are listed in Table S1 (ESI†). For **V** only one enantiomer was available, otherwise both enantiomers were measured and idealized "(*R*–*S*)/2" ROA spectra for the *R*-forms are presented. A fluorescence background in the Raman signal of **V** caused by impurities was subtracted using the asymmetric least squares algorithm,[29,30] with the asymmetry parameter 1×10^{-4} and smoothness 8.5×10^4. Experimental intensities are given as the number of detected electrons per excitation energy in a wavenumber interval (e^- cm J^{-1}).

2.4 Computations

Molecular dynamics (MD) was performed using the Tinker program.[31] Some computations were repeated or complemented using the Amber software,[32] which allowed for a more

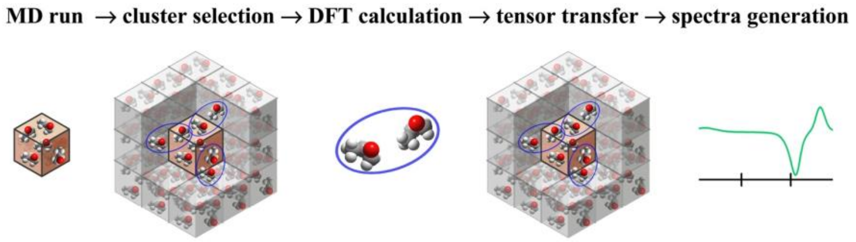

Fig. 2 Simulations of the spectra by the default crystal-like model. Intermolecular interactions within the periodic elementary cell (the brown/middle cube) and towards its environment were simulated for molecular pairs, in an arbitrary 27 cube "supercube". The pair parameters (force field, intensity tensors) were transferred back to the supercube, and the spectra were simulated using the periodic boundary conditions.

extensive parallelization and time saving, providing nearly identical results to Tinker. The OPLSAA force field was used,[33] with periodic boundary conditions, production run of 10 ns, 1 fs integration time, *NVT* ensembles, and temperature of 298 K. For methyloxirane the OPLSAA force field was modified to reproduce bond lengths and angles calculated by Gaussian[34] at the B3LYP/aug-cc-pVTZ/COSMO(THF) approximation level. Bigger periodic cubic boxes (about 40 Å a side) were used for investigations of the radial distribution functions, smaller ones (Table S2, ESI† containing 10 molecules) were used to generate many snapshots and their spectra.

Vibrational frequencies and spectral intensities were calculated using the Gaussian program and the B3PW91[35]/6-31G**/COSMO[36]/GD3BJ[37,38] method. Even 10 molecules in the box were too many for a direct calculation of a large number of snapshots needed for convergence. Therefore, smaller clusters were made, by default containing two close molecules, presumably comprising the strongest intermolecular interaction within the periodic box and 26 neighboring boxes (Fig. 2). The geometries of the pairs or larger clusters were partially optimized in the normal mode coordinates.[39–41] Modes with frequencies below 225 cm^{-1} (or below 100i cm^{-1} when imaginary, $i = \sqrt{-1}$) were fixed, and harmonic frequencies were calculated at the same level as the geometries. For Raman and ROA intensity tensors the rDPS[42] basis set was combined with the B3PW91/6-31G**/COSMO/GD3BJ force field. The rDPS basis set has been recommended for ROA because of a good balance between the computational demands and quality of the results.[42,43] For example, rDPS polarizability derivatives were calculated about 2–3 times faster than for a larger 6-31++G** basis set, giving almost identical results (Fig. S1, ESI†). The rDPS basis set alone is not suitable for the frequencies, underestimating them by about 40–50 cm^{-1} (*cf.* Fig. S1c and d, ESI†). A simpler BPW91 functional was tried

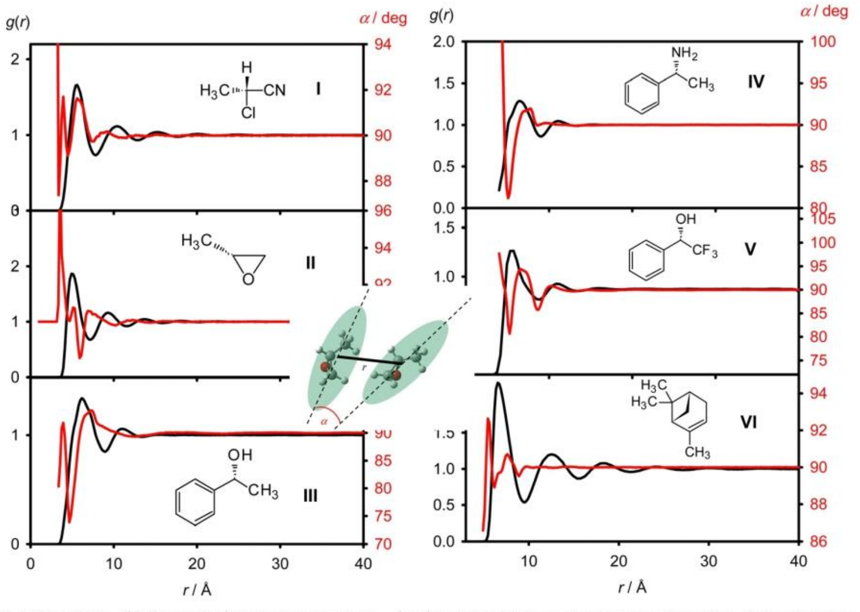

Fig. 3 Radial distribution functions *g*(*r*) (black line) and average angle α (red) between two molecules as a function of the distance. The angle is defined according to the main moments of inertia as indicated in the inset.

and gave qualitatively similar results to B3PW91; also the influence of the GD3BJ dispersion correction was rather minor (Fig. S2, ESI†).

Vibrational parameters (force field and polarizability derivatives) thus obtained for the smaller clusters were transferred back to the 3 × 3 × 3 supercube (Fig. 2) using the Cartesian coordinate transfer (CCT).[44,45] From the resultant force field we obtained the dynamic matrix (eqn (9)) and calculated the Raman and ROA intensities for each transition i (I_i, eqn (4) and (5)). Smooth spectra were obtained as

$$S(\omega)=\sum_i I_i\left[1-\exp\left(-\frac{\omega_i}{kT}\right)\right]^{-1}\left[4\left(\frac{\omega-\omega_i}{\Delta}\right)^2+1\right]^{-1}, \quad (11)$$

where ω_i is the transition frequency, k is the Boltzmann constant, Δ = 10 cm^{-1}, and temperature T = 298 K. The magnitude of the bandwidth (Δ) approximately corresponds to the experimental resolution and thus facilitates comparison to the experiment.

For testing, as an alternative to the default crystal-like model (part 2.2), larger clusters comprising one molecule and its first solvation sphere were also used for spectral generation, following ref. 14. Selected from MD with the bigger periodic boxes, the clusters were partially optimized and the spectra calculated following the procedure described above for the crystal model. Finally, we also experimented with the supercube (Fig. 2), which we used not only for the generation of the dynamic matrix in the crystal model, but directly as a cluster. Although these two cluster models miss the continuous character of the liquid, as shown below they also reproduce some of the features observed experimentally.

3. Results and discussion

3.1 Molecular dynamics simulations

The radial distribution functions (RDFs) calculated from MD provide insight into the range of intermolecular interactions in the studied liquids (Fig. 3). All exhibit a clear maximum of the first solvation sphere, at 5.6 Å (**I**), 5.1 Å (**II**), 6.2 Å (**III**), 6.5 Å (**IV**),

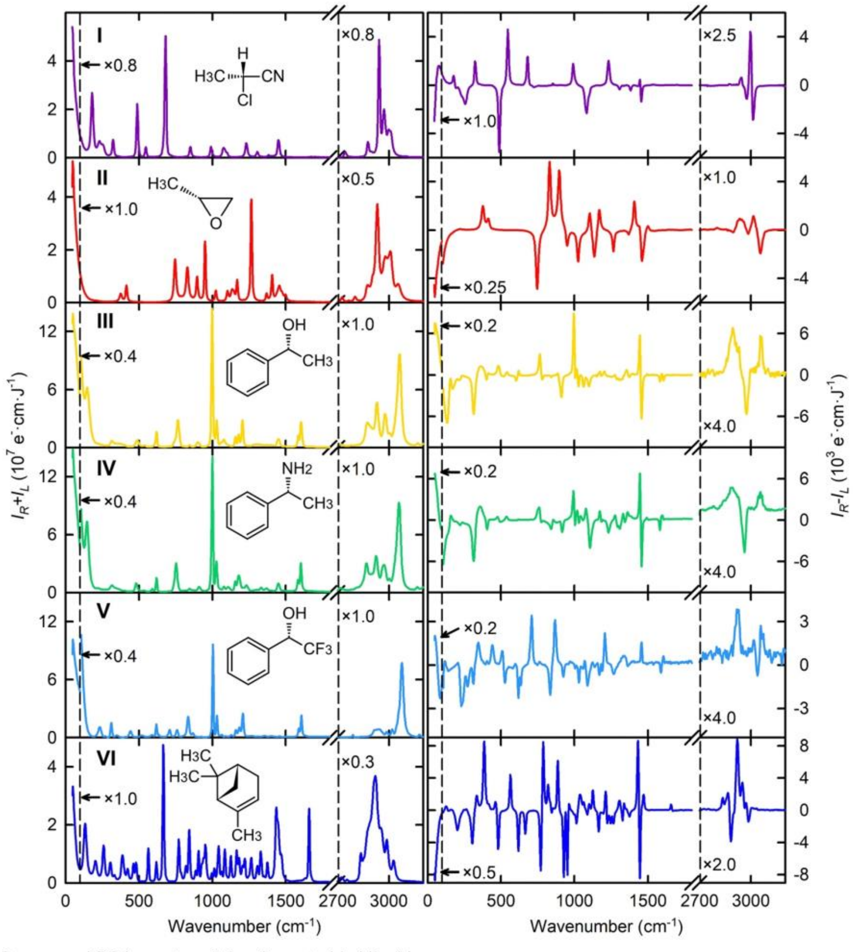

Fig. 4 Experimental Raman and ROA spectra of the six neat chiral liquids.

6.0 Å (**V**), and 6.5 Å (**VI**). Other maxima associated with higher solvation spheres are obviously less pronounced, although the fifth solvation sphere maximum of α-pinene at ∼30 Å is still visible. Also the RDFs of the other two "rigid" molecules, methyloxirane and nitrile, are structured up to a relatively long distance, whereas for the ethylbenzene derivatives the structure is nearly destroyed after the second maximum.

The angle α between the main axes of molecular moments of inertia (red lines in Fig. 3) averages to 90° for distant non-interacting molecules. At shorter distances molecules interact and adopt energetically favorable mutual orientations. The case when $\alpha \neq 90^\circ$ thus indicates that an additional source of chirality in the solution exists, apart from the absolute configuration of individual molecules. This can potentially contribute to low-frequency ROA. We can see that for the rigid molecules (nitrile, methyloxirane, and α-pinene) α does not deviate by more than 3° from the 90° average, except for the closest distance limit. Ethylbenzenes **III–V** adapt their shapes upon more contact and the deviations from 90° are bigger, with an extreme value of 15° for alcohol **III**.

For **III–V** the molecular flexibility can also be judged from the dependencies of the electronic energy (B3PW91/6-311++G**/COSMO) on the conformation of the phenyl, hydroxy and amine groups (Fig. S3, ESI†). All three molecules prefer the polar OH or NH groups pointing out of the phenyl plane ($\varphi \sim 100^\circ$). The OH/NH$_2$ groups are relatively freely rotating, with energy minima with ψ at about ±60° and 180°. The potential energy barriers between the minima are within 1–2 kcal mol^{-1} for **III** and **V**, and higher (3 kcal mol^{-1}) for **IV**. For **III** and **IV**, the calculated potential energy surfaces are consistent with a previous study.[28] However, the distributions of MD conformers (black dots in Fig. S3, ESI†) follow the DFT results only approximately. We explain this by the possibility of the molecules to form hydrogen bonds in MD, which is only partially simulated by the COSMO continuum solvent model.[46]

3.2 Experimental spectra

The experimental Raman and ROA spectra recorded in the whole range (∼50–3200 cm^{-1}) for the six compounds are plotted in Fig. 4. When available, enantiomers gave opposite

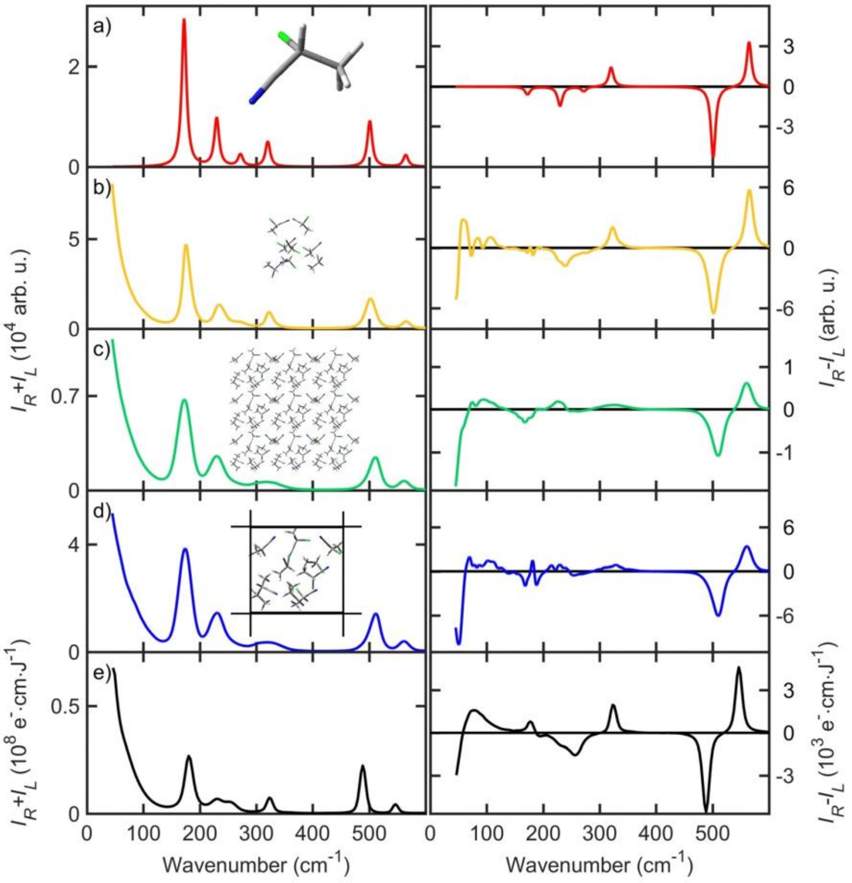

Fig. 5 Raman and ROA nitrile (**I**) spectra calculated with different models: (a) single molecule, (b) small cluster/all interactions, (c) large cluster/pair interactions, (d) periodic crystal/pair interactions (*cf.* Fig. 2), and (e) experimental spectrum. For b–d 200 MD snapshots were averaged.

ROA, suggesting a very low level of instrumental artifacts (Fig. S4, ESI†). The region within 1800–2700 cm^{-1} is not shown because there is only one fundamental band, nitrile $C{\equiv}N$ stretching. ROA signal at the CH stretching region ($>2700\ \text{cm}^{-1}$) is relatively weak, but the shapes therein are also characteristic for individual molecules. The strong "scissoring" signal of compounds containing methyl groups (±ROA couplet at $\sim 1450\ \text{cm}^{-1}$) is missing for **V**. We also see the bigger sensitivity of ROA spectra compared to Raman scattering; compounds **III–V** have very similar Raman spectra, but only some ROA features are alike.

Normalized circular intensity difference ratios (CID = ROA/Raman, Fig. S5, ESI†) in the CH stretching region are rather small (maximum of $\sim 1 \times 10^{-4}$ for **I**, 3×10^{-5} for **VI**, *etc.*). In the lower frequencies ($<2000\ \text{cm}^{-1}$) CIDs are higher, up to $\sim 9 \times 10^{-4}$ for the smaller molecules and $\sim 2 \times 10^{-3}$ for **VI**. At the 50 cm^{-1} instrumental limit CIDs are rather small again, **II** and **VI** giving the highest values of 4×10^{-4} and 6×10^{-4}, respectively. The CID parameters are important, for example, for determining the reliability of the measurement and for comparison to the simulations. Note, however, that the experimental values cannot be determined too accurately due to the fluorescent background in the Raman spectrum.

Below we focus on the lowest-wavenumber region, where all liquids have strong ROA even as the frequency approaches 50 cm^{-1}. For **I** and **III–V**, there are also strong bands at $\sim 90\ \text{cm}^{-1}$. These have opposite sign to the intensity at the 50 cm^{-1} limit. The six compounds studied suggest that the low frequency signal is not related to a particular molecular property, such as size, hydrophobicity, or the ability to make hydrogen bonds. This was also observed for a few other chiral liquids not shown here.

3.3 Strategies for spectra modeling

Fig. 5 compares spectra of **I** simulated with (a) one nitrile molecule, (b) molecular clusters, (c) bigger cluster with pair interactions only, and (d) the periodic crystal model; (e) is the experimental spectrum. The low-frequency intermolecular signal is obviously missing in the single molecule spectra (a). Also the inhomogeneous broadening of the bands within 150–350 cm^{-1} simulated by the arbitrary Lorentzian band is not realistic. The other models based on MD do provide the intermolecular signal with a correct ROA sign pattern, (positive at $\sim 80\ \text{cm}^{-1}$, negative close to 50 cm^{-1}). Minor spectral features are difficult to judge due to the limited precision of the calculations and limited experimental resolution.

The MD, however, except for the small cluster model (b), overestimates the broadening of the 242 and 325 cm^{-1} bands. As discussed previously[47] generation of the spectra using the instantaneous normal mode approximation and partial optimization[39] of MD geometries is a rather empirical procedure, which may contribute to this inconsistency. The widths of the intramolecular bands within 150–300 cm^{-1} are simulated qualitatively correctly. The periodic crystal-like model (d) is technically the most advanced one and avoids the surface cluster effects, but it comprises pair molecular interactions only. Some experimental features, like the relatively monotonic increase of the ROA intensity between 250 and 90 cm^{-1}, are therefore better reproduced with the smaller clusters containing more intermolecular interactions (b). The large cluster model (c) seems to give the worst results. Nevertheless, we see that all the cluster models are able to reasonably well reproduce also the intermolecular low-frequency ROA signal. Spectra simulated with the crystal-like model (d) for all compounds in a broad wavenumber range are summarized in Fig. S6 (ESI†). This model is also used as a default below, unless said otherwise.

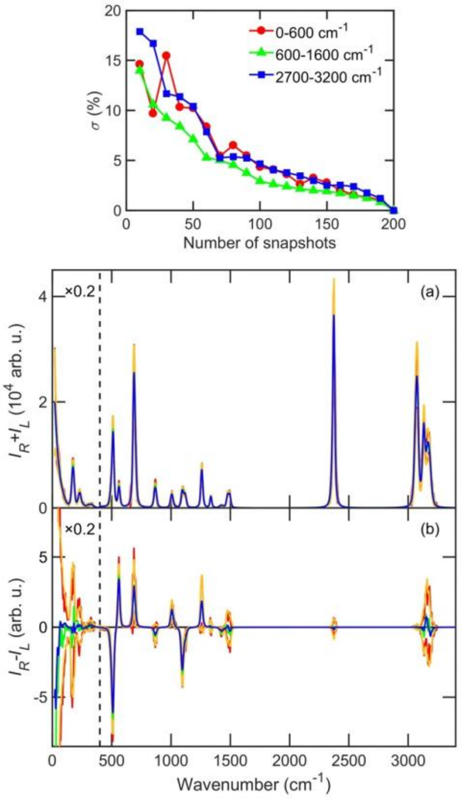

Fig. 6 Nitrile, (top) dependence of the ROA spectral average error ($\sigma = \int |S_i - S_f| d\nu / \int |S_f| d\nu$, S_i and S_f are the partial and final average) on the number of averaged snapshots, for three spectral regions, and (bottom) Raman and ROA nitrile spectra averaged from 20 (green) and 200 (blue) MD snapshots; standard deviations ($s = \sqrt{(N-1)^{-1} \sum (S_i - \bar{S})^2}$) at each point are plotted using red (20) and orange (200) lines.

A serious problem limiting the precision of the computations is a large number of MD snapshots that need to be averaged for low-frequency ROA. The convergence is documented at the top of Fig. 6. We can see the ROA spectral error as dependent on the number of averaged snapshots, in the low (0–600 cm^{-1}), middle (600–1600 cm^{-1}) and CH stretching (2700–3200 cm^{-1}) regions. The 200-snapshot average is taken as a reference. The low-frequency ROA signal converges more slowly than within 600–1600 cm^{-1}. About 100 snapshots need to be averaged to push the error below 5%. For Raman (not shown)

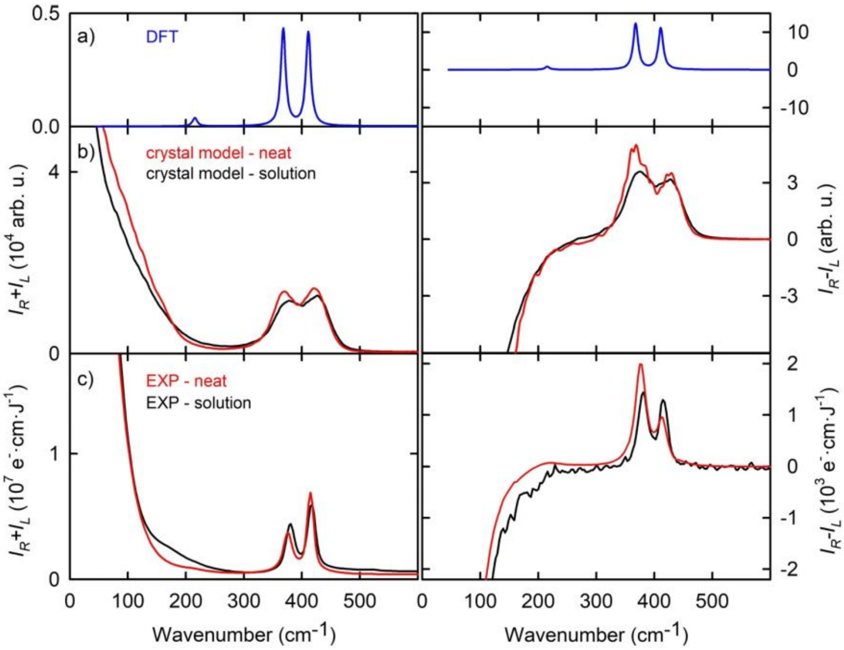

Fig. 7 Raman and ROA spectra of neat methyloxirane and its water solution: (a) single molecule computation, (b) crystal model, and (c) experiment.

about 10 snapshots would be enough. Somewhat surprising is a slow convergence of the CH ROA signal, similar to that for the low-frequency region. This can perhaps be explained by the extended coupling of the CH stretching motion with other modes.[48]

At the bottom of Fig. 6 Raman and ROA spectra of the nitrile are plotted as calculated from 20 and 200 MD snapshots. About 20 snapshots already provide many spectral features observed also experimentally, but the positive 80 cm^{-1} ROA maximum, for example, appears only after the whole set is included. The ROA sensitivity to a momentary MD geometry is also reflected by the standard deviations plotted using red and orange lines in Fig. 6. These clearly become extreme for low-frequency ROA. For bands above 400 cm^{-1} the 20 and 200 snapshot averages are nearly the same. The convergence problem makes the computation expensive. Note that one snapshot already involves some averaging over molecular orientations. For example, if there are 10 molecules in the elementary cell (Fig. 2) we need to calculate force fields for about 50 different pairs of molecules to comprise at least the main intermolecular interactions within this cell and to neighboring ones.

On one nitrile snapshot, we also tested the convergence of the spectra with respect to the number of molecules taken in the clusters to calculate the force field (Fig. S7, ESI†). Increasing this value is quite computationally demanding: one elementary cell of 10 molecules provides 10 monomers, roughly 50 dimers of close molecules, 390 trimers, 1300 tetramers, *etc.* In the trial snapshot, accounting for three and four-molecule interactions seems to produce some additional ROA features around 100 cm^{-1} compared to the pairs; however, this is not observed experimentally and likely disappears during the averaging. The low-frequency ROA signal for the monomers is caused by differences of equilibrium and MD geometries, which is an inherent restriction of our method, but may be significantly reduced during further averaging. Increasing the number of molecules in one elementary cell (*i.e.*, size of the MD box) did not seem to bring an improvement and 10 molecules in the box thus seem to be sufficient for a converged result (Fig. S8, ESI†).

3.4 Methyloxirane solution and vibrational mode analysis

Interestingly, neat methyloxirane gave nearly the same low-frequency ROA signal as its water solution, and this result could be reproduced by the crystal model (Fig. 7). To achieve a reasonable convergence, however, more MD snapshots (1000) were needed for the solution than for the neat liquids (200). In the experiment, compared to the neat liquid, the water solution has an extra Raman and ROA signal around 180 cm^{-1}, most probably originating in the methyl group rotation. Also the two fundamental bands of skeletal/bending modes around 400 cm^{-1} are shifted by ~3 cm^{-1} to the right. These details are partially reproduced by the calculations (band shift by ~8 cm^{-1}), and the overall reasonable agreement between the experiment and the modeling allows us to better understand the low-frequency ROA, primarily stemming from translational and rotational-like motions of individual chiral molecules. This observation is consistent with Fig. 3 showing that two methyloxirane molecules are not much mutually oriented even at the closest distances. In other words, a methyloxirane molecule senses the neighboring one primarily as spheres, and their shape or chirality plays a secondary role.

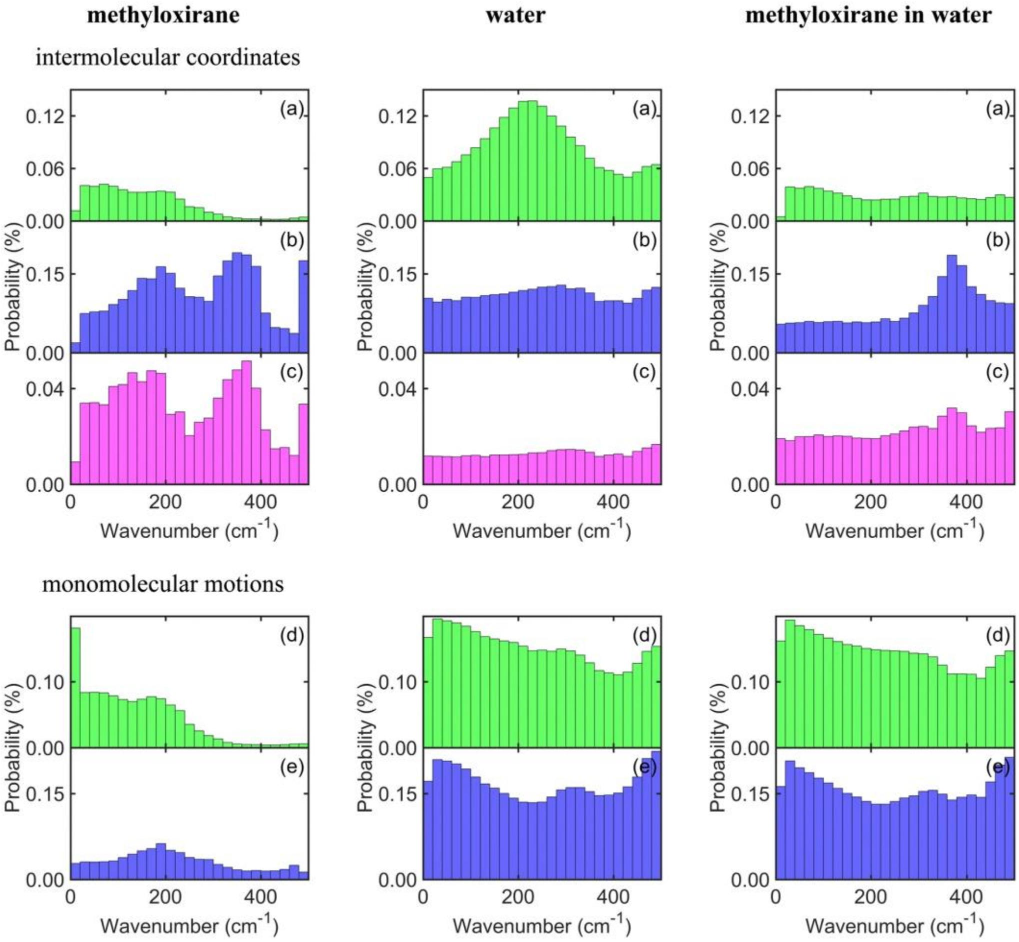

Fig. 8 Relative vibrational potential energies of intermolecular motions related to two (stretching (a), bending (b), torsion (c)) and one (translations (d), rotations (e)) molecules, for neat methyloxirane, water and a mixture.

In a different way we try to understand the low-frequency vibrations introducing intermolecular coordinates, or translations and rotations of one molecule.[14] The corresponding potential energy distributions (PEDs, see the definition in Fig. S9, ESI†) are plotted in Fig. 8. Note that redundant sets of the coordinates were created automatically and their PEDs are not unique. Nevertheless, in the current set we see that intermolecular motions formally contribute differently to the vibrational energy in water, methyloxirane, and the mixture. In pure water, a clear band around 220 cm^{-1} for the stretching (a) is developed. In neat methyloxirane the stretching starts to contribute in the lowest frequencies only, and the contribution is smoothed out in the mixture. The bending (b) and twisting (c) modes are most structured in neat methyloxirane, reflecting the more complicated shape of the molecule. At this level, it is difficult to interpret the histograms in more detail, but the broadness of the probability distributions does not suggest that a specific interaction would be responsible for the low-frequency ROA, and is thus consistent with the similarity of the neat liquid and solution spectra.

3.5 III–VI, theory *vs.* experiment

For the other molecules (**III–VI**) the vibrational potential energy distributions (Fig. S9, ESI†) are more complex than for water or methyloxirane. The intermolecular modes are more intertwined with low-frequency intramolecular motions, such as rotations of the phenyl, methyl, hydroxyl, trifluoromethyl and amine groups (*cf.* Table S3, ESI† with the normal mode assignment). The histogram distributions for **III–V** are quite similar, showing higher contributions of molecular translations, intermolecular stretchings and rotations with decreasing frequency. For α-pinene **VI** the stretching also becomes important for the lowest frequencies, while the intermolecular bending and twisting modes are more mixed with intramolecular ones and formally thus contribute even close to 500 cm^{-1}.

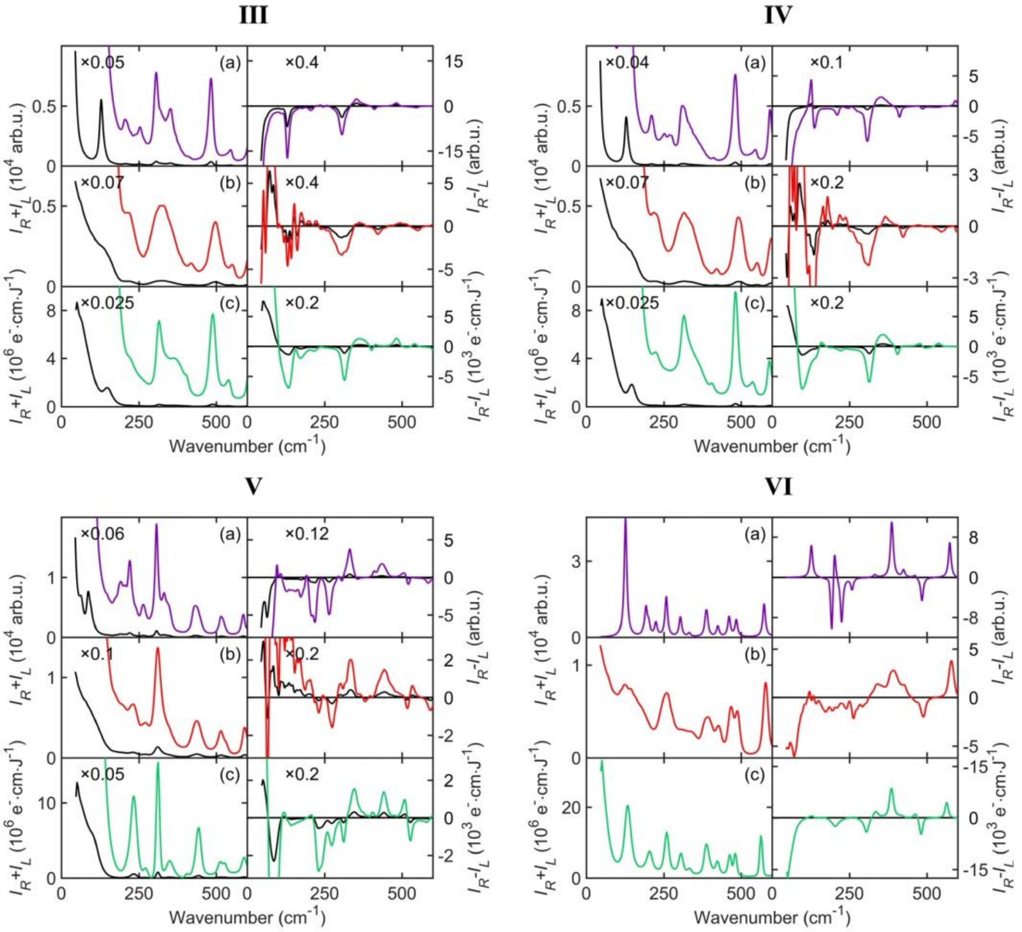

Fig. 9 Raman and ROA spectra of **III–VI** (a) simulation of one molecule (**III–V** conformer averaging, **VI** – minimum only), (b) the crystal model, and (c) the experiment.

Raman and ROA spectra of **III–VI** simulated with one molecule including averaging over the potential energy surface and the crystal-like approach are compared to those of the experiment in Fig. 9. These "more complicated" molecules possess many low-frequency intra(mono)molecular fundamental vibrational modes, and the single molecule simulation reasonably well describes some Raman and ROA spectral features down to ~ 200 cm^{-1}. However, in the lowest frequency region the multimolecular crystal model performs better. In particular, it correctly gives the ROA sign as the frequency approaches 50 cm^{-1}. Least satisfying is the simulation for the fluorine-containing compound **V**, probably because of inaccuracy of the OPLSAA force field. For example, the crystal model often gives the fundamental bands too broad and wrong signs of the 507 and 528 cm^{-1} ROA bands of **V**. In spite of these minor inconsistencies, we find it important that we can at least semi-quantitatively understand the observed data in terms of molecular structure and interactions. The modeling technology is also flexible and open to improvement when a bigger computer power becomes available.

4. Conclusions

We developed a crystal-like computational protocol that allowed us to analyze in detail low-frequency ROA spectra of six example chiral liquids. The results show that the signal is a complicated function of molecular structure that can be understood only on the basis of spectral simulations. The low-frequency modes are not too specific; nevertheless, the analysis of the vibrational potential energy suggests that for small rigid molecules (α-pinene, chloropropionitrile, and methyloxirane) the low-frequency signal comes primarily from molecular translations and rotations. For more flexible molecules the molecular/intermolecular low-frequency modes are mixed with monomolecular fundamentals. Very similar spectra were observed for neat methyloxirane and its water solution; this rather surprising observation could be reproduced with the crystal model and provided a phenomenological insight into the low-frequency chirality. Although the precision of the simulations is limited due to available computer power, they provide a sound theoretical basis to interpret the observed spectra and can be systematically improved in the future. The low-frequency ROA spectroscopy thus provides an interesting window into the world of chiral molecules, their structure and interactions, and can bring about useful knowledge about their behavior for biology and industry.

Conflicts of interest

J. Kapitán and P. Michal are involved in commercialization of the ROA technique. The other authors have no interest to declare.

Acknowledgements

This work was supported by the Czech Grant Agency (20-10144S, 22-04669S), the Ministry of Education (CZ.02.1.01/0.0/0.0/16_019/0000729 and e-INFRA CZ LM2018140), and student grant of the Palacký University Olomouc (IGA_PrF_2022_001).

References

1 K. Bērziņš, S. J. Fraser-Miller and K. C. Gordon, *Int. J. Pharm.*, 2021, **592**, 120034.

2 P. Ranzieri, A. Girlando, S. Tavazzi, M. Campione, L. Raimondo, I. Bilotti, A. Brillante, R. G. Della Valle and E. Venuti, *ChemPhysChem*, 2009, **10**, 657–663.

3 S. Yamamoto, Y. Morisawa, H. Sato, H. Hoshina and Y. Ozaki, *J. Phys. Chem. B*, 2013, **117**, 2180–2187.

4 J. J. Lazarević, S. Uskoković-Marković, M. Jelikić-Stankov, M. Radonjić, D. Tanasković, N. Lazarević and Z. V. Popović, *Spectrochim. Acta, Part A*, 2014, **126**, 301–305.

5 L. A. Blatz, in *Raman Spectroscopy*, ed. H. A. Szymanski, Springer, Boston, MA, 1970, DOI: 10.1007/978-1-4684-3027-1_4.

6 Q. Zhong and J. T. Fourkas, *J. Phys. Chem. B*, 2008, **112**, 15529–15539.

7 E. W. Castner and M. Maroncelli, *J. Mol. Liq.*, 1998, **77**, 1–36.

8 D. A. Turton, J. Hunger, A. Stoppa, A. Thoman, M. Candelaresi, G. Hefter, M. Walther, R. Buchner and K. Wynne, *J. Mol. Liq.*, 2011, **159**, 2–8.

9 L. Nafie, *Vibrational optical activity: Principles and applications*, Wiley, Chichester, 2011.

10 S. Yamamoto, S. Ishiro, J. Kessler and P. Bouř, *Phys. Chem. Chem. Phys.*, 2021, **23**, 26501–26509.

11 V. Palivec, P. Michal, J. Kapitán, H. Martinez-Seara and P. Bouř, *ChemPhysChem*, 2020, **21**, 1272–1279.

12 J. Kessler, J. Kapitán and P. Bouř, *J. Phys. Chem. Lett.*, 2015, **6**, 3314–3319.

13 T. Buffeteau, D. Pitrat, N. Daugey, N. Calin, M. Jean, N. Vanthuyne, L. Ducasse, F. Wien and T. Brotin, *Phys. Chem. Chem. Phys.*, 2017, **19**, 18303–18310.

14 P. Michal, R. Čelechovský, M. Dudka, J. Kapitán, M. Vůjtek, M. Berešová, J. Šebestík, K. Thangavel and P. Bouř, *J. Phys. Chem. B*, 2019, **123**, 2147–2156.

15 M. Brehm and M. Thomas, *J. Phys. Chem. Lett.*, 2017, **8**, 3409–3414.

16 Y. Yang, J. Cheramy, M. Brehm and Y. Xu, *ChemPhysChem*, 2022, **23**, e202200161.

17 L. Rayleigh, *Philos. Mag.*, 1899, **47**, 375–384.

18 L. I. Komarov and I. Z. Fischer, *Soviet Phys. JETP*, 1963, **16**, 1358–1361.

19 A. Einstein, in *Collected Papers of Albert Einstein, The Swiss Years: Writings 1909–1911*, ed. M. J. Klein, A. J. Kox, J. Renn and R. Schulmann, Princeton U. P., Princeton, 1994, vol. 3, pp. 231–249.

20 A. G. Rojo and P. R. Berman, *Am. J. Phys.*, 2010, **78**, 94–101.

21 L. D. Barron, *Molecular Light Scattering and Optical Activity*, Cambridge University Press, Cambridge, UK, 2004.

22 D. Pestov, G. O. Ariunbold, X. Wang, R. K. Murawski, V. A. Sautenkov, A. V. Sokolov and M. O. Scully, *Opt. Lett.*, 2007, **32**, 1725–1727.

23 L. Piseri and G. Zerbi, *J. Mol. Spectrosc.*, 1968, **26**, 254–261.

24 F. Lipparini, F. Egidi, C. Cappelli and V. Barone, *J. Chem. Theory Comput.*, 2013, **9**, 1880–1884.

25 T. D. Crawford and K. Ruud, *ChemPhysChem*, 2011, **12**, 3442–3448.

26 J. Šebestík and P. Bouř, *J. Phys. Chem. Lett.*, 2011, **2**, 498–502.

27 L. D. Barron, M. P. Bogaard and A. D. Buckingham, *J. Am. Chem. Soc.*, 1973, **95**, 603–605.

28 J. Kapitán, C. Johannessen, P. Bouř, L. Hecht and L. D. Barron, *Chirality*, 2009, **21**, E4–E12.

29 P. Eilers and H. Boelens, Leiden University Medical Centre report, 2005.

30 S. Baek, A. Park, Y. Ahn and J. Choo, *Analyst*, 2015, **140**, 250–257.

31 J. W. Ponder, *Tinker, Software Tools for Molecular Design*, Washington University School of Medicine, Saint Louis, 3.8 edn, 2000.

32 D. A. Pearlman, D. A. Case, J. W. Caldwell, W. S. Ross, T. E. Cheatham, S. Debolt, D. M. Ferguson, G. Seibel and P. A. Kollman, *Comput. Phys. Commun.*, 1995, **91**, 1–41.

33 R. C. Rizzo and W. L. Jorgensen, *J. Am. Chem. Soc.*, 1999, **121**, 4827–4836.

34 M. J. Frisch, G. W. Trucks, H. B. Schlegel, G. E. Scuseria, M. A. Robb, J. R. Cheeseman, G. Scalmani, V. Barone, G. A. Petersson and H. Nakatsuji, *et al.*, *Gaussian 16 Rev. A.03*, Gaussian, Inc., Wallingford, CT, 2016.

35 A. D. Becke, *J. Chem. Phys.*, 1993, **98**, 1372–1377.

36 A. Klamt, V. Jonas, T. Burger and J. C. W. Lohrentz, *J. Phys. Chem. A*, 1998, **102**, 5074–5085.

37 S. Grimme, J. Antony, S. Ehrlich and H. Krieg, *J. Chem. Phys.*, 2010, **132**, 154104.

38 S. Grimme, S. Ehrlich and L. Goerigk, *J. Comput. Chem.*, 2011, **32**, 1456–1465.

39 P. Bouř and T. A. Keiderling, *J. Chem. Phys.*, 2002, **117**, 4126–4132.
40 P. Bouř, *Collect. Czech. Chem. Commun.*, 2005, **70**, 1315–1340.
41 P. Bouř, *Qgrad*, Academy of Sciences, Prague, 2006.
42 G. Zuber and W. Hug, *J. Phys. Chem. A*, 2004, **108**, 2108–2118.
43 K. Ruud and J. Thorvaldsen, *Chirality*, 2009, **21**, E54–E67.
44 P. Bouř, J. Sopková, L. Bednárová, P. Maloň and T. A. Keiderling, *J. Comput. Chem.*, 1997, **18**, 646–659.
45 S. Yamamoto, X. Li, K. Ruud and P. Bouř, *J. Chem. Theory Comput.*, 2012, **8**, 977–985.
46 P. Bouř, D. Michalík and J. Kapitán, *J. Chem. Phys.*, 2005, **122**, 144501.
47 J. Hudecová, K. H. Hopmann and P. Bouř, *J. Phys. Chem. B*, 2012, **116**, 336–342.
48 J. Hudecová, V. Profant, P. Novotná, V. Baumruk, M. Urbanová and P. Bouř, *J. Chem. Theory Comput.*, 2013, **9**, 3096–3108.

Supporting Information

Low-frequency Raman Optical Activity Provides Insight into Structure of Chiral Liquids

Pavel Michal, Josef Kapitán, Jiří Kessler and Petr Bouř

Contents

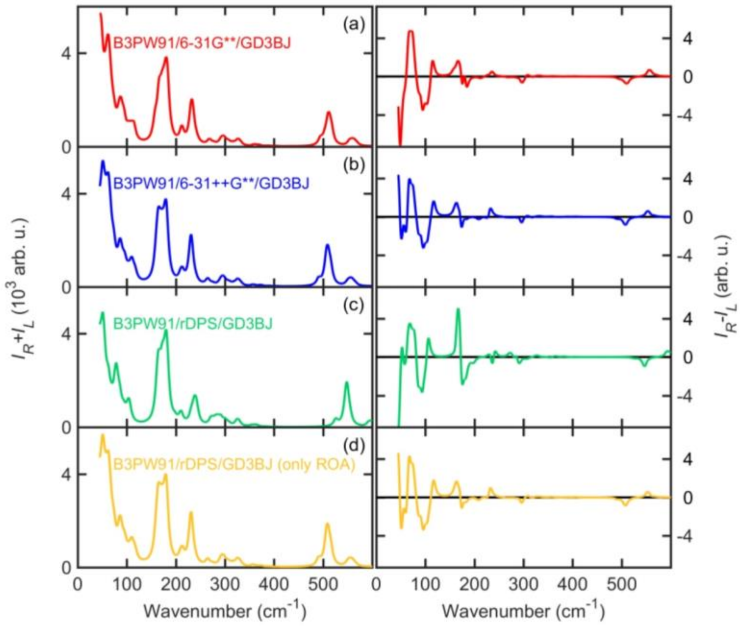

Figure S1. Raman and ROA spectra simulated for one snapshot of nitrile and three basis sets. For rDPS (d) the frequencies were calculated at the B3PW91/6-31++G**/COSMO(ACN)/GD3BJ level.

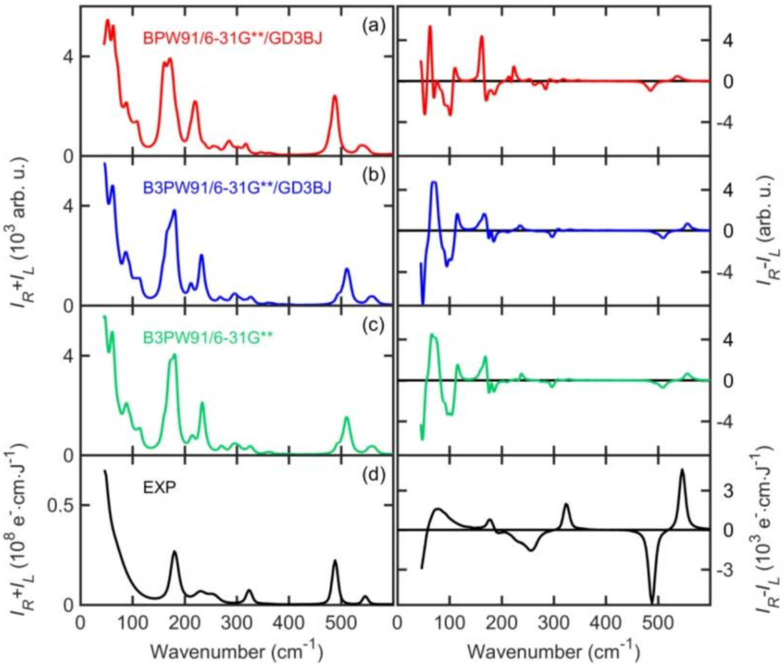

Figure S2. Nitrile Raman and ROA spectra calculated with the B3PW91 and BPW91 functionals, for B3PW91 with and without the GD3BJ dispersion correction, for the 6-31G** basis set and COSMO(ACN) solvent model.

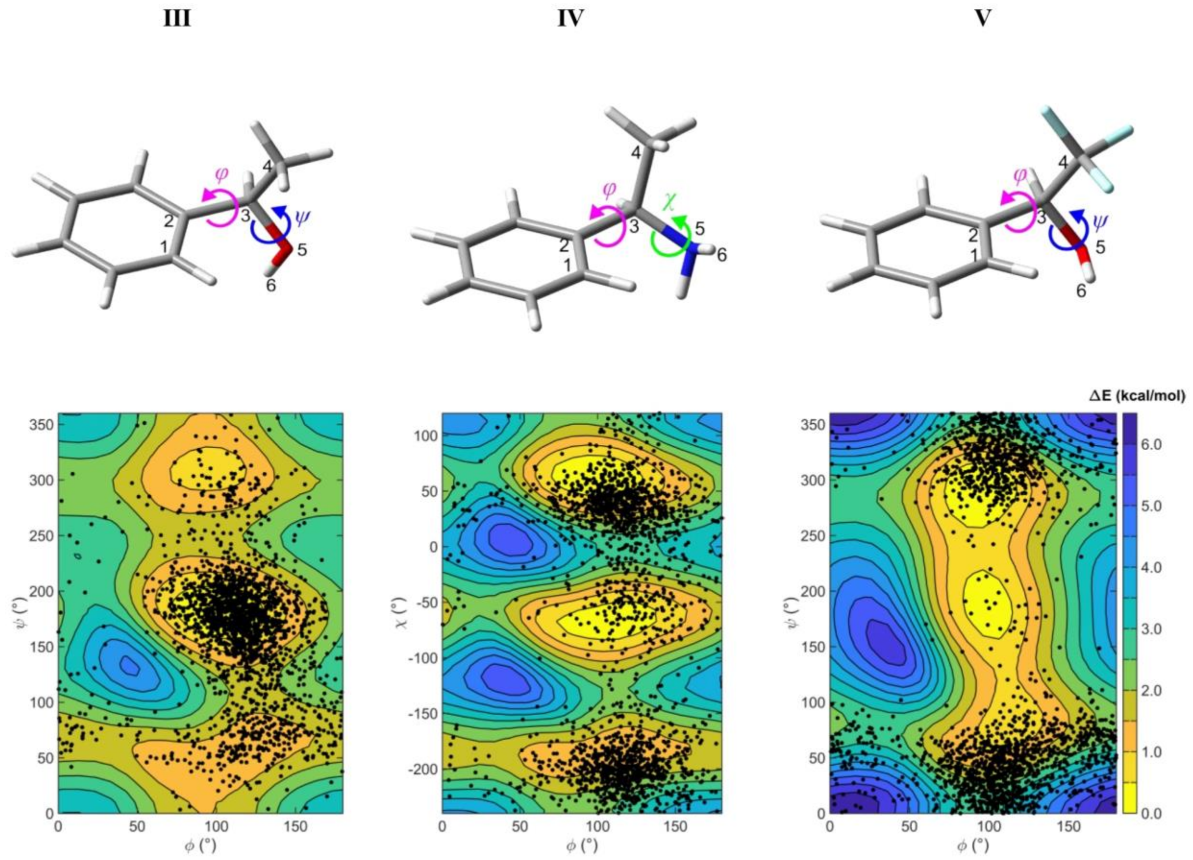

Figure S3. Dependencies of the electronic energy on selected torsion angles calculated at the B3PW91/6-311++G**/COSMO(benzylalcohol) level (contour map) and coordinates from 200 MD snapshots (black dots). The describe phenyl rotation, *φ* = C1-C2-C3-C4, hydroxyl rotation, *ψ* = C4-C3-O5-H6, and amine rotation, χ = C2-C3-N5-H6.

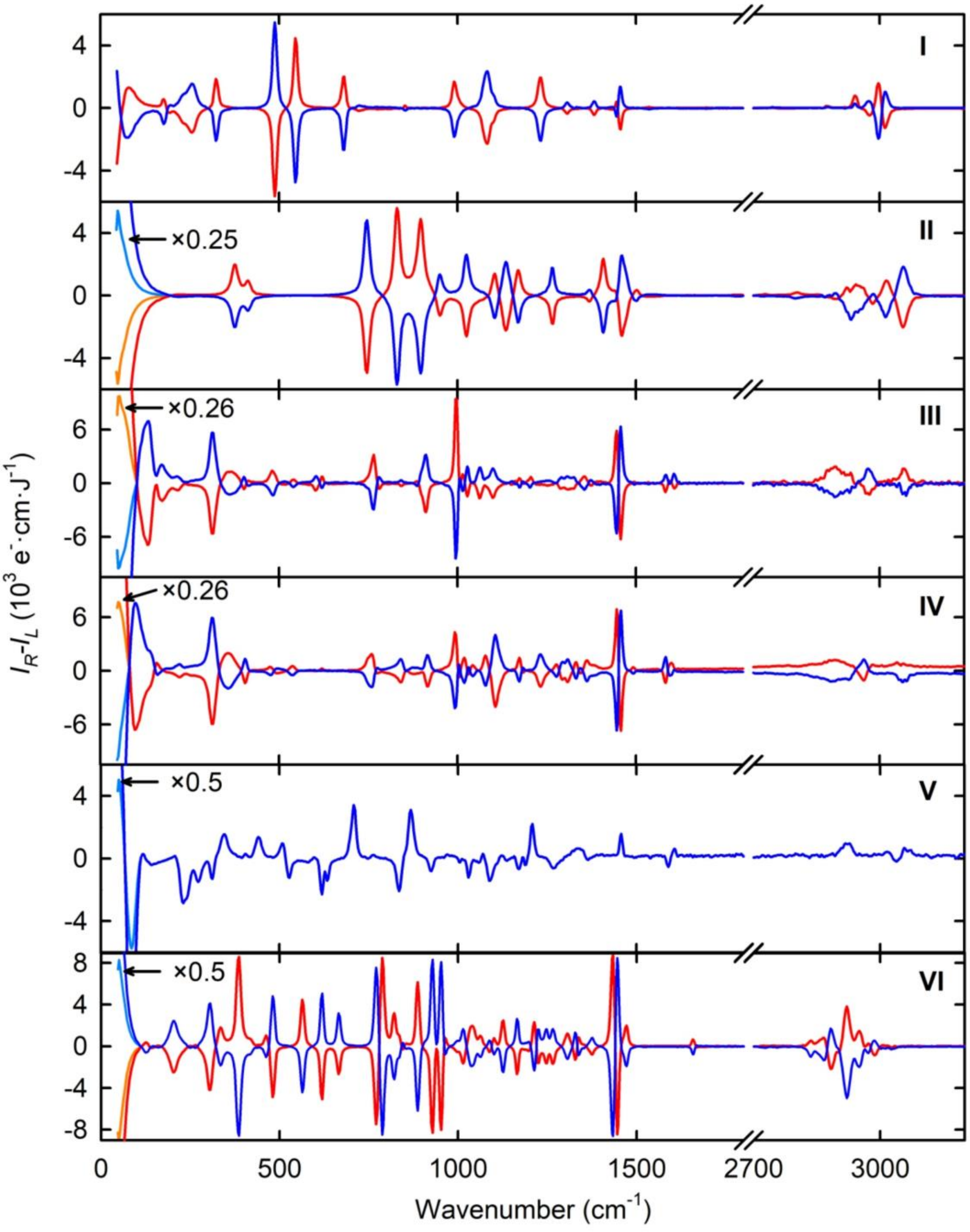

Figure S4. Experimental ROA spectra of the neat liquids, **I** 2-chloropropionitrile, **II** methyloxirane, **III** 1-phenylethanol, **IV** α-methylbenzylamine, **V** α-(trifluoromethyl)benzyl alcohol, and **VI** α-pinene. *R* and *S*-enantiomers are marked in red and blue, respectively.

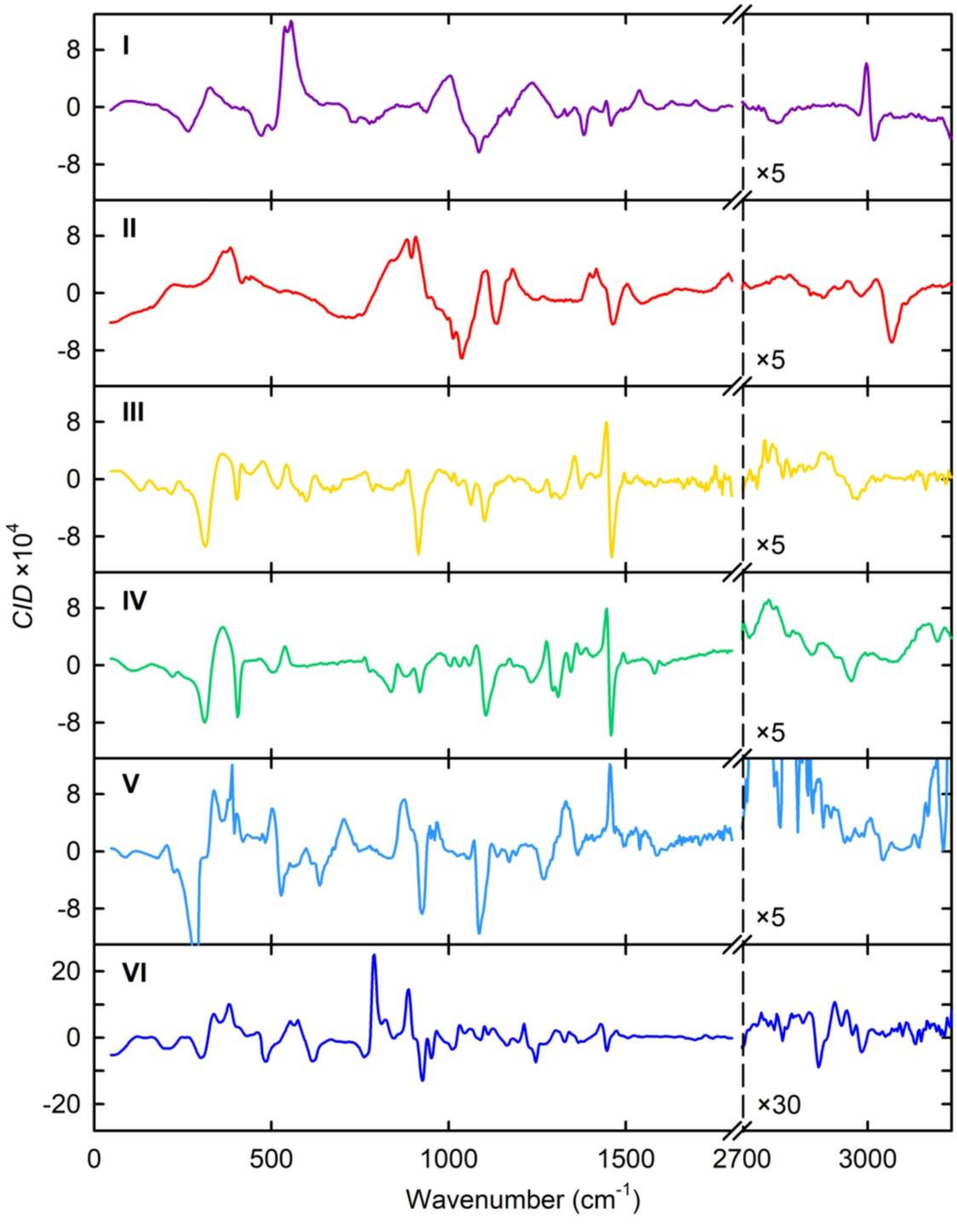

Figure S5. Experimental CID (ROA/Raman) ratios of **I** (*R*)-2-chloropropionitrile, **II** (*R*)-(+)-propylene oxide, **III** (*R*)-(+)-1-phenylethanol, **IV** (*R*)-(+)-α-methylbenzylamine, **V** (*S*)-(+)-α-(trifluoromethyl)benzyl alcohol, and **VI** (+)(1R,5R)-α-pinene.

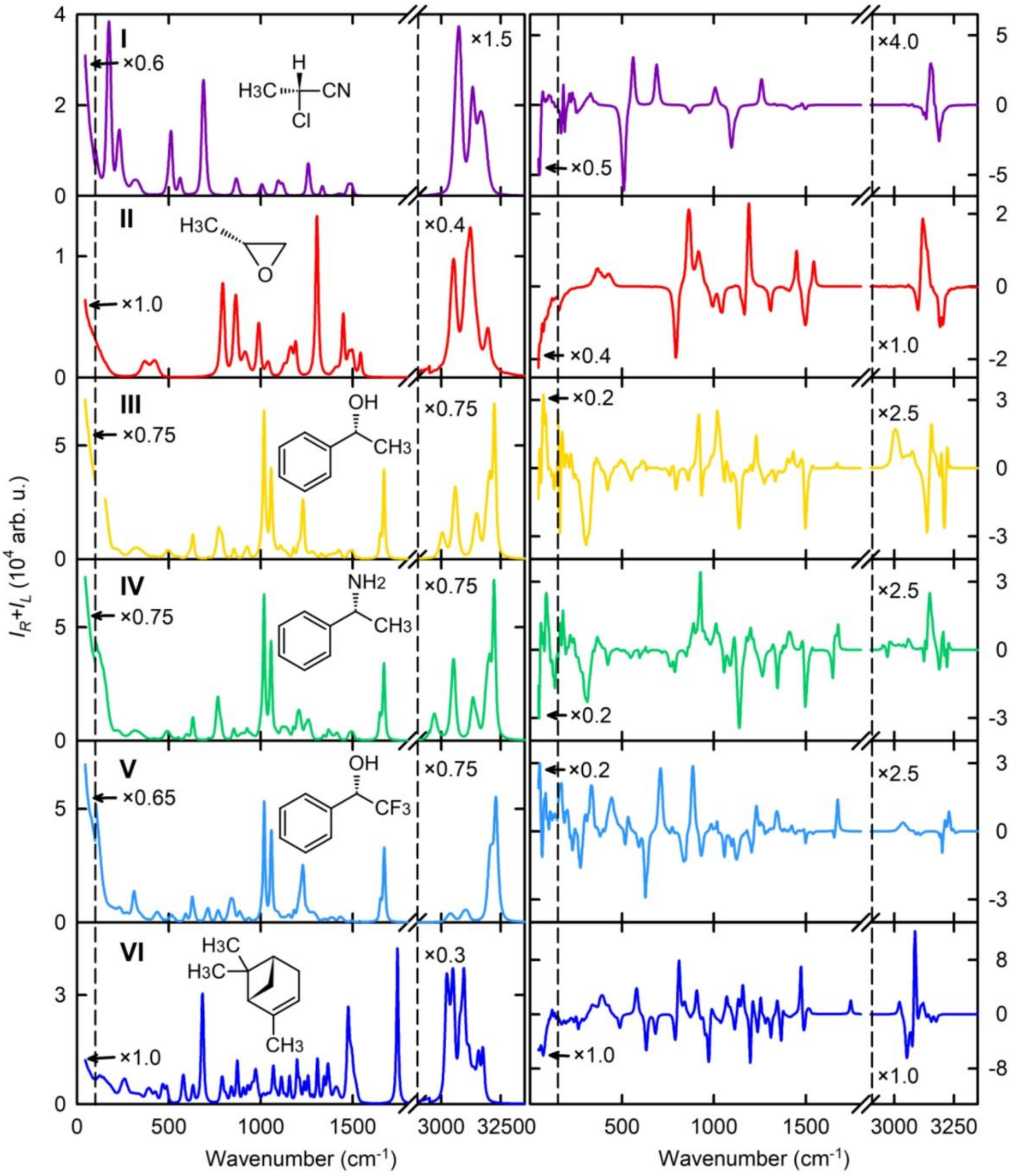

Figure S6. Raman and ROA spectra of **I**-**VI** simulated in the whole range, the crystal model.

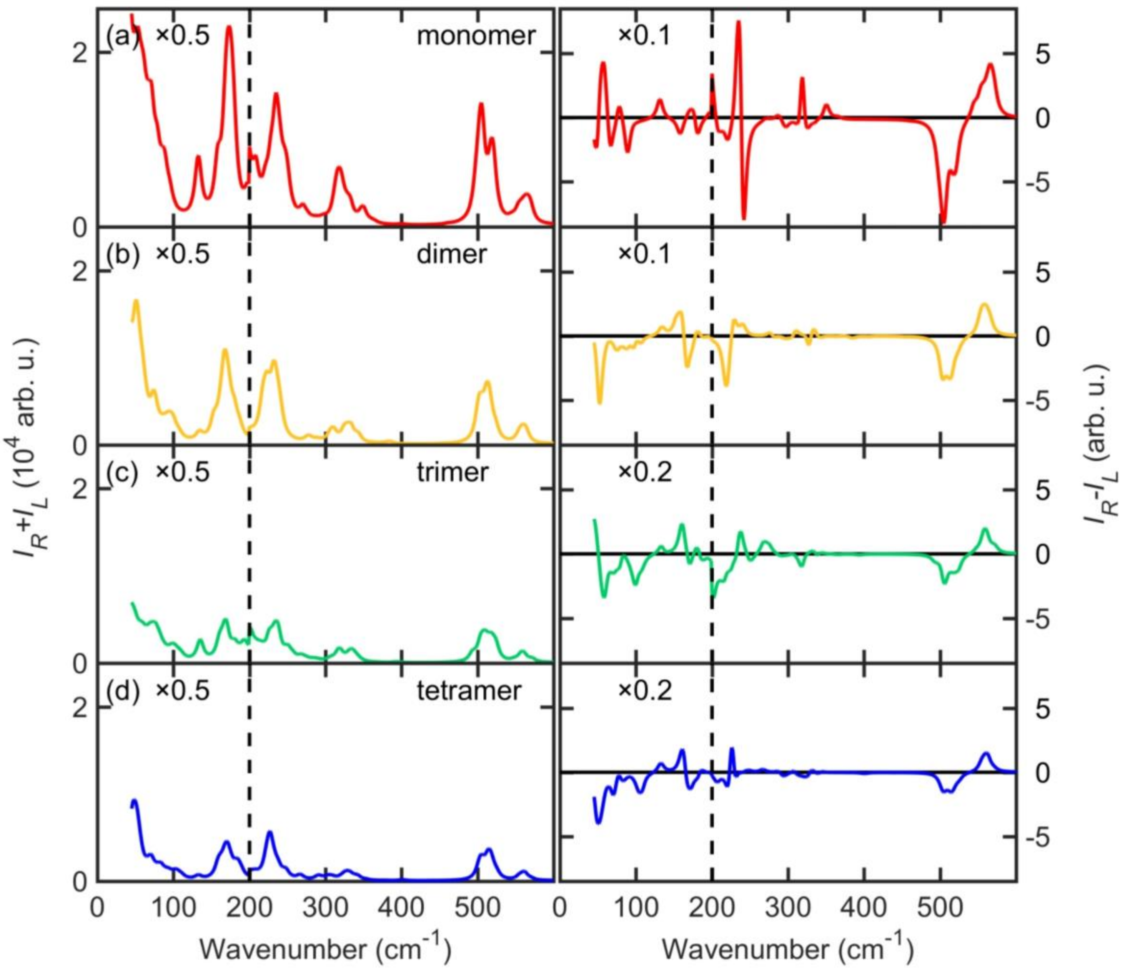

Figure S7. Raman and ROA spectra of one nitrile MD snapshot (10 molecules in the elementary cell) simulated from force field constructed from monomers, dimers, trimers and tetramers.

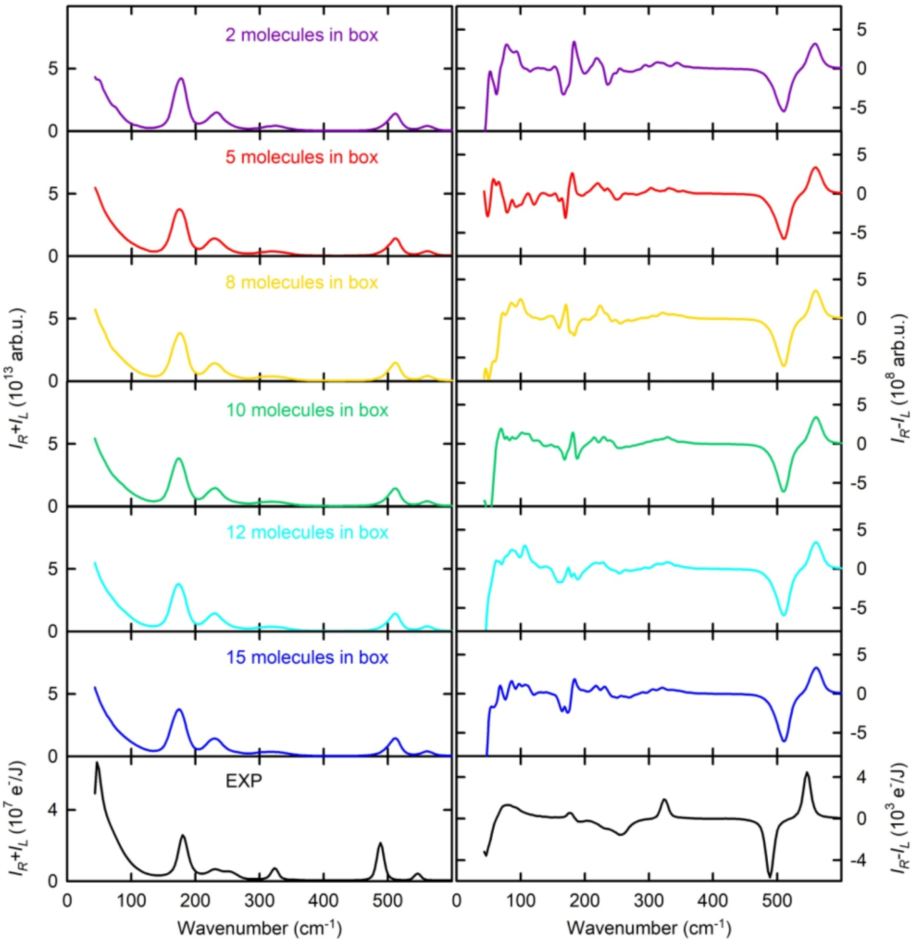

Figure S8. Calculated Raman and ROA nitrile spectra, using elementary cells containing 2, 5, 8, 10, 12 and 15 molecules, for 200 snapshots.

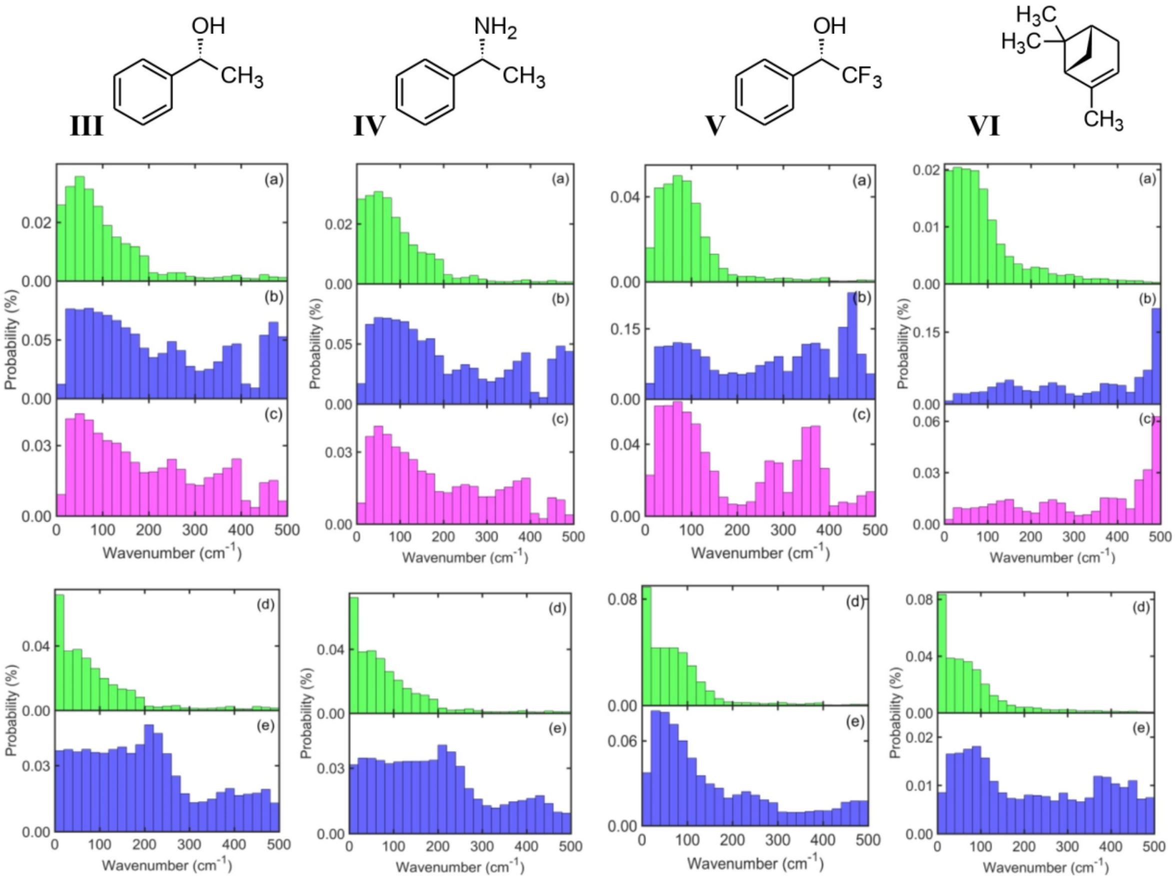

Figure S9. Relative vibrational potential energy distribution (PED) of intermolecular motions related to two (stretching (a), bending (b), torsion (c)) and one (translations (d), rotations (e)) molecule, for **III-V**.

PEDs of individual coordinates were calculated by the following procedure.

1) Transformation matrix **B** was defined, relating internal (I_i) and Cartesian (r_λ) coordinates, $I_i = \sum_\lambda B_{\lambda i} r_\lambda$. Using **B**, force field elements f_{ij} in the internal coordinates were calculated.

2) Within the harmonic approximation, Cartesian force field was normalized, so that the **S** matrix relating Cartesian and normal mode (Q_J) coordinates was obtained, $Q_J = \sum_\lambda S_{\lambda J} r_\lambda$

3) Relative energy contribution of coordinate I_i in mode J was calculated as $PED_{Ji} = \frac{A_{Ji}}{\sum_i A_{Ji}} \times 100\%$, where $A_{Ji} = b_{Ji}^2 f_{ii} \omega_J^{-1}$, $b_{Ji} = \sum_\lambda S_{\lambda J} B_{\lambda i} \sqrt{m_\lambda}$, ω_J is the normal mode frequency, m_λ is atomic mass. In the graphs, PED values were averaged over the snapshots and normal modes in a wavenumber interval.

Table S1 Laser powers at the sample *P* and total accumulation times *t* used in ROA measurements.

Compound	Enantiomer	*P* (mW)	*t* (h)
I nitrile	*R*	83	9.7
	S	83	13.2
II methyloxirane	*R*	540	34.6
	R @ water	338	5.5
	S	540	19.3
III phenylethanol	*R*	86	1.9
	S	82	2.9
IV benzylamine	*R*	69	7.8
	S	69	8.5
V 3F-benzyl	*S*	114	11.4
	R	266	5.5
VI α-pinene	*S*	266	5.5

Table S2. Dimensions of the elementary cells (10 molecules in the box) and densities used in the calculations

	Liquid	Box size (Å)	ρ (g/ml)	COSMO Solvent
I	nitrile	11.37	1.012	acetonitrile
II	methyloxirane	10.39	0.859	tetrahydrofuran
III	phenylethanol	12.61	1.012	benzylalcohol
IV	benzylamine	12.89	0.940	benzylalcohol
V	3F-benzyl	13.13	1.293	benzylalcohol
VI	α-pinene	13.82	0.858	cyclohexane

Table S3. Selected low-frequency fundamental modes in **III**-**V**.

v / cm-1	modes
III:	
36	Phe rotation
128	Me and Phe wagging
212	Me and Phe scissoring
266	Me and OH rotation
283	Me and OH rotation
305	deloc. def.
372	deloc. def.
411	Phe out of plane
482	deloc. def.
IV:	
29	Phe rotation
129	Me and Phe wagging
214	Me and Phe scissoring
268	Me rotation
303	deloc. def., NH_2 rotation
360	deloc. def.
411	Phe out of plane
480	NH_2 and Me wagging
V:	
27	Phe rotation
64	CF_3 rotation, Phe wagging
99	deloc. def.
199	OH rotation
233	deloc. def.
290	deloc. def.
308	deloc. def.
335	deloc. def.
412	Phe out of plane
428	deloc. def.

Appendix C – Analyst, 148 (6), 1337-1348 (2023).

PCCP

PAPER

Cite this: *Phys. Chem. Chem. Phys.*, 2022, **24**, 19722

Low-frequency Raman optical activity provides insight into the structure of chiral liquids†

Pavel Michal, *[a] Josef Kapitán, [a] Jiří Kessler [b] and Petr Bouř *[bc]

Vibrational frequencies of modes involving intermolecular motions in liquids are relatively small, in the Raman scattering close to the excitation frequency, and the bands may merge into a diverging uninterpretable signal. Raman optical activity (ROA) spectral shapes in this region, however, are structured more and may better reflect the nature of the studied systems. To understand the origin of the signal and its relation to the molecules, ROA spectra of six chiral neat liquids are recorded and analyzed on the basis of molecular dynamics and density functional theory computations. The theory of Raman scattering of liquids is discussed and adapted for modeling based on clusters and periodic boundary conditions. A plain cluster approach is compared to a crystal-like model. The results show that the low-frequency optical activity can be reliably modeled and related to the structure. However, momentary arrangement of molecules leads to large variations of optical activity, and a relatively large number of geometries need to be averaged for accurate simulations. The intermolecular modes are intertwined with intramolecular ones and start to dominate as the frequency goes down. The low-frequency ROA signal thus reflects the chemical composition and coupled with the modeling it provides a welcome means to study the structure and interactions of chiral liquids.

Received 20th May 2022,
Accepted 28th July 2022

DOI: 10.1039/d2cp02290g

rsc.li/pccp

1. Introduction

Low-frequency Raman spectroscopy has been possible due to the availability of narrow wavelength optical filters and stable diode lasers, and is gaining popularity in chemical and pharmaceutical analyses.[1] It is also referred to as terahertz (THz) or low-wavenumber Raman spectroscopy. In crystals and crystalline-like polymers, it can reveal their structure, polymorphism and phonon dynamics.[2,3] Both intra and intermolecular vibrational modes provide strong Raman signal.[4] On the other hand, it is very difficult to obtain useful information from the low-frequency Raman spectrum of a liquid, because the signal is rather unstructured, unresolved, and quickly increases when the frequencies approach the excitation line.[5] Better results are obtained by optical Kerr spectroscopy exploring time dependence of the liquid polarization induced by laser pulses. In this case, low-frequency Raman spectra can be obtained by Fourier transformation techniques.[6–8]

If we look at the differential scattering of the right and left circularly polarized light, chiral liquids and solutions may provide more diverse signals than for unpolarized Raman. The bands can be both positive and negative, and are more sensitive to chemical composition and conformation.[9] Usually, only the higher-frequency region (above ~400 cm^{-1}) is interpreted in terms of band assignment to the molecular structure. For a polyalanine solution in dichloroacetic acid, however, we observed a Raman optical activity (ROA) signal at 128 cm^{-1} that was about 10× stronger than the one typical for this spectroscopy.[10] Monosaccharide solutions gave rather weak low-frequency ROA,[11] whereas for several globular proteins dissolved in water the relative signal strength compared well to the big signal of polyalanine.[12] For a cryptophane molecule the intensity of the ROA band at 150 cm^{-1} significantly decreased in the presence of xenon.[13] These observations suggest that the low-frequency ROA well reacts to the structure and intermolecular interactions in the studied systems.

Also for a chiral neat liquid, 2-chloropropionitrile, we identified a strong low-frequency ROA outside the region of monomolecular fundamental modes.[14] On the basis of a cluster model the signal was assigned to intermolecular motions involving changing a distance (stretching) and mutual orientation between molecules. However, it was not clear if such a signal is related to specific intermolecular interactions, such as the ability of a molecule to make hydrogen bonds. *Ad hoc* computations based on large clusters have been quite costly in terms of computer time and memory. In the clusters most

---

[a] *Department of Optics, Palacký University Olomouc, 17. listopadu 12, 77146, Olomouc, Czech Republic. E-mail: michal@optics.upol.cz*

[b] *Department of Analytical Chemistry, University of Chemistry and Technology, Technická 5, 16628 Prague, Czech Republic*

[c] *Institute of Organic Chemistry and Biochemistry, Academy of Sciences, Flemingovo náměstí 2, 16610, Prague, Czech Republic. E-mail: bour@uochb.cas.cz*

† Electronic supplementary information (ESI) available: Further computational details and tests, measurement conditions, and complementary experimental data. See DOI: https://doi.org/10.1039/d2cp02290g

molecules remained at the surface, which did not correspond to the real situation. *Ab initio* molecular dynamics suggested for ROA relatively recently[15,16] is probably technically the most advanced way to simulate bulk phase spectra. However, it currently appears too computationally demanding.

In the present study we therefore use the cluster approach adapted to better correspond to the liquid phase, introducing a crystal-like periodicity. This enables us to investigate the low-frequency region more systematically. We also briefly review the theory of Raman scattering on liquids, which we believe has not been previously clearly linked to the cluster computational modeling. High-quality Raman and ROA experimental spectra were recorded for six chiral liquids of variable chemical structures, down to ~ 50 cm^{-1}. One of them, methyloxirane, was also investigated as an aqueous solution. Molecular dynamics is used to understand the structure of model liquids, and density functional theory is utilized for the spectroscopic properties. This computational approach seems to be fit to explain the main spectral features including low-frequency ROA signs and intensities, and thus to couple the chiral signals with the liquid structure.

2. Methods

2.1 Theory of Raman scattering in liquids

While the Rayleigh scattering[17] of gasses and liquids reflects long-range inhomogeneities in the structure, such as the radial distribution function,[18] opalescence and density fluctuations,[19,20] Raman scattering samples the structure more locally. This is because non-interacting molecules scatter Raman light in an incoherent way.[21,22]

As far as we know, there is no consistent theory comprising all quantum-mechanical and relativistic aspects of light scattering in bulk. Fortunately, the semiclassical approach based on the scattering of electromagnetic waves on individual molecules seems to provide a reasonable description of the experimental data.[9,21] To illustrate the physical basis of scattering and to justify our cluster approach, let us summarize some important relationships for the backscattering intensities. The light passing through the liquid induces time-dependent electric ($\boldsymbol{\mu}$) and magnetic ($\mathbf{m}$) dipoles and electric quadrupoles ($\boldsymbol{\Theta}$) in individual molecules, which then radiate part of the energy away. Higher moments can be neglected, because molecular dimensions are usually much smaller than the wavelength. The moments are related to the electric intensity of light through molecular polarizabilities. For example, x-polarized light of the electric field traveling along the z-direction induces a dipole moment in each molecule m[16]

$$\mu_{m\alpha} = \left(\alpha_{m\alpha x} - i\frac{k}{3}A_{m\alpha,xz} + i\frac{k}{\omega}G'_{m\alpha y}\right)E_x \tag{1}$$

where k is the wave vector, ω is the angular frequency, t is time, and α, A and G' are the electric dipole–dipole, electric dipole–quadrupole and electric dipole–magnetic dipole polarizabilities.

The induced moments are sources of scattered radiation. For Raman scattering the incident and scattered frequencies and wave vectors are close ($\omega \sim \omega'$, $k \sim k'$), so that $\Delta k = k - k' \sim 2k$ for backscattering. The electric field of light scattered from N molecules is[21]

$$\begin{aligned} E'_\alpha &= \frac{\omega^2\mu_0\mu_r}{4\pi r}E_0\sum_{m=1}^{N}\mathrm{e}^{\mathrm{i}(\Delta k z_m - \omega t)}\Bigg[\alpha_{m\alpha x} - \frac{ik}{3}(A_{m\alpha,xz} + A_{mx,\alpha z}) \\ &\quad + \frac{i}{c}\left(G'_{m\alpha y} - \varepsilon_{\alpha z\gamma}G'_{mx\gamma}\right)\Bigg] \end{aligned} \tag{2}$$

where μ_0 and μ_r are the vacuum and relative permeabilities, and r is the distance. Unpolarized (total) Raman intensity can be associated with the S_0 Stokes parameter,

$$\begin{aligned} I_R + I_L = S_0 = E'^2_x + E'^2_y &= 30\,K\sum_{m,n}\mathrm{e}^{\mathrm{i}\Delta k z_{mn}}\left(\alpha_{mxx}\alpha_{nxx} + \alpha_{myx}\alpha_{nyx}\right) \\ &= 30\,K\sum_{m}\left(\alpha_{mxx}\alpha_{mxx} + \alpha_{myx}\alpha_{myx}\right) \end{aligned} \tag{3}$$

where $K = \frac{1}{30}\left(\frac{\omega^2\mu_0\mu_r}{4\pi r}E_0\right)^2$, $z_{mn} = z_m - z_n$ is the difference of positions of molecules m and n, and $I_{R/L}$ is intensity of the right/left circularly polarized light. The double sum in (3) disappears because of different phase factors of transition vibrational polarizabilities of different molecules.[20,21] For isotropic samples we can further average over molecular orientations, and express S_0 with polarizabilities related to one molecule as follows:

$$S_0 = \frac{KN}{2}\left(7\alpha_{\alpha\beta}\alpha_{\alpha\beta} + \alpha_{\alpha\alpha}\alpha_{\beta\beta}\right). \tag{4}$$

In (4) the Greek indices are related to a molecule-fixed coordinate system and the Einstein summation convention is applied here and further in the text. Adding the magnetic dipolar and electric quadrupolar parts, we similarly get the ROA intensity related to the S_3 Stokes parameter as[21]

$$\begin{aligned} I_R - I_L = S_3 &= \frac{8KN}{c}\Bigg(3\alpha_{\alpha\beta}G'_{\alpha\beta} - \alpha_{\alpha\alpha}G'_{\beta\beta} \\ &\quad + \frac{1}{3}\,\omega\alpha_{\alpha\beta}\boldsymbol{\varepsilon}_{\alpha\gamma\delta}A_{\gamma,\delta\beta}\Bigg) \end{aligned} \tag{5}$$

where c is the velocity of light and $\boldsymbol{\varepsilon}$ is the antisymmetric tensor.

The single-molecule theory can be formally extended for simulations based on molecular clusters if we consider the liquid also as a sum of clusters. Any liquid volume V of N molecules can be divided into a sum of one molecule volumes v_i, volumes of molecular pairs $v_{ij} = v_i + v_j$, *etc.* (We do not consider the case when the size of the volume approaches the wavelength of the light.) For example, we can treat 3 molecules ($N = 3$) as monomers ($m = 1$) with $V = v_1 + v_2 + v_3$, dimers ($m = 2$) with $V = \frac{1}{2}(v_{12} + v_{13} + v_{23})$, where $v_{12} = v_1 + v_2$, *etc.* In general, for clusters of m molecules,

$$V = \frac{(m-1)!(N-m)!}{(N-1)!}\sum_{i_1 < i_2 < \ldots < i_m} v_{i_1 i_2 \ldots i_m}. \tag{6}$$

The total polarizability is then

$$\alpha = \frac{(m-1)!(N-m)!}{(N-1)!}\sum_{i_1 < i_2 < \ldots < i_m} \alpha_{i_1 i_2 \ldots i_m}, \tag{7}$$

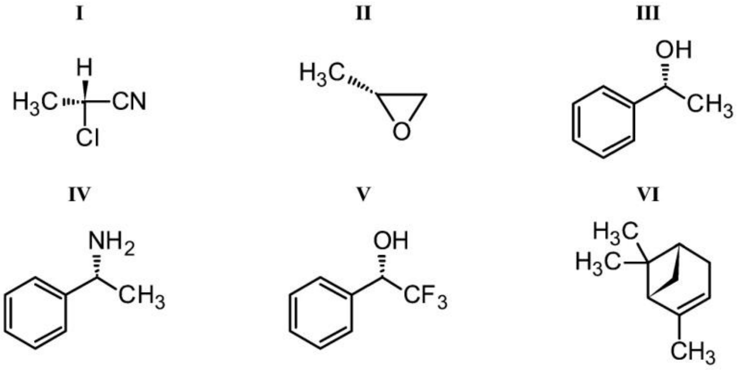

Fig. 1 Studied molecules: **I** (*R*)-2-chloropropionitrile (nitrile), **II** (*R*)-(+)-propylene oxide (methyloxirane,), **III** (*R*)-(+)-1-phenylethanol, **IV** (*R*)-(+)-α-methylbenzylamine, **V** (*S*)-(+)-α-(trifluoromethyl)benzyl alcohol, and **VI** (+)(1*R*,5*R*)-α-pinene.

where $\alpha_{i_1 i_2 \ldots i_m}$ is the polarizability of a cluster containing molecules $i_1 \ldots i_m$. The exact result is obtained for $m \to N$, when all important intermolecular interactions are included. Note that although eqn (6) and (7) may justify both the cluster and crystal-cell approaches they were not directly used in any calculation.

2.2 The periodic model

To well-represent the liquid, the clusters need to be in contact with the environment. This can be achieved using a periodic crystal-like model. Because of the periodicity, vibrational Hamiltonian H can be written as a sum over the phonon (wave) vectors $\mathbf{q}$ and atoms i within one cell only,[23]

$$H = \sum_{\mathbf{q}} \frac{1}{2} \left(\sum_i m_i \dot{x}_i^* \dot{x}_i + \sum_i \sum_j x_i^* D_{ij} x_j \right), \qquad (8)$$

where m_i and x_i are atomic masses and coordinates, and $\mathbf{D}(\mathbf{q})$ is the dynamic matrix. Only for $\mathbf{q} = 0$ we get non-zero Raman and ROA intensities. For other values signals of different elementary cells cancel out by interference. For zero wave vector,

$$D_{ij} = \sum_J f_{ij}, \qquad (9)$$

where J runs over the elementary cells containing the j-coordinate, f_{ij} are the harmonic force constants (force field). The Cartesian-normal mode transformation matrix $\mathbf{S}$ is obtained by the force field diagonalization, and the transition polarizabilities in (3) and (5) are obtained from the polarizability derivatives.[9] For example, for a fundamental transition involving the normal mode Q_J, the transition polarizability needed in eqn (4) and (5) for Raman scattering is[9]

$$\alpha(\omega, \omega') = \langle 0|\hat{\alpha}|1\rangle = \sqrt{\frac{\hbar}{2\omega_J}} S_{iJ} \alpha_i, \qquad (10)$$

where ω_J is the normal mode frequency, $\hat{\alpha}$ is the polarizability dependent on atomic coordinates, α_i is a derivative with respect to coordinate i.

2.3 Spectral measurement

The six molecules studied are summarized in Fig. 1. Experimental spectra of nitrile **I** were already published.[14] Its small size, availability of both enantiomers, and relative rigidity make it a convenient testing compound. Also methyloxirane **II** is used as a convenient benchmark model for the theory.[15,24–26] A series of the ethylbenzene derivatives **III**, **IV** and **V** allows one to evaluate the spectroscopic properties of similar molecules with a mixture of inter and intramolecular low-frequency vibrational modes. (For **III** and **IV**, the very first ROA spectra were observed in 1973.[27,28]) Finally, α-pinene **VI** is an example of a non-polar molecule with weak intermolecular interactions.

Raman and ROA spectra were acquired on a custom-made ROA instrument made at Palacký University Olomouc.[14] The samples were measured in a rectangular fused silica cell of 70 μl volume, the temperature was stabilized at (20.0 ± 0.1) °C, and the back-scattering scattered circular polarization (SCP) modulation scheme was used, with a 532 nm excitation wavelength. All compounds were measured as neat liquids, and methyloxirane was additionally measured in aqueous solution at a 1 : 22 methyloxirane : H_2O molar ratio. Lower temperature (6.0 ± 0.1) °C was used for the neat and dissolved methyloxirane (boiling point at 34 °C), to prevent its evaporation. Laser powers at the sample and accumulation times are listed in Table S1 (ESI†). For **V** only one enantiomer was available, otherwise both enantiomers were measured and idealized "$(R–S)/2$" ROA spectra for the *R*-forms are presented. A fluorescence background in the Raman signal of **V** caused by impurities was subtracted using the asymmetric least squares algorithm,[29,30] with the asymmetry parameter 1×10^{-4} and smoothness 8.5×10^4. Experimental intensities are given as the number of detected electrons per excitation energy in a wavenumber interval (e^- cm J^{-1}).

2.4 Computations

Molecular dynamics (MD) was performed using the Tinker program.[31] Some computations were repeated or complemented using the Amber software,[32] which allowed for a more

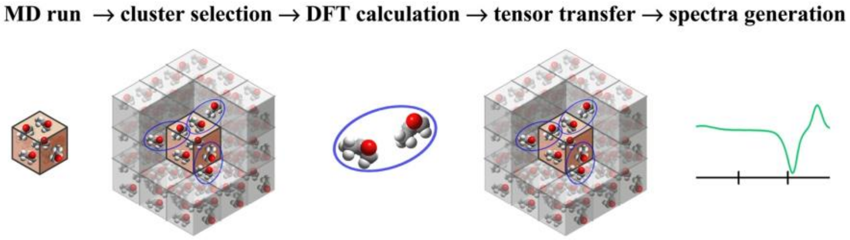

Fig. 2 Simulations of the spectra by the default crystal-like model. Intermolecular interactions within the periodic elementary cell (the brown/middle cube) and towards its environment were simulated for molecular pairs, in an arbitrary 27 cube "supercube". The pair parameters (force field, intensity tensors) were transferred back to the supercube, and the spectra were simulated using the periodic boundary conditions.

extensive parallelization and time saving, providing nearly identical results to Tinker. The OPLSAA force field was used,[33] with periodic boundary conditions, production run of 10 ns, 1 fs integration time, *NVT* ensembles, and temperature of 298 K. For methyloxirane the OPLSAA force field was modified to reproduce bond lengths and angles calculated by Gaussian[34] at the B3LYP/aug-cc-pVTZ/COSMO(THF) approximation level. Bigger periodic cubic boxes (about 40 Å a side) were used for investigations of the radial distribution functions, smaller ones (Table S2, ESI† containing 10 molecules) were used to generate many snapshots and their spectra.

Vibrational frequencies and spectral intensities were calculated using the Gaussian program and the B3PW91[35]/6-31G**/COSMO[36]/GD3BJ[37,38] method. Even 10 molecules in the box were too many for a direct calculation of a large number of snapshots needed for convergence. Therefore, smaller clusters were made, by default containing two close molecules, presumably comprising the strongest intermolecular interaction within the periodic box and 26 neighboring boxes (Fig. 2). The geometries of the pairs or larger clusters were partially optimized in the normal mode coordinates.[39–41] Modes with frequencies below 225 cm^{-1} (or below 100i cm^{-1} when imaginary, $i = \sqrt{-1}$) were fixed, and harmonic frequencies were calculated at the same level as the geometries. For Raman and ROA intensity tensors the rDPS[42] basis set was combined with the B3PW91/6-31G**/COSMO/GD3BJ force field. The rDPS basis set has been recommended for ROA because of a good balance between the computational demands and quality of the results.[42,43] For example, rDPS polarizability derivatives were calculated about 2–3 times faster than for a larger 6-31++G** basis set, giving almost identical results (Fig. S1, ESI†). The rDPS basis set alone is not suitable for the frequencies, underestimating them by about 40–50 cm^{-1} (*cf.* Fig. S1c and d, ESI†). A simpler BPW91 functional was tried

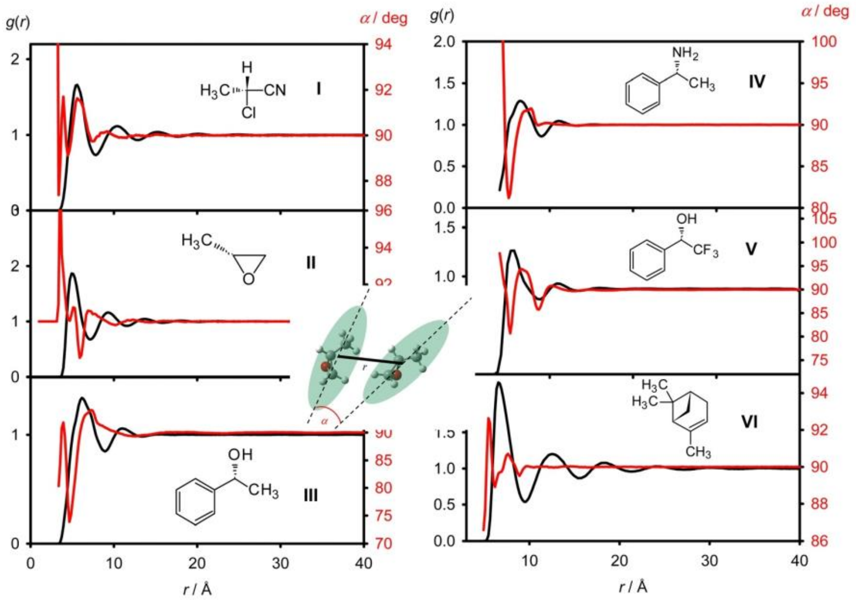

Fig. 3 Radial distribution functions $g(r)$ (black line) and average angle α (red) between two molecules as a function of the distance. The angle is defined according to the main moments of inertia as indicated in the inset.

and gave qualitatively similar results to B3PW91; also the influence of the GD3BJ dispersion correction was rather minor (Fig. S2, ESI†).

Vibrational parameters (force field and polarizability derivatives) thus obtained for the smaller clusters were transferred back to the 3 × 3 × 3 supercube (Fig. 2) using the Cartesian coordinate transfer (CCT).[44,45] From the resultant force field we obtained the dynamic matrix (eqn (9)) and calculated the Raman and ROA intensities for each transition i (I_i, eqn (4) and (5)). Smooth spectra were obtained as

$$S(\omega) = \sum_i I_i \left[1 - \exp\left(-\frac{\omega_i}{kT}\right)\right]^{-1} \left[4\left(\frac{\omega - \omega_i}{\Delta}\right)^2 + 1\right]^{-1}, \quad (11)$$

where ω_i is the transition frequency, k is the Boltzmann constant, Δ = 10 cm^{-1}, and temperature T = 298 K. The magnitude of the bandwidth (Δ) approximately corresponds to the experimental resolution and thus facilitates comparison to the experiment.

For testing, as an alternative to the default crystal-like model (part 2.2), larger clusters comprising one molecule and its first solvation sphere were also used for spectral generation, following ref. 14. Selected from MD with the bigger periodic boxes, the clusters were partially optimized and the spectra calculated following the procedure described above for the crystal model. Finally, we also experimented with the supercube (Fig. 2), which we used not only for the generation of the dynamic matrix in the crystal model, but directly as a cluster. Although these two cluster models miss the continuous character of the liquid, as shown below they also reproduce some of the features observed experimentally.

3. Results and discussion

3.1 Molecular dynamics simulations

The radial distribution functions (RDFs) calculated from MD provide insight into the range of intermolecular interactions in the studied liquids (Fig. 3). All exhibit a clear maximum of the first solvation sphere, at 5.6 Å (**I**), 5.1 Å (**II**), 6.2 Å (**III**), 6.5 Å (**IV**),

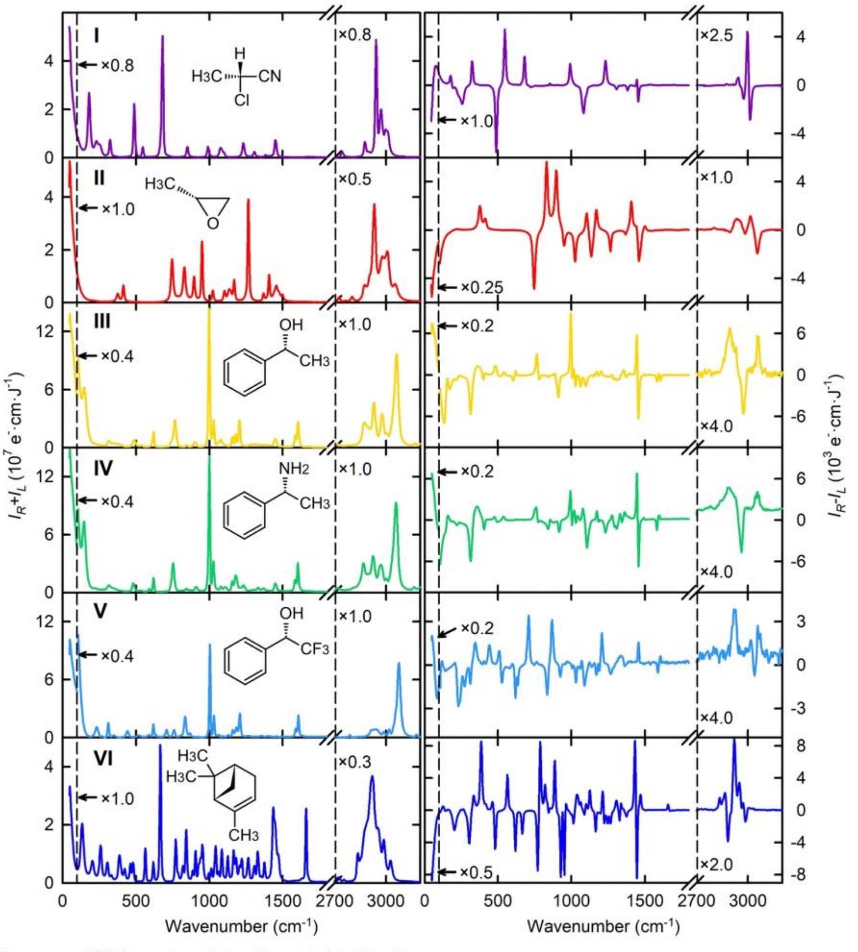

Fig. 4 Experimental Raman and ROA spectra of the six neat chiral liquids.

6.0 Å (**V**), and 6.5 Å (**VI**). Other maxima associated with higher solvation spheres are obviously less pronounced, although the fifth solvation sphere maximum of α-pinene at ~30 Å is still visible. Also the RDFs of the other two "rigid" molecules, methyloxirane and nitrile, are structured up to a relatively long distance, whereas for the ethylbenzene derivatives the structure is nearly destroyed after the second maximum.

The angle α between the main axes of molecular moments of inertia (red lines in Fig. 3) averages to 90° for distant non-interacting molecules. At shorter distances molecules interact and adopt energetically favorable mutual orientations. The case when $\alpha \neq 90^\circ$ thus indicates that an additional source of chirality in the solution exists, apart from the absolute configuration of individual molecules. This can potentially contribute to low-frequency ROA. We can see that for the rigid molecules (nitrile, methyloxirane, and α-pinene) α does not deviate by more than 3° from the 90° average, except for the closest distance limit. Ethylbenzenes **III–V** adapt their shapes upon more contact and the deviations from 90° are bigger, with an extreme value of 15° for alcohol **III**.

For **III–V** the molecular flexibility can also be judged from the dependencies of the electronic energy (B3PW91/6-311++G**/COSMO) on the conformation of the phenyl, hydroxy and amine groups (Fig. S3, ESI†). All three molecules prefer the polar OH or NH groups pointing out of the phenyl plane ($\varphi \sim 100^\circ$). The OH/NH_2 groups are relatively freely rotating, with energy minima with ψ at about ±60° and 180°. The potential energy barriers between the minima are within 1–2 kcal mol^{-1} for **III** and **V**, and higher (3 kcal mol^{-1}) for **IV**. For **III** and **IV**, the calculated potential energy surfaces are consistent with a previous study.[28] However, the distributions of MD conformers (black dots in Fig. S3, ESI†) follow the DFT results only approximately. We explain this by the possibility of the molecules to form hydrogen bonds in MD, which is only partially simulated by the COSMO continuum solvent model.[46]

3.2 Experimental spectra

The experimental Raman and ROA spectra recorded in the whole range (~50–3200 cm^{-1}) for the six compounds are plotted in Fig. 4. When available, enantiomers gave opposite

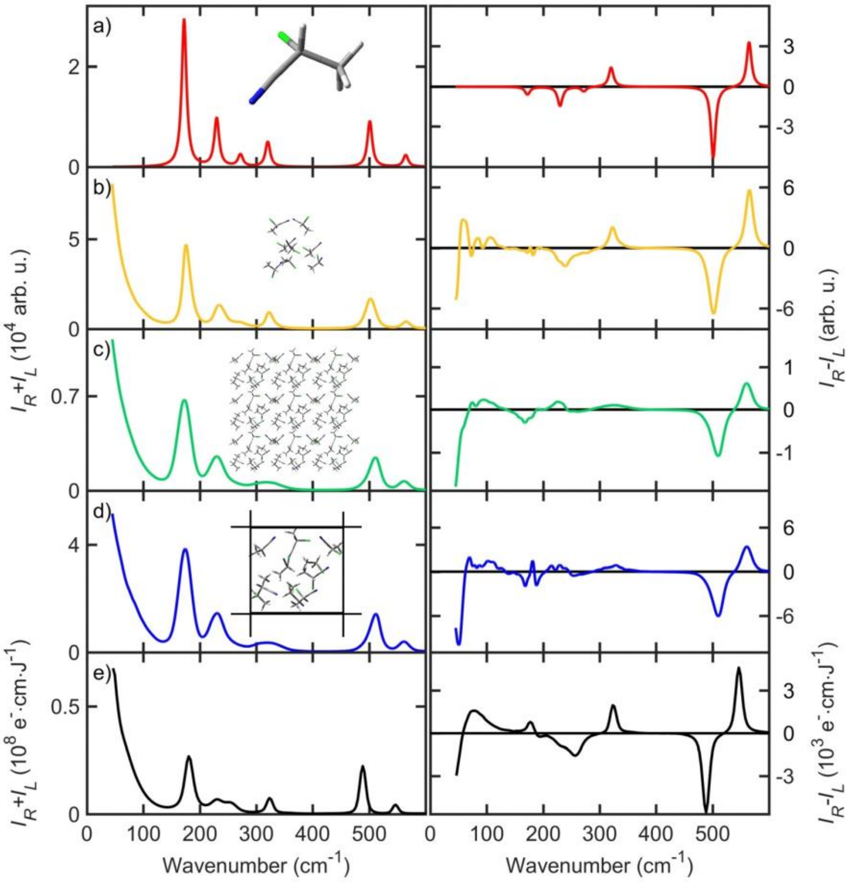

Fig. 5 Raman and ROA nitrile (**I**) spectra calculated with different models: (a) single molecule, (b) small cluster/all interactions, (c) large cluster/pair interactions, (d) periodic crystal/pair interactions (*cf.* Fig. 2), and (e) experimental spectrum. For b–d 200 MD snapshots were averaged.

ROA, suggesting a very low level of instrumental artifacts (Fig. S4, ESI†). The region within 1800–2700 cm^{-1} is not shown because there is only one fundamental band, nitrile C$\equiv$N stretching. ROA signal at the CH stretching region ($>$2700 cm^{-1}) is relatively weak, but the shapes therein are also characteristic for individual molecules. The strong "scissoring" signal of compounds containing methyl groups ($\pm$ROA couplet at $\sim$1450 cm^{-1}) is missing for **V**. We also see the bigger sensitivity of ROA spectra compared to Raman scattering; compounds **III–V** have very similar Raman spectra, but only some ROA features are alike.

Normalized circular intensity difference ratios (CID = ROA/Raman, Fig. S5, ESI†) in the CH stretching region are rather small (maximum of $\sim 1 \times 10^{-4}$ for **I**, 3×10^{-5} for **VI**, *etc.*). In the lower frequencies ($<$2000 cm^{-1}) CIDs are higher, up to $\sim 9 \times 10^{-4}$ for the smaller molecules and $\sim 2 \times 10^{-3}$ for **VI**. At the 50 cm^{-1} instrumental limit CIDs are rather small again, **II** and **VI** giving the highest values of 4×10^{-4} and 6×10^{-4}, respectively. The CID parameters are important, for example, for determining the reliability of the measurement and for comparison to the simulations. Note, however, that the experimental values cannot be determined too accurately due to the fluorescent background in the Raman spectrum.

Below we focus on the lowest-wavenumber region, where all liquids have strong ROA even as the frequency approaches 50 cm^{-1}. For **I** and **III–V**, there are also strong bands at $\sim$90 cm^{-1}. These have opposite sign to the intensity at the 50 cm^{-1} limit. The six compounds studied suggest that the low frequency signal is not related to a particular molecular property, such as size, hydrophobicity, or the ability to make hydrogen bonds. This was also observed for a few other chiral liquids not shown here.

3.3 Strategies for spectra modeling

Fig. 5 compares spectra of **I** simulated with (a) one nitrile molecule, (b) molecular clusters, (c) bigger cluster with pair interactions only, and (d) the periodic crystal model; (e) is the experimental spectrum. The low-frequency intermolecular signal is obviously missing in the single molecule spectra (a). Also the inhomogeneous broadening of the bands within 150–350 cm^{-1} simulated by the arbitrary Lorentzian band is not realistic. The other models based on MD do provide the intermolecular signal with a correct ROA sign pattern, (positive at $\sim$80 cm^{-1}, negative close to 50 cm^{-1}). Minor spectral features are difficult to judge due to the limited precision of the calculations and limited experimental resolution.

The MD, however, except for the small cluster model (b), overestimates the broadening of the 242 and 325 cm^{-1} bands. As discussed previously[47] generation of the spectra using the instantaneous normal mode approximation and partial optimization[39] of MD geometries is a rather empirical procedure, which may contribute to this inconsistency. The widths of the intramolecular bands within 150–300 cm^{-1} are simulated qualitatively correctly. The periodic crystal-like model (d) is technically the most advanced one and avoids the surface cluster effects, but it comprises pair molecular interactions only. Some experimental features, like the relatively monotonic increase of the ROA intensity between 250 and 90 cm^{-1}, are therefore better reproduced with the smaller clusters containing more intermolecular interactions (b). The large cluster model (c) seems to give the worst results. Nevertheless, we see that all the cluster models are able to reasonably well reproduce also the intermolecular low-frequency ROA signal. Spectra simulated with the crystal-like model (d) for all compounds in a broad wavenumber range are summarized in Fig. S6 (ESI†). This model is also used as a default below, unless said otherwise.

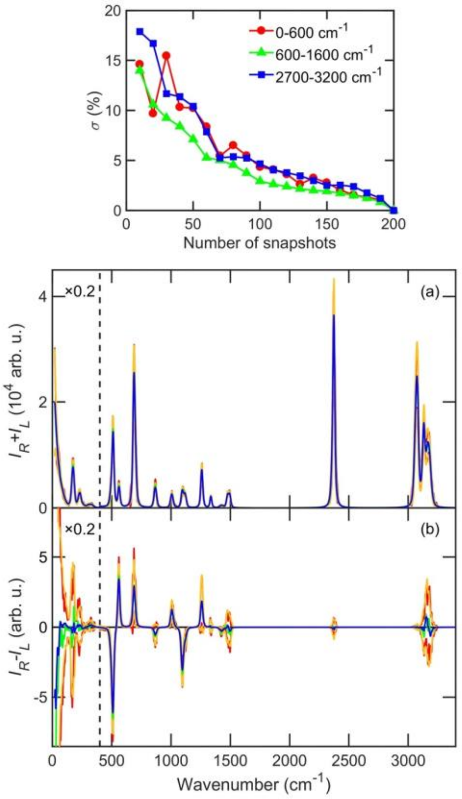

Fig. 6 Nitrile, (top) dependence of the ROA spectral average error ($\sigma = \int|S_\mathrm{i} - S_\mathrm{f}|\mathrm{d}\upsilon / \int|S_\mathrm{f}|\mathrm{d}\upsilon$, S_i and S_f are the partial and final average) on the number of averaged snapshots, for three spectral regions, and (bottom) Raman and ROA nitrile spectra averaged from 20 (green) and 200 (blue) MD snapshots; standard deviations ($s = \sqrt{(N-1)^{-1}\sum(S_\mathrm{i} - \bar{S})^2}$) at each point are plotted using red (20) and orange (200) lines.

A serious problem limiting the precision of the computations is a large number of MD snapshots that need to be averaged for low-frequency ROA. The convergence is documented at the top of Fig. 6. We can see the ROA spectral error as dependent on the number of averaged snapshots, in the low (0–600 cm^{-1}), middle (600–1600 cm^{-1}) and CH stretching (2700–3200 cm^{-1}) regions. The 200-snapshot average is taken as a reference. The low-frequency ROA signal converges more slowly than within 600–1600 cm^{-1}. About 100 snapshots need to be averaged to push the error below 5%. For Raman (not shown)

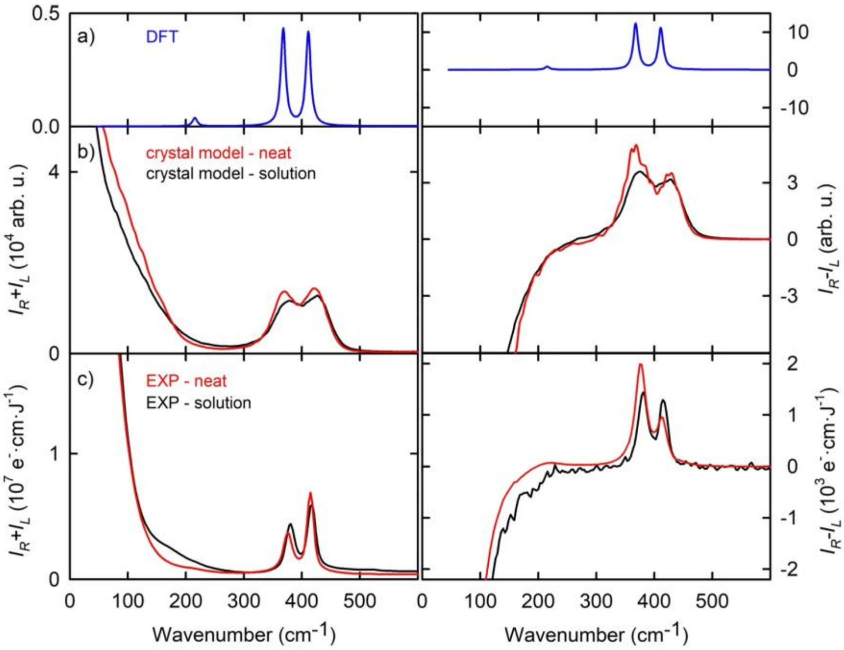

Fig. 7 Raman and ROA spectra of neat methyloxirane and its water solution: (a) single molecule computation, (b) crystal model, and (c) experiment.

about 10 snapshots would be enough. Somewhat surprising is a slow convergence of the CH ROA signal, similar to that for the low-frequency region. This can perhaps be explained by the extended coupling of the CH stretching motion with other modes.[48]

At the bottom of Fig. 6 Raman and ROA spectra of the nitrile are plotted as calculated from 20 and 200 MD snapshots. About 20 snapshots already provide many spectral features observed also experimentally, but the positive 80 cm^{-1} ROA maximum, for example, appears only after the whole set is included. The ROA sensitivity to a momentary MD geometry is also reflected by the standard deviations plotted using red and orange lines in Fig. 6. These clearly become extreme for low-frequency ROA. For bands above 400 cm^{-1} the 20 and 200 snapshot averages are nearly the same. The convergence problem makes the computation expensive. Note that one snapshot already involves some averaging over molecular orientations. For example, if there are 10 molecules in the elementary cell (Fig. 2) we need to calculate force fields for about 50 different pairs of molecules to comprise at least the main intermolecular interactions within this cell and to neighboring ones.

On one nitrile snapshot, we also tested the convergence of the spectra with respect to the number of molecules taken in the clusters to calculate the force field (Fig. S7, ESI†). Increasing this value is quite computationally demanding: one elementary cell of 10 molecules provides 10 monomers, roughly 50 dimers of close molecules, 390 trimers, 1300 tetramers, *etc.* In the trial snapshot, accounting for three and four-molecule interactions seems to produce some additional ROA features around 100 cm^{-1} compared to the pairs; however, this is not observed experimentally and likely disappears during the averaging. The low-frequency ROA signal for the monomers is caused by differences of equilibrium and MD geometries, which is an inherent restriction of our method, but may be significantly reduced during further averaging. Increasing the number of molecules in one elementary cell (*i.e.*, size of the MD box) did not seem to bring an improvement and 10 molecules in the box thus seem to be sufficient for a converged result (Fig. S8, ESI†).

3.4 Methyloxirane solution and vibrational mode analysis

Interestingly, neat methyloxirane gave nearly the same low-frequency ROA signal as its water solution, and this result could be reproduced by the crystal model (Fig. 7). To achieve a reasonable convergence, however, more MD snapshots (1000) were needed for the solution than for the neat liquids (200). In the experiment, compared to the neat liquid, the water solution has an extra Raman and ROA signal around 180 cm^{-1}, most probably originating in the methyl group rotation. Also the two fundamental bands of skeletal/bending modes around 400 cm^{-1} are shifted by ~3 cm^{-1} to the right. These details are partially reproduced by the calculations (band shift by ~8 cm^{-1}), and the overall reasonable agreement between the experiment and the modeling allows us to better understand the low-frequency ROA, primarily stemming from translational and rotational-like motions of individual chiral molecules. This observation is consistent with Fig. 3 showing that two methyloxirane molecules are not much mutually oriented even at the closest distances. In other words, a methyloxirane molecule senses the neighboring one primarily as spheres, and their shape or chirality plays a secondary role.

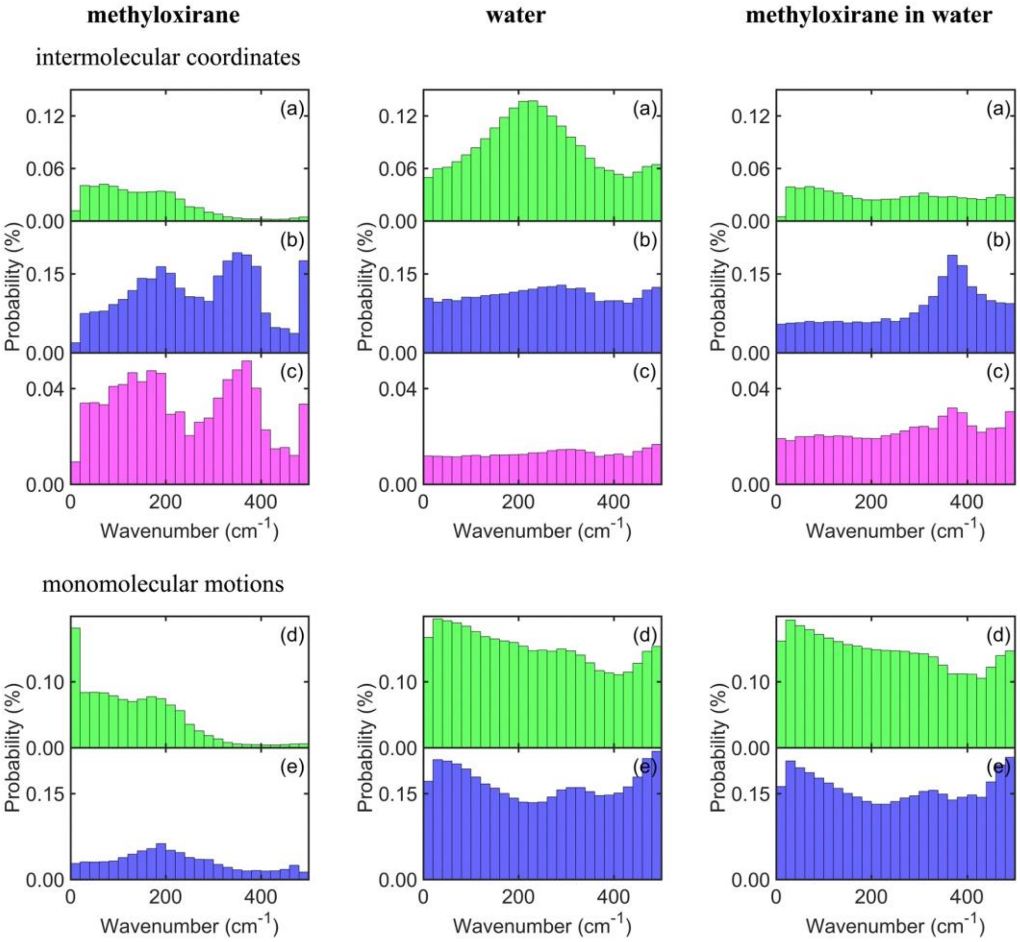

Fig. 8 Relative vibrational potential energies of intermolecular motions related to two (stretching (a), bending (b), torsion (c)) and one (translations (d), rotations (e)) molecules, for neat methyloxirane, water and a mixture.

In a different way we try to understand the low-frequency vibrations introducing intermolecular coordinates, or translations and rotations of one molecule.[14] The corresponding potential energy distributions (PEDs, see the definition in Fig. S9, ESI†) are plotted in Fig. 8. Note that redundant sets of the coordinates were created automatically and their PEDs are not unique. Nevertheless, in the current set we see that intermolecular motions formally contribute differently to the vibrational energy in water, methyloxirane, and the mixture. In pure water, a clear band around 220 cm^{-1} for the stretching (a) is developed. In neat methyloxirane the stretching starts to contribute in the lowest frequencies only, and the contribution is smoothed out in the mixture. The bending (b) and twisting (c) modes are most structured in neat methyloxirane, reflecting the more complicated shape of the molecule. At this level, it is difficult to interpret the histograms in more detail, but the broadness of the probability distributions does not suggest that a specific interaction would be responsible for the low-frequency ROA, and is thus consistent with the similarity of the neat liquid and solution spectra.

3.5 III–VI, theory *vs.* experiment

For the other molecules (**III–VI**) the vibrational potential energy distributions (Fig. S9, ESI†) are more complex than for water or methyloxirane. The intermolecular modes are more intertwined with low-frequency intramolecular motions, such as rotations of the phenyl, methyl, hydroxyl, trifluoromethyl and amine groups (*cf.* Table S3, ESI† with the normal mode assignment). The histogram distributions for **III–V** are quite similar, showing higher contributions of molecular translations, intermolecular stretchings and rotations with decreasing frequency. For α-pinene **VI** the stretching also becomes important for the lowest frequencies, while the intermolecular bending and twisting modes are more mixed with intramolecular ones and formally thus contribute even close to 500 cm^{-1}.

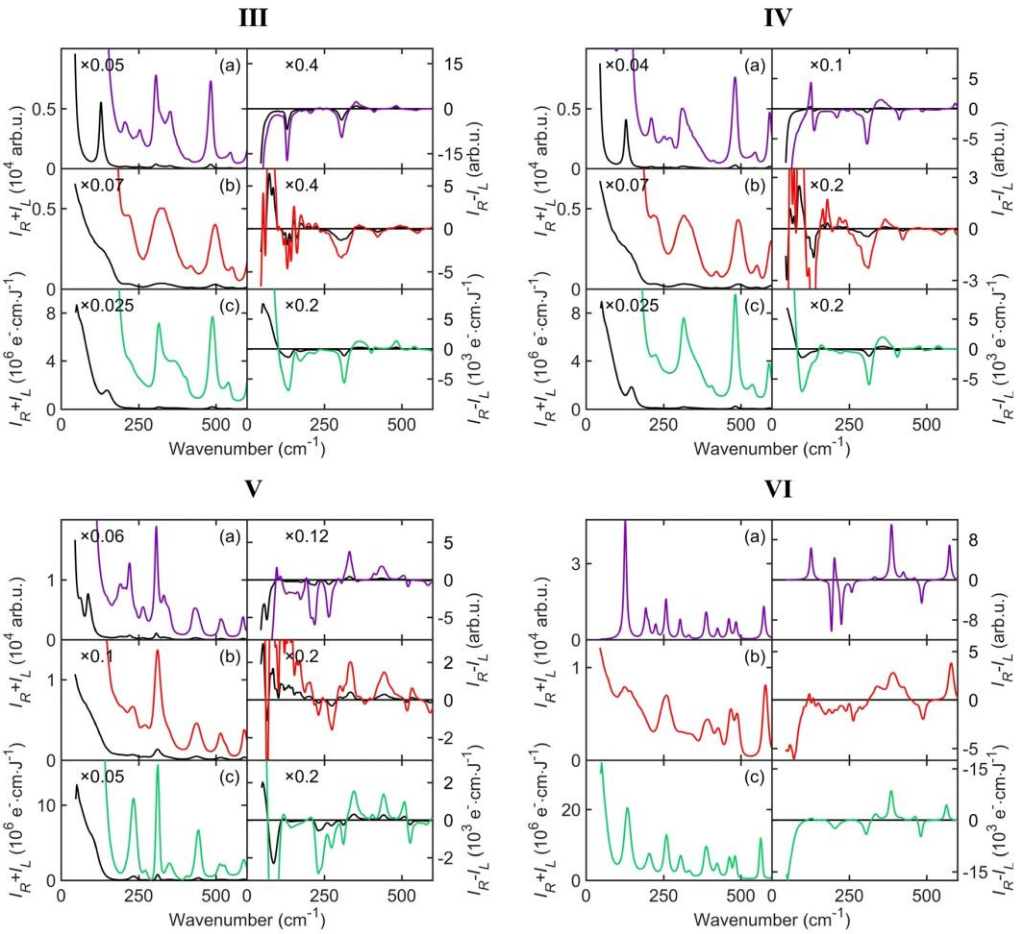

Fig. 9 Raman and ROA spectra of **III–VI** (a) simulation of one molecule (**III–V** conformer averaging, **VI** – minimum only), (b) the crystal model, and (c) the experiment.

Raman and ROA spectra of **III–VI** simulated with one molecule including averaging over the potential energy surface and the crystal-like approach are compared to those of the experiment in Fig. 9. These ''more complicated'' molecules possess many low-frequency intra(mono)molecular fundamental vibrational modes, and the single molecule simulation reasonably well describes some Raman and ROA spectral features down to ~200 cm^{-1}. However, in the lowest frequency region the multimolecular crystal model performs better. In particular, it correctly gives the ROA sign as the frequency approaches 50 cm^{-1}. Least satisfying is the simulation for the fluorine-containing compound **V**, probably because of inaccuracy of the OPLSAA force field. For example, the crystal model often gives the fundamental bands too broad and wrong signs of the 507 and 528 cm^{-1} ROA bands of **V**. In spite of these minor inconsistencies, we find it important that we can at least semi-quantitatively understand the observed data in terms of molecular structure and interactions. The modeling technology is also flexible and open to improvement when a bigger computer power becomes available.

4. Conclusions

We developed a crystal-like computational protocol that allowed us to analyze in detail low-frequency ROA spectra of six example chiral liquids. The results show that the signal is a complicated function of molecular structure that can be understood only on the basis of spectral simulations. The low-frequency modes are not too specific; nevertheless, the analysis of the vibrational potential energy suggests that for small rigid molecules (α-pinene, chloropropionitrile, and methyloxirane) the low-frequency signal comes primarily from molecular translations and rotations. For more flexible molecules the molecular/intermolecular low-frequency modes are mixed with monomolecular fundamentals. Very similar spectra were observed for neat methyloxirane and its water solution; this rather surprising observation could be reproduced with the crystal model and provided a phenomenological insight into the low-frequency chirality. Although the precision of the simulations is limited due to available computer power, they provide a sound theoretical basis to interpret the observed spectra and can be systematically improved in the future. The low-frequency ROA spectroscopy thus provides an interesting window into the world of chiral molecules, their structure and interactions, and can bring about useful knowledge about their behavior for biology and industry.

Conflicts of interest

J. Kapitán and P. Michal are involved in commercialization of the ROA technique. The other authors have no interest to declare.

Acknowledgements

This work was supported by the Czech Grant Agency (20-10144S, 22-04669S), the Ministry of Education (CZ.02.1.01/0.0/0.0/16_019/0000729 and e-INFRA CZ LM2018140), and student grant of the Palacký University Olomouc (IGA_PrF_2022_001).

References

1 K. Bērziņš, S. J. Fraser-Miller and K. C. Gordon, *Int. J. Pharm.*, 2021, **592**, 120034.

2 P. Ranzieri, A. Girlando, S. Tavazzi, M. Campione, L. Raimondo, I. Bilotti, A. Brillante, R. G. Della Valle and E. Venuti, *ChemPhysChem*, 2009, **10**, 657–663.

3 S. Yamamoto, Y. Morisawa, H. Sato, H. Hoshina and Y. Ozaki, *J. Phys. Chem. B*, 2013, **117**, 2180–2187.

4 J. J. Lazarević, S. Uskoković-Marković, M. Jelikić-Stankov, M. Radonjić, D. Tanasković, N. Lazarević and Z. V. Popović, *Spectrochim. Acta, Part A*, 2014, **126**, 301–305.

5 L. A. Blatz, in *Raman Spectroscopy*, ed. H. A. Szymanski, Springer, Boston, MA, 1970, DOI: 10.1007/978-1-4684-3027-1_4.

6 Q. Zhong and J. T. Fourkas, *J. Phys. Chem. B*, 2008, **112**, 15529–15539.

7 E. W. Castner and M. Maroncelli, *J. Mol. Liq.*, 1998, **77**, 1–36.

8 D. A. Turton, J. Hunger, A. Stoppa, A. Thoman, M. Candelaresi, G. Hefter, M. Walther, R. Buchner and K. Wynne, *J. Mol. Liq.*, 2011, **159**, 2–8.

9 L. Nafie, *Vibrational optical activity: Principles and applications*, Wiley, Chichester, 2011.

10 S. Yamamoto, S. Ishiro, J. Kessler and P. Bouř, *Phys. Chem. Chem. Phys.*, 2021, **23**, 26501–26509.

11 V. Palivec, P. Michal, J. Kapitán, H. Martinez-Seara and P. Bouř, *ChemPhysChem*, 2020, **21**, 1272–1279.

12 J. Kessler, J. Kapitán and P. Bouř, *J. Phys. Chem. Lett.*, 2015, **6**, 3314–3319.

13 T. Buffeteau, D. Pitrat, N. Daugey, N. Calin, M. Jean, N. Vanthuyne, L. Ducasse, F. Wien and T. Brotin, *Phys. Chem. Chem. Phys.*, 2017, **19**, 18303–18310.

14 P. Michal, R. Čelechovský, M. Dudka, J. Kapitán, M. Vůjtek, M. Berešová, J. Šebestík, K. Thangavel and P. Bouř, *J. Phys. Chem. B*, 2019, **123**, 2147–2156.

15 M. Brehm and M. Thomas, *J. Phys. Chem. Lett.*, 2017, **8**, 3409–3414.

16 Y. Yang, J. Cheramy, M. Brehm and Y. Xu, *ChemPhysChem*, 2022, **23**, e202200161.

17 L. Rayleigh, *Philos. Mag.*, 1899, **47**, 375–384.

18 L. I. Komarov and I. Z. Fischer, *Soviet Phys. JETP*, 1963, **16**, 1358–1361.

19 A. Einstein, in *Collected Papers of Albert Einstein, The Swiss Years: Writings 1909–1911*, ed. M. J. Klein, A. J. Kox, J. Renn and R. Schulmann, Princeton U. P., Princeton, 1994, vol. 3, pp. 231–249.

20 A. G. Rojo and P. R. Berman, *Am. J. Phys.*, 2010, **78**, 94–101.

21 L. D. Barron, *Molecular Light Scattering and Optical Activity*, Cambridge University Press, Cambridge, UK, 2004.

22 D. Pestov, G. O. Ariunbold, X. Wang, R. K. Murawski, V. A. Sautenkov, A. V. Sokolov and M. O. Scully, *Opt. Lett.*, 2007, **32**, 1725–1727.

23 L. Piseri and G. Zerbi, *J. Mol. Spectrosc.*, 1968, **26**, 254–261.

24 F. Lipparini, F. Egidi, C. Cappelli and V. Barone, *J. Chem. Theory Comput.*, 2013, **9**, 1880–1884.

25 T. D. Crawford and K. Ruud, *ChemPhysChem*, 2011, **12**, 3442–3448.

26 J. Šebestík and P. Bouř, *J. Phys. Chem. Lett.*, 2011, **2**, 498–502.

27 L. D. Barron, M. P. Bogaard and A. D. Buckingham, *J. Am. Chem. Soc.*, 1973, **95**, 603–605.

28 J. Kapitán, C. Johannessen, P. Bouř, L. Hecht and L. D. Barron, *Chirality*, 2009, **21**, E4–E12.

29 P. Eilers and H. Boelens, Leiden University Medical Centre report, 2005.

30 S. Baek, A. Park, Y. Ahn and J. Choo, *Analyst*, 2015, **140**, 250–257.

31 J. W. Ponder, *Tinker, Software Tools for Molecular Design*, Washington University School of Medicine, Saint Louis, 3.8 edn, 2000.

32 D. A. Pearlman, D. A. Case, J. W. Caldwell, W. S. Ross, T. E. Cheatham, S. Debolt, D. M. Ferguson, G. Seibel and P. A. Kollman, *Comput. Phys. Commun.*, 1995, **91**, 1–41.

33 R. C. Rizzo and W. L. Jorgensen, *J. Am. Chem. Soc.*, 1999, **121**, 4827–4836.

34 M. J. Frisch, G. W. Trucks, H. B. Schlegel, G. E. Scuseria, M. A. Robb, J. R. Cheeseman, G. Scalmani, V. Barone, G. A. Petersson and H. Nakatsuji, *et al.*, *Gaussian 16 Rev. A.03*, Gaussian, Inc., Wallingford, CT, 2016.

35 A. D. Becke, *J. Chem. Phys.*, 1993, **98**, 1372–1377.

36 A. Klamt, V. Jonas, T. Burger and J. C. W. Lohrentz, *J. Phys. Chem. A*, 1998, **102**, 5074–5085.

37 S. Grimme, J. Antony, S. Ehrlich and H. Krieg, *J. Chem. Phys.*, 2010, **132**, 154104.

38 S. Grimme, S. Ehrlich and L. Goerigk, *J. Comput. Chem.*, 2011, **32**, 1456–1465.

39 P. Bouř and T. A. Keiderling, *J. Chem. Phys.*, 2002, **117**, 4126–4132.
40 P. Bouř, *Collect. Czech. Chem. Commun.*, 2005, **70**, 1315–1340.
41 P. Bouř, *Qgrad*, Academy of Sciences, Prague, 2006.
42 G. Zuber and W. Hug, *J. Phys. Chem. A*, 2004, **108**, 2108–2118.
43 K. Ruud and J. Thorvaldsen, *Chirality*, 2009, **21**, E54–E67.
44 P. Bouř, J. Sopková, L. Bednárová, P. Maloň and T. A. Keiderling, *J. Comput. Chem.*, 1997, **18**, 646–659.
45 S. Yamamoto, X. Li, K. Ruud and P. Bouř, *J. Chem. Theory Comput.*, 2012, **8**, 977–985.
46 P. Bouř, D. Michalík and J. Kapitán, *J. Chem. Phys.*, 2005, **122**, 144501.
47 J. Hudecová, K. H. Hopmann and P. Bouř, *J. Phys. Chem. B*, 2012, **116**, 336–342.
48 J. Hudecová, V. Profant, P. Novotná, V. Baumruk, M. Urbanová and P. Bouř, *J. Chem. Theory Comput.*, 2013, **9**, 3096–3108.

Supporting Information

Low-frequency Raman Optical Activity Provides Insight into Structure of Chiral Liquids

Pavel Michal, Josef Kapitán, Jiří Kessler and Petr Bouř

Contents

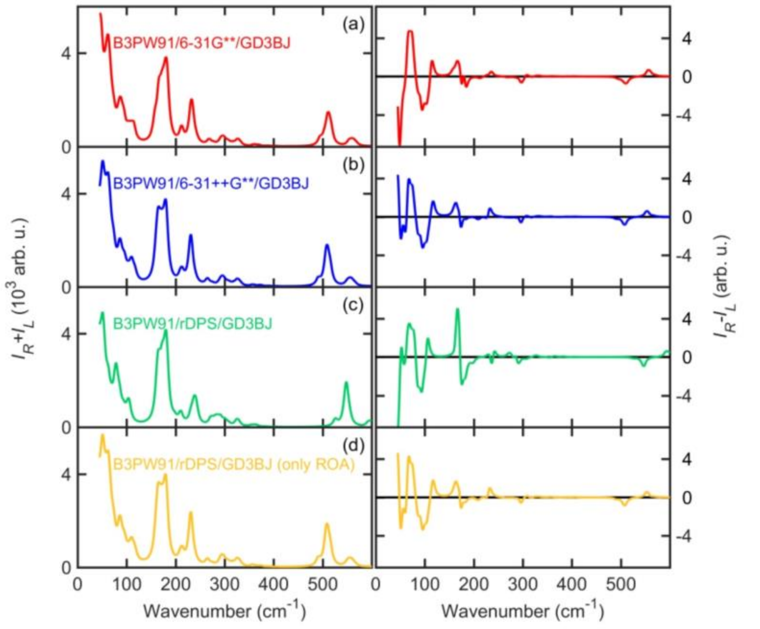

Figure S1. Raman and ROA spectra simulated for one snapshot of nitrile and three basis sets. For rDPS (d) the frequencies were calculated at the B3PW91/6-31++G**/COSMO(ACN)/GD3BJ level.

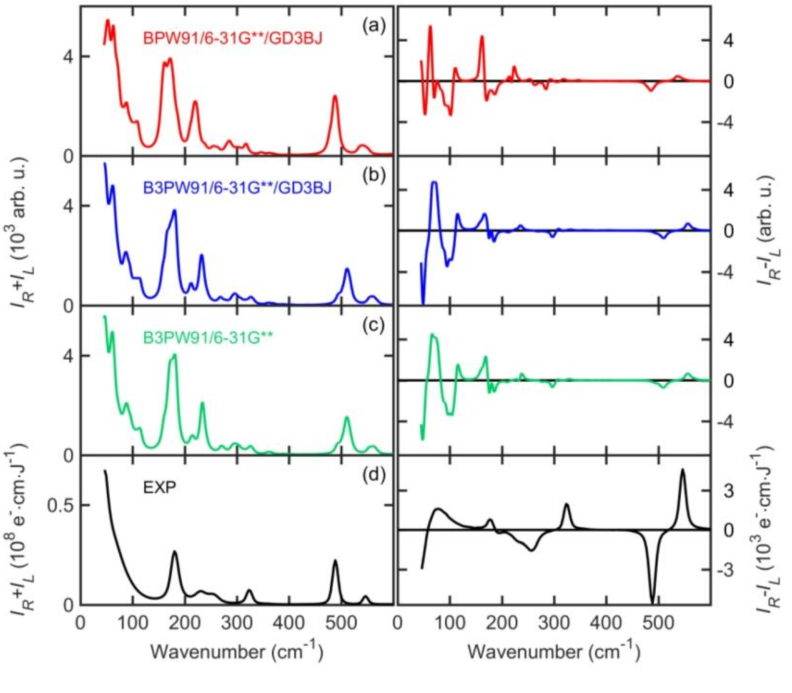

Figure S2. Nitrile Raman and ROA spectra calculated with the B3PW91 and BPW91 functionals, for B3PW91 with and without the GD3BJ dispersion correction, for the 6-31G** basis set and COSMO(ACN) solvent model.

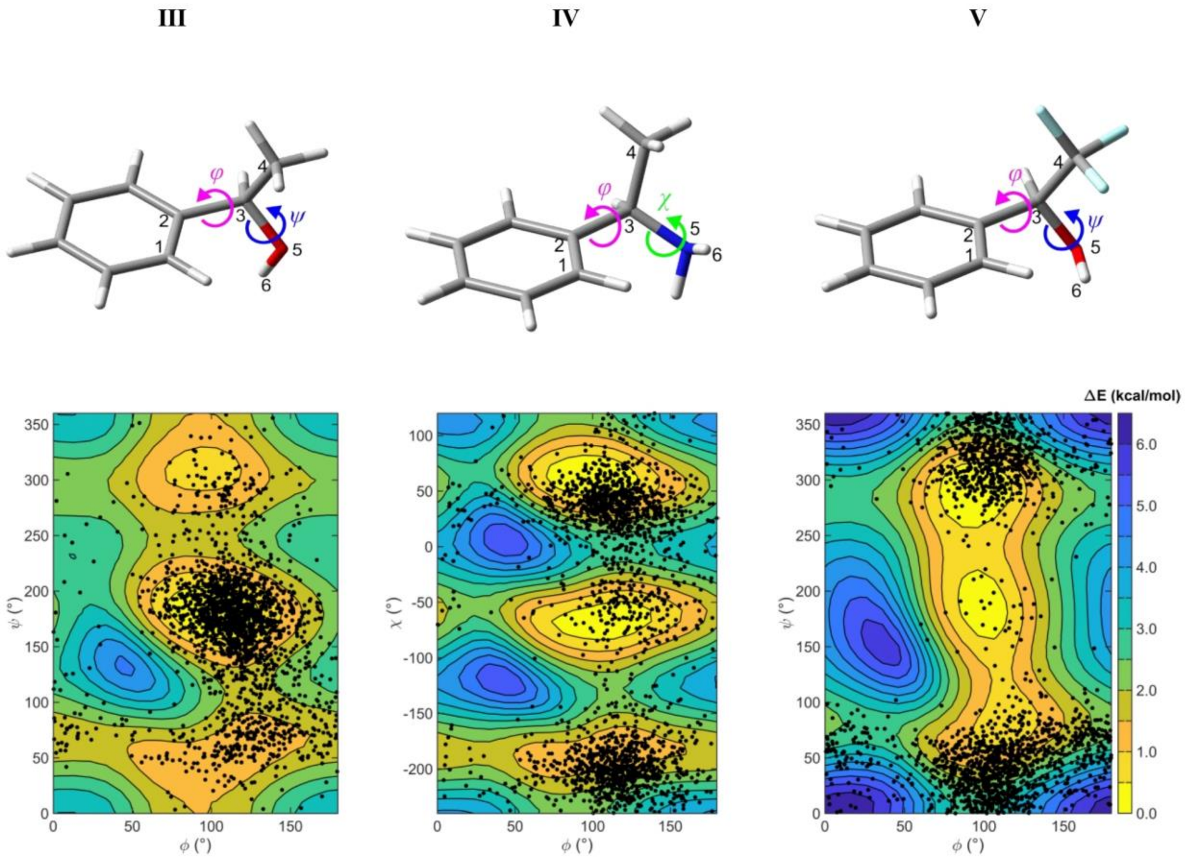

Figure S3. Dependencies of the electronic energy on selected torsion angles calculated at the B3PW91/6-311++G**/COSMO(benzylalcohol) level (contour map) and coordinates from 200 MD snapshots (black dots). The describe phenyl rotation, φ = C1-C2-C3-C4, hydroxyl rotation, ψ = C4-C3-O5-H6, and amine rotation, χ = C2-C3-N5-H6.

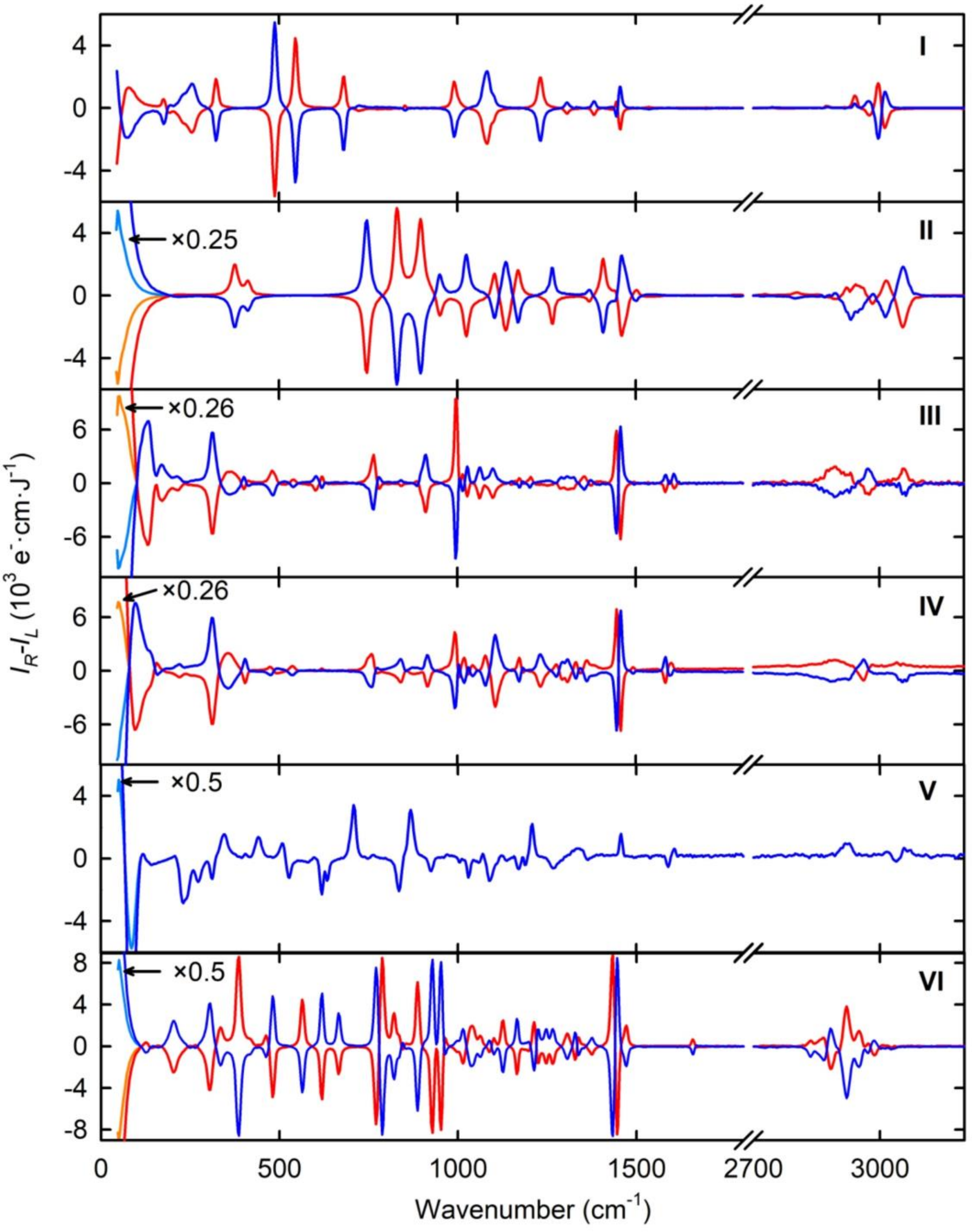

Figure S4. Experimental ROA spectra of the neat liquids, **I** 2-chloropropionitrile, **II** methyloxirane, **III** 1-phenylethanol, **IV** α-methylbenzylamine, **V** α-(trifluoromethyl)benzyl alcohol, and **VI** α-pinene. *R* and *S*-enantiomers are marked in red and blue, respectively.

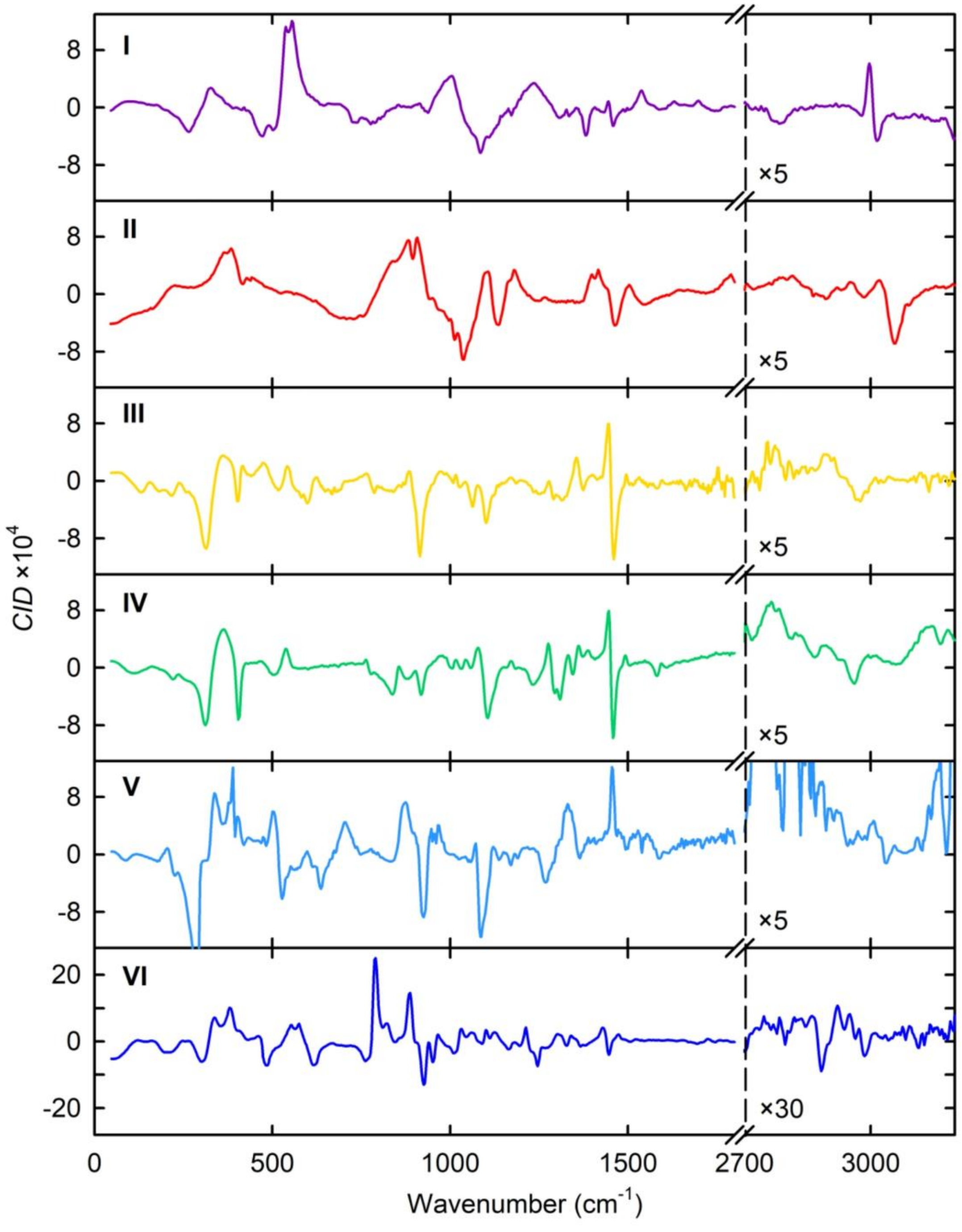

Figure S5. Experimental CID (ROA/Raman) ratios of **I** (*R*)-2-chloropropionitrile, **II** (*R*)-(+)-propylene oxide, **III** (*R*)-(+)-1-phenylethanol, **IV** (*R*)-(+)-α-methylbenzylamine, **V** (*S*)-(+)-α-(trifluoromethyl)benzyl alcohol, and **VI** (+)(1R,5R)-α-pinene.

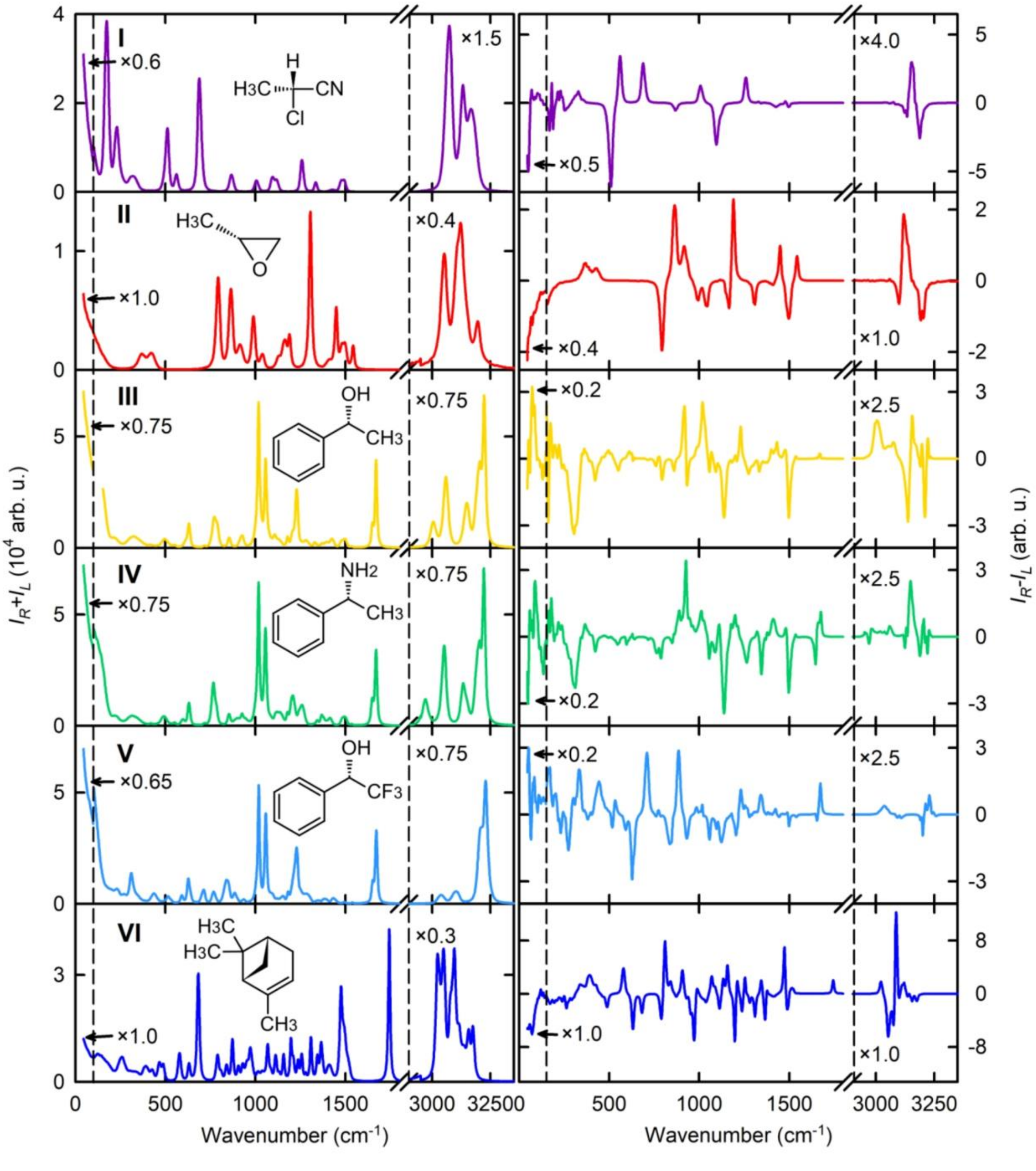

Figure S6. Raman and ROA spectra of **I-VI** simulated in the whole range, the crystal model.

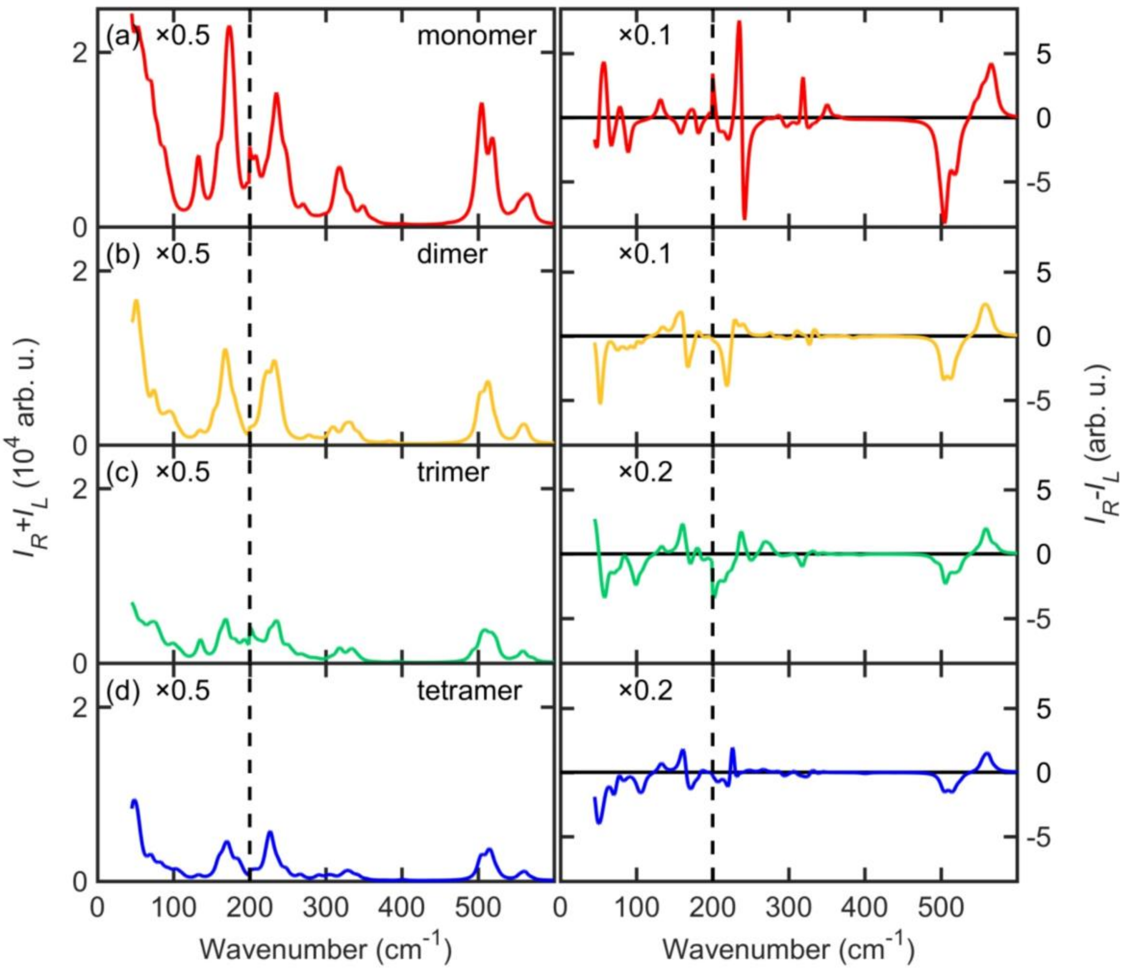

Figure S7. Raman and ROA spectra of one nitrile MD snapshot (10 molecules in the elementary cell) simulated from force field constructed from monomers, dimers, trimers and tetramers.

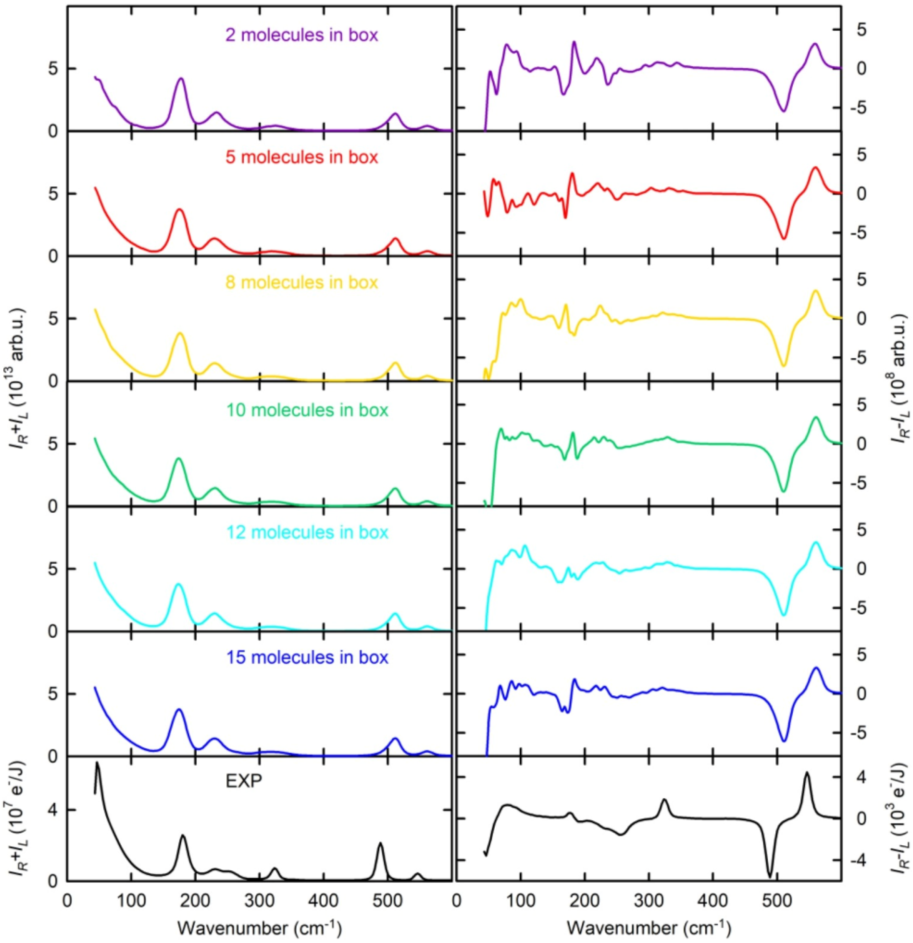

Figure S8. Calculated Raman and ROA nitrile spectra, using elementary cells containing 2, 5, 8, 10, 12 and 15 molecules, for 200 snapshots.

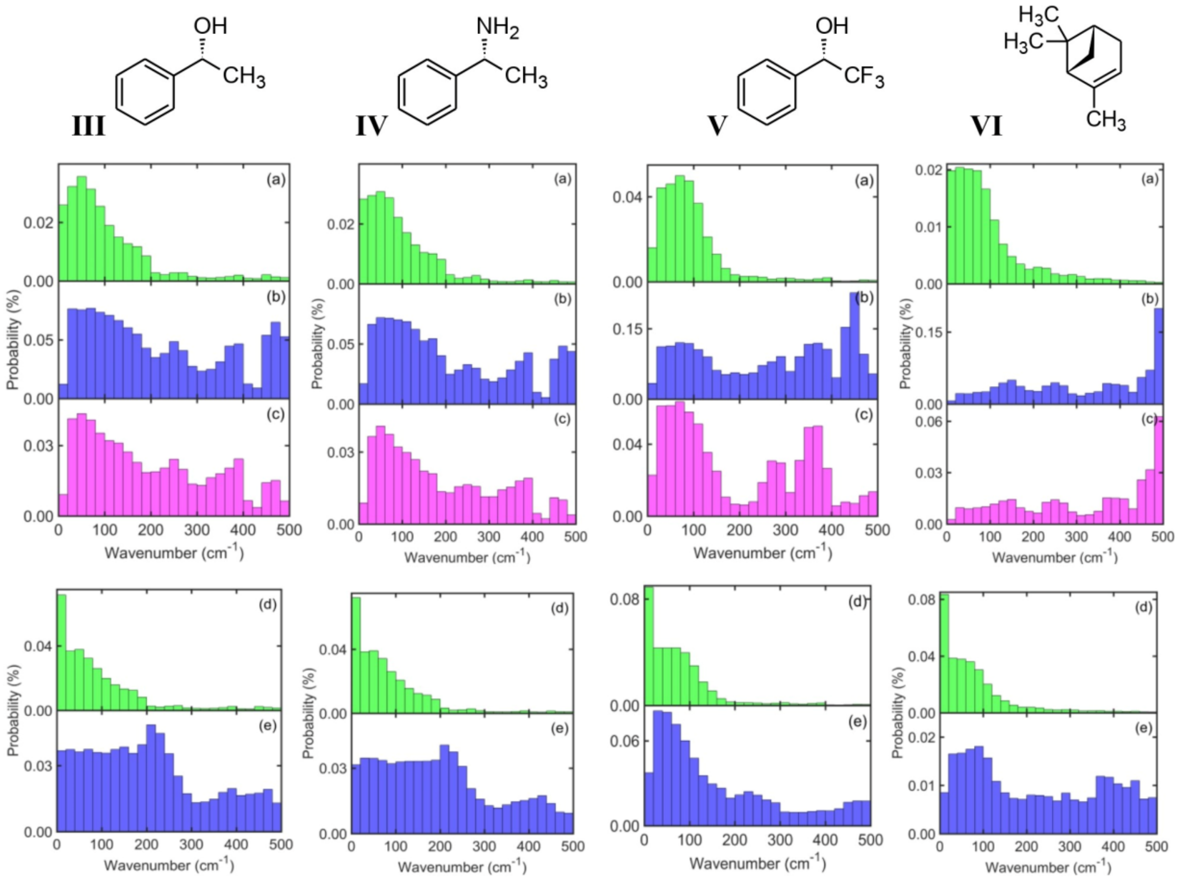

Figure S9. Relative vibrational potential energy distribution (PED) of intermolecular motions related to two (stretching (a), bending (b), torsion (c)) and one (translations (d), rotations (e)) molecule, for **III**-**V**.

PEDs of individual coordinates were calculated by the following procedure.

1) Transformation matrix **B** was defined, relating internal (I_i) and Cartesian (r_λ) coordinates, $I_i = \sum_\lambda B_{\lambda i} r_\lambda$. Using **B**, force field elements f_{ij} in the internal coordinates were calculated.

2) Within the harmonic approximation, Cartesian force field was normalized, so that the **S** matrix relating Cartesian and normal mode (Q_J) coordinates was obtained, $Q_J = \sum_\lambda S_{\lambda J} r_\lambda$

3) Relative energy contribution of coordinate I_i in mode J was calculated as $PED_{Ji} = \frac{A_{Ji}}{\sum_i A_{Ji}} \times 100\%$, where $A_{Ji} = b_{Ji}^2 f_{ii} \omega_J^{-1}$, $b_{Ji} = \sum_\lambda S_{\lambda J} B_{\lambda i} \sqrt{m_\lambda}$, ω_J is the normal mode frequency, m_λ is atomic mass. In the graphs, PED values were averaged over the snapshots and normal modes in a wavenumber interval.

Table S1 Laser powers at the sample P and total accumulation times t used in ROA measurements.

Compound	Enantiomer	P (mW)	t (h)
I nitrile	*R*	83	9.7
	S	83	13.2
II methyloxirane	*R*	540	34.6
	R @ water	338	5.5
	S	540	19.3
III phenylethanol	*R*	86	1.9
	S	82	2.9
IV benzylamine	*R*	69	7.8
	S	69	8.5
V 3F-benzyl	*S*	114	11.4
	R	266	5.5
VI α-pinene	*S*	266	5.5

Table S2. Dimensions of the elementary cells (10 molecules in the box) and densities used in the calculations

	Liquid	Box size (Å)	ρ (g/ml)	COSMO Solvent
I	nitrile	11.37	1.012	acetonitrile
II	methyloxirane	10.39	0.859	tetrahydrofuran
III	phenylethanol	12.61	1.012	benzylalcohol
IV	benzylamine	12.89	0.940	benzylalcohol
V	3F-benzyl	13.13	1.293	benzylalcohol
VI	α-pinene	13.82	0.858	cyclohexane

Table S3. Selected low-frequency fundamental modes in **III**-**V**.

v / cm-1	**modes**
III:	
36	Phe rotation
128	Me and Phe wagging
212	Me and Phe scissoring
266	Me and OH rotation
283	Me and OH rotation
305	deloc. def.
372	deloc. def.
411	Phe out of plane
482	deloc. def.
IV:	
29	Phe rotation
129	Me and Phe wagging
214	Me and Phe scissoring
268	Me rotation
303	deloc. def., NH_2 rotation
360	deloc. def.
411	Phe out of plane
480	NH_2 and Me wagging
V:	
27	Phe rotation
64	CF_3 rotation, Phe wagging
99	deloc. def.
199	OH rotation
233	deloc. def.
290	deloc. def.
308	deloc. def.
335	deloc. def.
412	Phe out of plane
428	deloc. def.

Appendix D – Symmetry, 14 (5), 990 (2022).

symmetry

MDPI

Article

Accurate Determination of Enantiomeric Excess Using Raman Optical Activity

Pavel Michal, Jana Hudecová, Radek Čelechovský, Milan Vůjtek, Michal Dudka and Josef Kapitán *

Department of Optics, Palacký University Olomouc, 771 46 Olomouc, Czech Republic;
michal@optics.upol.cz (P.M.); hudecova@optics.upol.cz (J.H.); celda@optics.upol.cz (R.Č.);
milan.vujtek@upol.cz (M.V.); michal.dudka@upol.cz (M.D.)
* Correspondence: kapitan@optics.upol.cz

Abstract: The optical purity of a chiral sample is of particular importance to the analytical chemistry and pharmaceutical industries. In recent years, the vibrational optical activity (VOA) has become established as a sensitive and nondestructive technique for the analysis of chiral molecules in solution. However, the relatively limited accuracy in the range of about 1–2% reported in published papers and the relatively small spread of experimental facilities to date have meant that vibrational spectroscopy has not been considered a common method for determining enantiomeric excess. In this paper, we attempt to describe, in detail, a methodology for the determination of enantiomeric excess using Raman optical activity (ROA). This method achieved an accuracy of 0.05% for neat α-pinene and 0.22% for alanine aqueous solution, after less than 6 h of signal accumulation for each enantiomeric mixture, which we believe is the best result achieved to date using vibrational optical activity techniques. An algorithm for the elimination of systematic errors (polarization artifacts) is proposed, and the importance of normalizing ROA spectra to correct for fluctuations in excitation power is established. Results comparable to those obtained with routinely used chemometric analysis by the partial least squares (PLS) method were obtained. These findings show the great potential of ROA spectroscopy for the quantitative analysis of enantiomeric mixtures.

Keywords: enantiomeric excess; Raman optical activity; Raman spectroscopy; vibrational optical activity; vibrational circular dichroism; optical activity; optical purity; α-pinene; alanine

check for updates

Citation: Michal, P.; Hudecová, J.; Čelechovský, R.; Vůjtek, M.; Dudka, M.; Kapitán, J. Accurate Determination of Enantiomeric Excess Using Raman Optical Activity. *Symmetry* **2022**, *14*, 990. https://doi.org/10.3390/sym14050990

Academic Editors: Cristóbal Pérez, Sérgio R. Domingos and Amanda Steber

Received: 4 April 2022
Accepted: 9 May 2022
Published: 12 May 2022

1. Introduction

Chiroptical spectroscopy involves spectroscopic techniques based on the differences in the interactions of left- and right-handed circularly polarized radiation with chiral molecules. In this article, we focus on vibrational Raman optical activity, which detects the differential signal in Raman scattering [1,2] and its use to detect enantiomeric excess.

Since the 1970s, vibrational optical activity techniques have been constantly improved. The first milestone for potential widespread use in this field was the first commercial vibrational circular dichroism (VCD) spectrometer introduced in 1997, followed by a commercial ROA spectrometer in 2005. As the VOA signal is usually four to five orders weaker than the parent signal, spectra are somewhat susceptible to experimental artifacts. In addition, relatively large sample volumes (usually tens of μL) and concentrations (usually tens of mg/mL) are needed. The advantage of ROA is the ease of measuring samples in aqueous solutions, while the advantage of VCD is less restrictions on sample fluorescence.

One of the main applications of VOA is the determination of the absolute configuration and the measurement of optical purity of chiral samples. The optical purity of a chiral sample can be characterized by the enantiomeric excess (EE) defined as

$$e = \frac{n_A - n_B}{n_A + n_B} \ (\times 100\%), \tag{1}$$

where n_A and n_B are the molar amounts of each enantiomer A and B in the sample. The absolute value of EE is 100% for the optically pure sample and 0% for the racemic mixture [2].

Thus far, the most common method for the determination of enantiomeric excess is chiral chromatography; however, this is a demanding experimental method, and special columns must be used for different chiral substances. Furthermore, chiral capillary electrophoresis (CE) is a promising method that allows enantioselective separation in a small volume. It is suitable for nonvolatile compounds and provides a better separation of both forms than does high-performance liquid chromatography (HPLC) [3].

Enantiomeric excess can be measured by optical rotation (OR) or optical rotary dispersion (ORD); however, the signals are often dependent on concentration and other experimental parameters. VOA spectroscopy is a noninvasive method where a large number of vibrational bands can be observed and are useful for determining EE. This also makes it possible to better identify experimental artifacts or other impurities present in the sample that make the determination of EE more reliable.

The first EE determination with the VCD spectrometer was done in 1990 with a remarkable accuracy of 1% measured for deuterated chiral hydrocarbons in the gas phase. The main instrumental limitation was a long-term instrumental drift caused by changes in temperature and humidity, small optical throughput and a low resolution around 14 cm^{-1} [4]. Five years later, the EE of α-pinene by ROA in the right-angle scattering geometry has been recorded with accuracies of 0.1% for the one-component chiral sample and 1.5% for the two-component chiral sample [5]. However, these results were based on a limited statistical ensemble, and they were never verified or reproduced.

The accuracy of EE determination by Fourier-transform VCD for one chiral species (α-pinene in CCl4) was found to be around 1% and for two chiral species (camphor and borneol) to be around 2% in the mid-IR region and 2% and 3% in the near-IR region [6,7].

In recent years, efforts have been made to determine the EE of chiral compounds in the solid state using VCD spectroscopy [8], which is important for compounds that are insoluble in organic solvents or when the racemization process in the chiral sample is too fast in the liquid phase; however, the solid sample required more care that the liquid isotropic samples [9]. Based on a linear regression for selected VCD bands, the accuracy of the EE determination was 2.4%. The study was supplemented by the EE determination of camphor in CCl_4 solution with an accuracy of 1.1% [4,6].

In this paper, we demonstrate the methodology of EE determination by the ROA measurement of two test compounds, neat α-pinene and alanine in an aqueous solution. We discuss limits of the presented method and compare the results with alternative statistical method known as partial least squares (PLS) [6,10]. An approach to effective systematic artifact elimination based on discrepancies in a mirror image of the opposite enantiomers is introduced, and a large improvement in the accuracy of the enantiomeric excess determination is achieved.

2. Procedure for Determining the Enantiomeric Excess

2.1. Sample Preparation

Suppose that we have two samples A and B of the same chiral substance with enantiomeric excesses e_A and e_B (the most common situation is $1 \cong e_A \cong -e_B$). We will mix these samples in mass ratios m_A and m_B to have a total of N different enantiomeric mixtures. For the i-th enantiomeric mixture, the enantiomeric excess is then given by:

$$e_i = \frac{e_A m_{Ai} + e_B m_{Bi}}{m_{Ai} + m_{Bi}} = e_A \frac{m_{Ai} - c_{BA} m_{Bi}}{m_{Ai} + m_{Bi}}, \quad i = 1, \ldots, N \tag{2}$$

where $c_{BA} = -e_B/e_A$ and $e_1 = e_A$ and $e_N = e_B$ by definition ("pure" enantiomeric forms are included in the set). For real samples, it is not possible to achieve exactly unit enantiomeric excess. Moreover, the enantiomeric excesses of the two "pure" forms are also often not precisely known. Thus, in practice, two approximations can be used: we declare both the enantiomeric excesses e_A and e_B to be in absolute value unitary, and then we can write:

$$e_i^0 = \frac{m_{Ai} - m_{Bi}}{m_{Ai} + m_{Bi}}, \tag{3}$$

or we declare the enantiomeric excess e_A to be unitary, and then the following approximation can be used:

$$e_i^1 = \frac{m_{Ai} - c_{B1} m_{Bi}}{m_{Ai} + m_{Bi}}, \tag{4}$$

where the constant c_{B1} needs to be determined.

2.2. Raman and ROA Spectra Measurements and Normalization

We measure Raman spectra $S_{i\nu}^{raw}$ (circular intensity sums) and ROA spectra $D_{i\nu}^{raw}$ (circular intensity differences) for N samples, all usually normalized to the used excitation energy (laser power measured at the sample multiplied by the acquisition time). The wavenumber index ν varies from *1* to M (the number of spectral points). Therefore, the dataset represents a matrix of size $N \times M$.

The ROA signal can be easily affected by intensity fluctuations caused by the laser instability or possibly also by thermal fluctuations in the sample. Therefore, the ROA intensity normalization according to the parent Raman spectra was necessary. The situation is often complicated by the fact that, in addition to the Raman signal, a fluorescent background from impurities in the sample is also detected in the spectrum. Moreover, this background is not stable and changes during the measurement. Therefore, before determining the Raman integral intensity, the background in all Raman spectra must first be subtracted to obtain the spectra $S_{i\nu}^{bas}$. Normalized ROA spectra are then calculated as

$$D_{i\nu} = D_{i\nu}^{raw} \frac{\sum\limits_{\nu} S_{A\nu}^{bas}}{\sum\limits_{\nu} S_{i\nu}^{bas}} = D_{i\nu}^{raw} n_{norm}, \tag{5}$$

where the sum (intensity integral) is performed over the selected spectral region. The selection of the reference spectra from the set is arbitrary; however, we chose our reference *A* for simplicity.

In the case of a chiral solute in solution, differences in the molar concentrations of "pure" forms must also be included in the Raman intensity normalization.

2.3. Enantiomeric Excess Determination—Method 1

The simplest method for determining the enantiomeric excess is to solve the linear equation:

$$D_{i\nu} = \hat{e}_i^D \, D_{A\upsilon}, \tag{6}$$

where $D_{i\nu}$ is one element of the matrix $N \times M$ of all ROA spectra, $\hat{e}_i^D$ is one element of the column vector $N \times 1$ representing the enantiomeric excesses that we want to determine (note that EE determined from the spectra will be labelled with a hat, while EE determined using weighed "pure" forms A and B will be labelled without a hat), and $D_{A\upsilon}$ is one element of the row vector $1 \times M$ representing the ROA spectra of reference *A*, which is usually the first row of matrix *D*. This is a set of overdetermined linear equations that can be solved by the least squares method as:

$$\min_{\hat{e}_i} \sum_{\nu=1}^{M} \left(D_{i\nu} - \hat{e}_i D_{A\nu} \right)^2 \tag{7}$$

The basic assumption of this method is that the enantiomeric excess of reference *A* is unity (100%). All spectra for which the enantiomeric excess is determined are compared with reference *A*. The smallest number of spectra used is therefore $N = 2$. The resulting enantiomeric excess is always determined relative to reference *A*.

2.4. Enantiomeric Excess Determination—Method 2

As an alternative and often used method a partial least squares algorithm (PLS) with five-fold cross-validation was used to construct predictive models for the EE determination using leave-one-out procedure. In this procedure, $N - 1$ ROA spectra and EE determined by weighting (e_k^0, $k \neq i$) were used as a training set and response to predict the EE of the omitted ROA spectrum $\hat{e}_i^{PLS}$. Only one PLS component was needed to adequately fit the ROA data.

The implementation of PLS regression in the MATLAB software was used [6,7,10–12]. It can be shown that at least two spectra (usually two "pure" enantiomers A and B) must be used for the training set of the PLS method; therefore, the minimum number of measured spectra is three. The determination of the enantiomeric excess may be subject to systematic error if the enantiomeric excesses in the training set are incorrectly determined, which may be the case if the relative enantiomeric excesses of the reference pure forms A and B from which the mixtures for the training set are prepared are not correctly determined.

2.5. Evaluation of Enantiomeric Excess Determination Errors

Enantiomeric excess determination errors are evaluated as differences between EE determined from spectra $\hat{e}_i$ and EE determined from the sample preparation e_i^0 (3):

$$\Delta_i^0 = e_i^0 - \hat{e}_i. \tag{8}$$

The enantiomeric excess of "pure" forms A and B is always specified by the manufacturers only with some precision, and therefore it can be assumed not to be the same. Therefore, we can try to determine the constant c_{B1} by determining the relative enantiomeric excess of form B according to relation (4) assuming that the average error (or sum of all errors) is zero.

$$\Delta_i^1(c_{B1}) = e_i^1(c_{B1}) - \hat{e}_i,\ \sum_{i=1}^{N} \Delta_i^1(c_{B1}) = 0. \tag{9}$$

We can then find a general idea of the correctness of the determination of EE by evaluating the standard deviation of the errors (from the assumed correct zero average error value) as:

$$\sigma(\Delta) = \sqrt{\frac{\sum_{i=1}^{N} \Delta_i^2}{N}}. \tag{10}$$

2.6. Correction of Artifacts in ROA Spectra

It is known that the artifacts occurring in ROA spectra are proportional to the degree of circularity (ref. Hug and Hangartner [13]) or the difference of the orthogonally polarized Raman spectra, and thus it is reasonable to assume that these artifacts will be the same in all ROA spectra of the enantiomeric mixtures used. In our experience, this condition is well satisfied in ROA spectrometers constructed according to the original work of W. Hug [14], which have precisely synchronized all motorized linear rotators.

The simplest and universally used method for determining artifacts a is to sum the ROA spectra of the two "pure" forms and similarly, by subtraction, receive the true ROA spectrum D^{true}.

$$a_\nu^{AB} = \frac{D_{A\nu} + D_{B\nu}}{2},\ D_\nu^{trueAB} = \frac{D_{A\nu} - D_{B\nu}}{2}. \tag{11}$$

However, if both "pure" forms are not available, or if we want to use all measured ROA spectra with different enantiomeric excess to increase the signal-to-noise ratio in the artifact spectrum, a set of linear equations can be used:

$$D_{i\nu}^{\exp} = D_\nu^{trueN} e_i + a_\nu^N \tag{12}$$

with unknowns D_v^{trueN} and a_v^N. This set is overdetermined for $N > 2$, and, in this case, the solution of ROA artifact-free spectrum D_v^{trueN} and artifact spectrum a_v^N can be found by the method of least squares. It is also worth noting that known enantiomeric excesses can be used from both sample preparation e_i or measurements $\hat{e}_i$. However, these values are usually a little different and have little effect on the resulting spectrum of artifacts a_v^N.

Finally, the artifact spectra are subtracted from ROA spectra:

$$D_{iv}^a = D_{iv} - a_v, \tag{13}$$

and the corrected spectra are used for further improved calculation of the enantiomeric excess.

3. Materials and Methods

3.1. Chemicals and Sample Preparation

Both enantiomers of α-pinene were purchased from Sigma-Aldrich, specifically (1S)-(−)-α-pinene (305715-5G) and (1R)-(+)-α-pinene (268070-5G), and the manufacturer states that the optical purity exceeds 97% for both samples. A relatively large total volume of 0.75 mL was used for each EE mixture of α-pinene, in order to reduce errors in the EE determination caused by weighting: first, the prevailing enantiomer of α-pinene was pipetted into a 1.5 mL glass vial and closed with a screw cap, which prevented evaporation of the sample. After weighting, the second enantiomer was added, and the sample was mildly stirred.

For alanine (Ala), aqueous stock solutions of both enantiomers L-Ala (Fluka 05129-25g, molar concentration 1.204 M) and D-Ala (Fluka 05140-5g, molar concentration 1.208 M) were prepared by adding deionized water to the weighted powder to match a 5 mL marker of a volumetric flask with volume error of 0.025 mL. Stock solutions were filtered through Millex-GV filters with PVDF membrane 0.22 μm pore size. The total volume 0.5 mL of solutions was then used for the final preparation of EE mixtures by weighting.

Analytical weights (Adam Equipment) with a 0.01 mg resolution were used in all cases. The maximal error given by mass measurement fluctuations was estimated to be 0.1 mg, which corresponds to approx. 0.02% error of the enantiomeric excess ee_i^0 determined according to Equation (3).

Nine samples of different EE (regularly distributed from −100% to 100%) were prepared (N = 9) and measured in nonconsecutive order: the measurement orders of the mixtures with approximate EEs for α-pinene and alanine were 100, −100, 0, 25, −25, 50, −50, 75 and −75 (see Table 1) and 100, −100, 75, 0, −75, 50, −50, 25 and −25 (see Table 2), respectively.

3.2. Instrumentation

All presented Raman and ROA spectra were measured using a ROA spectrometer developed by Palacký University Olomouc in collaboration with the companies ZEBR and Meopta-optica [15]. The instrument is based on W. Hug's design using back-scattering geometry, a scattered circular polarization (SCP) modulation scheme and a Nd:YAG laser with a 532 nm excitation wavelength [13,14]. The samples were measured in a rectangular fused silica cell of 70 μL volume in the temperature cell, thus, ensuring a stable temperature 25.0 ± 0.1 °C. The laser power at the sample was set to 266 mW for α-pinene and 772 mW for alanine, which are the usual powers used for similar samples [14].

Raman and ROA spectra were simultaneously collected in the full range from 40 to 4000 cm^{-1}. However, since the ROA:Raman ratio is small in the high-wavenumber spectral range around 3000 cm^{-1}, only data from one camera in spectral range 40 to 2400 cm^{-1} were used for further processing in all cases [15]. The spectral resolution was ~6 cm^{-1}, and the spectra intensity is given as the number of detected electrons per excitation energy, $\text{e}\cdot\text{J}^{-1}$, i.e., the intensity correction procedure was not applied.

3.3. Data Processing

Analyzed spectra were exported in 84 blocks (3.9 min per of accumulation time per block) and 10 blocks (34 min per of accumulation time per block) for α-pinene and alanine, respectively. The data were also smoothed with the Savitzky–Golay filter for further processing. Various limited spectral ranges from the full dataset were tested for Raman baseline correction, ROA intensity normalization (Equation (5)), EE determination (Equation (7) or PLS) and artifact correction (Equations (12) and (13)), and these will be discussed further.

The Raman baseline correction needed for ROA spectra normalization played a key role in the performance of the EE determination. For the baseline correction, we used asymmetric least square smoothing algorithm [16], where an optimal asymmetry parameter 1.3×10^{-4} and smoothness parameter 3.2×10^5 were set both for α-pinene and alanine. The chosen baseline parameters were relatively robust and, within one order of magnitude, led to similar results. An alternative approach to effectively estimate the baseline is the iterative polynomial smoothing method [17]. When applied to the presented data set, it led to similar results but with a longer computing time. All data were processed and further analyzed in MATLAB software.

4. Results and Discussion

Two samples were used to determine the enantiomeric excess: α-pinene, which occurs as a liquid at room temperature and is often used as a chiroptical calibration standard. Furthermore, alanine was used as a prototype chiral molecule investigated in aqueous solution. Alanine is the simplest chiral amino acid, which is also readily available in both enantiomers.

The procedure for processing the enantiomeric excess was first illustrated on spectra in the basic setup (parameters for Savitzky–Golay smoothing, spectral range selection for Raman baseline correction, ROA normalization, artifact correction and EE determination), and the basic observed aspects of the EE determination and possible sources of measurement errors will be explained by these results. Then, the refinement parameters for the spectra processing will be discussed in order to obtain the most accurate and precise results. Finally, we will discuss the question of how the overall accuracy of the EE determination (standard deviation of errors of the EE determination) depends on the required measurement time.

4.1. Basic Processing Routine

The Raman and ROA raw data used for the further analysis of α-pinene and alanine (nine enantiomeric mixtures) are presented in Figures 1a,b and 2a,b. All spectra were then subjected to third-order five-point Savitzky–Golay smoothing. The spectral region 100–2000 cm^{-1} was used in all mentioned aspects of data processing. Figures 1c and 2c show the Raman spectrum after baseline correction, and Figures 1d and 2d show the spectrum of the ROA artifacts determined by Equations (11) and (12). The elevated Raman baseline was effectively corrected by the asymmetric least squares smoothing algorithm taken from [16]. The aim of this procedure was not to make the baseline as flat as possible but to unify Raman spectra in the data set before the ROA normalization.

The results of the EE analysis for α-pinene and alanine aqueous solution are listed in Tables 1 and 2, respectively. The columns in these tables have the following meanings: i is the sample number (not in the order in which the spectra were measured; see Materials and Methods), n_{norm} is the ROA normalization factor determined according to Equation (5) after the Raman baseline correction, e_i^0 is the EE calculated from sample preparation according to Equation (3), $\hat{e}_i^D$ is the EE determined from ROA spectra according to Equation (6), Δ_i^{0D} is the corresponding EE determination error according to Equation (8), e_i^{1D} and Δ_i^{1D} are the recalculated EEs and corresponding errors calculated according to Equation (9) based on the assumption that reference B has a different EE than reference A and that the sum of errors Δ_i^{1D} is zero. The following four columns $\hat{e}_i^{Da}$, Δ_i^{0Da}, e_i^{1Da} and Δ_i^{1Da} have the same meaning; the artifact spectra according to Equation (13) were subtracted from the experimental ROA spectra to obtain the artifact-free ROA spectra needed for the calculation. The last two columns $\hat{e}_i^{PLS}$ and Δ_i^{0PLS} represent EEs determined by the leave-one-out PLS algorithm applied to baseline corrected and normalized spectra before the systematic artifact correction and their corresponding errors determined by Equation (8), respectively. The bottom line of the tables represents the standard deviation of the errors determined according to Equation (10) for the respective columns.

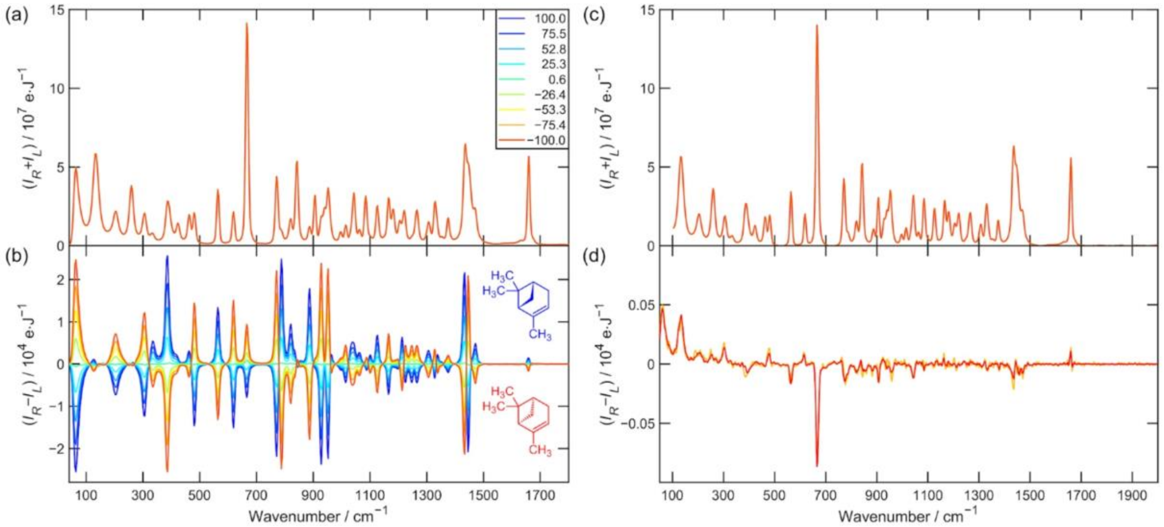

Figure 1. (**a**) Raman and (**b**) ROA spectra of neat liquid α-pinene enantiomeric mixtures after 5.5 h of exposition time each. The legend shows EE determined from sample preparation. (**c**) Raman spectra after baseline correction. (**d**) ROA artifact spectrum calculated according to Equation (11) is depicted in orange and calculated according to Equation (12) is red.

By comparing the standard deviations of the errors of EE determination $\sigma(\Delta_i^{0D})$ and $\sigma(\Delta_i^{1D})$, it can be said that using the assumption that the EE of the "pure" forms *A* and *B* need not be the same and that the sum of the errors is zero according to Equation (9) leads to a significant increase in the precision of the EE determination (the standard deviations of the errors of EE determination decreased roughly 1.6× for α-pinene and 9× in the case of alanine in aqueous solution) but not necessarily to improvement of the accuracy, which can be demonstrated by large deviations from −100% of EE of reference *B* (row $i = 9$, especially for alanine). Note that absolute values of EE of reference *B* above 100% are possible, since they are relative to reference *A* and indicate that reference *B* has a higher EE than reference *A*.

The data presented in Tables 1 and 2 for the ROA spectra after subtraction of artifacts and especially the values $\sigma(\Delta_i^{0Da})$ and $\sigma(\Delta_i^{1Da})$ do not suggest much improvement at first glance. However, the results for the determination of EE (row $i = 9$) clearly indicate that there has been a significant improvement in accuracy after artifact subtraction. The artifact spectra of α-pinene and alanine are plotted in Figures 1d and 2d. Strongly polarized and also the most intense Raman bands, such as α-pinene breathing vibration 667 cm^{-1} or alanine CN and CC stretching vibration 848 cm^{-1} are the most artifact prone [13]. They constitute approximately 10% of the measured ROA signal.

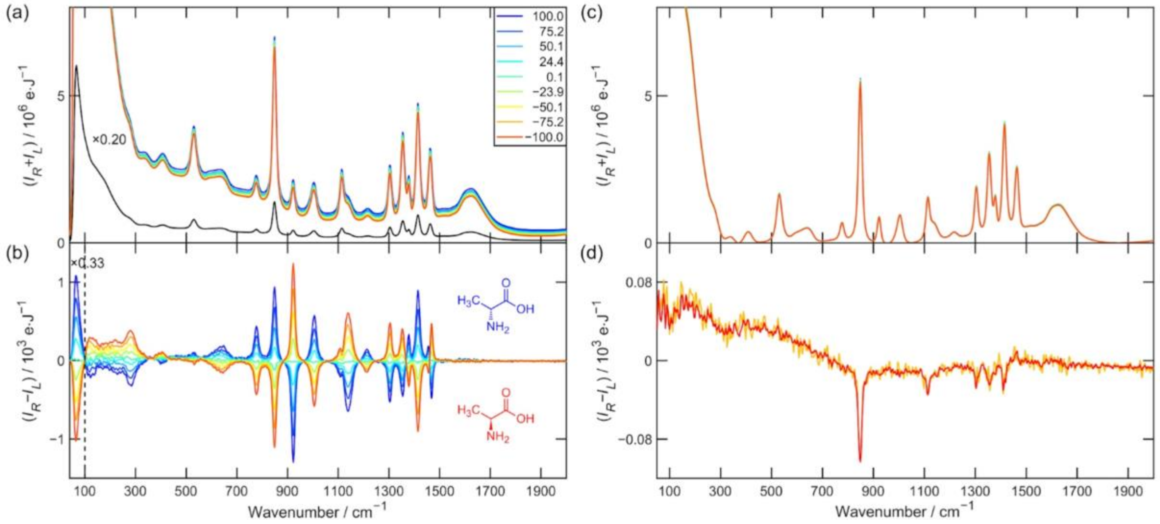

Figure 2. (**a**) Raman and (**b**) ROA spectra of alanine enantiomeric mixtures in water solution at a molar concentration cca 1.2 M after 5.7 h of exposition time each. The legend shows the EE determined from the sample preparation. The Raman spectrum of the reference (black) was multiplied by a factor of 0.2 in order to show strong low-wavenumber Raman scattering. (**c**) Raman spectra after baseline correction. (**d**) ROA artifact spectrum calculated according to Equation (11) is depicted in orange and calculated according to Equation (12) is red.

Table 1. Enantiomeric excess analysis of α-pinene spectra depicted in Figure 1. See text for detailed descriptions.

i	n_{norm}	e_i^0/%	$\hat{e}_i^D$/%	Δ_i^{0D}/%	e_i^{1D}/%	Δ_i^{1D}/%	$\hat{e}_i^{Da}$/%	Δ_i^{0Da}/%	e_i^{1Da}/%	Δ_i^{1Da}/%	$\hat{e}_i^{PLS}$/%	Δ_i^{0PLS}/%
1	1.000	100.00	100.00	0.00	100.00	0.00	100.00	0.00	100.00	0.00	100.34	−0.34
2	1.005	75.49	75.32	0.17	75.52	0.21	75.28	0.21	75.49	0.21	75.43	0.06
3	1.004	52.79	52.69	0.11	52.86	0.17	52.62	0.18	52.79	0.18	52.72	0.07
4	0.997	25.28	25.21	0.07	25.38	0.17	25.11	0.17	25.28	0.17	25.15	0.13
5	0.994	0.59	0.64	−0.06	0.72	0.08	0.51	0.08	0.59	0.08	0.50	0.08
6	1.004	−26.39	−26.22	−0.17	−26.22	0.00	−26.38	−0.01	−26.39	−0.01	−26.45	0.05
7	1.000	−53.28	−53.00	−0.27	−53.07	−0.07	−53.21	−0.07	−53.28	−0.07	−53.33	0.06
8	0.996	−75.41	−74.96	−0.45	−75.17	−0.21	−75.19	−0.21	−75.40	−0.21	−75.34	−0.07
9	0.995	−100.00	−99.39	−0.61	−99.73	−0.34	−99.65	−0.35	−100.00	−0.34	−99.80	−0.20
$\sigma(\Delta)$				0.28		0.17		0.18		0.18		0.15

Table 2. Enantiomeric excess analysis results of the alanine spectra depicted in Figure 2. See text for detailed descriptions.

i	n_{norm}	e_i^0/%	$\hat{e}_i^D$/%	Δ_i^{0D}/%	e_i^{1D}/%	Δ_i^{1D}/%	$\hat{e}_i^{Da}$/%	Δ_i^{0Da}/%	e_i^{1Da}/%	Δ_i^{1Da}/%	$\hat{e}_i^{PLS}$/%	Δ_i^{0PLS}/%
1	1.000	100.00	100.00	0.00	100.00	0.00	100.00	0.00	100.00	0.00	100.13	−0.13
2	1.021	75.23	74.24	0.99	74.74	0.51	74.73	0.50	75.23	0.50	74.78	0.45
3	1.009	50.08	48.84	1.23	49.09	0.25	49.78	0.30	50.08	0.30	49.89	0.19
4	1.028	24.37	23.13	1.24	22.87	−0.25	24.62	−0.25	24.37	−0.25	24.74	−0.38
5	1.003	0.08	−1.88	1.96	−1.89	−0.01	0.20	−0.12	0.08	−0.12	0.23	−0.15
6	1.035	−23.93	−26.33	2.41	−26.37	−0.04	−23.88	−0.05	−23.93	−0.05	−23.91	−0.02
7	1.020	−50.12	−53.24	3.12	−53.08	0.16	−50.24	0.12	−50.12	0.12	−50.40	0.28
8	1.027	−75.21	−78.26	3.04	−78.67	−0.41	−74.85	−0.37	−75.21	−0.37	−74.93	−0.29
9	1.022	−100.00	−103.74	3.74	−103.95	−0.20	−99.87	−0.13	−100.00	−0.13	−100.09	0.09
$\sigma(\Delta)$				2.28		0.26		0.26		0.26		0.26

The determination of EE by PLS is quite robust to artifacts in ROA spectra. ROA artifact correction had minimal influence on the results obtained from the PLS method, and therefore these results are not shown in the tables. The PLS method gives only slightly better results than the simple artifact reduction method that we described. A major advantage of our method may be that the stated accuracies are achieved for independent pairs of spectra (only two spectra are needed), one of which was chosen as reference *A*.

Coincidentally, the determined EE of reference *B* for both α-pinene and alanine is close to 100% within the error margin. Therefore, correction of the enantiomeric purity of reference *B* according to Equation (9) does not yield a significant improvement. However, if the EEs of the two "pure" forms were different, we believe that this correction may represent a substantial improvement in the results.

The importance of Raman baseline correction and ROA normalization is described by comparing Tables 1 and 2 with Tables 3 and 4, where the Raman baseline correction and ROA normalization were not applied (n_{norm} factor was set to unity). The results show that, unless the baseline correction and the resulting normalization of the ROA spectra is performed, it is not possible to reduce the standard deviation of the errors of EE below 0.26% for α-pinene and approximately 1% for alanine.

Table 3. Enantiomeric excess analysis results of α-pinene. This table has the same structure as Table 1, only the ROA normalization factors n_{norm} are set to unity.

i	n_{norm}	e_i^0/%	$\hat{e}_i^D$/%	Δ_i^{0D}/%	e_i^{1D}/%	Δ_i^{1D}/%	$\hat{e}_i^{Da}$/%	Δ_i^{0Da}/%	e_i^{1Da}/%	Δ_i^{1Da}/%	$\hat{e}_i^{PLS}$/%	Δ_i^{0PLS}/%
1	1.000	100.00	100.00	0.00	100.00	0.00	100.00	0.00	100.00	0.00	100.42	−0.42
2	1.000	75.49	74.93	0.57	75.49	0.56	74.93	0.57	75.49	0.57	75.00	0.49
3	1.000	52.79	52.46	0.34	52.79	0.33	52.46	0.34	52.79	0.34	52.56	0.24
4	1.000	25.28	25.28	−0.01	25.27	−0.02	25.29	−0.02	25.28	−0.02	25.37	−0.10
5	1.000	0.59	0.65	−0.06	0.57	−0.07	0.66	−0.07	0.59	−0.07	0.67	−0.08
6	1.000	−26.39	−26.13	−0.26	−26.41	−0.28	−26.11	−0.28	−26.39	−0.28	−26.15	−0.25
7	1.000	−53.28	−53.00	−0.28	−53.29	−0.30	−52.97	−0.30	−53.28	−0.30	−53.08	−0.20
8	1.000	−75.41	−75.27	−0.14	−75.43	−0.16	−75.25	−0.16	−75.40	−0.16	−75.47	0.06
9	1.000	−100.00	−99.95	−0.05	−100.02	−0.07	−99.92	−0.08	−100.00	−0.08	−100.31	0.31
$\sigma(\Delta)$				0.26		0.26		0.27		0.27		0.28

Table 4. Enantiomeric excess analysis results of alanine solutions. This table has the same structure as Table 2, only the ROA normalization factors n_{norm} are set to unity.

i	n_{norm}	e_i^0/%	$\hat{e}_i^D$/%	Δ_i^{0D}/%	e_i^{1D}/%	Δ_i^{1D}/%	$\hat{e}_i^{Da}$/%	Δ_i^{0Da}/%	e_i^{1Da}/%	Δ_i^{1Da}/%	$\hat{e}_i^{PLS}$/%	Δ_i^{0PLS}/%
1	1.000	100.00	100.00	0.00	100.00	0.00	100.00	0.00	100.00	0.00	102.09	−2.09
2	1.000	75.23	72.68	2.55	74.84	2.16	73.11	2.12	75.23	2.12	73.79	1.44
3	1.000	50.08	48.38	1.70	49.29	0.91	49.13	0.95	50.08	0.95	49.81	0.26
4	1.000	24.37	22.49	1.87	23.18	0.68	23.71	0.65	24.37	0.65	24.03	0.34
5	1.000	0.08	−1.87	1.95	−1.49	0.38	−0.20	0.28	0.08	0.28	−0.23	0.31
6	1.000	−23.93	−25.44	1.51	−25.88	−0.44	−23.47	−0.45	−23.93	−0.46	−23.77	−0.16
7	1.000	−50.12	−52.18	2.06	−52.48	−0.30	−49.79	−0.32	−50.12	−0.32	−50.58	0.47
8	1.000	−75.21	−76.23	1.02	−77.97	−1.74	−73.54	−1.67	−75.21	−1.67	−74.36	−0.85
9	1.000	−100.00	−101.49	1.49	−103.15	−1.66	−98.45	−1.55	−100.00	−1.55	−99.71	−0.29
$\sigma(\Delta)$				1.72		1.16		1.13		1.13		0.93

4.2. Optimization of Parameters for EE Determination

The first of the parameters whose optimal values that we attempted to find were the Savitzky–Golay smoothing parameters. The results of the determination of the standard deviation of the EE determination errors after artifact correction $\sigma(\Delta_i^{1Da})$, together with the coefficient c_{B1} indicating the determined EE of reference *B*, are shown in Table 5. Other parameters were set as in the previous section.

Table 5. Enantiomeric excess analysis results of α-pinene in the spectral range 100–2000 cm^{-1} for different Savitzky–Golay smoothing parameters.

Order	Window Size	$\sigma(\Delta_i^{1Da})$/%	c_{B1}/%	Order	Window Size	$\sigma(\Delta_i^{1Da})$/%	c_{B1}/%
0	1	0.18	100.00	2	9	0.18	100.00
0	3	0.18	100.00	2	11	0.16	100.00
0	5	0.18	100.00	2	13	0.25	100.00
0	7	0.19	100.00	2	15	0.36	100.00
0	11	0.20	100.00	3	5	0.18	100.00
0	15	0.22	100.00	3	9	0.18	100.00
1	3	0.18	100.00	3	11	0.16	100.00
1	5	0.18	100.00	3	13	0.25	100.00
2	5	0.18	100.00	3	15	0.36	100.00

The results show that a slight reduction in the standard deviation was achieved for mild smoothing; however, the overall accuracy of the EE determination was not very dependent on the smoothing parameters as long as the smoothing and subsequent resolution degradation was not overly significant.

Another important set of parameters was the spectral range selection for Raman baseline correction, ROA normalization, artifact correction and EE determination. For the evaluations, we used the standard deviation of the EE determination errors after artifact correction $\sigma(\Delta_i^{1Da})$ again with the coefficient c_{B1}, and the results are shown in Table 6 for α-pinene and in Table 7 for alanine. Individual EE determination errors for options in Tables 6 and 7 are depicted in Figure 3.

Table 6. Table for Figure 3a. Enantiomeric excess analysis results of α-pinene for different spectral ranges in each step of the EE determination.

Option	Baseline Correction		Raman Normalization		Artifact Correction		EE Determination		$\sigma(\Delta_i^{1Da})$/%	c_{B1}/%
1	100	1500	100	1500	50	1700	100	1500	0.19	100.00
2	100	1500	1000	1500	50	1700	100	1500	0.15	100.00
3	100	1500	1300	1500	50	1700	100	1500	0.13	100.00
4	100	2000	100	1500	50	2000	100	1500	0.19	100.00
5	100	1700	1500	1800	50	2000	100	1500	0.08	100.00
6	100	2000	1500	1800	50	2000	100	1500	0.10	100.00
7	100	2000	1500	1800	50	2000	50	300	0.20	100.00
8	100	2000	1500	1800	50	2000	700	940	0.05	100.00
9	100	2000	1500	1800	50	2000	700	1500	0.06	100.00

Table 7. Table for Figure 3b. Enantiomeric excess analysis results of alanine for different spectral ranges in each step of the EE determination.

Option	Baseline Correction		Raman Normalization		Artifact Correction		EE Determination		$\sigma(\Delta_i^{1Da})$/%	c_{B1}/%
1	50	2000	100	1500	50	2000	50	1500	0.47	100.00
2	50	2000	100	1500	50	2000	100	1500	0.24	100.00
3	50	2000	100	1500	50	2000	100	750	1.80	100.00
4	50	2000	100	1500	50	2000	750	1500	0.34	100.00
5	50	2000	100	1500	50	2000	900	1500	0.22	100.00
6	50	2000	100	1500	50	2000	820	890	1.04	100.00
7	50	2000	100	1500	50	2000	750	1050	0.53	100.00
8	50	2000	100	1500	50	2000	1280	1490	0.46	100.00
9	50	2000	100	1500	50	2000	50	105	0.66	100.00

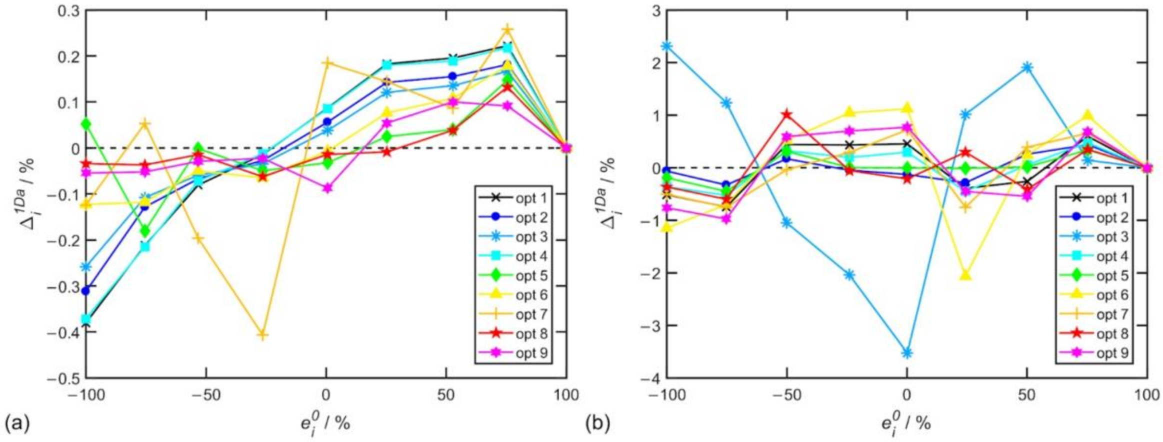

Figure 3. Errors of EE determination Δ_i^{1Da} for (**a**) α-pinene and (**b**) alanine for various options in spectral range selection described in Tables 6 and 7, respectively.

The spectral ranges were chosen considering the presence of dominant artifacts at 667 cm^{-1} for α-pinene and 848 cm^{-1} for alanine, which divide the spectrum into approximately two halves. For α-pinene, it was also important to include a relatively isolated polarized band around 1660 cm^{-1} and a region towards 2000 cm^{-1} where bands corresponding to fundamental vibrations do not occur; however, this region can be important for the correct determination of the background in Raman spectra.

These results confirm that the appropriate choice of spectral range for baseline correction and ROA normalization can lead to a substantial reduction in EE determination errors. Table 6 shows that, if the spectral range used for normalization of α-pinene's spectra is limited to 1500–1800 cm^{-1}, i.e., around the relatively isolated spectral band of 1660 cm^{-1}, the most accurate results can be obtained.

However, two caveats must be added. First, α-pinene is a substance that undergoes air oxidation over longer time scales of weeks and one of the most pronounced changes is in the vicinity of the 1660 cm^{-1} band (see Figure A1). Second, the region 1700 cm^{-1} and above, while free of fundamental vibrations, contains a number of low-intensity but significant bands from combinatorial vibrations (ref. [15]) that make proper baseline correction not an easy task.

Not overly surprisingly, the exclusion of the bands carrying the largest artifacts leads to an increase in the accuracy of the EE determination, for example, limiting the EE determination to the 700–1500 cm^{-1} range for α-pinene. However, it was surprising that even higher accuracy of EE determination for α-pinene was achieved for another drastic reduction of the spectral range for EE determination to only a few bands in the 700–940 cm^{-1} region. Admittedly, these bands achieve a large ROA to Raman ratio and are little burdened by artifacts.

Therefore, the whole reliable spectral region 100–2000 cm^{-1} can be used as the first choice; however, an appropriate choice of spectral ranges can lead to a substantial increase in the accuracy of the EE determination.

4.3. Dependence of EE Determination Accuracy on Measurement Time

In the last section, we attempted to use the measured data to investigate how the accuracy of the EE determination depends on the measurement time of the ROA spectra. In other words, we try to answer the question of how long ROA measurements are needed to be able to achieve a certain accuracy of EE determination.

The ROA spectra are generally shot-noise limited [13]. As the signal-to-noise ratio increases with a square root of the exposition time, it is reasonable to describe the standard deviation of EE determination errors as:

$$\sigma(t) = \sigma_\infty + \frac{\sigma_1}{\sqrt{t}}, \tag{14}$$

where σ_1 is the standard deviation expected for the unit exposition time t and σ_∞ is the limit of the standard deviation for infinite time measurement, which can be interpreted as a residual systematic error.

Raman and ROA spectra were exported periodically during the experiment, for α-pinene every 3.91 min and for alanine every 17.2 min. The time dependence of $\sigma(\Delta_i^{1D})$ was then calculated for every cumulative step for three different combinations of parameters listed in Tables 6 and 7 and results are depicted in Figure 4.

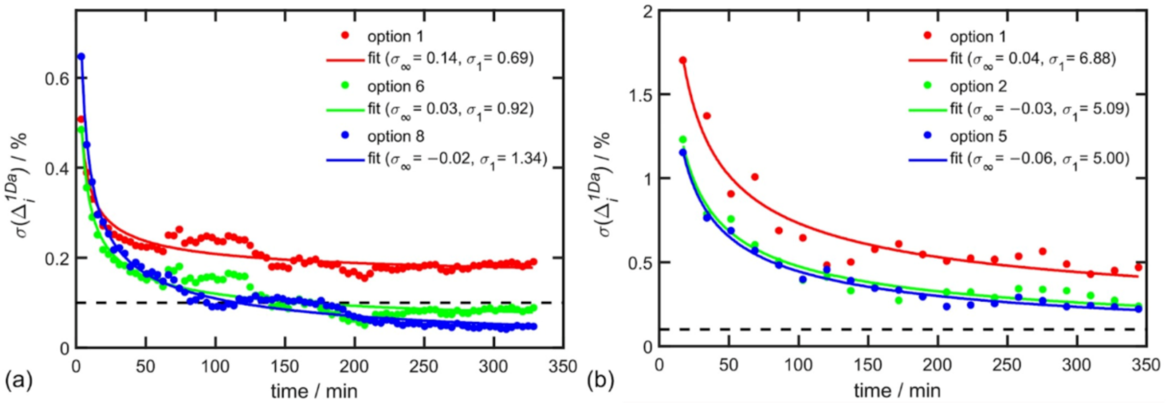

Figure 4. Dependence of $\sigma(\Delta_i^{1Da})$ on the total exposition time of one mixture for α-pinene (**a**), 3.91 min per step) and for alanine (**b**), 17.22 min per step). Selected options point to the parameters listed in Tables 6 and 7, respectively. The data were fitted by the function in Equation (14).

In the case of α-pinene, the EE accuracy of 0.1% was already achieved after 100 min of exposition time and accuracy of 0.05% after 330 min of exposition time for the best choice of parameters (option 8 in Table 6). A similar convergence was confirmed by alanine in aqueous solution but with a lower accuracy ~0.22% after 345 min. The worse accuracy for alanine is caused by the ten-times weaker ROA signal in comparison to α-pinene in the analyzed spectral region.

5. Conclusions

We demonstrated a new methodology of enantiomeric excess (EE) determination by Raman optical activity (ROA). This method is based on an effective algorithm that includes Raman baseline correction, ROA intensity normalization and a systematic error elimination procedure applied to the experimental ROA data. A large improvement in the precision, but not accuracy, was achieved when one of the reference samples was found to be less than 100% pure, and its enantiomeric purity was determined with respect to the zero-sum EE error assumption. When experimental artifacts were subtracted from the ROA experimental spectra, the accuracy of the EE determination was improved. Similarly, accurate predicted enantiomeric excess determination was achieved using the PLS algorithm.

Nine approximately equally distributed mixtures of neat α-pinene were used as the first chiral test. Special care had to be taken during the preparation as the α-pinene oxidation decomposition could affect the measured relative Raman intensities and disrupt the EE determination. An accuracy of 0.18% after 330 min of exposition was achieved when the full spectral region (100–2000 cm^{-1}) was chosen for normalization and EE determination.

For carefully selected spectral regions for the ROA normalization and the EE analysis, a higher accuracy of 0.05% could be achieved.

Another chiral sample often used for benchmark studies in vibrational spectroscopy is alanine in an aqueous solution. It has an approximately order of magnitude weaker ROA signal compared with α-pinene. The accuracy was determined to be 0.26% for nine enantiomeric mixtures of L-Ala and D-Ala after a 345 min accumulation measurement. A slightly better accuracy of 0.22% could be obtained for EE determination within a selected spectral region with stronger bands and a better signal-to-noise ratio.

We conclude that ROA spectroscopy proved to be a valuable non-destructive technique in the quantitative analysis of enantiomeric mixtures with an accuracy around 0.1% with reasonable accumulation times.

Author Contributions: J.K. conceived the presented idea and organized the project. P.M. and J.K. worked on the methodology. P.M., J.K. and J.H. co-wrote the manuscript. J.H. prepared samples. J.H. and P.M. conducted ROA experiments. P.M. wrote software for the spectra processing. J.K., R.Č., M.D. and M.V. collaborated on the ROA spectrometer construction. All authors have read and agreed to the published version of the manuscript.

Funding: This research was funded by the Czech Grant Agency (22-04669S) and by a student grant of the Palacký University Olomouc (IGA_PrF_2022_001).

Institutional Review Board Statement: Not applicable.

Informed Consent Statement: Not applicable.

Data Availability Statement: Raw data are available from the corresponding author on request.

Conflicts of Interest: The authors state that they pursue the commercialization of the ROA spectrometer as employees of Palacký University Olomouc in cooperation with ZEBR and Meopta-optica companies.

Appendix A

Appendix A.1 Note Regarding Oxidation of α-Pinene

It must be noted that α-pinene oxidizes while exposed to the air. The main oxidation products are α-pinene oxide, verbenyl hydroperoxide, verbenol and verbenone [18]. The oxidization is faster for smaller volumes and larger size of the area exposed to the air. Fortunately, Raman spectroscopy is a sensitive technique to monitor such changes as shown in Figure A1. Oxidization affects the relative Raman intensities and prevents the correct enantiomeric excess determination. The sideband 1622 cm^{-1} of α-pinene C=C stretching fundamental vibration 1660 cm^{-1} is a good marker of the oxidation beginning and the presence of oxidation products in the sample. Therefore, special care has to be taken during the preparation and measurement of α-pinene enantiomeric mixtures and to use α-pinene as a primary reference standard in general.

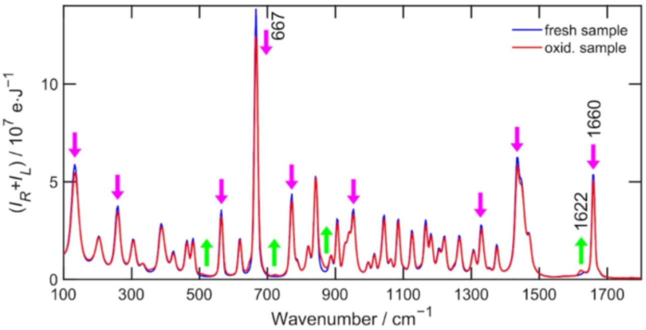

Figure A1. Raman spectrum of α-pinene as a fresh sample measured immediately after the bottle opening (blue) and an old oxidized sample (red). The significant intensity changes are marked by arrows. The most characteristic band is 1622 cm^{-1} sideband of C=C stretching 1660 cm^{-1}.

References

1. Barron, L.D. *Molecular Light Scattering and Optical Activity*, 2nd ed.; Cambridge University Press: Cambridge, UK, 2004.
2. Nafie, L.A. *Vibrational Optical Activity: Principles and Applications*; Wiley: Chichester, UK, 2011.
3. Chankvetadze, B. *Capillary Electrophoresis in Chiral Analysis*; John Wiley: Chichester, UK; New York, NY, USA, 1997.
4. Spencer, K.M.; Cianciosi, S.J.; Baldwin, J.E.; Freedman, T.B.; Nafie, L.A. Determination of Enantiomeric Excess in Deuterated Chiral Hydrocarbons by Vibrational Circular Dichroism Spectroscopy. *Appl. Spectrosc.* **1990**, *44*, 235–238. [CrossRef]
5. Hecht, L.; Phillips, A.L.; Barron, L.D. Determination of enantiomeric excess using Raman optical activity. *J. Raman Spectrosc.* **1995**, *26*, 727–732. [CrossRef]
6. Guo, C.; Shah, R.D.; Dukor, R.K.; Cao, X.; Freedman, T.B.; Nafie, L.A. Determination of Enantiomeric Excess in Samples of Chiral Molecules Using Fourier Transform Vibrational Circular Dichroism Spectroscopy: Simulation of Real-Time Reaction Monitoring. *Anal. Chem.* **2004**, *76*, 6956–6966. [CrossRef] [PubMed]
7. Guo, C.; Shah, R.D.; Dukor, R.K.; Cao, X.; Freedman, T.B.; Nafie, L.A. Enantiomeric Excess Determination by Fourier Transform Near-Infrared Vibrational Circular Dichroism Spectroscopy: Simulation of Real-Time Process Monitoring. *Appl. Spectrosc.* **2005**, *59*, 1114–1124. [CrossRef] [PubMed]
8. Quesada-Moreno, M.M.; Virgili, A.; Monteagudo, E.; Claramunt, R.M.; Avilés-Moreno, J.R.; López-González, J.J.; Alkorta, I.; Elguero, J. A Vibrational Circular Dichroism (VCD) Methodology for the Measurement of Enantiomeric Excess in Chiral Compounds in the Solid Phase and for the Complementary Use of NMR and VCD Techniques in Solution: The Camphor Case. *Analyst* **2018**, *143*, 1406–1416. [CrossRef] [PubMed]
9. Merten, C.; Kowalik, T.; Hartwig, A. Vibrational Circular Dichroism Spectroscopy of Solid Polymer Films: Effects of Sample Orientation. *Appl. Spectrosc.* **2008**, *62*, 901–905. [CrossRef]
10. Kinalwa, M.N.; Blanch, E.W.; Doig, A.J. Accurate Determination of Protein Secondary Structure Content from Raman and Raman Optical Activity Spectra. *Anal. Chem.* **2010**, *82*, 6347–6349. [CrossRef]
11. Rosipal, R.; Krämer, N. Overview and Recent Advances in Partial Least Squares. In Proceedings of the Subspace, Latent Structure and Feature Selection, Berlin/Heidelberg, Germany, 23–25 February 2005; pp. 34–51.
12. de Jong, S. SIMPLS: An Alternative Approach to Partial Least Squares Regression. *Chemom. Intell. Lab. Syst.* **1993**, *18*, 251–263. [CrossRef]
13. Hug, W.; Hangartner, G. A novel high-throughput Raman spectrometer for polarization difference measurements. *J. Raman Spectrosc.* **1999**, *30*, 841–852. [CrossRef]
14. Hug, W. Virtual Enantiomers as the Solution of Optical Activity's Deterministic Offset Problem. *Appl. Spectrosc.* **2003**, *57*, 1–13. [CrossRef] [PubMed]
15. Michal, P.; Čelechovský, R.; Dudka, M.; Kapitán, J.; Vůjtek, M.; Berešová, M.; Šebestík, J.; Thangavel, K.; Bouř, P. Vibrational Optical Activity of Intermolecular, Overtone, and Combination Bands: 2-Chloropropionitrile and α-Pinene. *J. Phys. Chem. B* **2019**, *123*, 2147–2156. [CrossRef] [PubMed]
16. Eilers, P.; Boelens, H. Baseline Correction with Asymmetric Least Squares Smoothing. *Leiden Univ. Med. Cent. Rep.* **2005**, *1*, 5.
17. Wang, T.; Dai, L. Background Subtraction of Raman Spectra Based on Iterative Polynomial Smoothing. *Appl. Spectrosc.* **2016**, *71*, 1169–1179. [CrossRef] [PubMed]
18. Neuenschwander, U.; Guignard, F.; Hermans, I. Mechanism of the Aerobic Oxidation of Alpha-Pinene. *ChemSusChem* **2010**, *3*, 75–84. [CrossRef] [PubMed]

Faculty
of Science

Palacký University
Olomouc

SUMMARY OF DOCTORAL THESIS

Mgr. Pavel Michal

Optimization of a Raman optical activity spectrometer for measurement in an extended spectral range

Olomouc 2024

Výsledky prezentované v disertační práci byly získány v rámci prezenčního doktorského studia studijního oboru Optika a optoelektronika (PRF/1701V029/02), ve studijním programu Fyzika (P1703) na Přírodovědecké fakultě Univerzity Palackého v Olomouci.

Doktorand: **Mgr. Pavel Michal**

Školitel: **RNDr. Josef Kapitán, Ph.D.**
Katedra optiky
Přírodovědecká fakulta
Univerzita Palackého v Olomouci
17. listopadu 12, 77146 Olomouc

Konzultant: **Prof. RNDr. Petr Bouř, DSc.**
Ústav organické chemie a biochemie AV ČR, v.v.i.
Flemingovo náměstí 2, 160 00 Praha 6

Oponent: **Prof. RNDr. Vladimír Baumruk, DrSc**
Fyzikální ústav UK
Matematicko-fyzikální fakulta UK
Ke Karlovu 5, 121 16 Praha 2

Oponent: **Dr. Grzegorz Zajac, Ph.D.**
Jagiellonian University
Jagiellonian Centre for Experimental Therapeutics (JCET)
Bobrzynskiego 14, 30-348 Krakow, Poland

Předseda komise: **prof. RNDr. Zdeněk Hradil, CSc.**
Katedra optiky
Přírodovědecká fakulta
Univerzita Palackého v Olomouci
17. listopadu 12, 77146 Olomouc

Autoreferát byl rozeslán dne ………………………… .

Obhajoba se koná dne ………………………… v ……….. hodin před komisí pro obhajobu disertační práce vědního oboru Fyzika, studijního oboru Optika a optoelektronika, na Katedře optiky Přírodovědecké fakulty Univerzity Palackého v Olomouci, na adrese 17. listopadu 12, 771 46 Olomouc.

S disertační prací je možné se seznámit na studijním oddělení Přírodovědecké fakulty Univerzity Palackého v Olomouci, sídlící na stejné adrese.

Results presented in the doctoral thesis were obtained during full-time doctoral study in study field Optics and optoelectronics (PRF/1701V029/02), study program Physics (P1703), of Faculty of Science, Palacký University in Olomouc.

Ph.D. candidate:	**Mgr. Pavel Michal**
Supervisor:	**RNDr. Josef Kapitán, Ph.D.** Department of Optics Palacký University Olomouc 17. listopadu 12, 77146 Olomouc
Co-Supervisor:	**Prof. RNDr. Petr Bouř, DSc.** Institute of Organic Chemistry and Biochemistry Czech Academy of Sciences Flemingovo náměstí 2, 160 00 Praha 6
Reviewer:	**Prof. RNDr. Vladimír Baumruk, DrSc** Institute of Physics of Charles University Faculty of Mathematics and Physics, Charles University Ke Karlovu 5, 121 16 Praha 2
Reviewer:	**Dr. Grzegorz Zajac, Ph.D.** Jagiellonian University Jagiellonian Centre for Experimental Therapeutics (JCET) Bobrzynskiego 14, 30-348 Krakow, Poland
Chairman of the committee:	**prof. RNDr. Zdeněk Hradil, CSc.** Department of Optics Palacký University Olomouc 17. listopadu 12, 77146 Olomouc

The summary was sent on ……………………….. .

The defense will take a place on ……………………….. at ……….. o’ clock in front of the committee for doctoral study program Optics and optoelectronics at the Department of Optics, Faculty of Science, Palacký University Olomouc, residing at 17. listopadu 12, 771 46 Olomouc, Czech Republic.

The doctoral thesis is available at the study department of Faculty of Science of Palacký University Olomouc, residing at the same address.

Declaration

This thesis is an original work of its author. All sources are cited under References. The thesis is based on scientific work that has been published in collaboration with other co-authors. The contribution of the author is outlined at the end of the thesis. This thesis may be freely distributed in an unchanged form. Palacký University Olomouc has the rights to archive, publish and distribute the thesis according to its internal regulations and Czech law.

In Olomouc 2nd January 2024

Annotation

This thesis focuses on the development of experimental methodology and interpretation of Raman and Raman optical activity (ROA) spectra. Results concerning absolute configuration, structure and dynamic behavior of various chiral substances in the extended spectral range from 50 to 4000 cm^{-1} are presented. Studied samples were measured on a Raman optical activity spectrometer developed at the Department of Optics, Palacký University Olomouc. The author of the thesis participated also in the instrumental development. In order to increase the potential of ROA spectroscopy in chemical practice, we suggested a new methodology for accurate determination of the enantiomeric excess of chiral samples. As another topic, a new approach to the conformational analysis of model biomolecules is discussed. We show that compared to the commonly analyzed range of 200–2400 cm^{-1}, the extended spectral region provides information about to date unexplored vibrational modes. The experimental data could be interpreted using quantum-chemical calculations and molecular dynamics. A crystal-like computational protocol to treat bulk liquid was developed, and a detailed analysis of low-frequency vibrational modes of small and medium-sized chiral molecules is performed. Some combination and overtone ROA bands were observed and successfully assigned for the first time.

Keywords: vibrational optical activity, Raman optical activity, quantum-chemical calculations, conformational analysis, molecular interactions, molecular dynamics, anharmonic corrections, enantiomeric excess

Anotace

Tato disertační práce je zaměřena na rozvoj metodiky měření a interpretace spekter Ramanovy optické aktivity (ROA). V práci jsou uvedeny výsledky studia struktury a dynamického chování různých chirálních látek v rozšířeném spektrální rozsahu od 50 do 4000 cm^{-1}, které jsou měřeny pomocí ROA spektrometru vyvinutého na Katedře optiky Univerzity Palackého v Olomouci. Autor se podílel i na vývoji přístroje. Abychom přispěli k užitečnosti ROA techniky v analytické chemii, vypracovali jsme metodiku přesnějšího určování enantiomerního přebytku u chirálních vzorků. Také je prezentován nový přístup ke konformační analýze studovaných molekul. Ukazujeme, že oproti běžně analyzovanému rozsahu 200–2400 cm^{-1} poskytuje rozšířená spektrální oblast navíc informaci o dosud neprobádaných vibračních pohybech molekul. Nedílnou součástí práce je také interpretace experimentálních dat s použitím kvantově-chemických a molekulárně dynamických metod. Je představen výpočetní protokol použitelný pro chirální kapaliny, založený na periodickém modelu kapaliny. S jeho pomocí je provedena podrobná analýza nízkofrekvenčních vibračních módů modelových chirálních molekul. Vůbec poprvé byl změřen ROA signál mnoha kombinačních a vyšších harmonických vibračních módů, a příslušné pásy byly přiřazeny ke konkrétním molekulovým vibracím.

Klíčová slova: vibrační optická aktivita, Ramanova optická aktivita, kvantově-chemické výpočty, konformační analýza, molekulární interakce, molekulární dynamika, anharmonické korekce, enantiomerní čistota/přebytek

Contents

1. Introduction

In recent years, ROA has become a quickly developing technique of vibrational spectroscopy. ROA has been established as a powerful and noninvasive tool to analyze molecular structures and interactions of chiral molecules in solution. One of the major advantages of ROA is the ease of measuring samples in aqueous solution. Second, a larger number of observable spectral bands compared to the complementary vibrational circular dichroism (VCD) spectroscopy provides a better basis for the analysis of observed spectra. A wide range of inorganic and organic molecules, including helicenes, peptides, proteins, fibrils, sugars, nucleic acids, or even viruses, have already been studied by this technique.

ROA provides extremely useful information about chiral molecules, however, the ROA signal is usually 4 to 5 orders of magnitude weaker than the already weak Raman scattering, so the spectra are sensitive to experimental artifacts. The signal can be affected by intensity fluctuations caused by the laser instability or by thermal fluctuations in the sample. Further, the baseline in the parent Raman spectrum can be plagued by the fluorescent background from impurities (e.g., dust) in the sample, which may change during the accumulation of the spectra. Last but not least, an experimental obstacle is also the need of relatively large sample volumes (~10 μL) and concentrations of at least 1 $\mathrm{mg{\cdot}mL^{-1}}$. In summary, ROA measurement is demanding and at least basic knowledge in optics is needed for conducting and understanding the experiment. So far, neither ROA nor VCD has been considered as a conventional tool for large-output structural and dynamical studies of chiral molecules or in such analyses of the optical purity – the relative amount of the opposite enantiomers contained in the sample. The goal of this work was to advance instrumentation and applications so that the advantage of ROA can be achieved.

The interpretation of experimental ROA spectra often relies on the comparison of the measured and calculated spectra looking for agreement of signs, relative intensities, and spectral shapes of the observed bands. Therefore, the development of simulation models is of particular importance. The simulations used in the thesis are based on a combined molecular dynamics and density functional theory approach. Simulations of large molecular complexes or solvent-solute systems are often computationally demanding, and a feasible computational protocol is required to overcome the computational limits.

The aim of our effort was to contribute to the development of experimental methodology and interpretation of Raman and ROA spectra of various chiral substances. The work is focused on unexplored spectral features within 50–4500 cm^{-1}, measured by a double-grating ROA spectrometer developed at the Department of Optics, Faculty of Science, Palacký University Olomouc. The thesis is based on four publications, published in high impact journals.

The summary of the thesis has the following structure:

> Chapter 2 provides a concise overview of the new methodology we introduced in the publications presented. In Subsection 2.1.1, a new periodic crystal-like computational protocol for improved treatment of chiral samples in a liquid phase is proposed. In Section 2.2 the setup of a new double-grating ROA spectrometer is described. Addressing the common issue of unstable baseline in measured Raman spectra, Section 2.3 briefly introduces two baseline correction techniques. Section 2.4 focuses on comparing experimental and predicted spectra. In Section 2.5 a novel methodology to accurate enantiomeric excess determination using ROA is described.
>
> The results discussed in Chapter 3 are grouped into three main topics. The conformational analysis of flexible molecules is explored in Subsection 3.1.1.The original approach to the conformational analysis based on the similarity of the observed and calculated spectra is introduced and demonstrated in Subsection 3.1.2 . Section 3.2 shows the results achieved in the extended spectral range. In Subsection 3.2.1, the origin of the low-frequency ROA signal is discussed based on the interpretation of ROA spectra by the new periodic crystal-like model. Strong optical activity of several overtone and combination bands described in Subsection 3.2.2 is measured for the first time and successfully assigned based on the perturbation and variational approaches. Finally, Section 3.3 demonstrates a novel approach to accurate determination of the enantiomeric excess based on ROA measurement.

2. Methods

2.1. Solvent modeling

Measured ROA signal reflects not only the molecular structure but may be also extraordinarily sensitive to the environmental effects and dynamics. Insufficient inclusion of intermolecular interactions into the *ab initio* calculations may lead to large errors in the interpretation of the experimental spectra, especially for strong intermolecular interactions, such as hydrogen bonding. Furthermore, it is difficult to distinguish between internal solute, solvent-solvent and solute-solvent spectral bands in the low-frequency region. Hence, the solvent models play an important role in correct Raman and ROA spectra interpretation. Incorporating solvent corrections can improve vibrational frequencies, provide the spectral band broadening, and more realistic intensities. The solvent can be included as a continuum (e.g. PCM, COSMO, …) or by explicitly incorporated solvent molecules into the calculations in a form of molecular clusters based on the molecular dynamics (MD).

The clusters need to be in contact with the environment to better represent the liquid. As a part of the cluster-based approaches we introduced a new crystal-like computational protocol, where the MD cluster is adapted to better correspond to the liquid phase introducing a crystal-like periodicity.

2.1.1. Crystal-like computational protocol

Based on the MD cluster of 10 molecules in the periodic elementary cell (cubic box, **Figure 1a**), smaller clusters were made by default containing two close molecules, presumably comprising the strongest intermolecular interaction within the periodic box and 26 neighboring boxes (**Figure 1b**).The geometries of the pairs were partially optimized in the normal mode coordinates (Bouř, 2005, 2006; Bouř & Keiderling, 2002). The modes within i100 – 225 cm^{-1} were fixed. The force field and polarizability derivatives obtained for the pairs (**Figure 1c**) were transferred back to the 3×3×3 supercube using the Cartesian coordinate transfer (CCT), see **Figure 1d** (Bouř et al., 1997; Yamamoto & Bouř, 2018). Because of the periodicity, vibrational Hamiltonian can be described as a sum over the wave vectors **q** and atoms *i* within one cell only,

$$\hat{H} = \sum_{\mathbf{q}} \frac{1}{2}\left(\sum_i m_i \dot{x}_i^* \dot{x}_i + \sum_i \sum_j x_i^* D_{ij} x_j\right), \tag{2.1}$$

where m_i are atomic masses and x_i are atomic coordinates. The dynamic matrix for $\mathbf{q} = 0$ is

$$D_{ij} = \sum_J f_{ij}, \tag{2.2}$$

where index J run over the elementary cells containing the j-coordinate and f_{ij} is the force field matrix. Since the Raman and ROA intensity tensors of symmetrical elementary cells ($\mathbf{q} \neq 0$) cancel out by the interference, only the basic elementary cell in the center ($\mathbf{q} = 0$) produces non-zero Raman and ROA signal (**Figure 1e**).

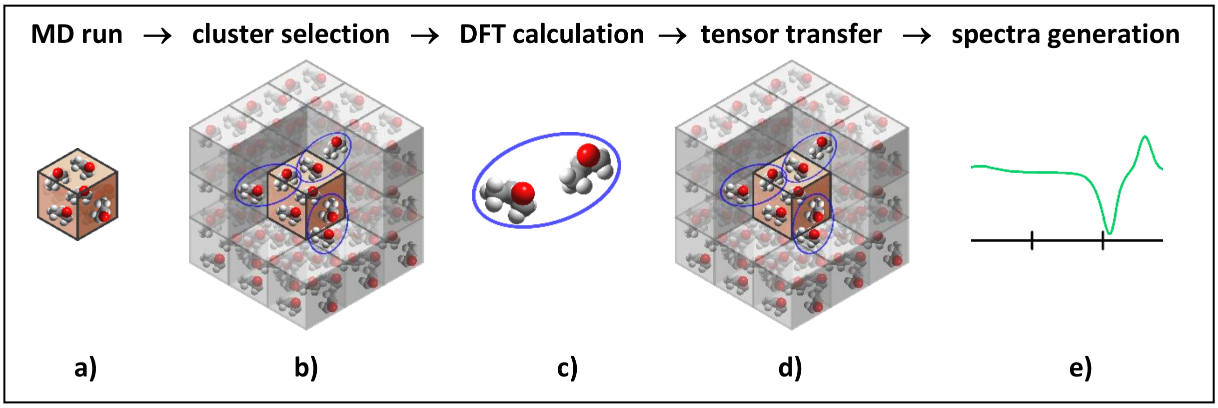

Figure 1: Simulations of the spectra by the default crystal-like model. Intermolecular interactions within the periodic elementary cell (brown/middle cube) and towards its environment were simulated for molecular pairs, in an arbitrary 27 cubes of the “supercube”. The pair parameters (force field, intensity tensors) were transferred back to the supercube, and the spectra were simulated using periodic boundary conditions.

2.2. Experimental setup of double-grating ROA spectrometer

In 2016 J. Kapitán developed a new back-scattering ROA instrument with the excitation wavelength 532 nm based on the W. Hug’s optical design, but with several novel features, such as additional use of the zero order of the diffraction grating to extend the measurement to the high-frequency spectral region. He also implemented a novel measurement algorithm of all ROA modulation forms simultaneously into the spectrometer (Li & Nafie, 2012). The instrument was built at Palacký University Olomouc and is commercially available since 2022 in collaboration with company ZEBR and Meopta. The experimental setup in the most recent configuration is depicted in **Figure 2**.

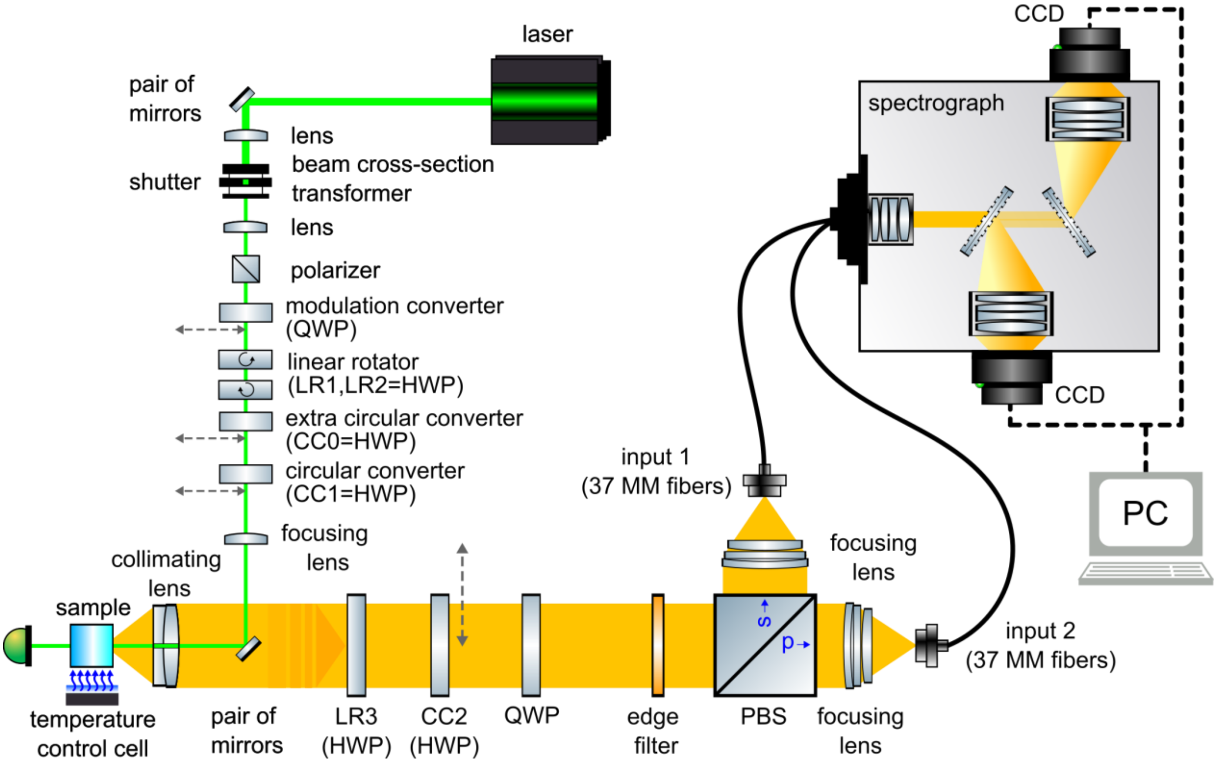

Figure 2: Optical layout of the back-scattering ROA spectrometer at Palacký University Olomouc.

2.3. Raman baseline correction

Measured Raman spectra often exhibit an unstable baseline. The acquired spectrum contains both the intended signal and unwanted elements, including background noise stemming from various sources such as the sample holder, instrumentation, and the samples themselves (e.g. impurities, chromophores, …). The baseline may cause detection issues if the CCD reaches its detection limits or prevent further data processing of useful signal. Several methods have been suggested with regards to the baseline correction. In this work we used two different semi-manual methods implemented in MATLAB.

Asymmetric least squares smoothing (ALSS) (Eilers & Boelens, 2005) is based on Whittaker smoother (Eilers, 2003), where ordinary least squares are penalized. Positive deviations with respect to the baseline are weighted less than negative deviations. The baseline correction can be controlled by two parameters, making ALSS completely reproducible.

The iterative polynomial smoothing algorithm (IPSA) (Wang & Dai, 2017) combines the advantages of polynomial filter and iteration method. Hence, IPSA effectively addresses certain limitations of conventional polynomial fitting algorithms, particularly their dependence on spectral range selection and the fixed polynomial order throughout the process, that can make the algorithm less robust when dealing with changes in the background in continuous measurements. Compared to ALSS method the IPSA led to similar results but with a longer computing time.

2.4. Quantitative comparison of experimental and calculated spectra

The efficiency of the molecular structural analysis from chiroptical spectra lies in the comparison of experimental and predicted spectra. If the spectral pattern of the specific predicted conformation meets the observed spectral pattern in the same wavenumber range, then the conformation can be assigned to the measured sample. In recent years, several diverse metrics of similarity have been introduced to address comparison of experimental and calculated spectra (Polavarapu, 2016).

2.4.1. Similarity factors

The similarity of the experimental and simulated experimental spectra can be quantitively compared using similarity overlap integral (Kuppens et al., 2003)

$$S_1 = \frac{\int f(\tilde{v})g(\tilde{v})d\tilde{v}}{\sqrt{\int f(\tilde{v})^2\, d\tilde{v} \int g(\tilde{v})^2\, d\tilde{v}}} = \int \hat{f}(\tilde{v})\hat{g}(\tilde{v})d\tilde{v}, \tag{2.3}$$

where $f(\tilde{v})$ and $g(\tilde{v})$ represents calculated and experimental spectrum, respectively, and the denominator implies normalization

$$\hat{f}(\tilde{v}) = \frac{f(\tilde{v})}{\sqrt{\int f(\tilde{v})^2\, d\tilde{v}}}, \tag{2.4}$$

$$\hat{g}(\tilde{v}) = \frac{g(\tilde{v})}{\sqrt{\int g(\tilde{v})^2\, d\tilde{v}}}. \tag{2.5}$$

In case of compared spectra possess zero intensity in analyzed region the denominator in (2.3) would be also zero, which causes numerical problems. Therefore, an alternative definition of similarity can be used as follows (Shen et al., 2010):

$$S_2 = \frac{I_{fg}}{I_{ff} + I_{gg} - |I_{fg}|}, \tag{2.6}$$

where the overlap integrals are given as:

$$I_{ff} = \int f(\tilde{v})f(\tilde{v})d\tilde{v}, \tag{2.7}$$

$$I_{gg} = \int g(\tilde{v})g(\tilde{v})d\tilde{v}, \tag{2.8}$$

$$I_{fg} = \int f(\tilde{v})g(\tilde{v})d\tilde{v}, \tag{2.9}$$

and $f(\tilde{v})$ and $g(\tilde{v})$ are not normalized. For $\hat{f}(\tilde{v})$ and $\hat{g}(\tilde{v})$, the overlap integrals are

$$I_{\hat{f}\hat{f}} = \int \hat{f}(\tilde{v})\hat{f}(\tilde{v})d\tilde{v} = 1, \tag{2.10}$$

$$I_{\hat{g}\hat{g}} = \int \hat{g}(\tilde{v})\hat{g}(\tilde{v})d\tilde{v} = 1, \tag{2.11}$$

$$I_{\hat{f}\hat{g}} = S_1, \tag{2.12}$$

and the similarity factor (2.6) is reduced to

$$S_2 = \frac{S_1}{2 - |S_1|}, \tag{2.13}$$

In the comparison of experimental and predicted Raman or ROA spectra, their magnitudes may not be on the same scale. Therefore, spectral normalization or multiplication by a constant is necessary. The similarity values in (2.3) and (2.13) vary in a range from 0 to 1 for the Raman spectra and within −1 and 1 for chiroptical spectra (ROA and CID – ratio of the ROA and Raman spectra). Calculated frequencies can be corrected introducing frequency (wavenumber) scaling factor or function in order to match corresponding experimental frequencies. By frequency scaling of the predicted spectra and calculating the similarity factor, the maximum similarity can be determined. Alternative criteria of the similarity factor exist and can be used as long as it is consistent in all spectral comparisons.

2.4.2. Methods of conformational analysis based on the spectral comparison

As was recently confirmed, the conformational analysis based on calculated energies suffers from large uncertainties (Bootsma & Wheeler, 2019; Koenis et al., 2019). The relative conformational contribution may vary more than 2 kcal·mol^{-1} based on the molecular structure, the chosen DFT approximation and the size of used integration grid. As an alternative, methods that fit a set of calculated spectra in order to minimize the difference with the experimental spectra were suggested.

The original approach to determine the conformer populations is based on maximizing the similarity overlap of the weighted conformer spectra with the experiment by employing a global minimization algorithm to optimize the conformer populations and wavenumber scaling factor. The experimental and simulated vibrational spectra were compared using introduced similarity factor (2.13). The real chiral sample is considered to be a mixture of all possible conformers with a different abundance. This can be specified by the normalized linear combination of all stable conformers in the predicted spectrum

$$f(\tilde{v}) = \sum_{i}^{N} c_i f_i(\tilde{v}), \tag{2.14}$$

where each linear combination coefficient c_i represents the relative abundance of conformer i and N is the number of conformers. For a molecule with N conformations, $N-1$ conformer populations c_i in relation (2.14) and the scaling factor for predicted wavenumbers is allowed to change towards maximizing similarity overlap. The remaining conformer population is calculated as

$$c_N = 1 - \sum_{i}^{N-1} c_i. \tag{2.15}$$

The MATLAB implementation of the algorithm for estimating conformational populations is exemplified in the following fragment, demonstrating reduced calculation for three conformers for clarity purposes.

```
% Spectral interval
IX = 300:1750;

% Linear combination of predicted spectra
f = @(P) (P(1).*interp1(P(3)*data1(:,1),data1(:,2),IX,'linear') +
P(2).*interp1(P(3).*data2(:,1),data2(:,2),IX,'linear')+ (1-P(1)-
P(2)).*interp1(P(3).*data3(:,1),data3(:,2),IX,'linear'));

% Experiment
g = interp1(dataexp(:,1),dataexp(:,2),IX,'linear');

% Overlap integrals
I_fg = @(P) trapz(f(P).*g)./sqrt(trapz(f(P).*f(P)).*trapz(g.*g));
I_ff = @(P) trapz(f(P).*f(P))./sqrt(trapz(f(P).*f(P)).*trapz(f(P).*f(P)));
I_gg = trapz(g.*g)./sqrt(trapz(g.*g).*trapz(g.*g));

S2 = @(P) -I_fg(P)./(2 - abs(I_fg(P))).*((1-P(1)-P(2))>=0 && P(1)>0 &&
P(2)>0) + 1.*((1-P(1)-P(2))<0);

% Starting points
P0 = [0.3;0.3;0.98]; % for P1, P2 and wavenumber factor

% Minimization
opts = optimset('MaxIter',1e8,'TolX',1e-8,'TolFun',1e-8,'MaxFunEvals',1e5);
P = fminsearch(S2,P0,opts);
P3 = 1-P(1)-P(2);    % P3

% Output
out = [P(3) P(1) P(2) P3 -S2([P(1) P(2) P(3)])]; % = [SCF P1 P2 P3 SIM];
```

As the complexity of conformational space increases with the flexibility of the studied molecular system, careful selection of the starting points in the optimization procedure is needed due to the tendency to slide down to the nearest local minimum. Therefore, a more general two-step global optimization procedure can be applied. In the first step M sets of $N-1$ randomly distributed coefficients are generated as the starting points (Monte-Carlo method), each satisfying condition

$$0 \leq \sum_{i}^{N-1} c_i \leq 1, \tag{2.16}$$

and the wavenumber scaling factor is left fixed in order to map the $N-1$ conformational space and localize a global maximum of equation (2.13). In the second stage, the process of local optimization is repeated, using the previously optimized $N-1$ set of coefficients as the new starting points and the wavenumber scaling factor is allowed to be modified in order to achieve the best possible similarity within the global maxima region.

2.5. Procedure for determining the enantiomeric excess

One of the main applications of ROA is the measurement of optical purity of chiral samples. In this work, we have demonstrated a new methodology of enantiomeric excess determination by ROA. It is based on an effective algorithm that includes Raman baseline correction, ROA intensity normalization, and systematic errors elimination procedure applied to experimental ROA data.

2.5.1. Sample measurement and ROA spectra normalization

At first, Raman and ROA spectra for *N* EE samples, containing *M* spectral points, are measured and usually normalized to the used excitation energy. The dataset is a matrix of size *N*×*M*. Secondly, the background in all Raman spectra must be subtracted in order to obtain the spectra $S_{i\nu}^{bas}$. Because of the intensity fluctuations caused by the laser instability or thermal fluctuations in the sample, the ROA spectra $D_{i\nu}^{raw}$ were then normalized according to the parent baseline corrected Raman spectra as

$$D_{i\nu} = D_{i\nu}^{raw} \frac{\sum_\nu S_{A\nu}^{bas}}{S_{i\nu}^{bas}} = D_{i\nu}^{raw} n_{norm}, \tag{2.17}$$

where the sum is performed over the selected spectral region, and index *A* denotes the Raman spectrum of the reference. For diluted stock samples, a variation in the molar concentration of analyzed mixtures must be taken into account.

2.5.2. Enantiomeric excess determination

The most straightforward approach to calculate the enantiomeric excess involves solving a system of overdetermined linear equations.

$$D_{i\nu} = \hat{e}_i^D D_{A\nu}, \tag{2.18}$$

by the least squares method, where $D_{i\nu}$ is one element of the matrix *N*×*M*, $\hat{e}_i$ is one element of the column vector *N*×1 representing unknown enantiomeric excess and $D_{A\nu}$ is one element of the row vector 1×*M* of ROA spectra of the reference *A*. The fundamental assumption of this approach is that the enantiomeric excess of reference *A* is set to the unity (100%). Subsequently, all spectra for which the enantiomeric excess is to be determined are compared to this reference *A*. Since, the minimum of used spectra is $N = 2$, the equation (2.18) represents overdetermined set of linear equations and can be solved by the least square method as follows:

$$\min_{\hat{e}_i} \sum_{\nu=1}^{M} (D_{i\nu} - \hat{e}_i D_{A\nu})^2. \tag{2.19}$$

2.5.3. Performance of enantiomeric excess determination

The correctness of the EE determination can be defined as the standard deviation of the errors

$$\sigma(\Delta) = \sqrt{\frac{\sum_{i=1}^{N} \Delta_i^2}{N}}, \tag{2.20}$$

where

$$\Delta_i = e_i - \hat{e}_i \tag{2.21}$$

is a difference of the EE determined from spectra $\hat{e}_i$ and from the sample preparation e_i.

2.5.4. Correction of residual artifacts in ROA spectra

Despite the fact that polarization artifacts can be significantly reduced by W. Hug's proposed concept of virtual enantiomers (Hug, 2003) generated during the measurement, residual artifacts that occur in ROA spectra are still proportional to the degree of circularity. Thus, all ROA spectra of the enantiomeric mixtures of same compounds will be affected by the same amount of artifacts. The accuracy of the EE determination can be further improved reducing the artifacts in the post-processing procedure.

The simplest method for determining artifacts is to sum the ROA spectra of the two optically pure opposite enantiomers:

$$a_\nu^{AB} = \frac{D_{A\nu} + D_{B\nu}}{2}. \tag{2.22}$$

On the contrary, by subtraction one can receive the artifact-free ROA spectrum:

$$D_\nu^{trueAB} = \frac{D_{A\nu} - D_{B\nu}}{2}. \tag{2.23}$$

If both pure enantiomeric forms are not available, an alternative and more universal approach is proposed, based on solving an overdetermined set of linear equations for $N > 2$:

$$D_{i\nu} = D_\nu^{trueN} e_i + a_\nu^N, \tag{2.24}$$

for different enantiomeric measurements i by the least squares method, where e_i is the known enantiomeric excess from the sample preparation and variables are the ROA artifact-free spectrum D_ν^{trueN} and artifact spectrum a_ν^N. The artifact spectrum determined by (2.24) possess better signal-to-noise ratio then using only the sum of opposite enantiomers.

3. Results

3.1. Conformational analysis

3.1.1. Conformational analysis based on the potential energy scan

The molecular flexibility of (*R*)-2-chloropropionitrile (nitrile) and three ethylbenzene derivatives ((*R*)-(+)-1-phenylethanol, (*R*)-(+)-α-methylbenzylamine, (*S*)-(+)-α-(trifluoromethyl)benzyl alcohol) was analyzed using potential energy surface scans. Nitrile was selected as a small yet relatively inflexible molecule ideal for representing a model liquid. The methyl group (CH_3) rotates freely within a limited range of 35° ($\Delta E < 2$ kcal·mol^{-1}). The nitrile's C−C≡N group is particularly well-suited for studying two-dimensional conformational changes. The energy dependence of the selected nitrile angles (Φ, ω) is displayed in **Figure 3** and overlayed by the distribution of 200 geometries of the MD clusters partially optimized in normal modes with fixed frequencies of i100–225 cm^{-1} ($i = \sqrt{-1}$ for imaginary frequencies). Various values of the normal mode frequency limit were tested. Reducing the upper frequency limit further would cause collapse of the MD geometries toward the equilibrium geometry in the center ($\Delta E = 0$ kcal·mol^{-1}). Surprisingly flexible C−C≡N bending angle (ω) was observed based on DFT calculation, requiring to overcome energy barrier of 2 kcal·mol^{-1} for deviation of 16° from the equilibrium angle ω ∼ 179°.

Spectral parameters, such as the relative ROA intensity or the frequency of normal modes, are to a large extent dependent on the selected angular coordinates, as can be seen for example, for the nitrile C−C−C≡N bending mode 561 cm^{-1}, C≡N stretching mode 2356 cm^{-1} or the intensity ratio of the 672 and 1003 cm^{-1} in **Figure 4**. Modes 561 cm^{-1} and 2356 cm^{-1} shifts in frequencies within ~ 10 cm^{-1}, while modes 672 and 1003 cm^{-1} are less frequency dependent. The corresponding C≡N stretching mode possesses positive sign for Φ ~ 90°, while it is negative for other selected conformers in **Figure 4d**. The frequency shift of the C≡N stretching mode is consistent with its harmonic nature (cf. **Figure 3** and **Figure 4b**).

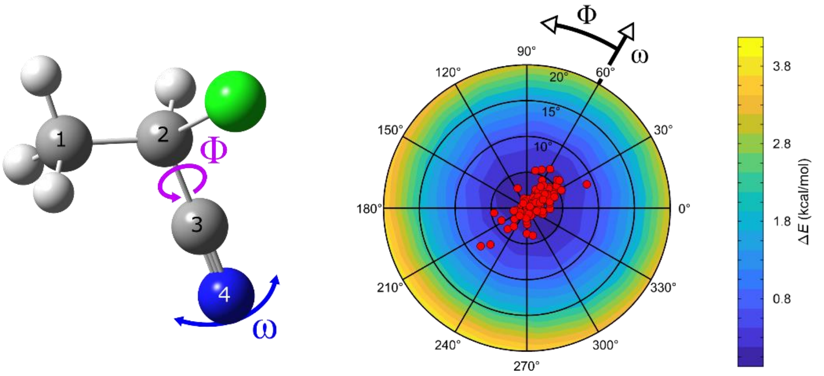

Figure 3: Dependence of nitrile electronic energy on selected angles Φ and 180° − ω calculated at the B3PW91/6-311++G**/COSMO(ACN) level (contour map) and coordinates of 200 MD clusters (red dots). Nitrile angular coordinates are defined as Φ = C1-C2-C3-N4 and ω = C2-C3-N4. The energy scan was controlled by 49 combinations of Φ and 155° < ω < 180°, selected, so that the resultant nitrogen positions were evenly distributed on a sphere around C3 atom.

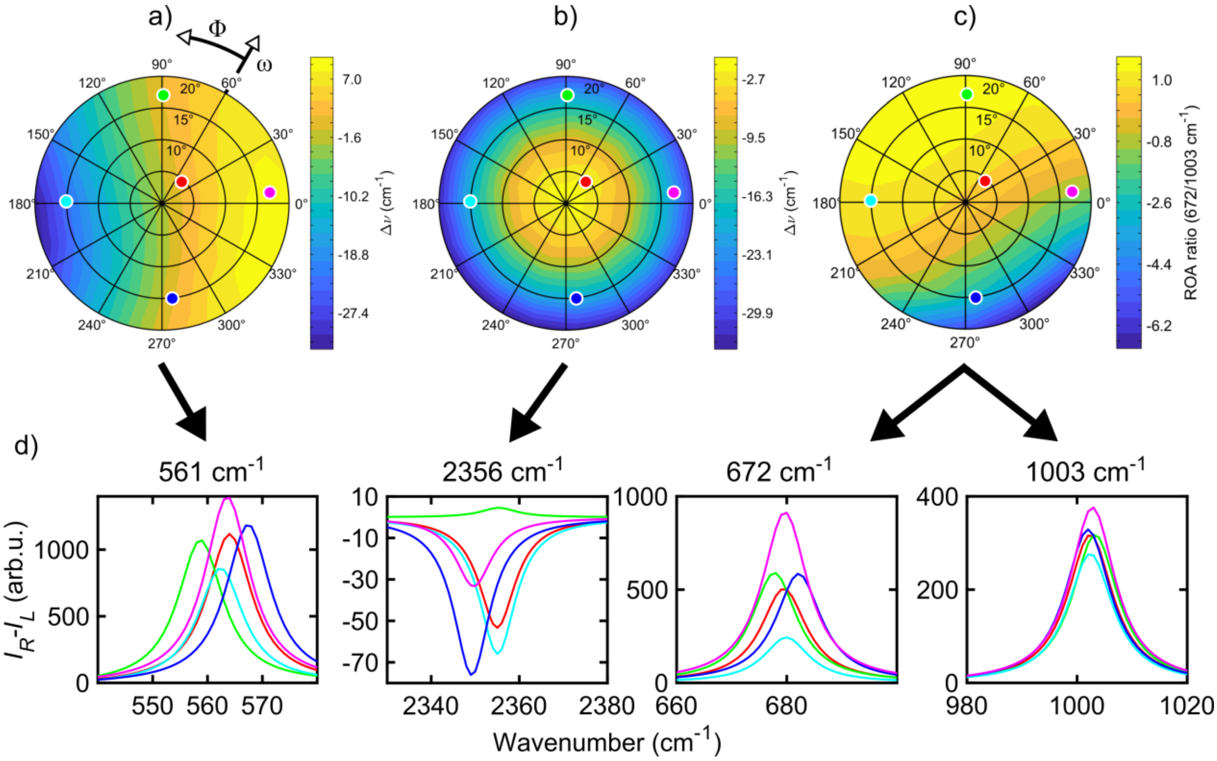

Figure 4: Frequency shift of selected nitrile normal modes 561 cm^{-1} **(a)** and 2356 cm^{-1} **(b)**, from values for the equilibrium geometry, and **(c)** ROA intensity ratio of the 672 and 1003 cm^{-1}, plotted as a function of the Φ and 180° − ω angles. Five ROA spectra of analyzed bands **(d)** for selected conformers **(a**, color points**)** are depicted.

The conformational analysis of (*R*)-(+)-1-phenylethanol, (*R*)-(+)-α-methylbenzylamine and (*S*)-(+)-α-(trifluoromethyl)benzyl alcohol is described by the rotation of the three functional groups (methyl, phenyl an hydroxyl/amine). The methyl group employs similar energetical barrier as for nitrile (~ 4 kcal·mol^{-1}). Rotation of the methyl group isolated from rotation of other groups has minor effect to resulting simulated spectra. Therefore, the conformational analysis of the ethylbenzene derivatives could be limited to the 2D PES scan only (Kapitán et al., 2009). The 2D PES scan as a function of the phenyl (φ), hydroxyl (ψ) and amine (χ) groups is shown in **Figure 5** and Boltzmann-averaged Raman and ROA spectra are plotted in **Figure 6**. The orientation of the polar OH or NH groups out of the phenyl plane ($\varphi \sim 100°$) is preferred by each of the three molecules. The freely rotating NH and OH groups give arise to three local minima ($\psi = -60°$, 60° and 180°) with small energy barrier up to ~ 2 kcal·mol^{-1} (3 kcal·mol^{-1} for methylbenzylamine). Revised PES calculations at the B3PW91/6-311++G**/COSMO(benzylalcohol) are consistent with the previous study of phenylethanol and methylbenzylamine at the B3LYP/6-311++G**/vacuum level (Kapitán et al., 2009). 2D PES scans are overlayed by the conformer distribution from the MD models. The MD distributions differ from the PES scan because of hydrogen bonding to the explicit solvent molecules in the cluster-based model. The effect of the different computational models on the conformational preference is discussed further in Subsection 3.1.2.

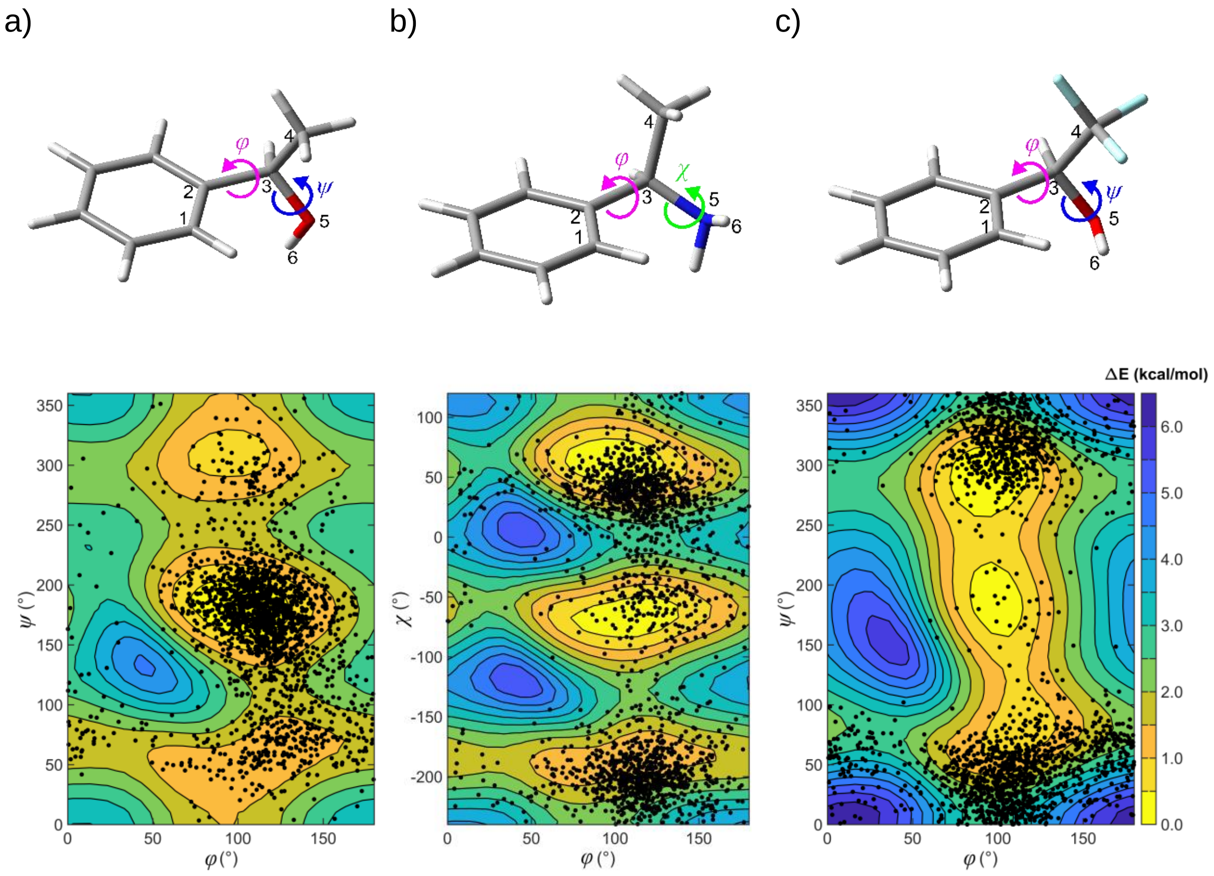

Figure 5: Dependencies of the (*R*)-(+)-1-phenylethanol, (*R*)-(+)-*α*-methylbenzylamine, (*S*)-(+)-*α*-(trifluoromethyl)benzyl alcohol electronic energy on selected torsion angles calculated at the B3PW91/6-311++G**/COSMO(benzylalcohol) level (contour map) and coordinates from 200 MD snapshots (2000 black dots in total). The describe phenyl rotation, φ = C1-C2-C3-C4, hydroxyl rotation, ψ = C4-C3-O5-H6, and amine rotation, χ = C2-C3-N5-H6.

The Boltzmann averaging for conformers below 2 kcal·mol^{-1} clearly reflects the flexibility of studied molecules and improves single molecule Raman and ROA spectra (**Figure 6**). Conformer averaging is especially important for interpretation of low-frequency modes (< 400 cm^{-1}) but the experimental spectra are reproduced only partially as the intermolecular interactions are not included in the 2D PES scan.

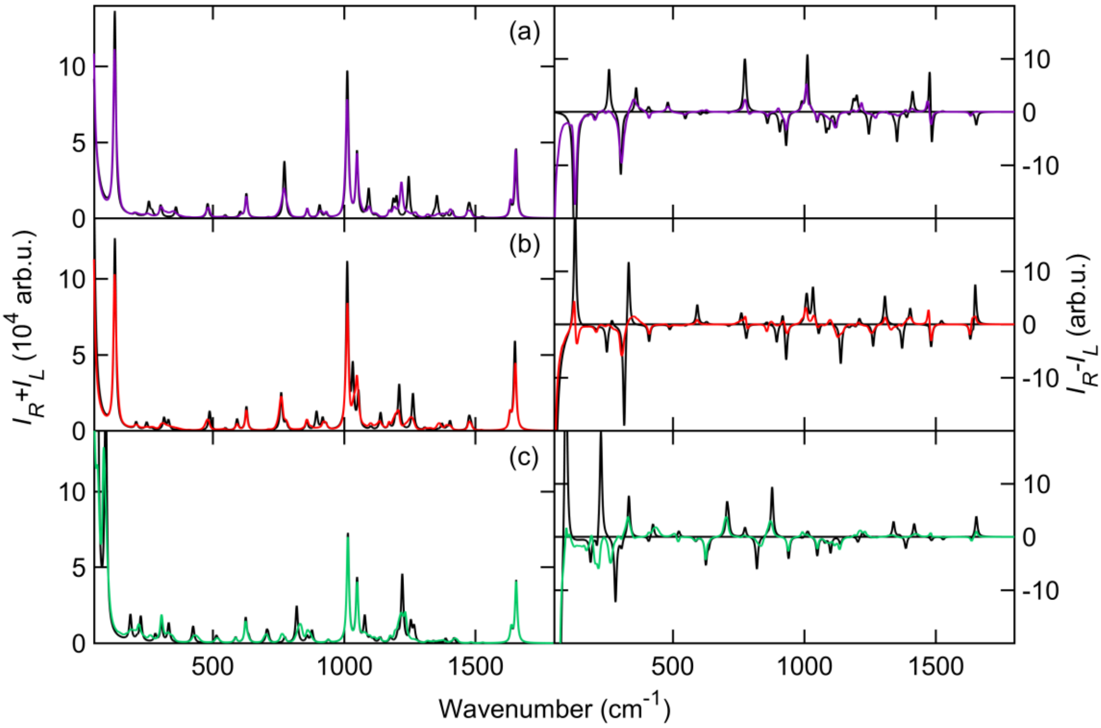

Figure 6: Boltzmann-averaged Raman (left) and ROA (right) spectra of (*R*)-(+)-1-phenylethanol (a), (*R*)-(+)-*α*-methylbenzylamine (b) and (*S*)-(+)-*α*-(trifluoromethyl)benzyl alcohol (c) for conformers below 2 kcal·mol^{-1} according to 2D PES scan. Black spectra represent single molecule DFT (B3PW91/6-311++G**/COSMO) calculation.

3.1.2. Conformational analysis based on the spectral similarity

One of the main applications of ROA is the structural analysis of chiral molecules in a solution. Therefore, a reliable methodology is required for the quantitative comparison of experimental and calculated spectra and subsequent determination of conformer populations. The original approach was applied to IR, Raman, VCD, and ROA spectra of amphetamine and methamphetamine hydrochloride in an aqueous solution supplemented by corresponding dimensionless quantities, dissymmetry factor (DF=VCD/IR) and normalized circular intensity difference (CID=ROA/Raman). Conducting the PES-based conformational analysis is not within the scope of this study; however, given the flexibility of amphetamine derivatives, it presents a multidimensional challenge.

The conformational analysis of amphetamine and its derivatives is complex because of the flexibility of the alkyl chain and interactions with surrounding water molecules. Thus, different computational models, namely, conformers derived from the single molecule (SM)

DFT calculations using only the implicit solvent model (COSMO), MD geometries with fixed selected torsion angles and excluded solvent molecules, and partially optimized MD solute-solvent clusters with varying numbers of water molecules, were discussed.

The results of the conformational analysis for amphetamine hydrochloride are summarized in **Table 1** and the corresponding VCD and ROA spectra are depicted in **Figure 7** for all computational models and the experiment. Determined conformational ratios are same for similarity factor defined by equation (2.3) and (2.13). Corresponding similarity values are depicted in **Table 1**. The accuracy of the reliable conformer determination by the similarity overlap mainly depends on the spectral range selection, the number of compared vibrational bands, the band integral intensity, and the number of conformations taking into account. Therefore, it is desirable to compare the experimental and calculated spectra in the widest possible spectral range. The IR and VCD spectra were compared in the spectral range from 1250 to 1700 cm^{-1}, while the Raman, ROA and CID spectra made it possible to compare them in a wider spectral range of 300–1750 cm^{-1}. The VCD spectral region was limited by the D_2O absorption bands. Additionally, due to uncertain and large values caused by dividing VCD signal by IR numbers close to zero, the dimensionless DF spectra were the most limited in the compared spectral range of 1300–1550 cm^{-1}, therefore the conformer populations based on the DF similarity factor cannot be trusted. However, this is not the case for ROA and CID spectra, where recording of the data in a wider spectral range is clearly beneficial (**Figure 8**). Although the Raman and ROA measurements were conducted within the range of 50–4500 cm^{-1}, the spectral region utilized for analysis was limited to 300–1800 cm^{-1}. The CH stretching vibrations are highly anharmonic with a relatively low ROA to Raman ratio, and a different scaling factor is needed. The region below 300 cm^{-1} is usually plagued by intermolecular vibrations (described in Subsection 3.2.1) that can bias the conformer population determination.

Table 1: Optimized conformer populations for (*S*)-amphetamine hydrochloride obtained from the comparison of experimental spectra and different calculation models. The population derived from the NMR study (Neville et al., 1971) is shown for reference.

Type	Spectral Range	Scaling Factor	c_1	c_2	c_3	S_1^*	$S_2^\dagger$
NMR	-	-	0.45	0.50	0.05	-	-
Single molecule geometry B3PW91/6-311++G**/COSMO							
IR	1250–1700	0.98	0.70	0.09	0.20	0.85	0.75
VCD	1250–1700	0.98	0.36	0.60	0.04	0.67	0.50
DF	1300–1550	0.98	0.24	0.55	0.22	0.87	0.77
Raman	300–1750	0.99	0.35	0.41	0.24	0.80	0.68
ROA	300–1750	0.98	0.60	0.13	0.26	0.51	0.34
CID	300–1750	0.98	0.59	0.25	0.16	0.50	0.34
Geometries from MD, water molecules excluded, B3PW91/6-311++G**/COSMO level with rDPS for Raman, ROA and CID							
IR	1250–1700	0.98	0.96	0.00	0.04	0.88	0.79
VCD	1250–1700	0.98	0.52	0.32	0.15	0.70	0.54
DF	1300–1550	0.98	0.25	0.36	0.40	0.85	0.74
Raman	300–1750	0.99	0.25	0.61	0.14	0.80	0.67
ROA	300–1750	0.98	0.58	0.25	0.17	0.49	0.33
CID	300–1750	0.99	0.42	0.33	0.25	0.59	0.42
Geometries from MD with explicit 1st solvation shell, B3PW91/6-31G**/GD3BJ/COSMO level with rDPS for Raman, ROA and CID							
IR	1250–1700	0.97	0.80	0.00	0.20	0.90	0.82
VCD	1250–1700	0.97	0.40	0.47	0.13	0.90	0.82
DF	1300–1550	0.97	0.28	0.54	0.19	0.94	0.88
Raman	300–1750	0.98	0.70	0.09	0.21	0.80	0.66
ROA	300–1750	0.97	0.43	0.41	0.16	0.78	0.64
CID	300–1750	0.97	0.42	0.46	0.12	0.69	0.52

* According to equation (2.3).

† According to equation (2.13).

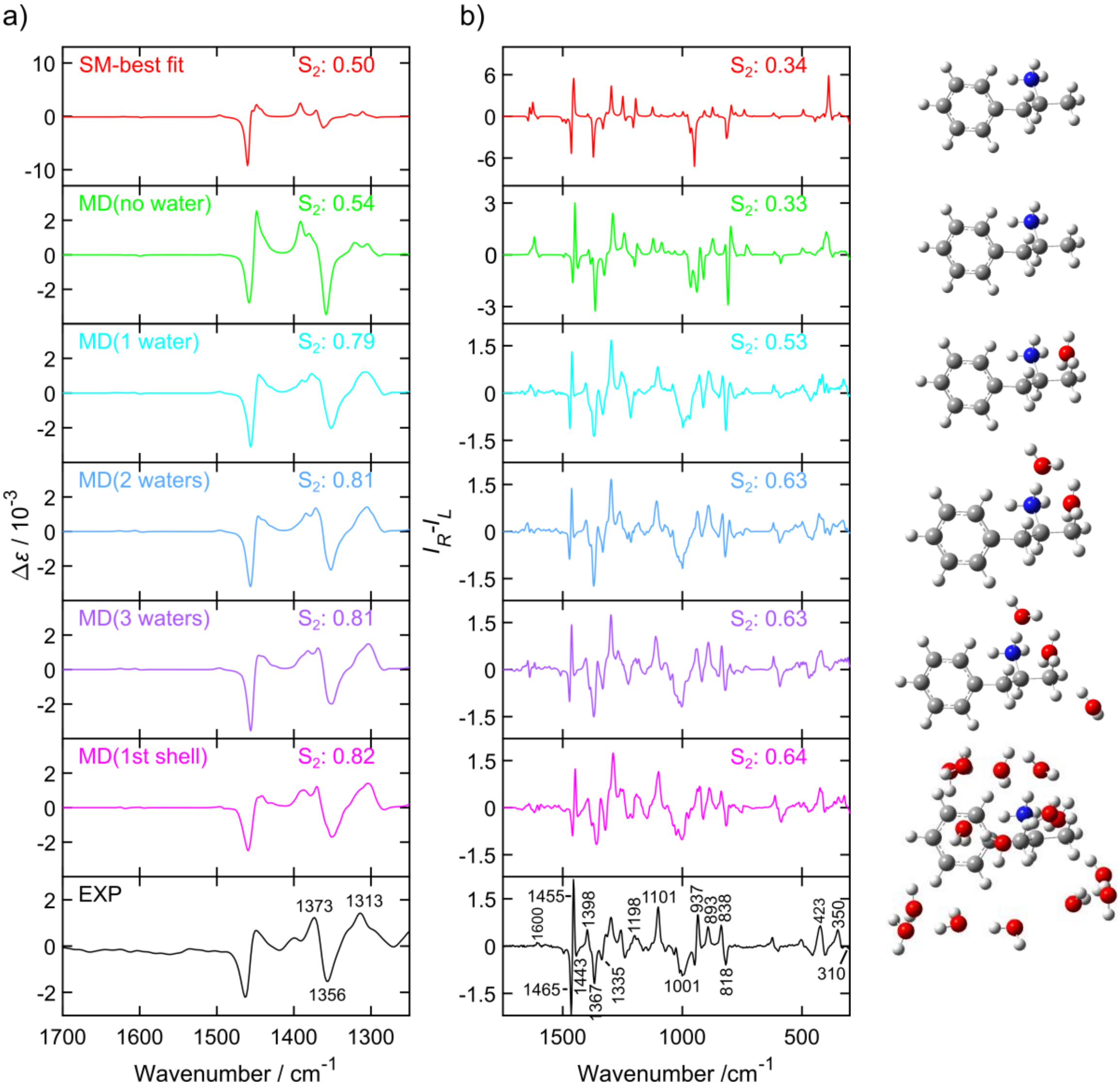

Figure 7: VCD (a) and ROA (b) spectra of (*S*)-amphetamine hydrochloride. Experimental spectra (black, bottom) were compared to the single molecule geometry (red), MD cluster-based models including only one (cyan), two (blue), or three (purple) closest water molecules, the cluster of the first water shell (magenta) and without explicit water molecules (green). For all MD cluster-based models 100 snapshots per conformer were averaged. The similarity factors (S_2) are given for individual spectra. Conformer populations and wavenumber scaling factors for selected models (SM, MD no water and MD 1st shell) are listed in **Table 1**. The VCD intensities are in epsilon units ($\mathrm{L \cdot mol^{-1} \cdot cm^{-1}}$), the ROA experiment in ($\mathrm{e^{-} \cdot cm \cdot J^{-1} \cdot g^{-1} \cdot L}$) and the ROA calculations are in arbitrary units.

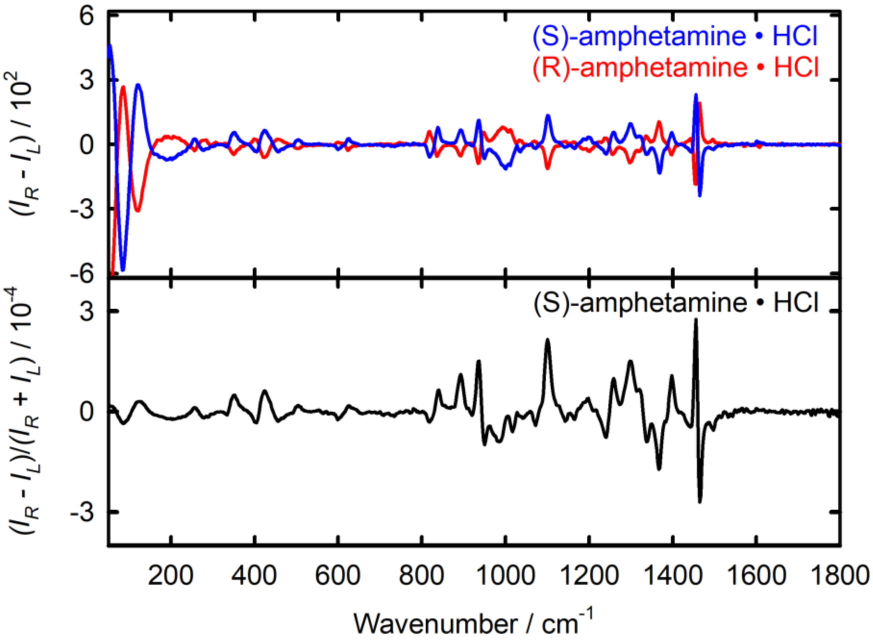

Figure 8: Experimental ROA (I_R–I_L) spectra of both amphetamine hydrochloride enantiomers (top), and CID ((I_R–I_L)/(I_R+I_L)) spectrum of (S)-amphetamine hydrochloride enantiomer (bottom); the intensity is in (e^- cm J^{-1}).

Overall, the similarity of IR and Raman spectra obtained with optimized populations for all different computational approaches are larger than for the corresponding chiroptical spectra (except for the DF case). However, the determined conformer populations are burdened with a large error, since the Raman and IR spectra reflect the conformations of chiral molecules only partially and the optimization algorithm tends to favor one conformer if the conformers' spectra are nearly identical.

The comparison between VCD and ROA methods is intriguing. The achieved results showed that both VCD and ROA give a significantly smaller similarity index for simpler models, and with a more advanced model of the molecular system including more realistic solvent and conformational effects, the similarity index increases substantially, and the determination of the population of states thus better converges to reliable values (the NMR values 0.45/0.50/0.05 from the previous study were taken as the reference (Neville et al., 1971)).

The simplified MD cluster models with different numbers of water molecules show that ROA is even able to distinguish the influence of different numbers of solvent molecules. The closest water molecules are mainly bound to charged NH_3^+ groups of amphetamines, see **Figure 9**. The most significant improvement in similarity overlap with the experiment is already achieved for the average spectra of the clusters with a single water molecule. Subsequent improvement with increasing number of water molecules in the cluster is rather minor but systematical, which can be demonstrated by the monotonously increasing similarity factor and noticeable improvements for the ROA bands around 300–500, 800, 1000, 1200 and 1600 cm^{-1} in **Figure 7**. On the opposite, VCD spectra of clusters with an increasing number of water molecules are almost identical.

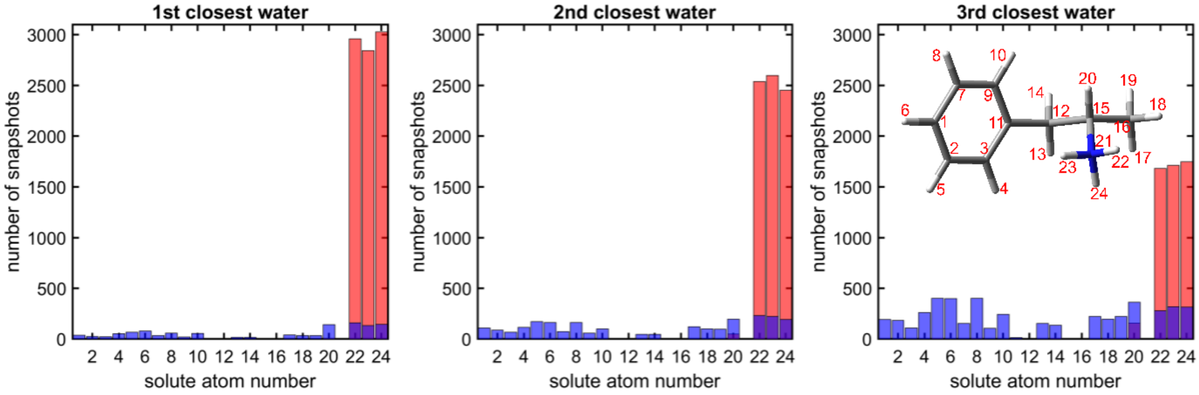

Figure 9: MD distribution of three water molecules to the amphetamine (100 ns MD, 10000 snapshots). The blue bars mark the interaction with H-atom, while the red bars with O-atom of H_2O molecule.

With its broad spectral range and numerous compared bands, ROA proved to be the most sensitive technique of vibrational optical activity for identifying the spatial arrangement and dominant conformation of the amphetamine and its derivatives. The amphetamine conformational ratio for the most advanced computational model determined from ROA spectra (0.43/0.41/0.16), CID spectra (0.42/0.46/0.12) and also VCD spectra (0.40/0.47/0.13) in **Table 1** are in good agreement with the conformational ratio 0.45/0.50/0.05 determined by NMR (Neville et al., 1971). According to the results, conformational averaging and the need for explicit solvent models are essential for the interpretation of the amphetamine vibrational spectra.

The conformational analysis of methamphetamine hydrochloride is more complex as the number of stable conformers increases due to a longer alkyl chain. Similarity overlaps for different spectroscopic methods confirm the findings discussed for amphetamine hydrochloride. Similarity overlaps with corresponding conformer populations are listed in **Table 2**.

Table 2: Optimized conformer populations for (*S*)-methamphetamine hydrochloride obtained from the comparison of experimental spectra and different calculation models.

Type	Spectral Range	Scaling Factor	c_1	c_2	c_3	c_4	c_5	c_6	S_1^*	$S_2^\dagger$
Single molecule geometry B3PW91/6-311++G**/COSMO										
IR	1250–1700	0.98	0.00	0.08	0.04	0.52	0.37	0.00	0.91	0.84
VCD	1250–1700	0.98	0.00	0.33	0.00	0.39	0.04	0.23	0.50	0.34
DF	1300–1700	0.98	0.83	0.00	0.00	0.08	0.00	0.08	0.60	0.43
Raman	300–1750	0.99	0.17	0.44	0.20	0.00	0.00	0.18	0.83	0.71
ROA	300–1750	0.98	0.21	0.16	0.07	0.11	0.36	0.08	0.58	0.41
CID	300–1750	0.99	0.32	0.40	0.08	0.06	0.10	0.05	0.57	0.40
Geometries from MD, water molecules excluded, B3PW91/6-311++G**/COSMO level with rDPS for Raman, ROA and CID										
IR	1250–1700	0.98	0.07	0.36	0.00	0.58	0.00	0.00	0.90	0.82
VCD	1250–1700	0.98	0.00	0.00	0.00	0.50	0.14	0.36	0.54	0.37
DF	1300–1700	0.98	0.00	0.39	0.00	0.61	0.00	0.00	0.63	0.46
Raman	300–1750	0.99	0.00	0.76	0.18	0.00	0.00	0.07	0.84	0.72
ROA	300–1750	0.99	0.43	0.00	0.00	0.00	0.49	0.08	0.62	0.45
CID	300–1750	0.99	0.40	0.26	0.00	0.00	0.21	0.13	0.60	0.43
Geometries from MD with explicit 1st solvation shell, B3PW91/6-31G**/GD3BJ/COSMO level with rDPS for Raman, ROA and CID										
IR	1250–1700	0.97	0.06	0.38	0.00	0.00	0.00	0.56	0.97	0.95
VCD	1250–1700	0.97	0.10	0.08	0.14	0.34	0.33	0.00	0.81	0.68
DF	1300–1700	0.97	0.00	0.00	0.15	0.51	0.34	0.00	0.67	0.50
Raman	300–1750	0.98	0.11	0.49	0.00	0.00	0.00	0.40	0.80	0.66
ROA	300–1750	0.98	0.37	0.29	0.05	0.00	0.26	0.03	0.77	0.63
CID	300–1750	0.98	0.40	0.27	0.00	0.00	0.27	0.07	0.68	0.52

* According to equation (2.3).

† According to equation (2.13).

3.2. ROA in the extended spectral range

3.2.1. Low-frequency ROA

Vibrational frequencies of intermolecular modes in liquids are close to the excitation frequency. The corresponding Raman signal is rather unstructured, unresolved, and quickly increases towards the excitation line. On the other hand, ROA low-frequency spectra are more structured and better reflect the conformational changes and intermolecular interactions in the studied system. An unexpectedly strong ROA signal of (*R*)-2-chloropropionitrile (nitrile) has been observed (see **Figure 10**) within the low-frequency region (50–150 cm^{-1}), carrying information about intermolecular interactions. On the basis of the combined MD cluster model and DFT theory, the signal was assigned to intermolecular vibrations. However, it remained unclear whether this signal had a direct connection to particular intermolecular interactions, like a molecule's capability to engage in hydrogen bonding.

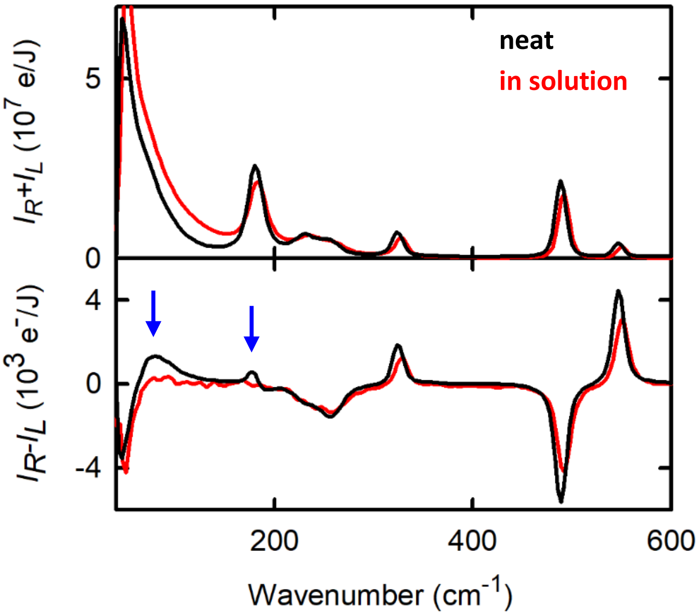

Figure 10: Raman and ROA spectra of (*R*)-2-chloropropionitrile in the low-frequency region for pure liquid (black) and its about 10 % solution in methanol (red). Clearly vanishing ROA bands are marked by blue arrows.

Ad hoc MD calculations of large clusters have been computationally demanding, and the simulation of the first solvation shell did not correspond to the real situation. Hence, ROA spectra of six chiral neat liquids[†] were recorded and a crystal-like computational protocol (see Subsection 2.1.1) that allowed us to analyze in detail the origin of the low-frequency modes was developed.

Various computational strategies used for modeling nitrile spectra are demonstrated and compared to the experiment in **Figure 11**. The low-frequency intermolecular signal is obviously missing in the single molecule spectra. The periodic crystal-like model is technically the most advanced one and avoids the surface cluster effects, but it comprises pair molecular interactions only. Some experimental features, such as the relatively monotonic increase in ROA intensity between 250 and 90 cm^{-1}, are therefore better reproduced with smaller clusters containing more intermolecular interactions. The large cluster model seems to give the worst results. Increasing the number of molecules in one elementary cell (i.e., size of the MD box) or including more than pairs interactions did not seem to bring improvement and is computationally demanding. A serious problem limiting the precision of the all MD computations is the large number of MD snapshots that need to be averaged for low-frequency ROA. Even 10 molecules in the box were too many for the direct calculation of a large number of snapshots needed for convergence, especially for larger molecules, such as phenylethanol or α-pinene, in the cluster. The convergence problem makes the computation expensive. Thus, the crystal-like approach is a useful alternative, providing satisfactory agreement with the experiment.

[†] (*R*)-2-chloropropionitrile (nitrile), (*R*)-(+)-propylene oxide (methyloxirane), (*R*)-(+)-1-phenylethanol (phenylethanol), (*R*)-(+)-α-methylbenzylamine (MBA), (*S*)-(+)-α-(trifluoromethyl)benzyl alcohol (TFB), and (+)(1*R*,5*R*)-α-pinene (α-pinene)

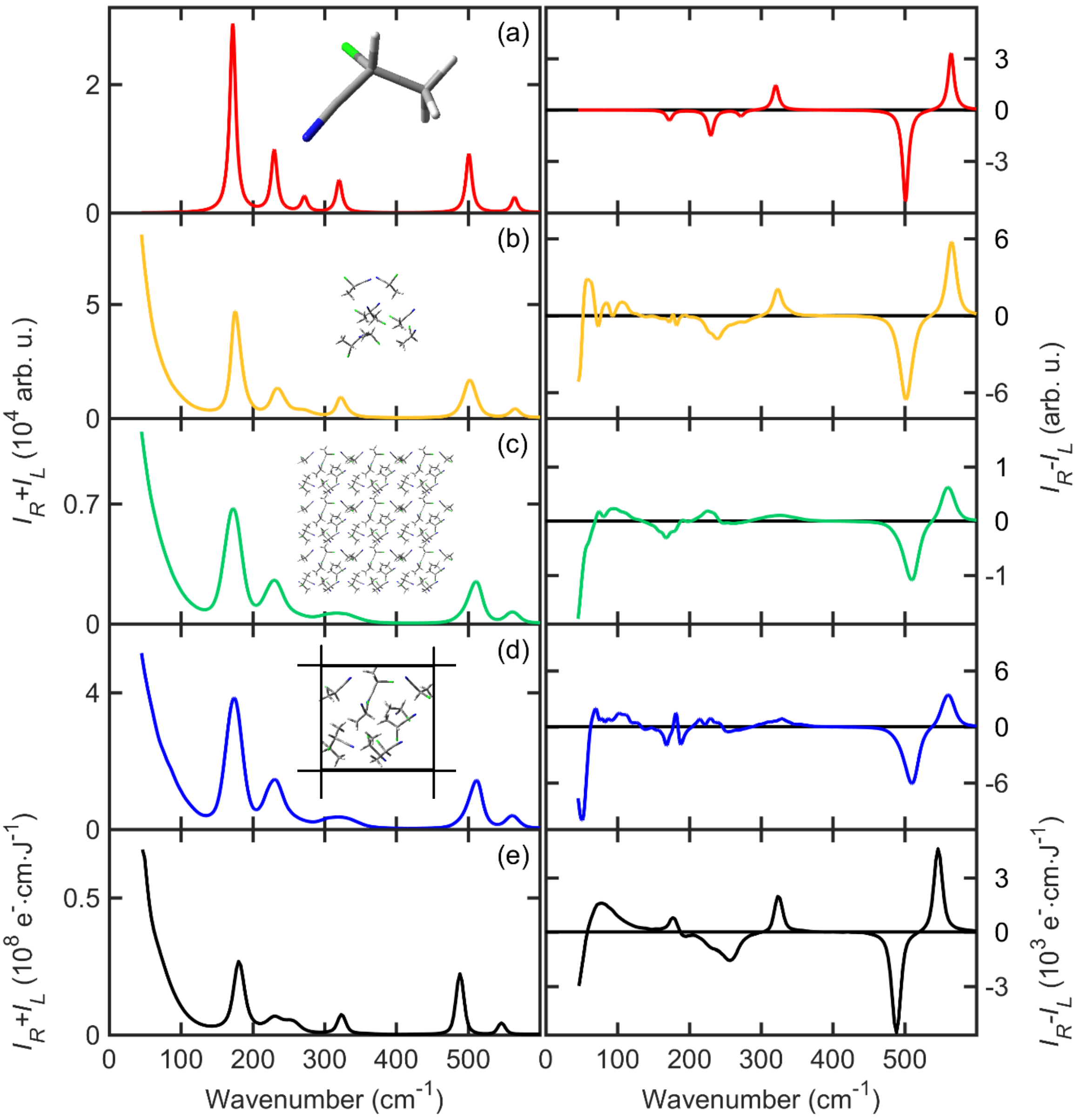

Figure 11: Raman and ROA nitrile spectra calculated with different models: (a) single molecule, (b) small cluster of ~ 15 nitrile molecules/all interactions, (c) large cluster/pair interactions (supercube), (d) periodic crystal/pair interactions, and (e) experimental spectrum. For b – d 200 MD snapshots were averaged.

Interestingly, neat methyloxirane gave nearly the same low-frequency ROA signal as its water solution (**Figure 12**). This observation was successfully reproduced by the crystal-like model and provided a phenomenological insight into the low-frequency chirality.

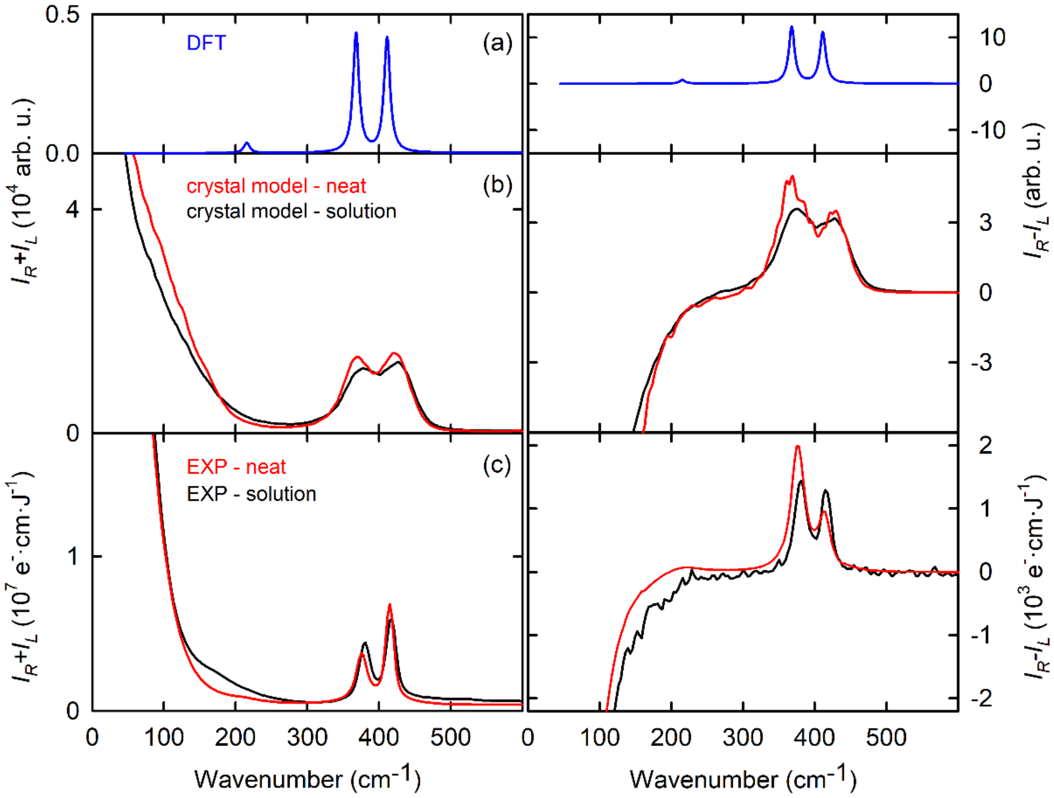

Figure 12: Raman and ROA spectra of neat methyloxirane and its water solution (1:22 methyloxirane:H_2O molar ratio): (a) single molecule computation, (b) crystal model, and (c) experiment.

To understand the low-frequency vibrations introducing intermolecular coordinates, or translations and rotations of one molecule, the potential energy distribution (PED) has been used. Same as for groups within one molecule, six coordinates describing the molecular positions were defined, see **Figure 13**.

The low-frequency modes are not too specific; nevertheless, the PED analysis suggests that for small rigid molecules (e.g. nitrile and methyloxirane) the low-frequency signal comes primarily from translations and rotations of individual chiral molecules (**Figure 14d, e**). For instance, the PED analysis of the methyloxirane (**Figure 14a-c**) reveals that intermolecular motions formally contribute differently to the vibrational energy in methyloxirane, water, and the mixture. Obviously, a pure water band ~ 220 cm^{-1} can be predominantly assigned to the intermolecular stretching. The stretching modes of the neat methyloxirane start to contribute in the lowest frequencies only, and the contribution is smoothed out in the mixture. The contribution of bending and torsion modes is more structured, reflecting the more complicated shape of the molecule.

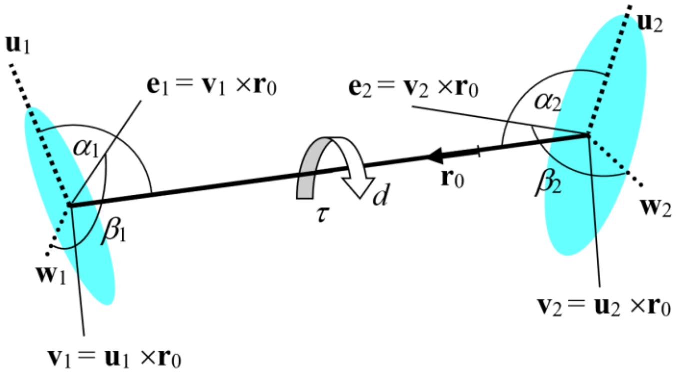

Figure 13: Definition of the six coordinates used for the characterization of intermolecular vibrational modes: (d) distance of the mass centers, (α_1 and α_2) angles between the largest moments of inertia and the distance vector, (β_1 and β_2) rotation angles, and (τ) the torsion angle. For the rotation angles, arbitrary vectors $\mathbf{e}_1$ and $\mathbf{e}_1$ were defined, using the largest (direction $\mathbf{u}_i$) and second largest ($\mathbf{w}_i$) moments of inertia. Lengths of all vectors $\mathbf{u}_i$, $\mathbf{w}_i$, $\mathbf{v}_i$, $\mathbf{e}_i$, $\mathbf{r}_i$, and $\mathbf{r}_0$ are equal to one.

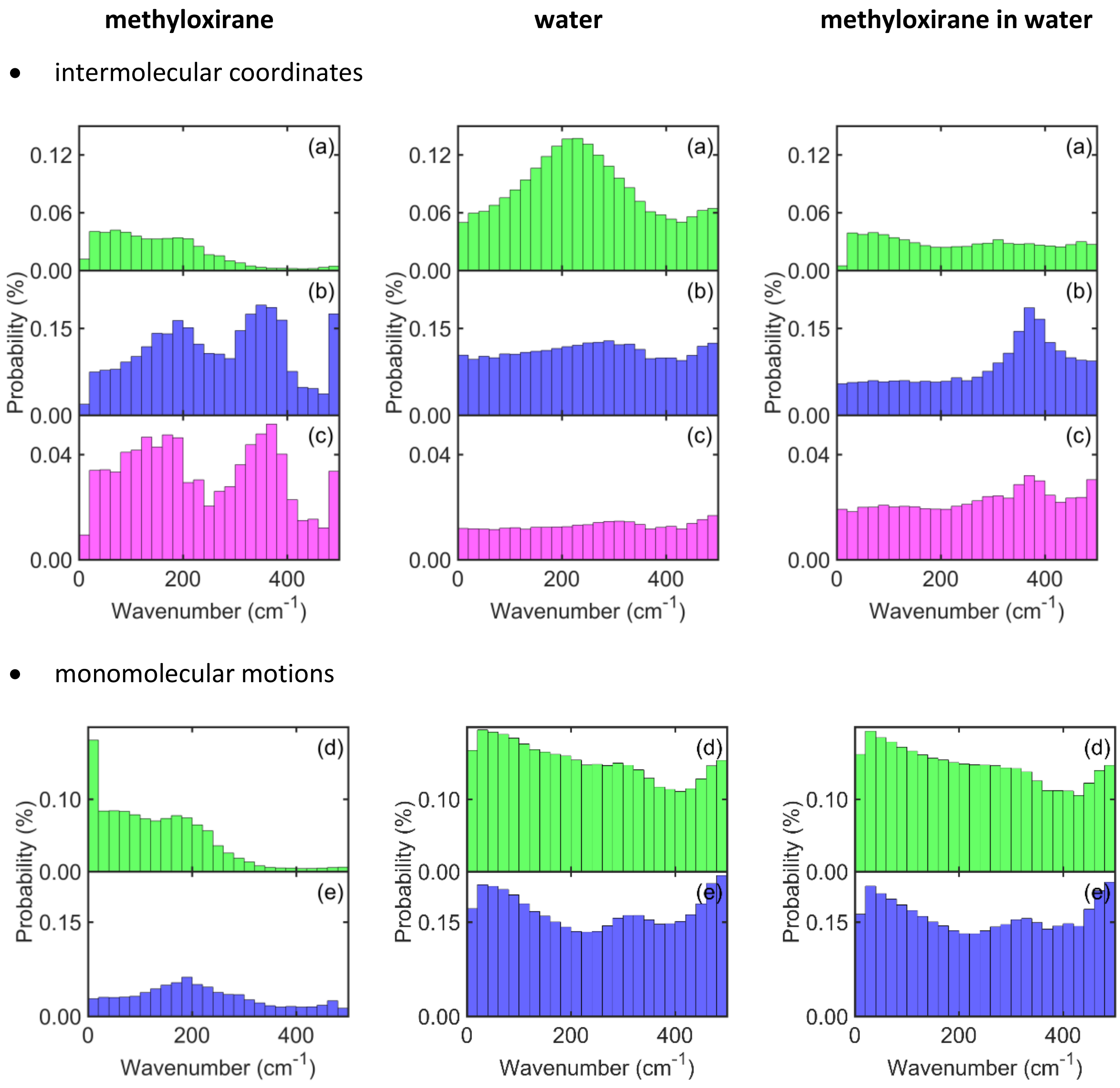

Figure 14: Relative vibrational potential energies of intermolecular motions related to two (stretching (a), bending (b), torsion (c)) and one (translations (d), rotations (e)) molecule, for neat methyloxirane, water and a mixture. Displayed PED values are averaged over the snapshots and normal modes in a wavenumber interval.

For more flexible molecules (phenylethanol, MBA, TFB) the intermolecular low-frequency modes are mixed with intramolecular motions, such as rotations of the phenyl, methyl, hydroxyl, trifluoromethyl and amine groups. The interpretation of the phenylethanol spectra is shown in **Figure 15**. Although the single molecule calculation reproduces some main features of the low-frequency region reasonably well, the crystal-like model performs better. Although the precision of used simulations is limited due to available computer power, they provide a sound theoretical basis to interpret the observed spectra and can be systematically improved in the future.

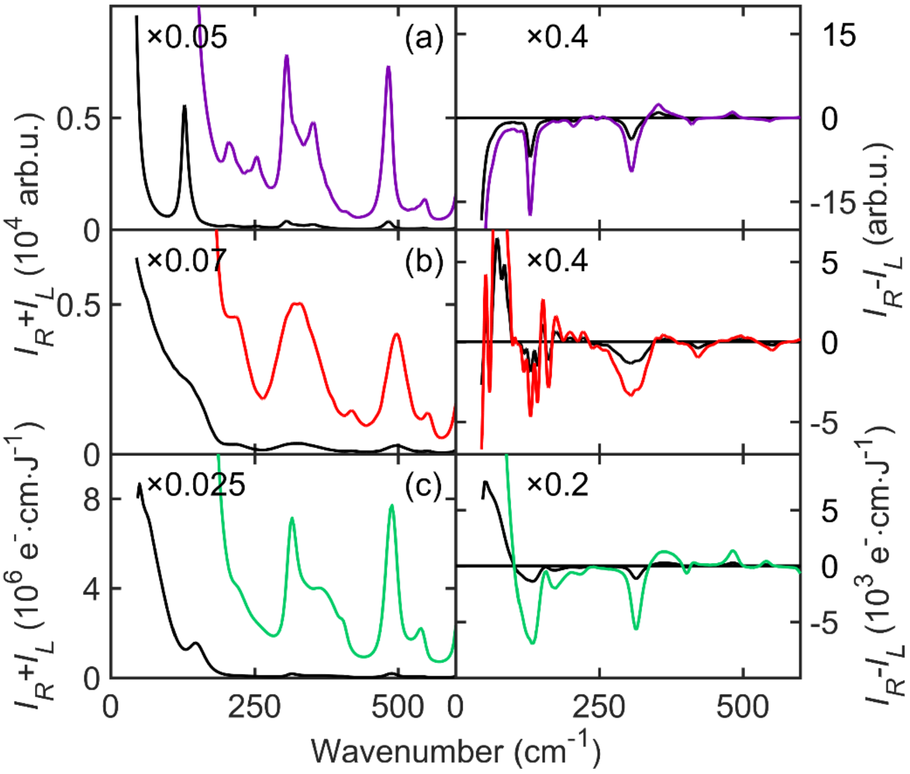

Figure 15: Raman and ROA spectra of (*R*)-(+)-1-phenylethanol; (a) simulation of one molecule (weighted average of 386 conformers < 2 kcal·mol^{-1}), (b) the crystal-like model, and (c) the experiment.

3.2.2. Anharmonic overtone and combination bands

The new double-grating ROA spectrometer exhibits a large signal-to-noise ratio and a flat baseline. On the other edge of the spectrum, using this instrument we thus were able to measure not only high-energy CH stretching fundamental transitions (2700–3300 cm^{-1}) but also a set of almost two orders weaker overtone and combination bands, largely ignored in previous studies. For the first time, many combination and overtone ROA bands have been observed for 2-chloropropionitrile and α-pinene, mostly within 1490–3800 cm^{-1}. Simulations of high-frequency molecular vibrational properties in general require treatment beyond the harmonic approximation. Using the 2nd order vibrational perturbation approach (VPT2), its modification (GVPT2), better treating the Fermi and Darling−Dennison resonances (Bloino et al., 2015), and limited vibrational configuration interaction (LVCI) (Daněček & Bouř, 2007), the most intense bands were unambiguously assigned to double-excited overtone or combination transitions.

For nitrile, the experimental and simulated Raman and ROA spectra within 1490−3800 cm^{-1} are displayed in **Figure 16**. Only the fundamental modes comprising C≡N stretching and CH stretching are plotted scaled in the gray areas. The spectral shape of the fundamentals was already reproduced by the harmonic level (B3PW91/6-311++G**/COSMO(ACN)). However, both the VPT2 and LVCI anharmonic methods significantly reduced the frequency error and provided nearly the experimental CH stretching frequencies. For the C≡N band, the error about 73 cm^{-1} remains most probably due to an inherent inaccuracy of the B3PW91 and similar functionals for molecular systems with triple bonds.

Below 3100 cm^{-1}, the VPT2 and LVCI methods provide similar Raman shapes, whereas for ROA, the VPT2 simulation looks more realistic when compared with experiment. The GVPT2 introduced only minor corrections in this case, however, for larger molecules (α-pinene) provides a very good agreement with the experimental spectra, whereas the VPT2 failed in the entire spectral region. The VPT2 results diverge due to the higher number of resonances in the molecule. Only LVCI includes up to five times excited modes. Based on the similarity between LVCI and VPT2 simulations, we can conclude that double-excited overtones and combination transitions dominate, while the contribution of higher excitations is minor.

Based on VPT2, many combination and overtone bands can be unambiguously assigned to the experiment. Moreover, the main contributions to the overtone and combination bands can be classified, see the color legend at the top of **Figure 16**. For example, within 1500−2220 cm^{-1}, CH_3 rocking and CC stretching seem to generate most of the spectral intensities. In wavenumber regions closer to the fundamental CH stretching bands (2600−2900 cm^{-1}), the CH bending modes, such as the CH_3 umbrella or CH_3 scissoring, dominate. Above 3000 cm^{-1}, higher-energy fundamental modes, such as C≡N stretching, contribute more. In addition, the lower-frequency fundamental motions can combine with the CH stretching modes.

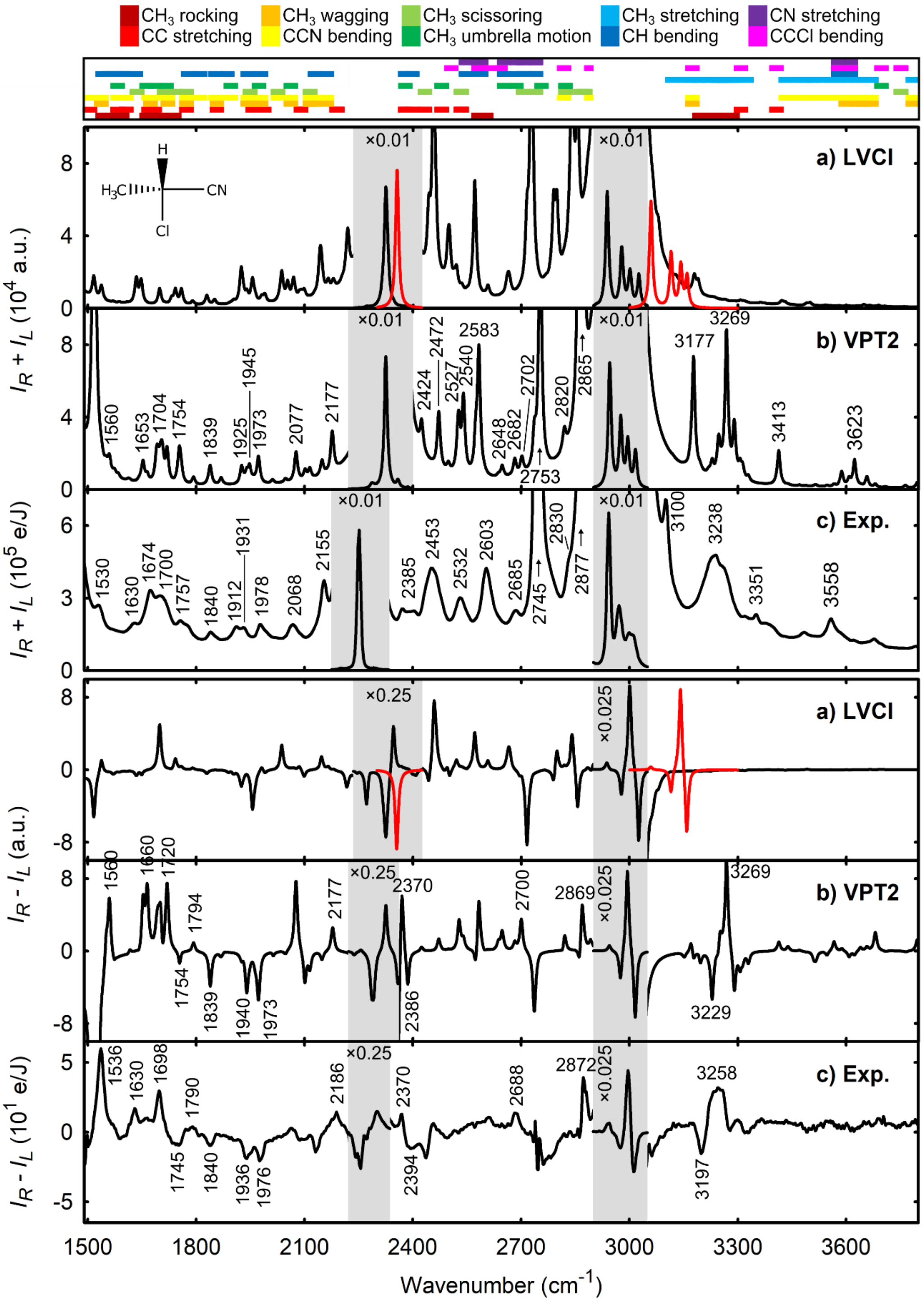

Figure 16: Raman and ROA spectra of (*R*)-2-chloropropionitrile, plotted within 1490–3800 cm^{-1}, as calculated using the limited vibrational configuration interaction (LVCI; a), vibrational second-order perturbation calculus (VPT2; b), and the experiment (c). The fundamental bands (scaled gray area) are compared to the harmonic approximation (red line). At the top, main coordinate contributions to the overtone and combination bands are indicated.

3.3. Enantiomeric excess determination

Another principal application of ROA spectroscopy is the measurement of optical purity of chiral samples. To date, the most commonly employed approach for determining enantiomeric excess (EE) involves chiral chromatography. However, this method is demanding from an experimental perspective and necessitates the use of specialized columns designed for different chiral substances. VOA spectroscopy in general, being a noninvasive technique, allows for the observation of a significant number of vibrational bands. This feature proves valuable in assessing enantiomeric excess while enhancing the ability to detect experimental artifacts or impurities within the sample, thereby improving the reliability of EE. The EE determination of a chiral sample is of particular importance, especially to the analytical chemistry and pharmaceutical industries. With the aim of augmenting the utility of ROA spectroscopy in the realm of chemical practice, we have proposed a new methodology for the precise assessment of EE in chiral samples.

Conventional methods of EE determination from the VOA spectra were based on band-to-band comparison or the partial least squares analysis (PLS) (Guo et al., 2004; Hecht et al., 1995). However, published methods reported a relatively limited accuracy in the range of about 1–2 %, mostly caused by a limited statistical ensemble of the experimental data, spectral range or insufficient data post-processing. Therefore, we have demonstrated a new methodology of enantiomeric excess determination described in Section 2.5. It is based on an effective algorithm that includes Raman baseline correction (see Section 2.3), ROA intensity normalization (Subsection 2.5.1), and systematic errors elimination procedure (Subsection 2.5.4) applied to experimental ROA data.

The new methodology is demonstrated on nine approximately equally distributed enantiomeric mixtures of neat α-pinene and alanine in an aqueous solution. Neat α-pinene is often used as a chiroptical calibration standard. Alanine was chosen as representative of chiral sample in aqueous solution, which is difficult or nearly impossible to measure by complementary VCD technique. For both α-pinene enantiomers the manufacturer states that the optical purity exceeding 97 % and for alanine the optical purity is not declared. Analytical weights (Adam Equipment) with a 0.01 mg resolution were used for the sample preparation. In order to reduce systematic errors in the EE determination caused by weighing, a relatively large stock volumes of 0.75 mL and 0.50 mL had to be prepared for α-pinene and alanine solution, respectively. The maximal error caused by weighing was estimated approximately to 0.02 % of the EE. Only volumes of 70 μL per sample were used for the ROA measurement.

The Raman and ROA raw data within 100–2000 cm^{-1} used for the further analysis of α-pinene and alanine EE are presented in **Figure 17** and **Figure 18**, respectively. **Figure 17c** and **Figure 18c** show the Raman spectrum after the ALSS baseline correction. The aim of this procedure was not to make the baseline as flat as possible but to unify Raman spectra in the data set before the ROA normalization. Even a relatively minor baseline corrections as were applied for α-pinene have a crucial effect on the performance of the EE determination. Clearly, the baseline correction procedure was essential for alanine measurements, as the background exhibits substantial variability across each EE mixture. **Figure 17d** and **Figure 18d** show the artifact ROA spectrum of α-pinene and alanine, respectively, determined by equations (2.22) and (2.24) in Subsection 2.5.4. Strongly polarized and also the most intense Raman bands, such as α-pinene breathing vibration 667 cm^{-1} are the most artifact prone. Their contribution to the relatively weak ROA signal is approximately 10%.

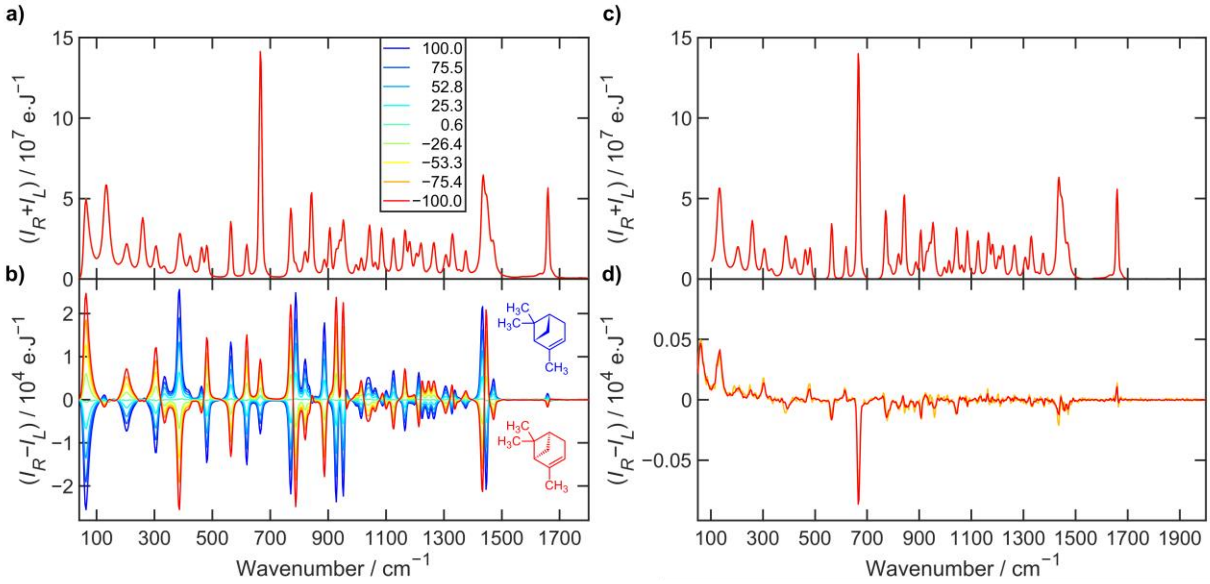

Figure 17: a) Raman and b) ROA spectra of neat liquid α-pinene enantiomeric mixtures after 5.5 hours of exposition time each. The legend shows EE determined from sample preparation. c) Raman spectra after baseline correction. d) ROA artifact spectrum calculated according to Eq. (2.22) is depicted in orange and according to eq. (2.24) is red. All spectra were subjected to third-order five-point Savitzky–Golay smoothing.

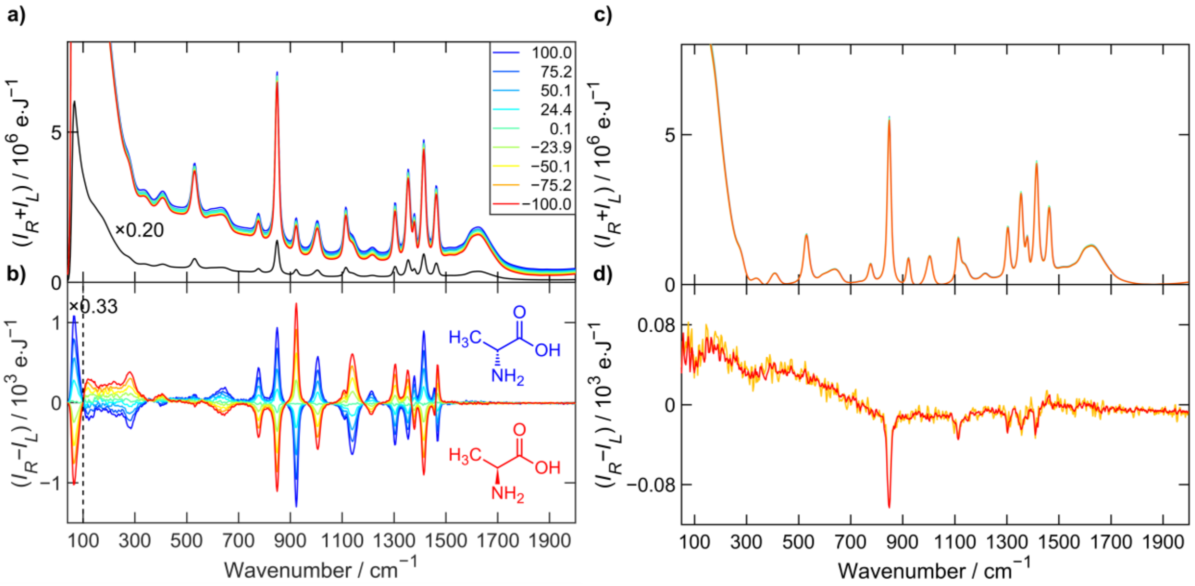

Figure 18: a) Raman and b) ROA spectra of alanine enantiomeric mixtures in water solution at a molar concentration ~1.2 M after 5.7 hours of exposition time each. The legend shows EE determined from sample preparation. The Raman spectrum of the reference (black) was multiplied by a factor of 0.2 in order to show strong low-wavenumber Raman scattering. c) Raman spectra after baseline correction. d) ROA artifact spectrum calculated according to Eq. (2.22) is depicted in orange and according to eq. (2.24) is red. All spectra were subjected to third-order five-point Savitzky–Golay smoothing.

The results of the EE analysis for α-pinene and alanine are summarized in **Table 3** and **Table 4**, respectively. The columns in these tables represent the spectral range selection for different steps of the EE determination routine (Raman baseline correction, ROA intensity normalization, artifact correction and EE determination). For the evaluation, last two columns show the standard deviation of the EE errors ($\sigma(\Delta_i)$) and determined EE of enantiomer B according to the reference enantiomer A ($\hat{e}_B$), calculated by equations (2.20) and (2.21). Individual EE determination errors for options in the tables are depicted in **Figure 19**.

The importance of introduced post-processing procedure is supported by comparison of the first and second row in the tables. The results show that, unless the baseline correction, Raman normalization and the artifacts spectra subtraction is performed, it is not possible to reduce the standard deviation of the EE errors below 0.26 % for α-pinene and approximately 1.72 % for alanine. The significant improvement in accuracy of the EE determination is mainly caused by the subtraction of calculated artifacts. Alanine in **Table 4** shows large deviations from −100 % of EE of reference B. Note that absolute values of EE determination for enantiomer *B* above 100 % are possible, since it is a relative value to the reference enantiomer *A*.

The spectral range selection for Raman baseline correction, ROA normalization, artifact correction and EE determination was also tested. These results confirmed that the appropriate choice of spectral range especially for baseline correction and ROA normalization can lead to a substantial reduction in EE determination errors. This is illustrated by examining option 2 and 3 in **Table 3** and **Table 4** in contrast to option 1, where a fixed spectral range was used in the whole post-processing procedure. For example, if the spectral range used for ROA normalization of α-pinene is limited around the relatively isolated C=C stretching band of 1660 cm^{-1}, the most accurate results can be achieved. However, two caveats must be noted. Due to the oxidation of the α-pinene the relative Raman band intensities change, especially the sideband 1622 cm^{-1} appears in the presence of the oxidation products in the measured sample. Despite that the region 1700 cm^{-1} and above is free of fundamental vibrations, there are numerous low-intensity anharmonic combination and overtone modes, that make proper baseline correction not an easy task. Not overly surprisingly, the exclusion of the bands carrying the largest polarization artifacts (667 cm^{-1} for α-pinene and 848 cm^{-1} for alanine) leads to an increase in the accuracy of the EE determination. For example, limiting the EE determination of α-pinene to the 700–940 cm^{-1} range, the outstanding accuracy of 0.05 % was achieved. This can be explained by a large ROA to Raman ratio and minimal occurrence of artifacts in the selected region.

Table 3: Enantiomeric excess analysis results of α-pinene for different spectral ranges in each step of EE determination.

Option	Baseline correction		Raman normalization		Artifact correction		EE determination		$\sigma(\Delta_i)$ / %	$\hat{e}_B$ / %
0	-	-	-	-	-	-	100	2000	0.26	-99.95
1	100	2000	100	2000	100	2000	100	2000	0.18	-99.65
2	100	2000	1500	1800	100	2000	100	2000	0.08	-99.92
3	100	2000	1500	1800	100	2000	700	940	0.05	-100.00

Table 4: Enantiomeric excess analysis results of alanine for different spectral ranges in each step of EE determination.

Option	**Baseline correction**		**Raman normalization**		**Artifact correction**		**EE determination**		$\boldsymbol{\sigma(\Delta_i)}$ **/ %**	$\boldsymbol{\hat{e}_B}$ **/ %**
0	-	-	-	-	-	-	100	2000	1.72	-101.49
1	100	2000	100	2000	100	2000	100	2000	0.26	-99.87
2	100	2000	100	1500	100	2000	100	2000	0.25	-99.88
3	100	2000	100	1500	100	2000	900	1500	0.24	-99.77

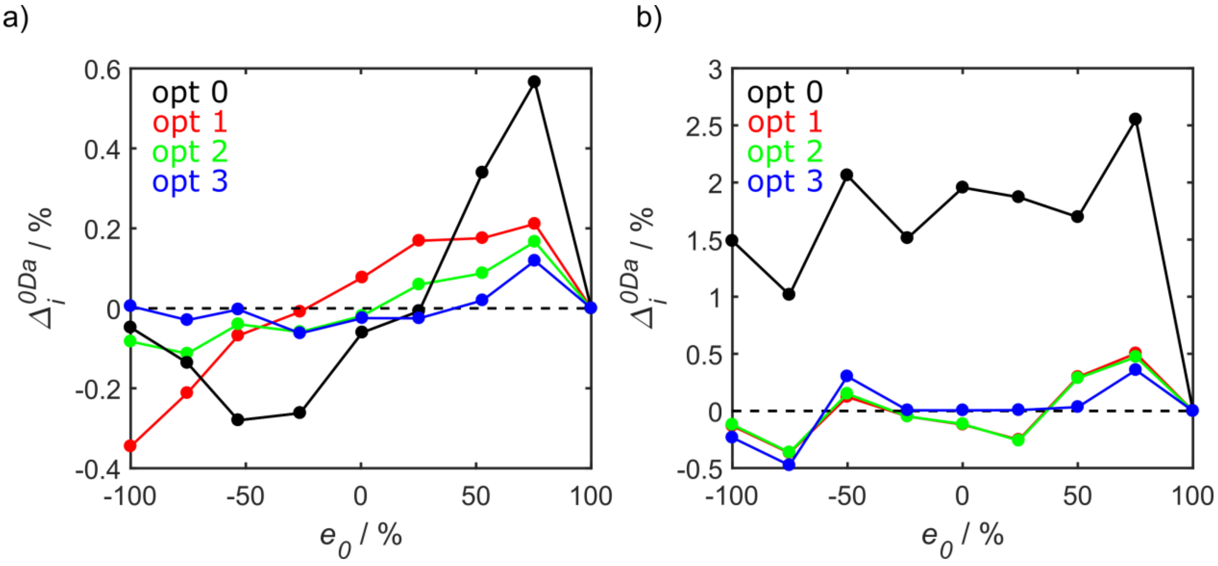

Figure 19: Errors of EE determination $\boldsymbol{\Delta_i}$ for a) α-pinene and b) alanine for various options in spectral range selection described in **Table 3** and **Table 4**, respectively.

We also investigated dependence of accuracy of the EE determination on the measurement time of the ROA spectra. Raman and ROA spectra were exported periodically during the experiment and the time dependence is calculated for every cumulative step. The results for different spectral range options from **Table 3** and **Table 4** are summarized in **Figure 20**. Since the signal-to-noise ratio increases with a square root of the exposition time, it is reasonable to fit datapoints of the standard deviation of EE determination errors by the equation

$$\sigma(t) = \sigma_\infty + \frac{\sigma_1}{\sqrt{t}}, \tag{3.1}$$

where σ_1 is the standard deviation expected for the unit exposition time t and σ_∞ is the limit of standard deviation for infinite time measurement, which can be interpreted as a residual systematic error. For α-pinene, the EE accuracy of 0.1 % was already achieved after 100 minutes of exposition time and accuracy of 0.05 % after 330 minutes of exposition time for the best choice of parameters. Alanine in an aqueous solution exhibited a comparable convergence pattern, albeit with lower precision, reaching approximately 0.22 % after 345 minutes. The diminished accuracy of alanine can be attributed to its ROA signal being ten times weaker than that of α-pinene.

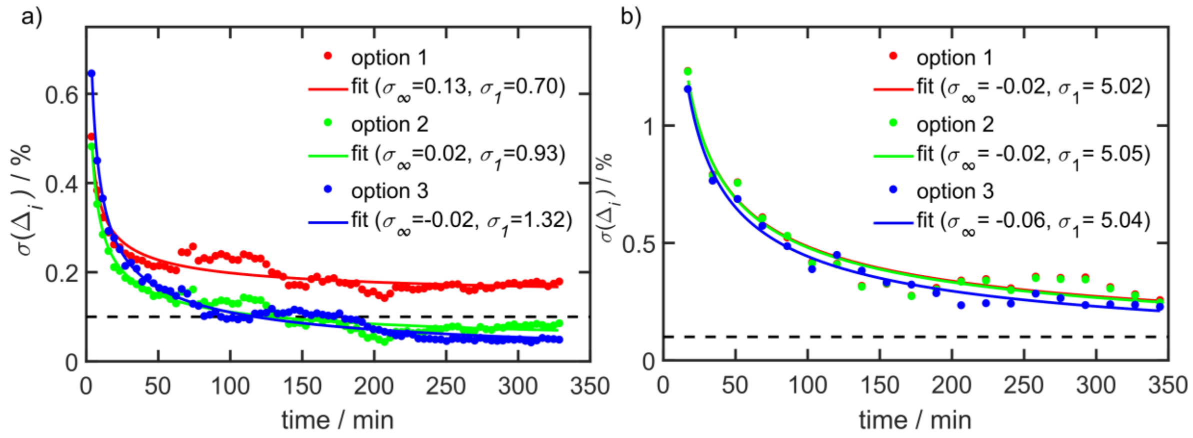

Figure 20: Dependence of standard deviation of the errors of EE determination $\sigma(\Delta_i)$ on the total exposition time of one mixture of α-pinene (a; 3.91 min per step) and alanine in aqueous solution (b; 17.22 min per step). Selected options point to the parameters listed in **Table 3** and **Table 4**, respectively. Data were fitted by the function in eq. (3.1).

4. Conclusions

In our work we focused on the developing of experimental methodology for Raman and Raman optical activity spectra (ROA). We also explored spectral interpretation and simulation procedures, and the information we can get from measured spectra of various chiral substances. An extended spectral range 50–4500 cm^{-1} was reached by the unique double-grating ROA spectrometer developed at the Department of Optics Of Palacký University Olomouc.

We explored the sensitivity of ROA to the geometry, absolute configuration, structure and dynamic behavior on various chiral substances. Compounds, such as 2-chloropropionitrile, methyloxirane and ethylbenzene derivatives were studied. The full spectral range from 50 to 4000 cm^{-1} was measured, although not all bands could be simulated with sufficient accuracy. For 2-chloropropionitrile, a detailed dependence of the spectral parameters and potential energy on selected coordinates was discussed. Rather surprising flexibility of the C−C≡N group was observed. The distribution of conformers obtained from molecular dynamics differed from that obtained from DFT; the former one was more consistent with the spectroscopic data.

In other conformational analysis, we developed an approach maximizing the similarity overlap of weighted conformer spectra with the experiment. Then IR, Raman, VCD, and ROA spectra of amphetamine and methamphetamine hydrochlorides in aqueous solution were interpreted, using DFT and molecular dynamics simulations. Relative populations of three and six stable conformers of amphetamine and methamphetamine, respectively, were determined and found consistent with a previous NMR study. Cluster-based simulations with different number of water molecules also allowed us to track the solvation effects in ROA spectra, not much seen in VCD.

The measurement in the broader vibrational range significantly extended the information that could be obtained by optical spectroscopy from the spectra. For example, we found that intermolecular interactions contribute to ROA in the wavenumber range lower than 150 cm^{-1}. To understand origin of this low-frequency ROA signal, we developed a crystal-like computational protocol to model bulk liquids. For molecules like methyloxirane or α-pinene the signal originates predominantly in molecular translations and rotations. For more flexible and polar molecules, intramolecular motions, specific intramolecular interactions, such as hydrogen bond stretching, also contribute.

Within 1490−3800 cm^{-1} we observed for the first time a large set of overtone and combination ROA bands in the spectra of 2-chloropropionitrile and α-pinene. Using various perturbation and variational approaches, the most intense bands were assigned, mostly to double-excited overtone and combination transitions. The results were verified by comparison of Raman, IR absorption and VCD measurements. The perturbational approach as implemented in Gaussian 16 software appeared as more practical than the limited vibrational configuration method.

We proposed accurate methodology for determining the enantiomeric excess (EE) of chiral samples. The algorithm consists of the Raman baseline correction, ROA intensity normalization and systematic error elimination procedures. It was applied to nine enantiomeric mixtures of neat α-pinene and alanine in aqueous solutions. The enantiomeric excess was determined by solving an overdetermined set of linear equations. The accuracy of the EE determination was discussed with respect to the spectral range analyzed, purity of the reference, and the accumulation time of the ROA spectra. After exclusion of the strongly polarized Raman bands and with spectral range optimal for ROA normalization, accuracy of about 0.05 % and 0.22 % was achieved within reasonable accumulation times for α-pinene and alanine, respectively. ROA spectroscopy can thus serve as a non-destructive and very accurate technique for the enantiomeric excess determination. This may find applications in organic chemistry as well as in the pharmaceutical industry, where the chiral purity is often a critical factor for reactivity and biological activity.

Overall, the results indicate that the synergy of the experimental and computational Raman and ROA methodologies may be useful to understand fundamental molecular properties, with applications including analytical chemistry, biology, or medicine.

5. Stručné shrnutí v českém jazyce

Tato dizertační práce byla zaměřena na vývoj experimentální metodiky pro Ramanova spektra a spektra Ramanovy optické aktivity (ROA). Dále bylo věnováno úsilí metodám interpretace spekter, jejich simulacím a následné analýze z experimentálních spekter různých chirálních látek. Rozšířeného spektrálního rozsahu 50–4500 cm^{-1} bylo dosaženo za pomoci unikátního ROA spektrometru, vyvinutého na Katedře optiky Univerzity Palackého v Olomouci.

Podrobněji byla studována citlivost ROA na geometrii, absolutní konfiguraci, strukturu a dynamické chování různých chirálních látek, například molekuly 2-chloropropionitrilu, methyloxiranu a derivátů ethylbenzenu. Experimentální spektra byla měřena v rozsahu od 50 do 4000 cm^{-1}, i když ne všechny pásy bylo možné simulovat s dostatečnou přesností. U 2-chloropropionitrilu byla diskutována detailní závislost spektrálních parametrů a potenciální energie na vybraných úhlech. Byla zjištěna poměrně velká flexibilita C−C≡N skupiny této molekuly. Distribuce konformerů, generovaná molekulovou dynamikou, se lišila od distribuce získané z DFT výpočtů, přičemž výsledky byly více v souladu s experimentálními daty.

Pro účely konformační analýzy byl vyvinut originální algoritmus založený na podobnosti experimentálního a simulovaného spektra, který byl následně využit při analýze IČ, Ramanových, VCD a ROA spekter amfetaminu a jeho derivátů ve vodném prostředí. Interakce s prostředím byla simulována za pomoci implicitních modelů (PCM, COSMO) a explicitním zahrnutím modelů rozpouštědla do výpočtu. Ve shodě s předchozí NMR studií, bylo úspěšně stanoveno relativní zastoupení tří stabilních konformerů amfetaminu a šesti stabilních konformerů methamfetaminu. Systematickým zahrnutím molekul vody do výpočtů bylo možné analyzovat vlivy jednotlivých mezimolekulárních interakcí na ROA spektra, zatímco u VCD spekter byl jejich vliv zanedbatelný.

ROA měření v rozšířeném spektrálním rozsahu významně rozšířilo informace, které lze z vibračních spekter získat prostřednictvím optické spektroskopie. Bylo zjištěno, že mezimolekulární interakce přispívají k ROA signálu pod 150 cm^{-1}. Pro pochopení původu tohoto nízkofrekvenčního ROA signálu byl vyvinut výpočetní protokol pro modelování kapalin s periodickou strukturou podobnou krystalu. Bylo zjištěno, že signál jednoduchých molekul, jako je methyloxiran nebo α-pinen, má původ převážně v translačních a rotačních pohybech molekul. U více flexibilních molekul přispívají do této oblasti také intramolekulární interakce, jako například protahování vodíkových vazeb.

V rozsahu 1490−3800 cm^{-1} byly vůbec poprvé pozorovány vyšší harmonické a kombinační módy v ROA spektrech 2-chloropropionitrilu a α-pinenu. Za pomoci různých perturbačních a variačních modelů byly nejintenzivnější pásy přiřazeny dvojitě excitovaným překryvovým a kombinačním přechodům. Tyto výsledky byly rovněž podpořeny porovnáním Ramanových, IČ a VCD spekter. Perturbační přístup implementovaný v softwaru Gaussian 16 poskytoval lepší výsledky než metoda omezené vibrační konfigurace.

Dále byla navržena metodologie pro přesné určování enantiomerního přebytku (EE) chirálních vzorků. Algoritmus zahrnující korekci fluorescenčního pozadí v Ramanových spektrech, normalizaci intenzity ROA a proceduru systematické eliminace chyb byl aplikován na devět směsí α-pinenu a alaninu ve vodných roztocích o různém enantiomerním složení. Enantiomerní přebytek byl stanoven řešením přeurčené soustavy lineárních rovnic. Přesnost určení EE byla diskutována s ohledem na analyzovaný spektrální rozsah, enantiomerní čistotu reference a dobu měření ROA spekter. Po vyloučení silně polarizovaných Ramanových pásů a s optimálním spektrálním rozsahem pro normalizaci ROA byla dosažena přesnost přibližně 0.05 % pro α-pinen a 0.22 % pro alanin v relativně krátkém čase. ROA spektroskopie tak může být využita jako nedestruktivní a velmi přesná technika pro určování enantiomerního přebytku, například v organické chemii nebo ve farmaceutickém průmyslu, kde je chirální čistota často kritickým faktorem pro reaktivitu a biologickou aktivitu.

Celkově výsledky naznačují, že synergie experimentálních a výpočetních metodik Ramanovy a ROA spektroskopie může být užitečná pro porozumění základním molekulárním vlastnostem s aplikací na poli analytické chemie, biologie nebo medicíny.

6. References

Bloino, J., Biczysko, M., and Barone, V. (2015). Anharmonic effects on vibrational spectra intensities: infrared, Raman, vibrational circular dichroism, and Raman optical activity. *The Journal of Physical Chemistry A, 119*(49), 11862-11874.

Bootsma, A. N., and Wheeler, S. (2019). Popular integration grids can result in large errors in DFT-computed free energies. *ChemRxiv*.

Bouř, P. (2005). Convergence Properties of the Normal Mode Optimization and its Combination with Molecular Geometry Constraints. *Collect. Czech. Chem. Commun., 70*, 1315-1340.

Bouř, P. (2006). Qgrad. Prague, Czech Republic: IOCB, Academy of Sciences.

Bouř, P., and Keiderling, T. A. (2002). Partial optimization of molecular geometry in normal coordinates and use as a tool for simulation of vibrational spectra. *J. Chem. Phys., 117*, 4126-4132.

Bouř, P., Sopková, J., Bednárová, L., Maloň, P., and Keiderling, T. A. (1997). Transfer of molecular property tensors in Cartesian coordinates: A new algorithm for simulation of vibrational spectra. *J. Comput. Chem., 18*, 646-659.

Daněček, P., and Bouř, P. (2007). Comparison of the numerical stability of methods for anharmonic calculations of vibrational molecular energies. *Journal of Computational Chemistry, 28*(10), 1617-1624.

Eilers, P. H. C. (2003). A perfect smoother. *Analytical chemistry, 75*(14), 3631-3636.

Eilers, P. H. C., and Boelens, H. F. M. (2005). *Baseline Correction with Asymmetric Least Squares Smoothing*. Leiden University Medical Centre report.

Guo, C., Shah, R. D., Dukor, R. K., Cao, X., Freedman, T. B., and Nafie, L. A. (2004). Determination of Enantiomeric Excess in Samples of Chiral Molecules Using Fourier Transform Vibrational Circular Dichroism Spectroscopy: Simulation of Real-Time Reaction Monitoring. *Analytical chemistry, 76*(23), 6956-6966.

Hecht, L., Phillips, A. L., and Barron, L. D. (1995). Determination of enantiomeric excess using Raman optical activity. *Journal of Raman spectroscopy, 26*(8-9), 727-732.

Hug, W. (2003). Virtual Enantiomers as the Solution of Optical Activity's Deterministic Offset Problem. *Applied spectroscopy, 57*(1), 1-13.

Kapitán, J., Johannessen, C., Bouř, P., Hecht, L., and Barron, L. D. (2009). Vibrational Raman Optical Activity of 1-Phenylethanol and 1-Phenylethylamine: Revisiting Old Friends. *Chirality, 21*, E4-E12.

Koenis, M. A. J., Xia, Y., Domingos, S. R., Visscher, L., Buma, W. J., and Nicu, V. P. (2019). Taming conformational heterogeneity in and with vibrational circular dichroism spectroscopy. *Chemical Science, 10*(33), 7680-7689.

Kuppens, T., Langenaeker, W., Tollenaere, J. P., and Bultinck, P. (2003). Determination of the Stereochemistry of 3-Hydroxymethyl-2,3-dihydro-[1,4]dioxino[2,3-b]- pyridine by Vibrational Circular Dichroism and the Effect of DFT Integration Grids. *The Journal of Physical Chemistry A, 107*(4), 542-553.

Li, H., and Nafie, L. A. (2012). Simultaneous acquisition of all four forms of circular polarization Raman optical activity: results for α-pinene and lysozyme. *Journal of Raman spectroscopy, 43*(1), 89-94.

Neville, G. A., Deslauriers, R., Blackburn, B. J., and Smith, I. C. (1971). Conformational studies of amphetamine and medicinally important derivatives by nuclear magnetic resonance spectroscopy. *J Med Chem, 14*(8), 717-721.

Polavarapu, P. L. (2016). *Chiroptical Spectroscopy: Fundamentals and Applications* (1 ed.). Boca Raton: CRC Press.

Shen, J., Zhu, C., Reiling, S., and Vaz, R. (2010). A novel computational method for comparing vibrational circular dichroism spectra. *Spectrochimica Acta Part A: Molecular and Biomolecular Spectroscopy, 76*(3), 418-422.

Wang, T., and Dai, L. (2017). Background subtraction of Raman spectra based on iterative polynomial smoothing. *Applied spectroscopy, 71*(6), 1169-1179.

Yamamoto, S., and Bouř, P. (2018). Calculation of Vibrational Spectra of Large Molecules from Their Fragments. In *Frontiers of Quantum Chemistry* (pp. 181-197): Springer.

7. List of Author's Publications

Publications covering the presented results:

[1] Michal, P., Čelechovský, R., Dudka, M., Kapitán, J., Vůjtek, M., Berešová, M., Šebestík, J., Thangavel, K., and Bouř, P. (**2019**). Vibrational Optical Activity of Intermolecular, Overtone, and Combination Bands: 2-Chloropropionitrile and α-Pinene. *The Journal of Physical Chemistry B*, *123*(9), 2147-2156.
DOI: 10.1021/acs.jpcb.9b00403

[2] Michal, P., Kapitán, J., Kessler, J., and Bouř, P. (**2022**). Low-frequency Raman optical activity provides insight into the structure of chiral liquids. *Physical Chemistry Chemical Physics*, *24*(33), 19722-19733.
DOI: 10.1039/d2cp02290g

[3] Michal, P., Hudecová, J., Čelechovský, R., Vůjtek, M., Dudka, M., and Kapitán, J. (**2022**). Accurate Determination of Enantiomeric Excess Using Raman Optical Activity. *Symmetry*, *14*(5), 990.
DOI: 10.3390/sym14050990

[4] Dobšíková, K., Michal, P., Spálovská, D., Kuchař, M., Paškanová, N., Jurok, R., Kapitán, J., and Setnička, V. (**2023**). Conformational analysis of amphetamine and methamphetamine: a comprehensive approach by vibrational and chiroptical spectroscopy. *Analyst*, *148*(6), 1337-1348.
DOI: 10.1039/d2an02014a

Other publications:

[5] Palivec, V., Michal, P., Kapitán, J., Martinez-Seara, H., and Bouř, P. (**2020**). Raman Optical Activity of Glucose and Sorbose in Extended Wavenumber Range. *ChemPhysChem, 21*(12), 1272-1279.
DOI: 10.1002/cphc.202000261

[6] Das, M., Gangopadhyay, D., Šebestík, J., Habartová, L., Michal, P., Kapitán, J., and Bouř, P. (**2021**). Chiral detection by induced surface-enhanced Raman optical activity. *Chemical Communications, 57*(52), 6388-6391.
DOI: 10.1039/d1cc01504d

[7] Hudecová, J., Kapitán, J., Dračínský, M., Michal, P., Profant, V., and Bouř, P. (**2022**). Structure of Zinc and Nickel Histidine Complexes in Solution Revealed by Molecular Dynamics and Raman Optical Activity. *Chemistry – A European Journal, 28*(59), e202202045.
DOI: 10.1002/chem.202202045

[8] Corujo, M. P., Michal, P., Wesson, R., Amarasinghe, D. P., Rodger, A., and Chmel, N. P. (**2022**). Reduction of Background Fluorescence from Impurities in Protein Samples for Raman Spectroscopy. *Journal of Spectroscopy, 2022*, 1928091.
DOI: 10.1155/2022/1928091

[9] Wormell, P., Michal, P., Scott, A., Venkatesan, K., Mylvaganam, K., von Arx, T., Kitamura, J., Koshoubu, J., and Rodger, A. (**2023**). New Approaches to Stretched Film Sample Alignment and Data Collection for Vibrational Linear Dichroism. *ACS Omega, 8*(40), 37490-37500.
DOI: 10.1021/acsomega.3c05774